Vol. 22 No. 02
July 2025

p-ISSN 1412-2960
e-ISSN 2579-521X

Indonesian Physics Communication

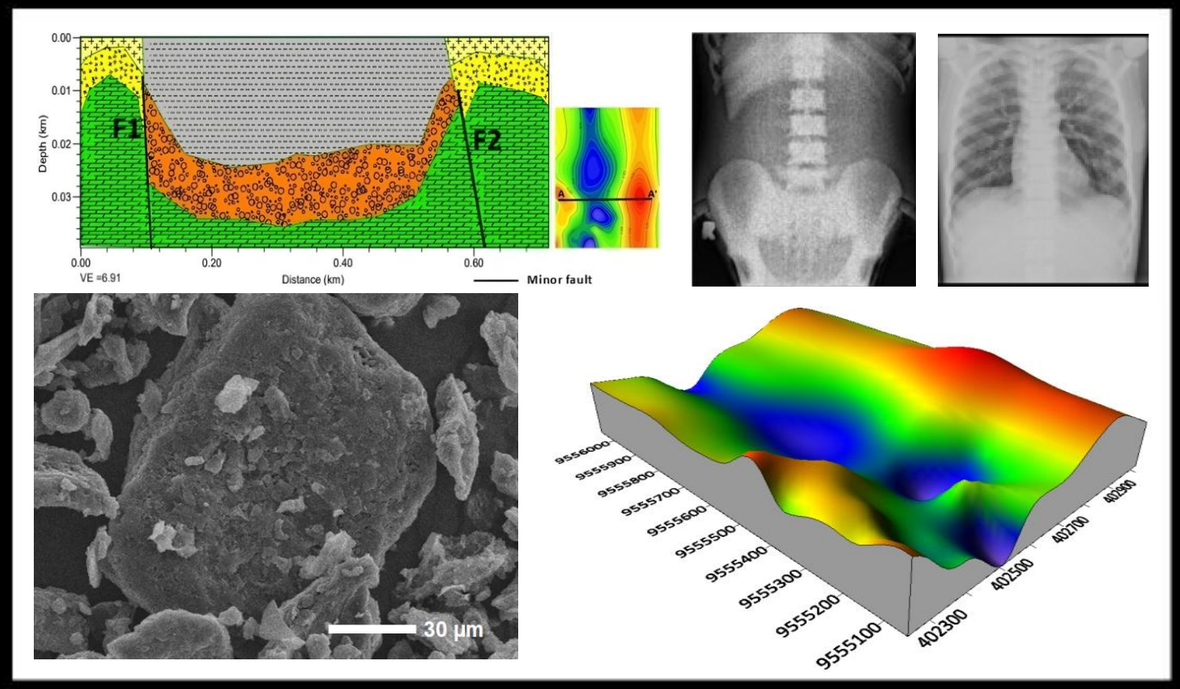

ISSN 1412 2960

Indonesian Physics Communication
Vol. 22 No. 02
July 2025
Department of Physics, Universitas Riau
Pekanbaru

Department of Physics
Faculty of Mathematics and Natural Sciences
Universitas Riau
Kampus Bina Widya Jl. HR. Soebrantas Km. 12.5
Simpang Baru Panam, Pekanbaru 28293

Vol. 22 No. 02
July 2025

p-ISSN 1412-2960
e-ISSN 2579-521X

Indonesian Physics Communication

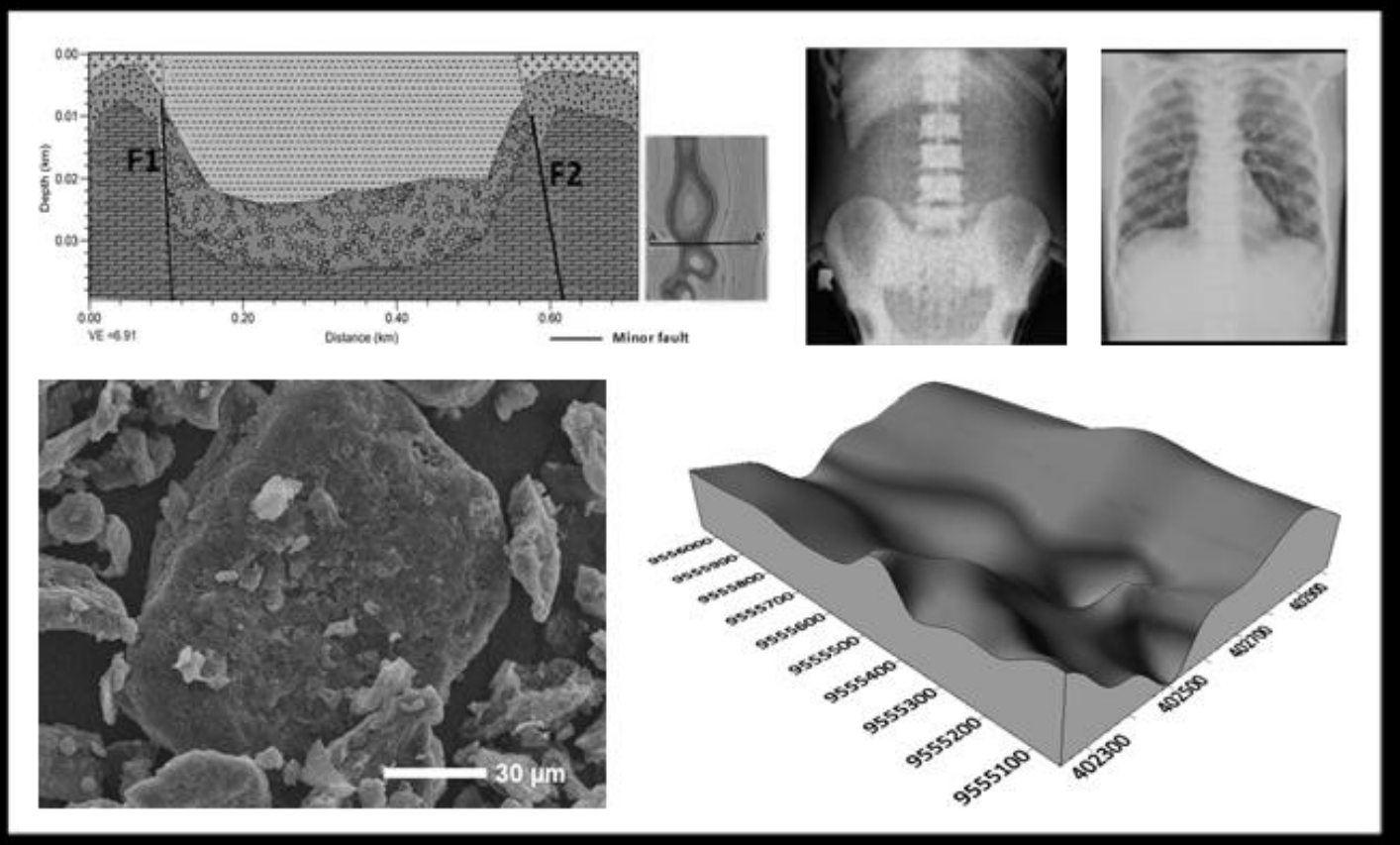

Department of Physics
Faculty of Mathematics and Natural Sciences
Universitas Riau
Kampus Bina Widya Jl. HR. Soebrantas Km. 12.5
Simpang Baru Panam, Pekanbaru 28293

Indonesian Physics Communication
Department of Physics, Universitas Riau, Pekanbaru, Indonesia
p-ISSN 1412-2960 | e-ISSN 2579-521X
Web: https://kfi.ejournal.unri.ac.id
E-mail: kfi@ejournal.unri.ac.id

Editorial Board of the Indonesian Physics Communication (IPC) Journal
Department of Physics, Faculty of Mathematics and Natural Sciences, Universitas Riau

Editorial Address:

Department of Physics, Faculty of Mathematics and Natural Sciences, Universitas Riau
Kampus Bina Widya Km 12.5 Simpang Baru Pekanbaru
Homepage: https://kfi.ejournal.unri.ac.id/index.php/JKFI
E-mail: kfi@ejournal.unri.ac.id

LIST OF CONTENTS

IPC

Indonesian Physics Communication

Department of Physics, Universitas Riau, Pekanbaru, Indonesia
p-ISSN 1412-2960 | e-ISSN 2579-521X

Vol. 22 | No. 2
July 2025

Web: https://kfi.ejournal.unri.ac.id
E-mail: kfi@ejournal.unri.ac.id

Literature study on the evaluation of lead apron thickness in radiology service units

Sharon Gracia Edward
Department of Physics, Matana University, Tangerang 15810, Indonesia

Corresponding author: shrngracia@gmail.com

ABSTRACT

Radiation protection is an effort that can be undertaken to reduce the dangers of radiation. The ALARA principle of radiation protection is needed to minimize the radiation exposure received by workers based on three components: exposure time, distance, and the use of protective equipment. Therefore, an analysis of the effectiveness of lead aprons in protecting workers from radiation exposure is conducted. The method employed involves conducting a literature review on three journals discussing the effectiveness of lead aprons in protecting workers from radiation exposure based on varying apron thicknesses and exposure factors. At 100 kVp tube voltage, a lead apron with 0.25 mmPb thickness and exposure time of 100 mAs has an effectiveness of 25% (15 years old) and 98.1% (3 years old), while a thickness of 0.35 mmPb with an exposure time of 5 mAs has an effectiveness of 93%. At 70 kVp tube voltage, a lead apron of 0.35 mmPb thickness with an exposure time of 5 mAs has an effectiveness of 98.4%. A 0.5 mmPb lead apron with exposure times ranging from 20 mAs to 72 mAs has an effectiveness between 93.75% and 99.219%. The effectiveness of a lead apron is influenced by tube voltage, exposure time, age, and quality of the lead apron. A thick apron does not necessarily have high effectiveness in protecting workers if it has poor quality, and vice versa.

Keywords: Dose; lead apron; radiation protection; radiology

Received 25-04-2025 | Revised 15-05-2025 | Accepted 05-06-2025 | Published 31-07-2025

INTRODUCTION

Radiation worker protection, also known as radiation protection, is an effort to reduce the dangers of radiation. Therefore, the principle of ALARA (As Low As Reasonably Achievable) radiation protection is needed to minimize radiation exposure received by workers based on three components: exposure time, which refers to the length of time a person is exposed to radiation; distance, which refers to how far a person is from the radiation source; and use of shielding, which refers to whether the person near the radiation source is equipped with shielding capable of protecting them from direct radiation exposure.

According to BAPETEN Regulation No. 8 of 2011, every service provider must have radiation protection equipment with a minimum of 0.25 mmPb, and its size/design must provide adequate protection to the user's body and gonads from direct radiation [1]. The protective equipment in question includes Pb aprons, Pb goggles, Pb gloves, Pb thyroid protectors, and gonad protectors. Protective equipment with a thickness equivalent to 0.25 mmPb can withstand radiation up to 100 kVp. However, increasing the exposure factors (tube voltage and exposure time) will affect the amount of radiation received. This is because tube voltage affects the radiation's penetration power, and exposure time affects the dose. Therefore, a thicker apron is required.

Based on this, an analysis was conducted on the effectiveness of aprons in protecting workers from radiation exposure with varying thicknesses: 0.25 mmPb, 0.35 mmPb, and 0.5 mmPb. This was done to determine the effectiveness of the aprons used in protecting workers from radiation exposure.

RESEARCH METHODS

This research was conducted using a literature review method, compiling references

from several previous studies and then compiling them into a conclusion [2].

The data analysis technique used in this study was content analysis to obtain valid data. The analysis involved sorting, comparing, combining, and selecting data to obtain relevant data [3]. The journals analyzed were "Radiological Evaluation of Lead Apron Integrity in Five Selected Hospitals in Abuja, Nigeria" [4] as the first journal; "Analysis of the Effectiveness of 0.35 mmPb Apron in Protecting Radiation Workers in Radiography Examination" [5] as the second journal; and "Evaluation of the Adequacy of Lead Apron Thickness to Support Radiation Safety Assurance in Hospital Radiology Service Units" [6] as the third journal. These three journals were then analyzed to obtain a conclusion.

RESULTS AND DISCUSSION

This study compared the effectiveness of aprons in protecting workers from radiation exposure based on their thickness: 0.25 mmPb, 0.35 mmPb, and 0.5 mmPb.

Based on the first journal, "Radiological Evaluation of Lead Apron Integrity in Five Selected Hospitals in Abuja, Nigeria" [4], an evaluation of lead apron quality was conducted. An X-ray source, an Optically Stimulated Luminescence Dosimeter (OSLD) as the detector, and a lead apron with a thickness equivalent to 0.25 mmPb were used. The exposure factors applied to the source were 100 kVp and 100 mAs; and the measurement distance used was 100 cm. The measurement procedure involved placing the OSLD before and after the apron and phantom to determine the dose received (incoming dose) and the dose transmitted (outgoing dose). The obtained data was then processed to obtain the percentage transmitted dose using Equation (1).

$$Transmission\ T = \frac{Dose\ out}{Dose\ in} \times 10 \qquad (1)$$

This yields a transmitted dose percentage of 75% for 15-year-old lead apron A, with an incoming dose of 0.12 Gy and an outgoing dose of 0.09 Gy. For 3-year-old lead apron B, the transmitted dose percentage was 1.9%, with an incoming dose of 0.108 Gy and an outgoing dose of 0.02 Gy.

Based on the second journal article, "Analysis of the Effectiveness of 0.35 mmPb Aprons in Protecting Radiation Workers in Radiography Examination" [5], a test was conducted on the effectiveness of aprons with a thickness equivalent to 0.35 mmPb on radiation workers during radiography examinations. The analysis was conducted using a GE multipurpose 500 mA X-ray machine as the radiation source, a radiation multidetector as the detector, and an anthropomorphic phantom as the target. The radiation exposure measurement procedure involved positioning the detector above the phantom to obtain radiation exposure data without an apron, or as described in the data as "non-apron." The apron was then placed over the detector to obtain radiation exposure data when using an apron, or as described in the data as "apron." The exposure factor was adjusted with varying tube voltages of 45-100 kVp and exposure times of 5 mAs; a measurement distance from the X-ray tube to the detector of 100 cm; and varying the irradiation field sizes, namely 18 × 24 cm and 43 × 35 cm.

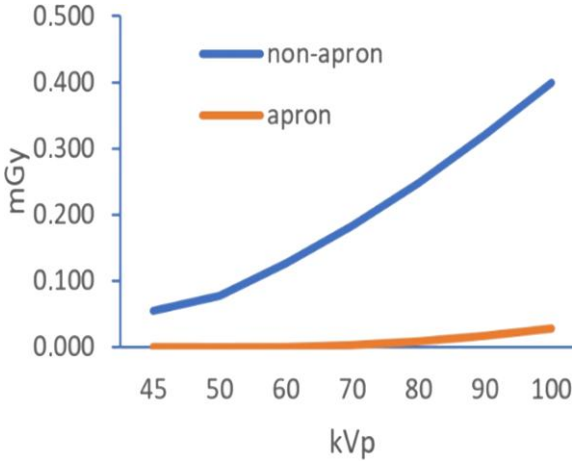

Figure 1. Radiation exposure measurement curve in an 18 × 24 cm irradiation field.

In the irradiation fields of 18 × 24 cm (Figure 1) and 43 × 35 cm (Figure 2), with

varying tube voltages of 45-100 kVp, the radiation exposure results were the same for the "non-apron" (0.050 – 0.400 mGy) and for the "apron" (0 – 0.020 mGy).

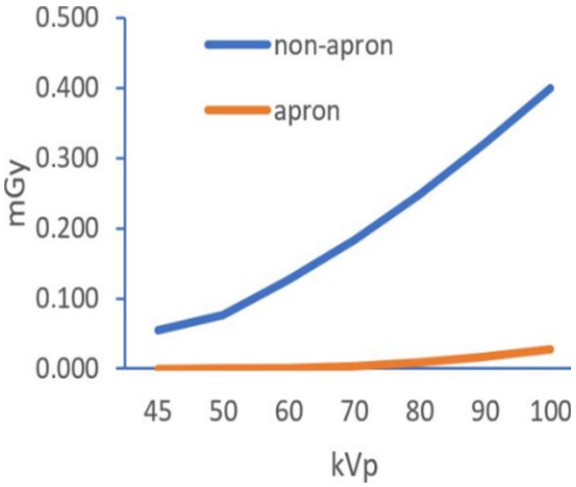

Figure 2. Radiation exposure measurement curve in an 43 × 35 cm irradiation field.

A calculation was then performed to determine the percentage effectiveness of the apron used, using Equation (2).

$$Eff\,(\%) = \left(1 - \frac{apron\ exposure\ (mGy)}{non-apron\ exposure\ (mGy)}\right) \times 100 \quad (2)$$

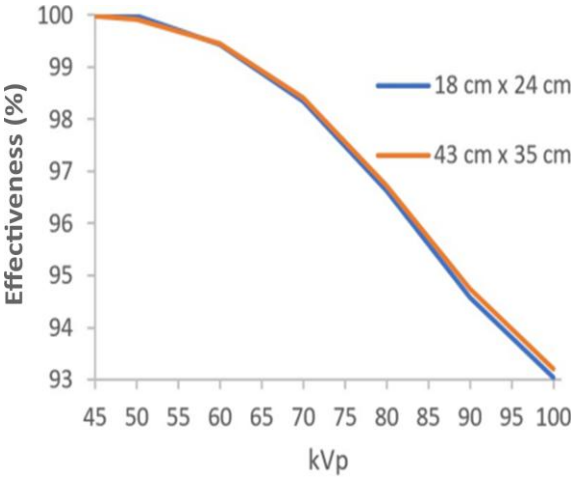

Figure 3. Curve of the effect of tube voltage on the effectiveness of a 0.35 mmPb lead apron.

The percentage effectiveness of the apron is depicted in the curve (Figure 3), where the apron with a thickness equivalent to 0.35 mmPb and a tube voltage variation of 45 – 100 kVp is 93% – 100%.

Based on the third journal, "Evaluation of the Adequacy of Lead Apron Thickness to Support Radiation Safety Guarantees in Hospital Radiology Service Units" [6], an evaluation was conducted to determine the adequacy of lead aprons with a thickness equivalent to 0.5 mmPb in each radiology unit in hospitals in Semarang. This evaluation was conducted using a conventional X-ray machine as a radiation source, which was directly fired at an apron with a thickness equivalent to 0.5 mmPb, which was stretched on an examination table at a distance of 100 cm from the X-ray tube. Two dose rate measurement conditions were performed: the dose rate before passing through the lead apron and the dose rate after passing through the lead apron. Using 11 apron samples obtained from four different radiology units with the same thickness, but exposed to X-rays with different exposure factors, the HVL value was calculated using Equation (3).

$$D_t = D_0 \left(\frac{1}{2}\right)^{\frac{x}{HVL}} \quad (3)$$

where:

D_t = dose rate after passing through the lead apron.
D_0 = dose rate before passing through the lead apron.
x = lead apron thickness.
HVL = lead apron thickness.

In radiology unit A, irradiation was performed on two aprons with an exposure factor of 70 kV and 40 mAs, resulting in a dose rate transmitted to both aprons of 6.25%, with an HVL value of 4 HVL. In radiology unit B, irradiation was performed on two aprons with the lead aprons in the condition shown in Figure 4, with cracks on the bottom and sides of the aprons. Irradiation was performed with an exposure factor of 70 kV and 20 mAs, resulting in a dose rate transmitted to both aprons of 6.25%, with an HVL value of 4 HVL. In radiology unit C, irradiation was carried out on 2 (two) lead aprons with an exposure factor of

70 kV and 72 mAs, the dose rate transmitted by both aprons was 6.25% and the HVL value was 4 HVL. In radiology unit D, irradiation was carried out on 6 (six) lead aprons with an exposure factor of 70 kV and 30 mAs, the dose rate transmitted by the five aprons was 3.125% and the HVL value was 5 HVL; and the dose rate transmitted by the only apron in radiology unit D was 0.781% and the HVL value was 7 HVL. The linear attenuation coefficient was then calculated using Equation (4).

$$\mu = \frac{\ln 2}{HVL} = \frac{0{,}693}{HVL} \quad (4)$$

This concludes that the attenuation coefficient and HVL are inversely proportional, where the larger the HVL, the smaller the linear attenuation coefficient.

According to Aizah, the larger the exposure factor applied, the greater the resulting exposure dose, thus requiring thicker protective equipment to protect against radiation exposure; in this case, the protective equipment in question is a lead apron [7]. However, several factors can influence the effectiveness of the lead apron, one of which is ensuring the quality of the lead apron used.

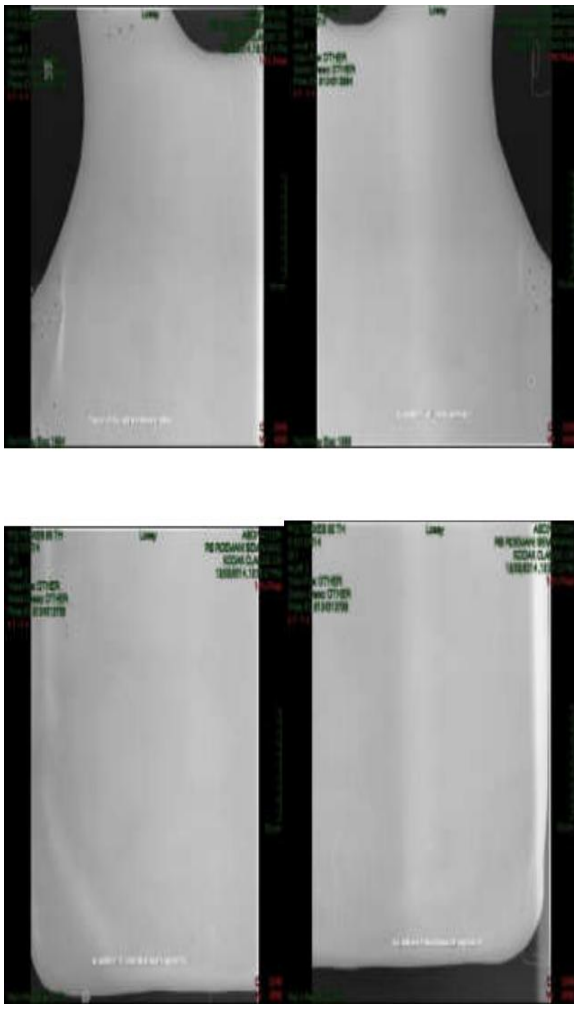

Figure 4. Results of lead apron irradiation in radiology unit B.

Table 1. Results of the lead apron effectiveness evaluation.

Journal	Tube voltage (kVp)	Exposure time (mAs)	Apron thickness (mmPb)	Effectiveness (%)
2	70	5	0.35	98.4
3		20	0.5	93.75
		40		93.75
		30		93.75
		72		96.88
1	100	100	0.25 (3 year)	98.1
			0.25 (15 year)	2
2		5	0.35	93

Based on the results obtained from the analysis of the effectiveness of lead aprons at thicknesses of 0.25 mmPb, 0.35 mmPb, and 0.5 mmPb through a literature review of three scientific journals, the percentage value of lead apron effectiveness was obtained using Equations (5) and (6).

$$Eff\ (\%) = 100\% - rate\ dose\ (\%) \quad (5)$$

$$Eff\ (\%) = 100\% - transmitted\ dose\ (\%) \quad (6)$$

At a tube voltage of 100 kVp, lead aprons A (age 15) and B (age 3) with a thickness of 0.25 mmPb and an exposure time of 100 mAs have a

transmitted dose of 75% and 1.9%, respectively, meaning the lead apron's effectiveness is 25% and 98.1%, respectively. This is due to the difference in age of the lead aprons. Meanwhile, a 0.35 mmPb lead apron with an exposure time of 5 mAs has a 93% effectiveness. In this case, the apron thickness does not affect its effectiveness in protecting against radiation exposure. The radiation dose delivered to the 0.25 mmPb lead apron is greater than that delivered to the 0.35 mmPb lead apron. However, the 0.25 mmPb lead apron is 98% effective.

At a tube voltage of 70 kVp, a lead apron with a thickness of 0.35 mmPb with an exposure time of 5 mAs, has an effectiveness percentage of 98.4%. Meanwhile, for a lead apron thickness of 0.5 mmPb with an exposure time of 20 mAs, 40 mAs, 30 mAs, 72 mAs, respectively, has an effectiveness percentage of 93.75%, 93.75%, 93.75%, and (96.875% and 99.219%). Based on (Aizah, 2023), mAs affects the dose generated by an X-ray radiation exposure. However, in the case of a lead apron with a thickness of 0.5 mmPb, there is an increase in the effectiveness percentage when the exposure time is increased (40 mAs to 72 mAs). This is very possible to occur, seen from the number of samples used for testing, namely 12 lead aprons. It is very possible that the members of the sample are aprons with the same thickness but have different qualities.

CONCLUSION

Based on the literature review, it was concluded that at a tube voltage of 100 kVp, a 0.25 mmPb lead apron (aged 3 years) with an exposure time of 100 mAs had a higher effectiveness percentage than a 0.35 mmPb lead apron with an exposure time of 5 mAs, at 98.1%. At a tube voltage of 70 kVp, a 0.35 mmPb lead apron with an exposure time of 5 mAs had a higher effectiveness percentage than a 0.5 mmPb lead apron with exposure times of 20 mAs, 40 mAs, 30 mAs, and 72 mAs, at 98.4%.

Factors that influence the effectiveness of lead aprons as personal protection from radiation exposure include: the specified exposure time, as this will affect the resulting dose; the age of the lead apron; and the quality of the lead apron; the presence of cracks and/or other conditions. Because it has been proven that good quality lead aprons are more effective in protecting yourself from radiation exposure compared to thick lead aprons of poor quality.

REFERENCES

1. BAPETEN. (2011) *Peraturan Kepala Badan Pengawas Tenaga Nuklir Nomor 8 Tahun 2011 tentang Keselamatan Radiasi Dalam Penggunaan Pesawat Sinar X Radiologi Diagnostik dan Intervensional*. Jakarta, Indonesia.
2. Mardalis, M. (1993). *Metode penelitian: suatu pendekatan proposal*. Jakarta, Indonesia.
3. Krippendorff, K. (1991). *Analisis isi: Pengantar teori dan metodologi*. Jakarta, Indonesia.
4. Ilupeju, Y., Ibrahim, U., Yusuf, S. D., Mundi, A. A., & Idris, M. M. (2021). Radiological evaluation of lead apron integrity in five selected hospitals in Abuja, Nigeria. *Journal of Radiography and Radiation Sciences*, **35**(1), 1–5.
5. Irsal, M., Sutoro, S. G., Widiamoko, M. E., Tarigan, A., Winarno, G., & Prananto, L. (2023). Analisis Efektivitas Apron 0.35 mmPb dalam Melindungi Pekerja Radiasi pada Pemeriksaan Radiografi. *Jurnal Kesehatan Vokasional*, **8**(3), 134–142.
6. Kartikasari, Y., Darmini, D., & Rochmayanti, D. (2015). Evaluasi Kecukupan Tebal Lead Apron Guna Mendukung Jaminan Keselamatan Radiasi pada Unit Pelayanan Radiologi Rumah Sakit. *LINK*, **11**(2), 995–1002.

7. Aizah, H. S. (2023). *Pengaruh faktor eksposi terhadap dosis radiasi dan kualitas citra pesawat radiografi umum pada pemodelan phantom thoraks*. Doctoral dissertation, Universitas Islam Negeri Maulana Malik Ibrahim.

IPC

Indonesian Physics Communication

Department of Physics, Universitas Riau, Pekanbaru, Indonesia
p-ISSN 1412-2960 | e-ISSN 2579-521X

Vol. 22 | No. 2
July 2025

Web: https://kfi.ejournal.unri.ac.id
E-mail: kfi@ejournal.unri.ac.id

Literature study on the effect of exposition factors on image quality in the aspect of gray degree

Nicholas Austrin Theos
Department of Physics, Matana University, Tangerang 15810, Indonesia

Corresponding author: nicholastheos09@gmail.com

ABSTRACT

This literature study aims to examine the influence of exposure factors on the quality of radiographic images in the field of radiodiagnostics. Three scientific journals were used as research materials, focusing on adjusting tube voltage (kV) and exposure time (mAs) to optimize image quality. Experiments were conducted using Computed Radiography (CR) and Digital Radiography (DR) on different phantoms, such as water in a plastic bag as phantom, ossa manus phantom (hand), and abdominal phantoms. The results of the study indicate that the optimal combination of tube voltage and exposure time varies depending on the density and thickness of the tissues being examined. In conclusion, the proper adjustment of exposure factors is key to obtaining high-quality radiographic images for diagnosing diseases or lesions.

Keywords: Exposure factors; images; phantom; radiography

Received 25-04-2025 | Revised 09-05-2025 | Accepted 06-06-2025 | Published 31-07-2025

INTRODUCTION

Ideal healthcare for the entire community requires a supporting field. One such field is the examination field, which assists in diagnosing lesions. One field capable of diagnosing disease is radiodiagnostics. This field diagnoses lesions or diseases using X-ray radiation. This is possible thanks to technological advances in health examinations. Generally, every hospital already has these devices; the most common devices found in hospitals are Computed Radiography (CR) and Digital Radiography (DR) [1].

CR and DR require regular Quality Control (QC) to maintain and ensure the quality of the equipment and maximize the quality of the images produced. If the image quality is poor, the information provided by the image will not be optimal. If the information provided is not optimal, it will be difficult to diagnose a disease or lesion. The examination is expected to produce high-quality radiographic images with minimal radiation exposure [2]. This fulfills one of the principles of radiation protection, namely justification. Justification states that the benefits obtained from the use of radiation far outweigh the risks posed by the radiation [3].

Several factors influence the quality of radiographic images, including density, contrast, and sharpness. One of these factors is the exposure factor. The exposure factor is a factor that influences the quality and quantity of X-ray radiation emitted by the X-ray machine required to produce a radiographic image. The exposure factor consists of tube voltage (kV) and current-time (mAs). Proper adjustment of these exposure factors can produce optimal image contrast to provide maximum information [4].

RESEARCH METHODS

This research was conducted using a literature study method. The literature study method is one way of research by collecting library data, reading, recording, and processing the data into a study [5]. For this research, 3 libraries were used in the form of scientific journals whose contents were about the effect of exposure factors on the quality of radiographic images, by varying the tube voltage (kV) and time-current (mAs) to obtain

the optimum exposure factor to obtain good image quality. The scientific journals used in this literature study are entitled "The Effect of Exposure Factors on Radiographic Image Quality" (2017), "The Effect of Tube Voltage (kV) on Radiographic Image Quality of Digital Radiography (DR) X-ray Machines on the Abdomen Phantom" (2017), and "The Effect of Exposure Factors on Radiographic Image Quality on Thorax Phantom with PA Projection" (2022).

RESULTS AND DISCUSSION

In the journal "The Effect of Exposure Factors on Radiographic Image Quality," a study was conducted on X-ray irradiation using CR on a phantom consisting of water in a plastic bag placed on a CR cassette, and its distance from the tube was set at 1 m. Several experiments were conducted with variations in tube voltage (kV), namely, 60 kV; 65 kV; 70 kV; 75 kV; and 80 kV, and current-time (mAs) of 20 mAs; 25 mAs; and 30 mAs. The following are the results of the experiments conducted.

Table 1 shows that at a 20 mAs current-time voltage, the water phantom image has fairly good quality at the 60 kV and 65 kV tube voltages, due to the clear sharpness and contrast. For the 70 kV tube voltage, the contrast is predominantly gray, making it difficult to distinguish the individual parts, indicating poor image quality. Meanwhile, for the 75 kV and 80 kV tube voltages, the dominant color is black or darker. This indicates that the water phantom image quality at the 75 kV and 80 kV tube voltages cannot be considered good, as it is difficult to see the object.

Table 2 shows the image results from a 25 mAs current-time voltage with various tube voltages. Only the 60 kV tube voltage image shows good contrast and sharpness, allowing objects to be clearly visible. The 65 kV, 70 kV, 75 kV, and 80 kV tube voltage images show poor quality, as the grayscale is predominantly black, making objects difficult to see, or even completely invisible.

Table 1. Radiographic image results with a 20 mAs current-time voltage [1].

Tube voltage	Radiography image results	Image grayscale
60 kV	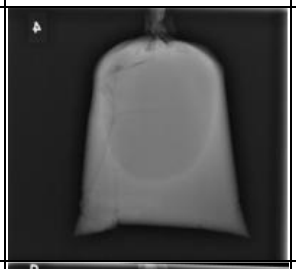	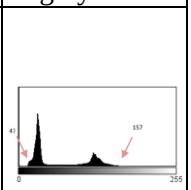
65 kV	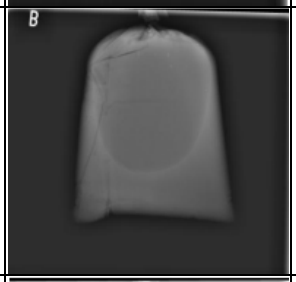	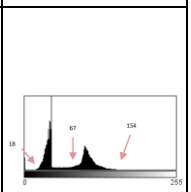
70 kV	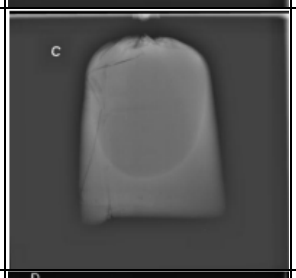	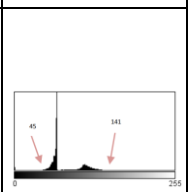
75 kV		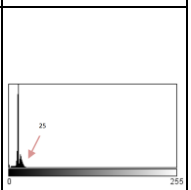
80 kV	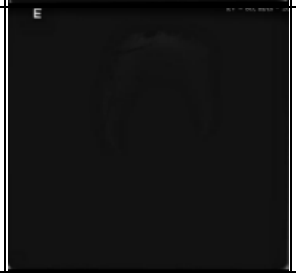	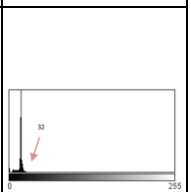

Table 3 shows the image results at a 30 mAs current-time voltage. This table shows that at 60 mAs and 65 mAs tube voltages, the object is still visible but with very low contrast and sharpness. At 60 mAs, the image is too dark or predominantly black, and at 65 mAs, the image is too light or predominantly gray. For 70 kV,

75 kV, and 80 kV tube voltages, the image results show no image (the phantom is not visible). This indicates that the water phantom with a 30 mAs current-time voltage does not produce good image quality for the tube voltage variations specified for this experiment.

Table 2. Radiographic image results with a 25 mAs current-time voltage [1].

Tube voltage	Radiography image results	Image grayscale
60 kV	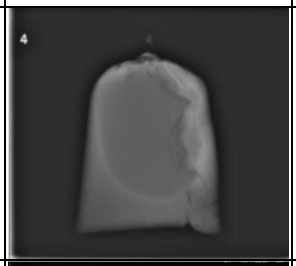	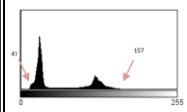
65 kV		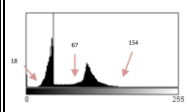
70 kV	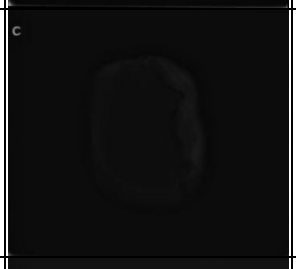	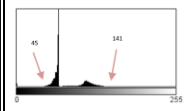
75 kV	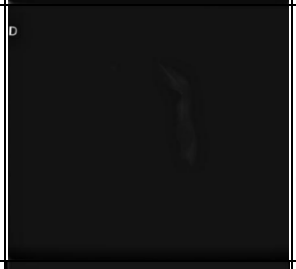	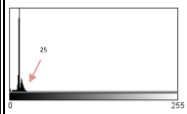
80 kV	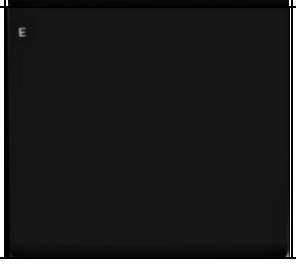	

The journal, "The Effect of Tube Voltage (kV) on the Quality of Digital Radiography (DR) X-ray Images on an Abdominal Phantom," the journal presents the results of a study using DR to obtain images from an abdominal phantom. This experiment was conducted 10 times with varying tube voltages: 40 kV, 45 kV, 50 kV, 55 kV, 60 kV, 65 kV, 70 kV, 75 kV, 80 kV, and 85 kV. The following table shows the results of the experiment.

Table 3. Radiographic image results with a 30 mAs current-time voltage [1].

Tube voltage	Radiography image results	Image grayscale
60 kV		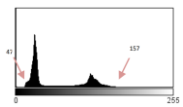
65 kV	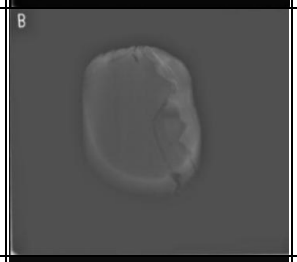	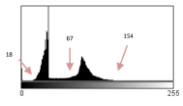
70 kV	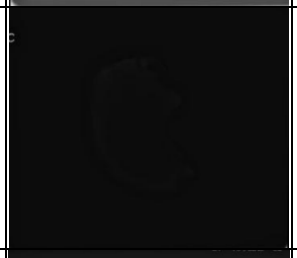	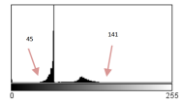
75 kV	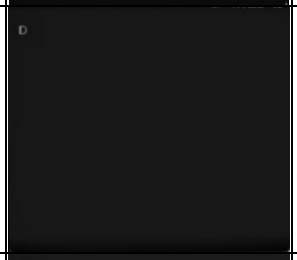	
80 kV	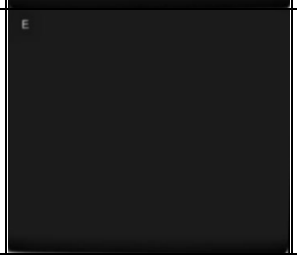	

Table 4 shows the results of DR images with an unknown current-time value but varying tube voltages.

Table 4. Radiographic image results with a 30 mAs current-time value [2].

Tube voltage	Radiography image results	Image grayscale
40 kV		
45 kV		
50 kV		
55 kV		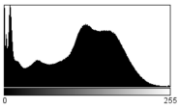
60 kV		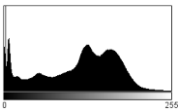
65 kV		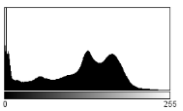
70 kV		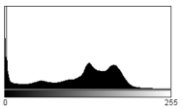
75 kV		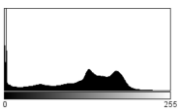
80 kV		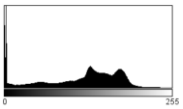
85 kV		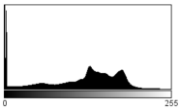

Table 5. Radiographic image results with 30 mAs current-time [4].

kV	mAs	Radiography image results	Image grayscale
55	10	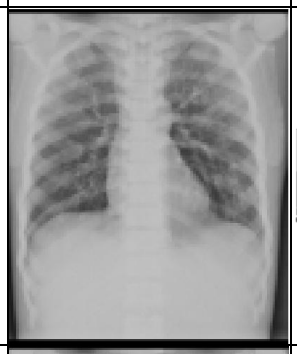	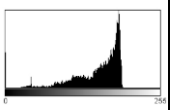
55	12		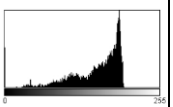
60	10	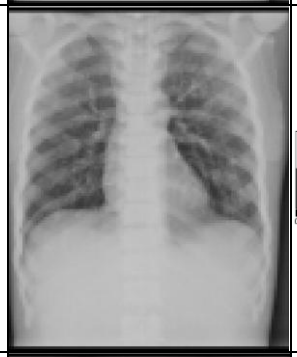	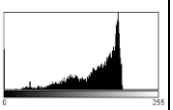
60	12	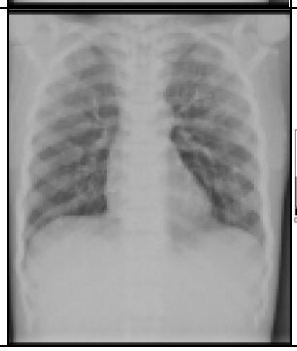	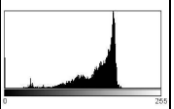

Tube voltages of 40 kV, 45 kV, 50 kV, and 55 kV produced images with good sharpness and clarity, but noise interfered with the images, making them less than satisfactory. A tube voltage of 60 kV produced good image quality because the image had good sharpness and contrast, as evidenced by the nearly even distribution of grayscale colors, allowing for

clear image visibility and maximum information. At tube voltages of 65 kV, 70 kV, 75 kV, 80 kV, and 85 kV, the dominant color tends to be bright, which reduces contrast. This can be seen in the grayscale histogram, which tends to be high in the lighter areas. Consequently, the image quality can be considered poor or not providing optimal information.

A recent paper entitled "The Effect of Exposure Factors on Radiographic Image Quality on a Thorax Phantom with PA Projection" presents the results of a study using CR to obtain images from a thorax phantom. This experiment was conducted in The experiment was performed four times with varying combinations of tube voltage and current-time: 55 kV with 10 mAs, 55 kV with 12 mAs, 60 kV with 10 mAs, and 60 kV with 12 mAs. The following table shows the results of the experiments.

Table 5 shows the CR image results with several different exposure factor combinations: 55 kV with 10 mAs, 55 kV with 12 mAs, 60 kV with 10 mAs, and 60 kV with 12 mAs. It was found that there were no significant differences between the resulting images, as can be seen visually and from the grayscale. It can be concluded that all of the images are of good quality and provide sufficient information.

CONCLUSION

Based on the data obtained from this literature study, in the first journal entitled "The Effect of Exposure Factors on Radiographic Image Quality" it is known that the optimum exposure factor to obtain good image quality is at a tube voltage of 60 kV and a current-time of 25 mAs. For the second journal entitled "The Effect of Tube Voltage (kV) on the Quality of Radiographic Images of Digital Radiography (DR) X-ray Machines on the Abdomen Phantom" the optimum exposure factor for the abdominal phantom to obtain good quality images is at a tube voltage of 60 kV and an unknown current-time. In the last journal entitled "The Effect of Exposure Factors on Radiographic Image Quality on Thorax Phantom with PA Projection" the optimum exposure factor for the thorax phantom to obtain good quality images is at different combinations, namely, 55 kV with 10 mAs, 55 kV with 12 mAs, 60 kV with 10 mAs, 60 kV with 12 mAs. The images produced by different exposure factors do not have much difference in image quality, this can be seen visually and in the degree of gray. It can be concluded from the three journals that each part of the human body requires a different combination of exposure factors depending on the thickness and density, because if the body part has a high density or thickness, the X-rays will be absorbed more than the body part or object with low or thin density [6].

REFERENCES

1. Nehru, N. (2017). Pengaruh Faktor Eksposi Terhadap Kualitas Citra Radiografi. *Journal Online of Physics*, **3**(1), 14–22.
2. Sriwahyuni, S. (2017). Pengaruh Tegangan Tabung (Kv) terhadap Kualitas Citra Radiografi Pesawat Sinar-X Digital Radiography (DR) pada Phantom Abdomen. *SPEKTRA: Jurnal Fisika Dan Aplikasinya*, **2**(2), 113–118.
3. Cahyati, Y., Prisyanto, R., & Kurniawan, R. (2017). Analisa Tingkat Paparan Radiasi Pesawat Sinar-X Konvensional Terhadap Besar Dosis Yang Diterima Pekerja Di Laboratorium Dan Klinik Radiologi (STIKes Widya Cipta Husada Malang). *Jurnal Health Care Media*, **3**(1), 20–24.
4. Prayoga, A. N., Suraningsih, N., & Puspita, M. I. (2022). The effect of exposure factors on radiographic image quality on thorax phantom with PA projection. *Jurnal Ilmu dan Teknologi Kesehatan STIKES Widya Husada*, **13**(1).

5. Kartiningrum, E. D. (2015). *Panduan Penyusunan Studi Literatur*. LPPM, Politeknik Kesehatan Majapahit, Mojokerto.
6. Yufita, E. & Safitri, R. (2023). Analisa Pengaruh Faktor Eksposi Pesawat Sinar-X Terhadap Densitas Optik Film Radiografi. *Jurnal Hadron*, **5**(1), 9–14.

IPC

Indonesian Physics Communication

Department of Physics, Universitas Riau, Pekanbaru, Indonesia
p-ISSN 1412-2960 | e-ISSN 2579-521X

Vol. 22 | No. 2
July 2025

Web: https://kfi.ejournal.unri.ac.id
E-mail: kfi@ejournal.unri.ac.id

Identification of subsurface structure using the pseudo-gravity method of magnetic data at the geothermal area of Sonai Village and its surroundings, Puriala, Konawe Regency

Misbayanti Dian Ratu[1], Abdul Manan[1,*], Bahdad[2], and Rani Chahyani[3]
[1]Department of Geophysical Engineering, Universitas Halu Oleo, Kendari 93232, Indonesia
[2]Department of Oceanography, Universitas Halu Oleo, Kendari 93232, Indonesia
[3]Study Program of Physics Education, Institut Agama Islam Negeri Kendari, Kendari 93116, Indonesia

*Corresponding author: amanan@uho.ac.id

ABSTRACT

It has been conducted a geomagnetic research in the geothermal area of Sonai Village and its surroundings, Puriala, Konawe Regency, which aims to identify the structure of the subsurface using the pseudo-gravity method. After performing diurnal and IGRF corrections on the measurement data, the residual magnetic field anomaly is obtained around -150 to 90 nT. Furthermore, transformation process using the pseudo-gravity method is carried out, and the anomaly contour density is obtained around -0.07 to 0.06 mGal. The results of 2D modeling of 2 slices on the residual magnetic anomaly map that have undergone pseudo-gravity transformation show that the subsurface layers of the research area are composed of 3 formations. Layers with density values of 1.5 and 2.5 g/cm^3 are thought to be Alluvium Deposits in the form of sand and clay, layers with density values of 2.6 and 2.78 g/cm^3 are sandstone and conglomerate in the Alangga Formation, and a layer with a density value of 2.84 g/cm^3 is peridotite in the Ultramafic Complex (bedrock layer). In addition, several minor faults were also found, and among them 2 minor faults adjacent to geothermal manifestation are located at coordinates of approximately 4^{o}1'16.149" South Latitude dan 122^{o}7'9.609" East Longitude with a distance of ±15 meters, and at coordinates of approximately 4^{o}1'23.388" South Latitude dan 122^{o}7'24.326" East Longitude which is ±28 meters from the manifestation. These minor faults cut through the peridotite layer and the conglomerate layer, and are thought to be the migration path of hot fluids towards the surface.

Keywords: Geothermal area; magnetic anomaly; pseudo-gravity method; subsurface structure

Received 01-06-2025 | Revised 30-06-2025 | Accepted 08-07-2025 | Published 31-07-2025

INTRODUCTION

Sulawesi Island is one of the islands where most of the geothermal potential is associated with a non-volcanic geological environment. The Sulawesi region in the southeast has the geothermal potential spread from mainland Sulawesi to Buton Island. The geothermal system on the mainland is more influenced by the combination of the influence of geological structure and the remaining heat from magmatic activity, generally appearing in the metamorphic and sedimentary rock environment [1, 2]. The non-volcanic geothermal system is usually associated with the existence of faults in the subsurface of the Earth [3-5]. One area in the Southeast Sulawesi that has the geothermal potential is in Sonai Village, Puriala District, Konawe Regency.

Geothermal system is a natural heat transfer in a certain volume of the Earth's crust that carries heat from the heat source to the place of heat release, which is generally the ground surface. Generally, rocks in geothermal systems have low magnetization due to the demagnetization process by the hydrothermal alteration process. This process changes existing minerals into paramagnetic and diamagnetic minerals [4, 5].

The Sonai geothermal area was studied by the Geological Agency of the Ministry of Energy and Mineral Resources RI in 2015 in the form of a preliminary geochemical survey [6]. Then [7] also studied this area to determine

the distribution of hot fluids using the Wenner-Schlumberger configuration geoelectric method. The latest, [8] studied this geothermal area using the Euler Deconvolution method.

In this research, the magnetic method was used to determine the types of rock layers and the possibility of faults existence in the Earth's subsurface. The geomagnetic method works based on the magnetic properties of subsurface rocks which are known through measurements of the intensity of the magnetic field on the Earth's surface [9, 10]. To clarify the location of the object causing the subsurface anomaly, a transformation using the pseudo-gravity method was carried out on residual magnetic field anomaly data.

Geophysical researches on geothermal using geomagnetic method, some of which have been conducted by [11] at Buaran geothermal manifestation area Brebes Regency, [12] at geothermal area of Umbul-Telomoyo Temple Magelang Regency, [13] at geothermal manifestation of Karangrejo Pacitan Regency, [14] at the Banyu Biru hotspring Nganjuk Regency, [15] at Sampuraga geothermal manifestation area Mandailing Natal Regency, [16] at Nagari Aie Angek geothermal prospect area Tanah Datar Regency, and [17] at the Tinggi Raja geothermal area Simalungun Regency. The results of these studies show that the magnetic method provides good results in identifying the subsurface structure of geothermal potential area.

LITERATURE REVIEW

Regional Geology of Research Area

Regionally, Puriala District is included in the geological map of the Kolaka Sheet [18]. Based on the rock assemblage and its characteristics, the geology of the Kolaka Sheet can be divided into two geological belts, namely the Tinodo Belt and the Hialu Belt. The rocks found in the Tinodo Belt which are the basement rocks are Paleozoic Metamorphic Rocks (Pzm) and are thought to be of Carboniferous age, consisting of mica schist, quartz schist, chlorite schist, graphite mica schist, slate and gneiss. Meanwhile, the rocks found in the Hialu Belt are Ophiolite Rocks (Ku) consisting of peridotite, harzburgite, dunite and serpentinite. These Ophiolite rocks are unconformably overlain by the Matano Formation (Km) of Late Cretaceous age and consist of layered limestone intercalated with chert at the bottom. Molasse type sedimentary rocks of Late Miocene-Early Pliocene age form the Pandua Formation (Tmpp) consisting of conglomerate and sandstone intercalated with silt. This formation unconformably overlaps all older formations, both in the Tinodo Belt and the Hialu Belt. In the Late Pleistocene, coral reef limestone (Ql) and the Alangga Formation (Qpa) were formed, consisting of sandstone and conglomerate. The youngest rocks in this sheet are Alluvium (Qa) consisting of river, swamp and beach deposits [19, 20].

The Sonai area which is the research location is included in the Hialu Belt which consists of Alluvium Deposits, the Alangga Formation and the Ultramafic Complex. The distribution of the geological conditions of the research location is shown in Figure 1.

Magnetic Method

The magnetic method is one of the geophysical methods interpreted in the form of magnetic material distribution based on the measurement of variations in magnetic field intensity on the earth's surface. This method is carried out based on the results of magnetic field intensity measurements caused by differences in susceptibility contrast or magnetic permeability of rocks from the surrounding area [10, 21].

The basis of the magnetic method is the Coulomb force F (dyne). If there are two magnetic poles P1 and P2 that are separated by a distance of r (cm), then there will be a Coulomb force F of [10]:

$$\vec{F} = \frac{P_1 P_2}{\mu_o r^2} \hat{r} \quad (1)$$

where, μ_o is the permeability of the medium in a vacuum, is dimensionless and has a value of 1, and r represents a unit vector in the direction from P_1 to P_2. The value of μo in SI units is $4\pi \times 10^{-7}$ N/A^2.

Pseudo-Gravity Method

[22] explained that the pseudo-gravity method is a transformation that makes the magnetic anomaly value comparable to the gravity anomaly value. Pseudo-gravity transformation is one method that functions to clarify the location of objects causing subsurface anomalies [23]. The working principle of the pseudo-gravity method uses the Poisson relation. This relation states that the magnetic potential V and the gravitational potential U originating from a uniform density or a uniformly magnetized object have a relationship like the formula below [22]:

$$V = \frac{C_m}{\gamma}\frac{M}{\rho} m \bullet \nabla_p U = -\frac{C_m}{\gamma}\frac{M}{\rho} g_m \qquad (2)$$

where, V is the magnetic potential, U the gravitational potential (m/s^2), m the direction of magnetization, gm the component of the gravitational force in the direction of magnetization, γ Newton's constant (6.67 × 1011 m^{3}kg^{-1}sec^{-2}), ρ the density of the rock (kg/m^3), C_m the magnetic constant, and M the magnetization (A/m).

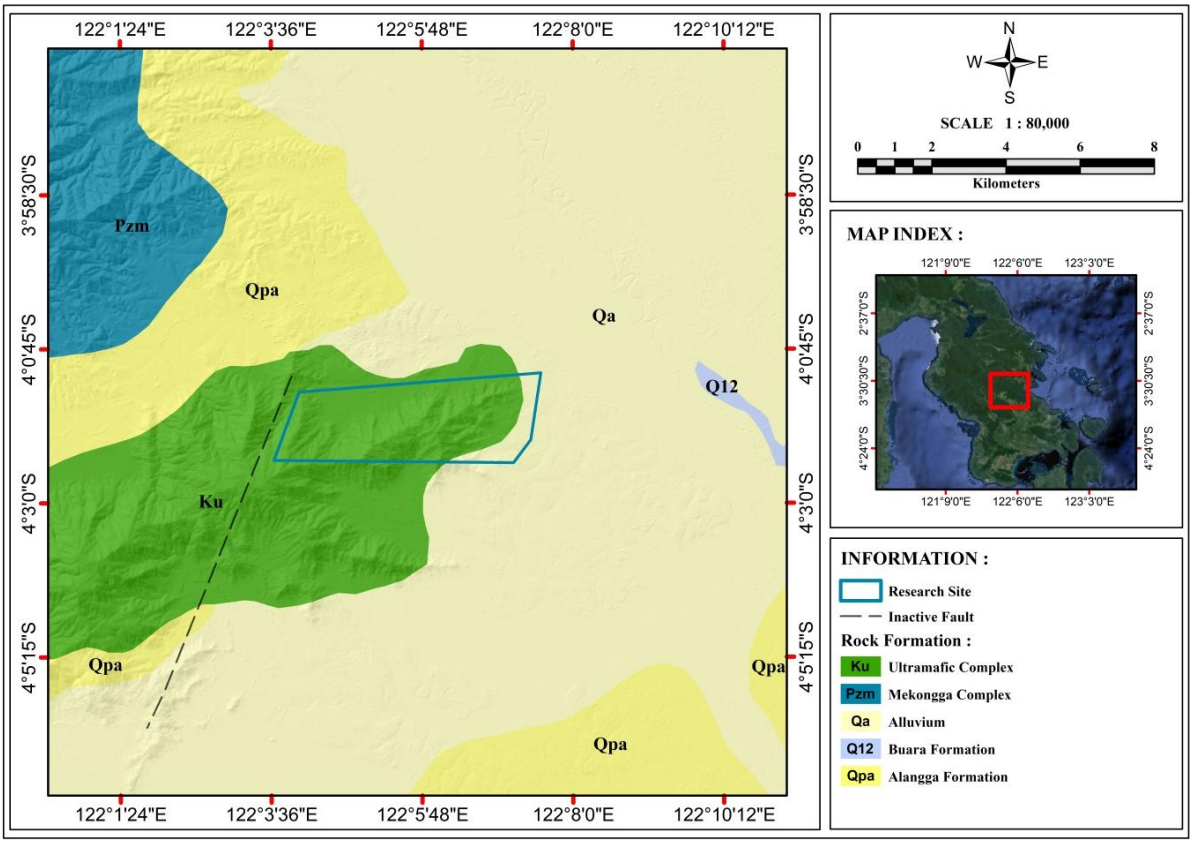

Figure 1. Regional geological distribution for the research area [8].

RESEARCH METHODS

Research Location and Data

This research uses measurement data from 1 set of Proton Magnetometer and Gradiometer PMG-2 instruments carried out on November 12 – 13, 2023 at Sonai Village and its surroundings, Puriala District, Konawe Regency, Southeast Sulawesi Province. Measurements were carried out at 126 points in

6 trajectories in the N180°S direction. The location of the measurement points can be seen in Figure 2. In addition, this research also uses secondary data in the form of magnetic inclination and declination angles of the research area sourced from the International Association of Geomagnetism and Aeronomy (IAGA) website.

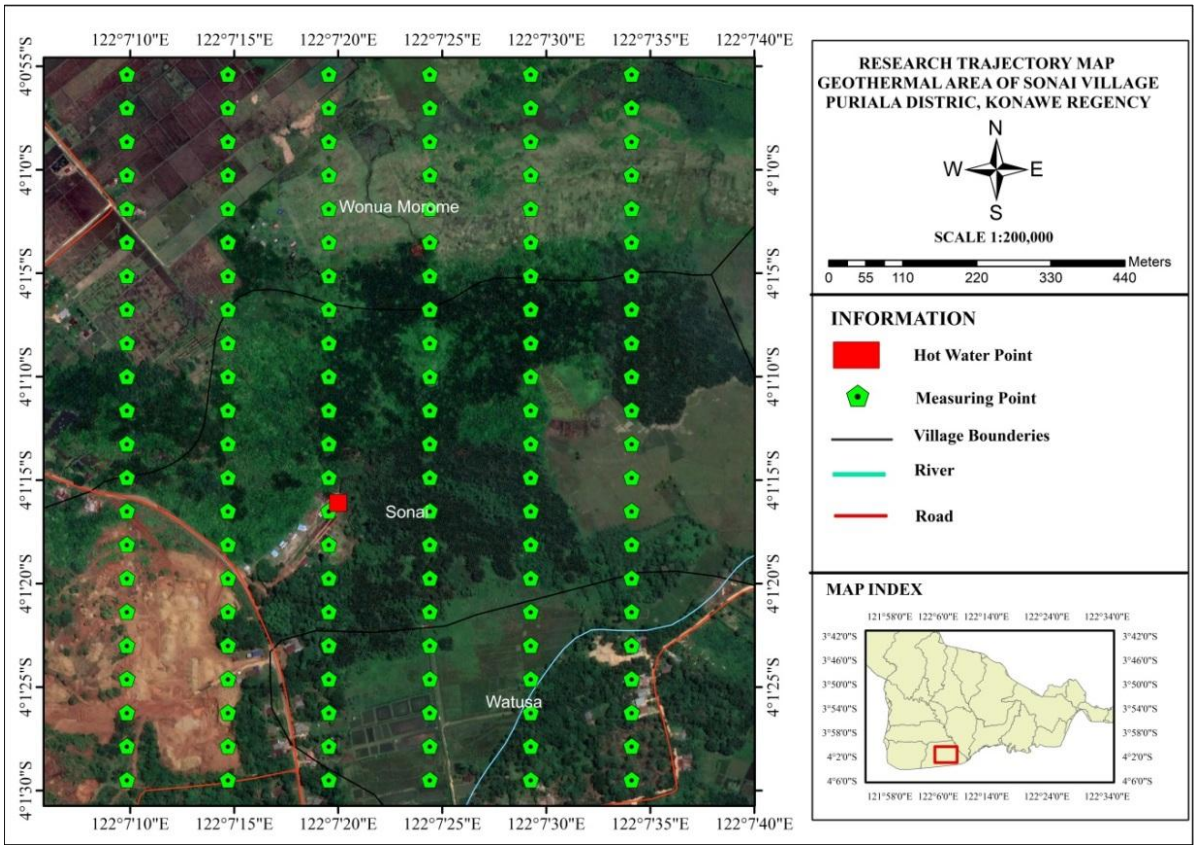

Figure 2. Distribution of measurement points.

Data Processing

Diurnal Correction

Diurnal Correction is a correction made to magnetic field data measured in the field to eliminate the influence of external magnetic fields or daily variations. The calculation of diurnal correction is done using Microsoft Excel 2016 with the formula [24, 25]:

$$\Delta H_{daily} = \left(\frac{t_n - t_{in}}{t_e - t_{in}} \right) \left(H_e - H_{in} \right) \quad (3)$$

where, ΔH_{daily} is the diurnal correction, H_e is the magnetic field value at the end point, H_{in} is the magnetic field value at the starting point, tin is the measurement time at the starting point, te is the measurement time at the end point, and tn is the measurement at point n.

IGRF Correction

IGRF correction is a correction performed to measured magnetic field data that has undergone diurnal correction to eliminate the influence of the Earth's main magnetic field. IGRF values is obtained from the website of The International Association of Geomagnetism and Aeronomy (IAGA). IGRF correction is calculated using the equation [24, 25]:

$$\Delta H_t = H_{daily} \pm \Delta H_{daily} - H_o \quad (4)$$

where, ΔH_t is the total magnetic field anomaly, Hdaily is the H value at each measurement point, ΔH_{daily} is the diurnal correction, and H_o is

the IGRF correction of the Sonai Village geothermal area and its surroundings.

Upward Continuation Transformation

Upward Continuation transformation is the process of transforming potential field data from a flat plane to a higher flat plane. In magnetic method data processing, this process functions to reduce residual magnetic effects originating from various sources of magnetic objects spreaded on the topographic surface that are not related to the survey [26, 27]. The result is a regional magnetic field anomaly (ΔH_{upward}).

Obtaining Residual Magnetic Field Anomaly

The regional magnetic anomaly that have been obtained is further processed to obtain residual (local) magnetic anomaly that are the target of the research. The anomaly is obtained following the equation [8, 24, 25]:

$$\Delta H_{res} = H_t - \Delta H_{upward} \quad (5)$$

where, ΔH_{res} is the residual magnetic anomaly, ΔH_t is the total magnetic anomaly and ΔH_{upward} is the regional magnetic anomaly resulting from Upward Continuation transformation.

Application of Pseudo-Gravity Method

The pseudo-gravity method is carried out to eliminate the polarity effects of the magnetic method by converting magnetic anomaly data as if it were a gravity anomaly or pseudo-gravity. This transformation process follows equation (2). The density contrast value according to [26] is 0.1 gr/cm$_3$ per A/m where 1 A/m is 0.001 Gauss.

Performing 2D Modeling

2D modeling is generated from slices made on the residual magnetic anomaly map that has undergone pseudo-gravity transformation. The goal is to obtain a 2D cross-section of the layers and subsurface geological structures of the Sonai Village geothermal area and its surroundings.

RESULTS AND DISCUSSION

Total Magnetic Field Measurement Results

Based on the results of magnetic field measurements measured directly in the field using 1 set of Magnetometer and Gradiometer PMG-2 instruments, it is known that the total magnetic field value of the geothermal area of Sonai Village and its surroundings ranges from 42,220.59 nT to 42,469.21 nT. Figure 3 shows the contour of the total magnetic field anomaly that has not been corrected with Diurnal and IGRF corrections on the topography.

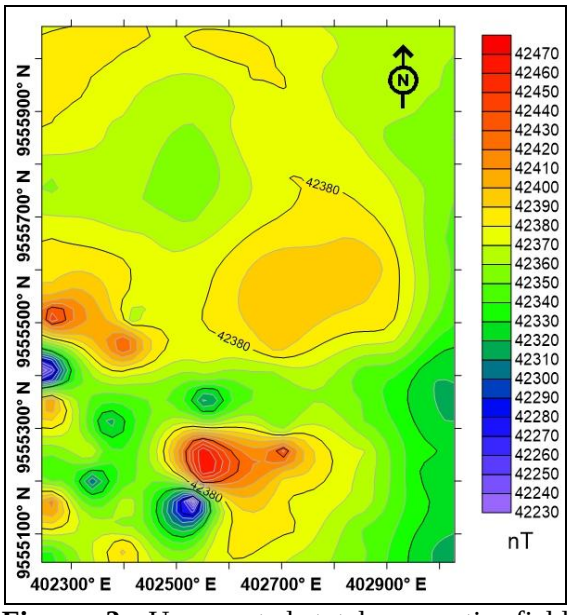

Figure 3. Uncorrected total magnetic field contour of the measurement results.

Corrected Total Magnetic Field Anomaly

The total magnetic field anomaly value that has undergone diurnal and IGRF corrections in the research area is around -171.17 nT to 82.47 nT. In general, the distribution of the total magnetic field anomaly pattern in the research area has three different anomaly trends which can be seen in Figure 4. The distribution of the high anomaly pattern with an anomaly range of around 10 nT to 82 nT is dominant in the North

with a lineage direction from West to Northeast. This high anomaly pattern decreases towards the West. The moderate anomaly pattern with an anomaly value range of around -90 nT to 10 nT is dominant in the South of the research area. This moderate anomaly has a decreasing trend from North-Northwest to West-Northwest. While the low anomaly pattern of around -171 nT to -90 nT is dominant in the South and Southwest of the research area.

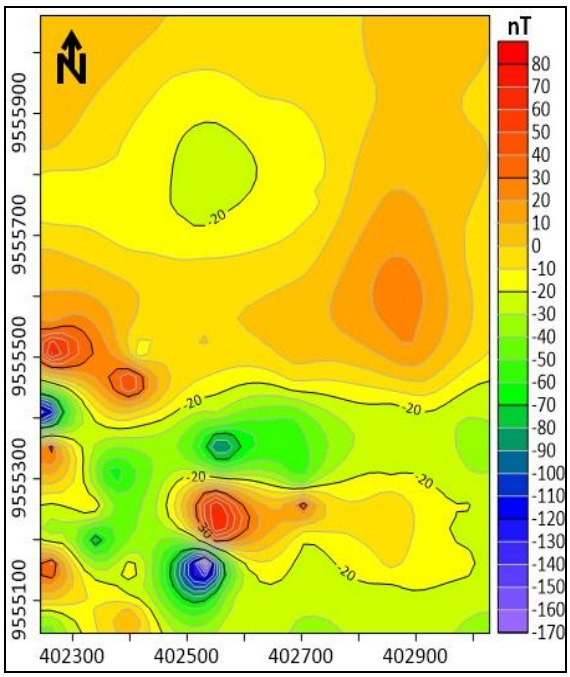

Figure 4. Corrected total magnetic field anomaly contour.

Performing Upward Continuation

Upward Continuation transformation of total magnetic field anomaly data was performed at heights of 100 m, 150 m, 200 m and 250 m as shown in Figure 5. This was done to see whether there were differences in the regional anomaly contour patterns of the research area at each specified height. In this research, the Upward Continuation process was stopped at a height of 250 m because the pattern on the contour map had shown a fairly smooth pattern and no longer experienced significant changes in closure. This shows that the pattern at this height can be considered to have experienced a separation between regional anomalies from the total magnetic field anomaly.

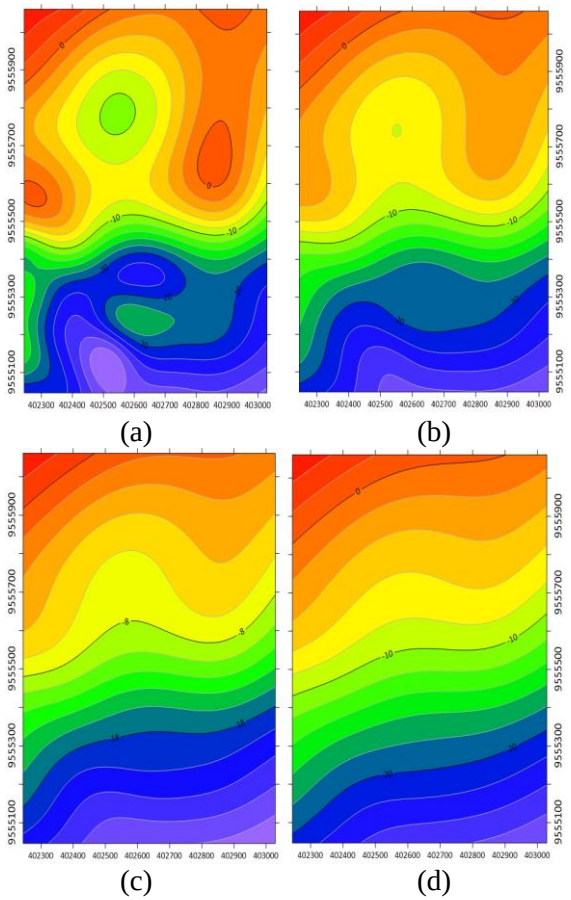

Figure 5. Contours of Upward Continuation at heights of (a). 100 meters, (b). 150 meters, (c). 200 m, and (d). 250 m.

Distribution of Residual Magnetic Field Anomaly

Separating the anomaly with Upward Continuation produces a regional anomaly map, so to get the residual anomaly it is done by subtracting the total magnetic field anomaly map and the resulting map from Upward Continuation. The residual magnetic anomaly contour map depicts the regional geological structure pattern in the research area.

The contours in Figure 6 show qualitatively areas with high and low susceptibility. The residual magnetic anomaly value contour obtained ranges from around -150 nT to 90 nT where moderate to high anomalies are dominant in the Northern part of the research area and low anomaly contours are dominant in the Southern part.

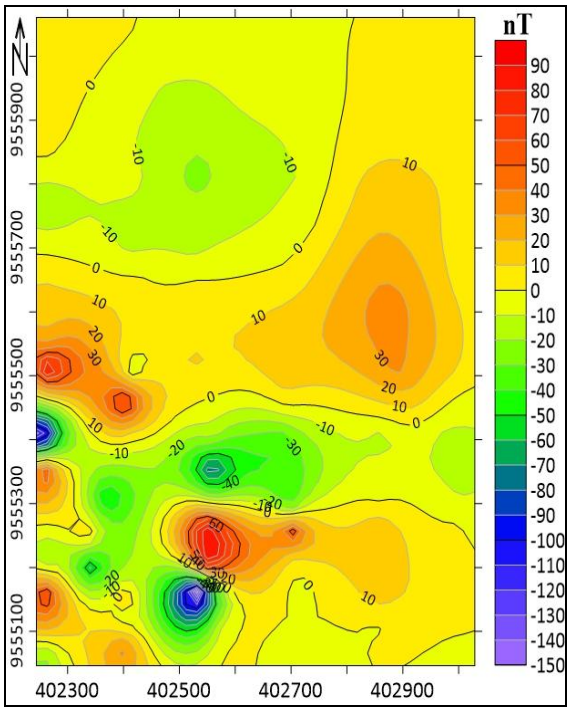

Figure 6. Contour of residual magnetic field anomaly.

Application of Pseudo-Gravity Method on Residual Magnetic Field Anomaly Data

The results of the pseudo-gravity method applied to the residual anomaly data have clarified the location of the subsurface anomaly target by displaying a simpler and more informative pseudo-gravity anomaly contour with a contour density of around -0.07 mGal to 0.06 mGal which can be seen in Figure 7 (a). This figure shows that the positive anomaly contour closure dominates in the North to the South of the research area. This positive anomaly is thought to be caused by rocks that have a relatively high density, so that in this section it is estimated to be dominated by ultrabasic rocks which in this case are peridotite rocks. While the West is dominated by negative anomalies which are interpreted to be composed of Alluvium Deposits.

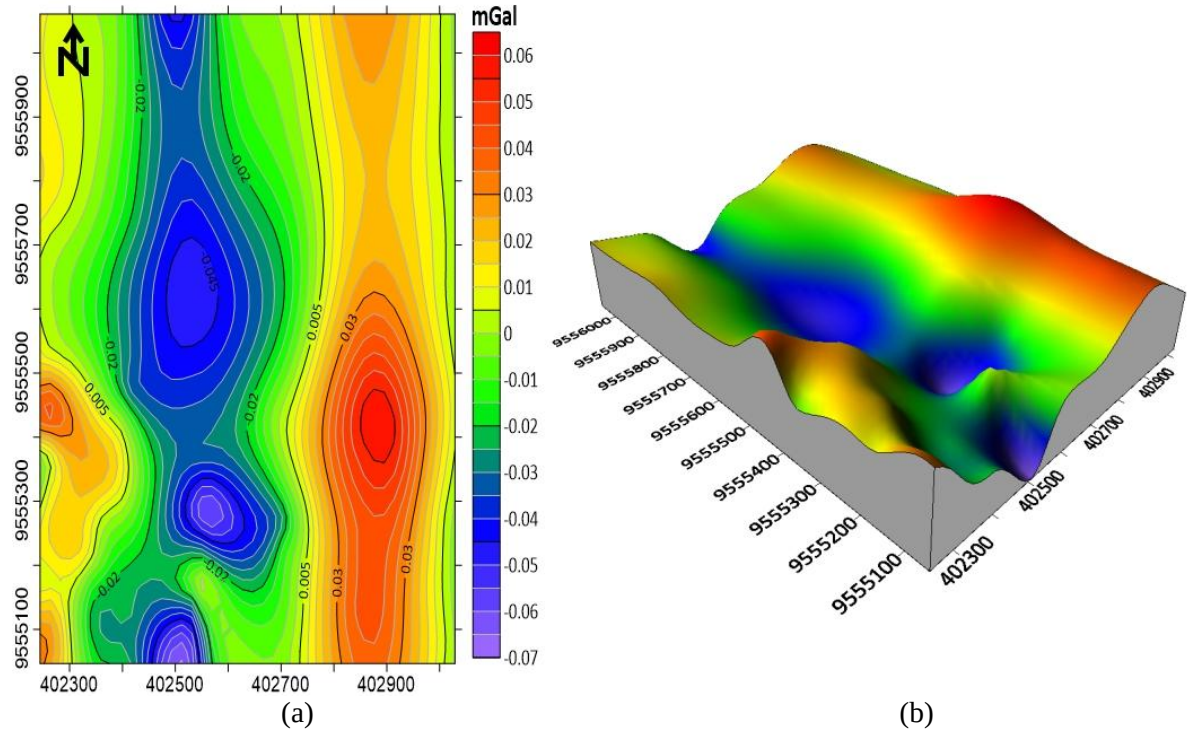

(a) (b)

Figure 7. (a) Pseudo-gravity anomaly contour and (b) 3D map of pseudo-gravity anomaly.

In the research area, there is a fluid basin marked by the presence of different height distributions as can be seen in 3D in Figure 7 (b). The dense contour indicates a relatively high-density area, marked with green to red colors which are interpreted as contour patterns that characterize the height that limits the fluid basin. While the loose contour indicates a relatively low-density area, marked with purple to blue colors which are a fluid basin.

The existence of geological structures in the form of faults in the research area can be

estimated from Figure 7 (a). This is based on the characteristics of the existence of fault in the form of anomalous lineation, contour density, anomalous deflection and anomalous polarization (negative and positive). Therefore, the White Box in Figure 8 is the estimated location of the existence of faults in the research area.

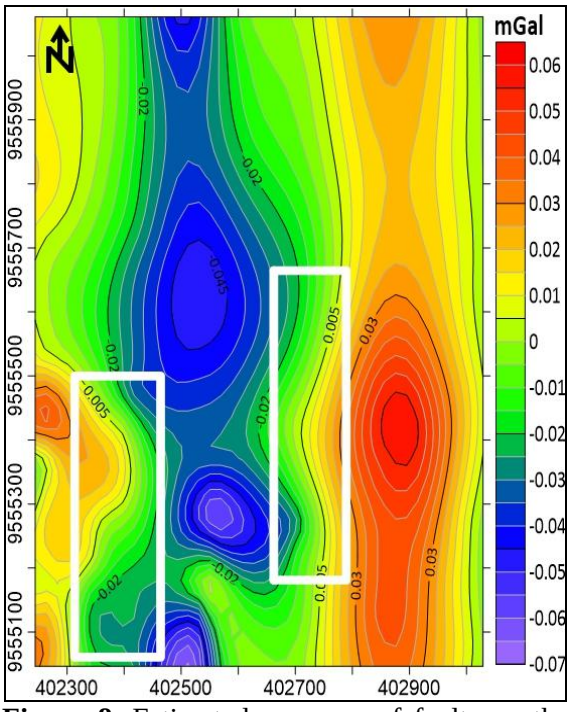

Figure 8. Estimated presence of faults on the pseudo-gravity anomaly map.

Creating Slices on Pseudo-Gravity Map

In this research, the number of slices modeled in an effort to know the existence of subsurface structures is 2 slices which are considered to have represented the research area. The drawing of slices is carried out from West to East or slice A-A' and from East-Southeast to Northwest or slice B-B', and the drawing of these slices can be seen in Figure 9.

2D Modeling and Geothermal Resources

The 2D modeling performed based on the results of the slices in Figure 9 is shown in Figure 10 and Figure 11 respectively. Interpretation of the 2D model was performed at an error value of <10%. The slices on the pseudo-gravity anomaly map will produce an observation graph that can be used as a reference to estimate the layer structure and the presence of geological contacts in the subsurface. Based on the results of 2D modeling, the results for the A-A' and B-B' slices generally pass through 3 formations, namely Alluvium Deposits, Alangga Formation and Ultramafic Complex.

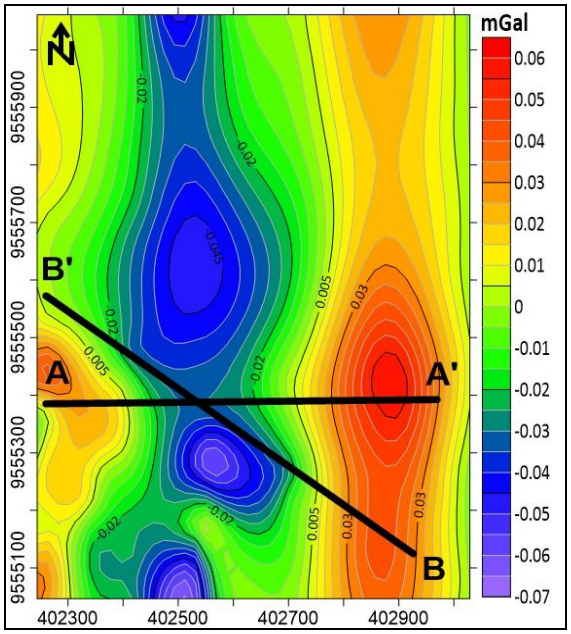

Figure 9. Direction of slices A-A' and B-B'.

2D modeling of the A-A' section in Figure 10 shows the presence of 3 layers. The first layer is composed of material with a density value of 1.5 g/cm^3 which is thought to be sand and a density of 2.5 g/cm^3 which is thought to be claystone. The material in the first layer is part of the Alluvium Deposit in the form of swamp and river deposits located near the manifestation (hot springs). In the second layer, a density value of 2.78 g/cm^3 is thought to be conglomerate rock and a density value of 2.6 g/cm^3 which is thought to be sandstone, and both are part of the Alangga Formation. In the third layer, there is an Ultramafic Complex with a density value of 2.84 g/cm^3 which is thought to be peridotite rock.

For Figure 11 which is the result of 2D modeling for the B-B' slice, 3 layers were also obtained. For the first layer, there is rock with a density value of 2.32 g/cm^3 which is thought to

be sandstone and is a part of the Alangga Formation, rock with a density value of 2.5 g/cm^3 which is thought to be Alluvium Deposits in the form of claystone, and rock with a density value of 1.5 g/cm^3 which is thought to be sand. In the second layer, there are rocks with a density value of 2.78 g/cm^3 which is thought to be conglomerate, dominant in the East-Southeast part of the research area, while in the Northwest part there is sandstone. In the third layer, there is rock with a density value of 2.84 g/cm^3 which is thought to be peridotite from the Ultramafic Complex.

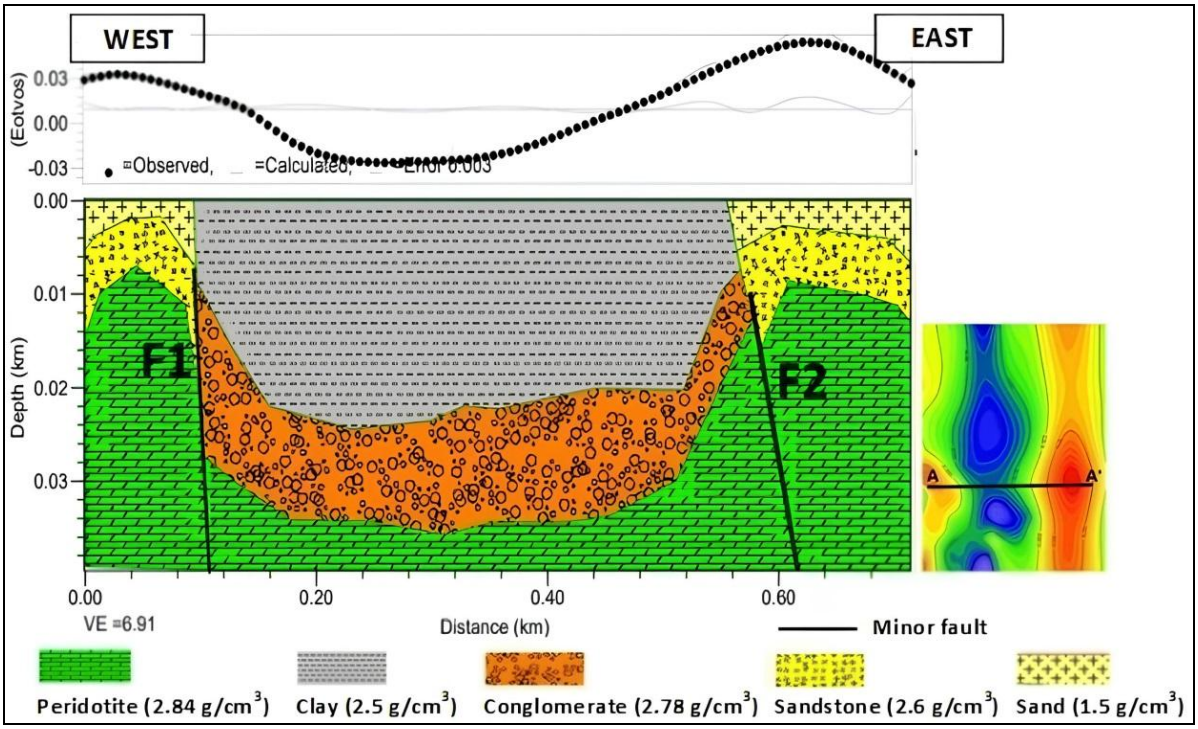

Figure 10. 2D modeling results for slice A-A'.

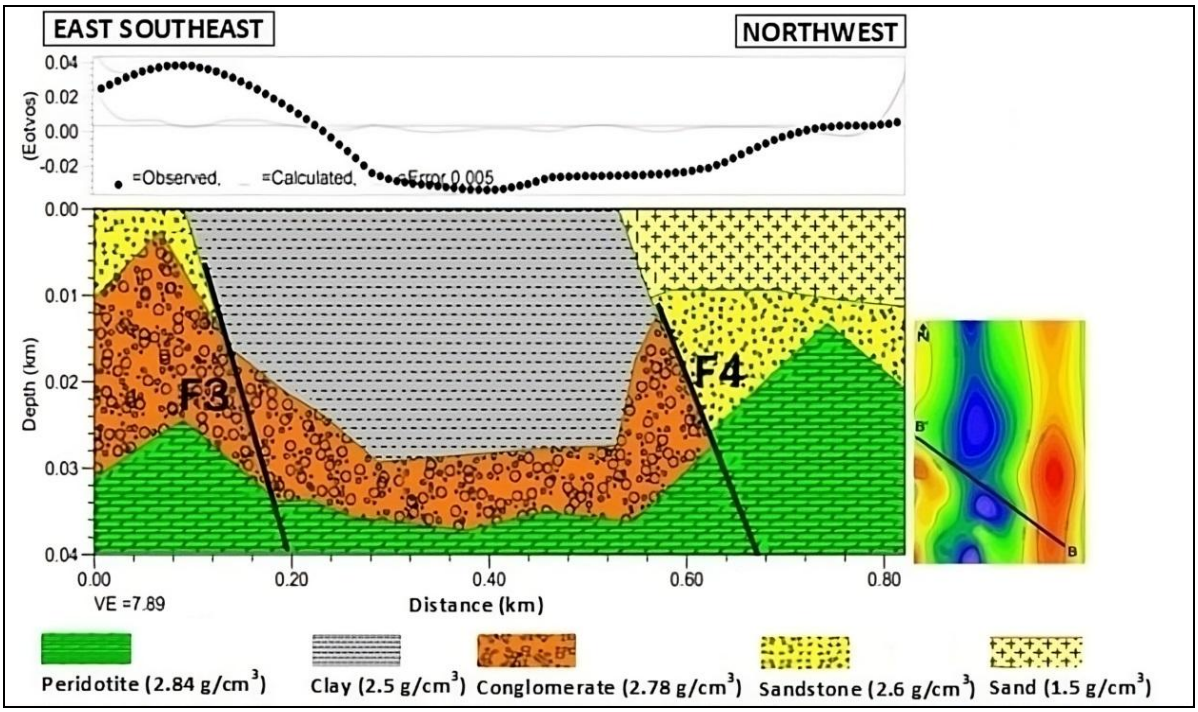

Figure 11. 2D modeling results for slice B-B'.

The results of the research in Figure 10 and Figure 11 are in accordance with regional geological data and previous researches. In addition, it is also supported by the findings of outcrops in the form of weathered peridotite outcrops and the presence of swamps in the manifestation area which can be seen in Figure 12.

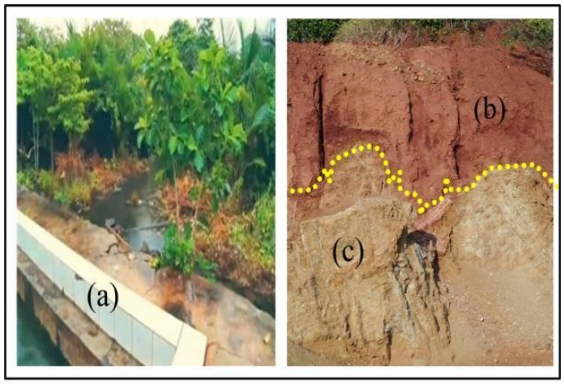

Figure 12. (a) Alluvium deposits in the form of swamps, (b) laterite soil, and (c) weathered peridotite outcrop.

Figure 10 and Figure 11 also show that in the research area there are several minor faults that pass through the peridotite and conglomerate layers. The estimated locations of these minor faults are:

1. Fault F1 is thought to be located at coordinates 4°1’16.149” South Latitude and 122°7’9.609” East Longitude to 4o1’18.488” South Latitude and 122°7’15.384” East Longitude which is ±15 meters from the geothermal manifestation (hot springs).
2. Fault F2 is thought to be located at coordinates 4°1’23.388” South Latitude and 122°7’24.326” East Longitude to 4°1’27.501” South Latitude and 122°7’33.012” East Longitude, which is ±28 meters from the manifestation (hot springs).
3. Fault F3 is thought to be located at coordinates 4°1’10.041” South Latitude and 122°7’10.589” East Longitude to 4°1’13.041” South Latitude and 122°7’14.705” East Longitude with a distance of ±35 meters from the manifestation (hot springs).
4. Fault F4 is thought to be located at coordinates 4°1’22.315” South Latitude and 122°7’25.689” East Longitude to 4°1’27.109” South Latitude and 122°7’31.910” East Longitude with a distance of ±30 meters from the manifestation (hot springs).

Regionally, the research area is influenced by the Konaweha shear fault which is trending Northwest-Southeast [28]. It is suspected that the movement of this shear fault has caused minor faults in the geothermal area of Sonai Village and its surroundings. These minor faults become the migration path for hot fluids to the surface. Meanwhile, the impermeable peridotite layer functions as bedrock in the geothermal area of Sonai Village and its surroundings.

The geothermal type of Sonai Village and its surroundings is non-volcanic geothermal, whose fluids come from surface water or meteoric water, and are controlled by fractures in the form of minor faults. The existence of a basin (Figure 7 (b)) which has a thick sedimentary layer in the form of sand and clay at the research location allows hot fluids to be distributed or infiltrated through this layer which has high permeability.

CONCLUSION

2D modeling of pseudo-gravity transformation results on residual magnetic field anomaly maps provides an overview of the subsurface layers and structures. The subsurface layers of the research area are composed of 3 formations, namely Alluvium Deposits, Alangga Formation and Ultramafic Complex. Alluvium deposits are in the form of sand with a density value of 1.5 mGal and claystone with a density value of 2.5 mGal. In the Alangga Formation, it consists of sandstone with a density value of 2.32 mGal to 2.6 mGal and conglomerate with a density value of 2.78 mGal. While in the Ultramafic Complex, there is peridotite with a density value of 2.84 mGal. This layer functions as bedrock in the geothermal area of Sonai Village and its

surroundings because of its impermeable nature.

The geological structures found are several minor faults. These minor faults are thought to be the migration path of hot fluids towards the surface. The two minor faults closest to the manifestation (hot springs) are located at coordinates around 4°1'16.149" South Latitude and 122°7'9.609" East Longitude which are ±15 meters away and at coordinates around 4°1'23.388" South Latitude and 122°7'24.326" East Longitude which are ±28 meters away from the geothermal manifestation.

REFERENCES

1. Hermawan, D., Sugianto, A., Yushantarti, A., Dahlan, Munandar, A., dan Widodo, S. (2011). Kajian Panasbumi Non Vulkanik Daerah Sulawesi Bagian Tenggara. Bandung: Pusat Sumber Daya Geologi, Kementerian ESDM.
2. Surono. (2013). Geologi Lengan Tenggara Sulawesi. Bandung: Badan Geologi, Kementerian ESDM.
3. Risdianto, D., Permana, L. A., Wibowo, A. E., Sugianto, A., & Hermawan, D. (2015). Sistem Panasbumi Non Vulkanik di Sulawesi. Bandung: Pusat Sumber Daya Mineral, Batubara dan Panas Bumi, Badan Geologi, Kementerian ESDM.
4. Brophy, P. (2011). An Introduction to Geothermal Energy. CGEC Geothermal Outreach Workshop. California: EGS Inc.
5. Grupta, H. & Roy, S. (2007). Geothermal Energy. Amsterdam: Elsevier.
6. Anonymous. (2017). Buku Potensi Panas Bumi Indonesia Jilid 2. Jakarta: Pusat Sumber Daya Mineral, Batubara dan Panas Bumi, Badan Geologi, Kementerian ESDM.
7. Baskara, M. Y. (2020). Identifikasi Sebaran Fluida Panas Daerah Panasbumi Puriala, Kabupaten Konawe Menggunakan Metode Geolistrik Resistivitas Konfigurasi Wenner-Schlumber. Skripsi. Universitas Halu Oleo.
8. Sariani, Manan, A., Bahdad & Chahyani, R. (2024). Estimation of subsurface structure using Euler Deconvolution method of magnetic data at the geothermal area of Sonai Village and its surroundings, Konawe Regency. *Jurnal Geocelebes*, **8**(2), 162–177.
9. Medhus, A. B. & Klinkby, L. (2023). Engineering Geophysics, 1st Edition. Leiden: CRC Press.
10. Telford, M. W., Geldard, L. P., Sheriff, R. E., & Keys, D.A. (1990). Applied Geophysics 2nd ed. London: Cambridge University Press.
11. Safrilia, P., Muhardi & Perdhana, R. (2024). Pemodelan 2D Struktur Geologi Bawah Permukaan di Daerah Manifestasi Panas Bumi Buaran, Kabupaten Brebes, Berdasarkan Anomali Magnetik. *JFT: Jurnal Fisika dan Terapannya*, **11**(1), 91–106.
12. Hanatha, F. D. & Hamid, H. (2024). Integrasi metode gravity dan metode geomagnetik menggunakan Dekonvolusi Euler untuk delineasi struktur pada sistem panas bumi di kawasan Candi Umbul-Telomoyo, Magelang, Jawa Tengah. *Jurnal Geosains dan Teknologi*, **7**(1), 19–28.
13. Puspita, M. B., Perwita, C. A., Maryanto, S., & Suyanto, I. (2023). Analisis Metode Magnetik pada Daerah Manifestasi Panas Bumi Karangrejo, Kabupaten Pacitan. INSOLOGI: *Jurnal Sains dan Teknologi*, **2**(5), 907–916.
14. Luthfin, A. & Jubaidah, N. A. (2023). Identification of geothermal distribution in the Banyu Biru hot water source using the magnetic method. *Indonesian Journal of Applied Physics (IJAP)*, **13**(2), 215–25.
15. Tanjung, R. U. S., Pujiastuti, D., & Putra, A. (2023). Interpretasi struktur bawah permukaan menggunakan data anomali medan magnet daerah manifestasi panas bumi Sampuraga Kabupaten Mandailing Natal. *Jurnal Fisika Unand*, **12**(4), 554–560.

16. Hidayat, H., Putra, A., & Pujiastuti, D. (2021). Identifikasi sebaran anomali magnetik pada daerah prospek panas bumi Nagari Aie Angek, Kabupaten Tanah Datar. *Jurnal Fisika Unand (JFU)*, **10**(1), 48–54.
17. Sitorus, E. & Tampubolon, T. (2018) Penentuan struktur bawah permukaan area panas bumi Tinggi Raja Kabupaten Simalungun dengan menggunakan metode magnetik. *Jurnal Einstein*, **6**(1), 26–33.
18. Simandjuntak, T. O., Surono, & Hadiwijoyo, S. (1993). Peta Geologi Lembar Kolaka Skala 1:250.000. Pusat Penelitian dan Pengembangan Geologi.
19. Zakaria, Z. & Sidarto. (2015). Aktifitas tektonik di Sulawesi dan sekitarnya sejak mesozoikum hingga kini sebagai akibat interaksi aktifitas tektonik lempeng tektonik utama di sekitarnya. *Jurnal Geologi dan Sumberdaya Mineral*, **16**(3), 115–127.
20. Surono & Hartono, U. (2013). Geologi Sulawesi. Jakarta: LIPI Press.
21. Schmidt, A. (2009). Electrical and magnetic methods in archeological prospection. *Geophysics and Landscape Archeology*, 67–81.
22. Baranov, V. (1957) A new method for interpretation of aeromagnetic maps, pseudo-gravimetric anomalies. *Geophysics*, **22**, 359–363.
23. Alamdar, K., Ansari, A. H., & Ghorbani, A. (2009). Edge detection of magnetic body using horizontal gradient of pseudogravity anomaly. *Geophysical Research*, **4082**.
24. Pancasari, A., Safani, J., & Manan, A. (2020). Interpretasi struktur bawah permukaan daerah Kota Kendari berdasarkan data anomali medan magnetik lokal. *Jurnal Rekayasa Geofisika Indonesia (JRGI)*, **2**(2), 45–53.
25. Fikar, M., Hamimu, L., Manan, A., & Suyanto, I. (2019). Pemodelan 2D data magnetik menggunakan transformasi RTP untuk pendugaan sesar di Daerah Kasihan, Pacitan, Jawa Timur. *Jurnal Rekayasa Geofisika Indonesia (JRGI)*, **2**(01), 33–42.
26. Blakely, R. J. (1995). Potensial Theory in Gravity and Magnetics Applications. Cambridge: Cambridge University Press.
27. Blakely, R J. & Simpson, W. (1986). Approximating edge of source bodies from magnetic or gravity anomalies. *Geophysics*, **7**(51), 1.494–1.498.
28. Tamburaka, E. (2019). Resiko dan mitigasi bencana gempa tektonik di Kabupaten Konawe. *Jurnal Askara Publik*, **3**(2), 222–235.

IPC

Indonesian Physics Communication

Department of Physics, Universitas Riau, Pekanbaru, Indonesia
p-ISSN 1412-2960 | e-ISSN 2579-521X

Vol. 22 | No. 2
July 2025

Web: https://kfi.ejournal.unri.ac.id
E-mail: kfi@ejournal.unri.ac.id

A medical physics review of the use of contrasodium in hysterosalpingography (HSG) examinations

Aidil Akbar[1], Alltop Amri Ya Habib[2], Asnika Putri Simanjuntak[3], Tengku Emrinaldi[4,*]

[1]Departement of Obstetrics and Gynecology, Universitas Muhammadiyah Sumatera Utara, Medan 20217, Indonesia
[2]Department of Chemical Engineering, Universitas Riau, Pekanbaru 28293, Indonesia
[3]Department of Socio Economic of Fisheries, Universitas Riau, Pekanbaru 28293, Indonesia
[4]Department of Physics, Universitas Riau, Pekanbaru 28293, Indonesia

*Corresponding author: tengku.emrinaldi@lecturer.unri.ac.id

ABSTRACT

Hysterosalpingography (HSG) is a widely used radiological procedure for evaluating female infertility, particularly in assessing fallopian tube patency and uterine anatomy. A critical component of HSG is the use of contrast media. Water-based contrast agents, such as contrasodium, are often preferred due to their favorable safety profile. The field of medical physics plays a vital role in ensuring diagnostic image quality while minimizing biological risks from radiation exposure. This article reviews the effectiveness of contrasodium in HSG procedures from a medical physics perspective, comparing it to other contrast agents and examining radiation dose management in women of reproductive age. The study is a literature review of scientific publications from the past decade (2015–2024), including clinical trials, meta-analyses, and international guidelines from the WHO and ICRP. The analysis focuses on imaging physics parameters, contrast efficiency, biological safety, and radiation dose evaluation. Findings indicate that contrasodium provides sufficient radiological imaging with minimal biological risk. Although oil-based contrast agents are associated with higher post-HSG pregnancy rates, they pose greater risks of adverse biological effects. Medical physicists are instrumental in optimizing imaging protocols, managing radiation doses, and selecting exposure parameters in accordance with the ALARA (As Low As Reasonably Achievable) principle. In conclusion, the use of contrasodium in HSG offers an optimal balance between diagnostic efficacy and patient safety. The standardization of evidence-based HSG protocols at the national level is recommended to enhance clinical practice in Indonesia.

Keywords: Hysterosalpingography; contrast sodium; medical physics; radiation dose; female infertility

Received 25-05-2025 | Revised 12-06-2025 | Accepted 17-07-2025 | Published 31-07-2025

INTRODUCTION

Hysterosalpingography (HSG) is a conventional radiological imaging procedure widely used to evaluate uterine morphology and fallopian tube patency, particularly in women experiencing infertility [1]. In this procedure, a contrast agent is injected into the uterine cavity through a cervical cannula, and its flow is monitored using X-ray-based fluoroscopy. One of the commonly used contrast agents in HSG is contrasodium, a water-soluble iodine-based compound such as sodium diatrizoate or a mixture with meglumine diatrizoate. These agents are radiopaque due to their high atomic number, allowing significant X-ray absorption and producing a clear contrast between the uterine/tubal cavity and surrounding tissues [2]. Compared to oil-based contrast agents, contrasodium offers advantages in terms of biological safety and rapid clearance from the body.

From a medical physics perspective, the use of contrasodium in HSG involves several key considerations, including the interaction of ionizing radiation with matter, the X-ray absorption characteristics of iodine, and the optimization of exposure parameters to achieve high-quality imaging at the lowest reasonable radiation dose [3]. In this context, sodium-based contrast media—typically low-osmolar and non-ionic—are preferred due to their ability

to produce excellent imaging quality with a lower incidence of adverse reactions [4]. A recent meta-analysis reported that oil-based contrast agents are associated with higher post-HSG pregnancy rates, with an odds ratio of 1.51 (95% CI 1.23 – 1.86; $p < .0001$), but also with a higher incidence of intravasation compared to water-based agents (OR = 2.09; $p = .03$) [5].

From a safety standpoint, meta-analyses show an intravasation incidence of 2.7% (95% CI 1.7 – 3.8) for oil-based media, with four cases of serious embolism (retinal/cerebral), albeit with no fatalities, while water-based media exhibit an incidence of 2.0% (95% CI 1.2 – 3.0) [4]. A national Dutch survey (2017) involving 5,165 HSG procedures reported an intravasation rate of 4.8% with oil-based agents versus 1.3% with water-based agents, with no cases of embolism or mortality [6].

In terms of radiation dose, a Nigerian study (2020) recorded average entrance surface doses (ESD) ranging from 15 – 34 mGy and effective doses between 1.2 – 2.5 mSv [7]. In Sudan (2015), ESD ranged from 13.6–35.7 mGy, with effective doses between 1.6 – 4.3 mSv, highlighting considerable variation across facilities [8]. The implementation of digital fluoroscopy has been shown to reduce patient doses by up to threefold compared to conventional techniques [3].

Additionally, physical parameters such as tube voltage (kV), tube current (mAs), pulse mode, and the use of automatic exposure control (AEC) systems contribute to reducing radiation doses while maintaining diagnostic image quality [7].

This review aims to summarize the interaction between medical physics aspects (such as X-ray–contrasodium dynamics and dose optimization) and clinical outcomes (diagnostic effectiveness and safety) in HSG procedures over the past decade, in support of evidence-based practice in reproductive radiology.

As imaging technologies advance and awareness of patient safety increases, medical physics–based evaluations of contrast agent utilization in HSG have become increasingly relevant. This article reviews the fundamental physical and radiological characteristics of contrasodium, its influence on image quality, and radiation protection considerations.

THEORITICAL BACKGROUND

Basic Principles of X-Ray Imaging in Diagnostic Radiology

X-ray imaging is based on the differential absorption of radiation by various body tissues. As an X-ray beam passes through the patient's body, part of the radiation is absorbed (absorption) while the remainder is transmitted. These differences result in contrast variations that form diagnostic images captured by a digital detector or film [9]. X-ray absorption is influenced by several factors:

a) **X-ray energy (kVp)**: Higher energy results in lower image contrast but greater tissue penetration.
b) **Effective atomic number (Z)**: Materials with high Z, such as iodine (Z = 53), absorb X-rays more effectively than soft tissue ($Z \approx 7$).
c) **Tissue density and thickness**: Within the diagnostic energy range (30 – 120 keV), the dominant interactions are the photoelectric effect and Compton scattering. The photoelectric effect, which is more prevalent in high-Z materials, significantly contributes to image contrast [3].

Radiopaque Contrast Agents: Physical Properties of Contrasodium

Contrasodium is a water-soluble iodine-based contrast agent, commonly composed of sodium and/or meglumine diatrizoate. It enhances contrast by increasing the X-ray absorption difference between contrast-filled body cavities and surrounding tissues [10, 11]. Key physical properties of contrasodium include:

a) **High atomic number (iodine)**: Enhances X-ray absorption via the photoelectric effect.
b) **High osmolality**: May affect patient comfort but facilitates rapid excretion.
c) **Moderate viscosity**: Enables easier injection and distribution within the uterine and tubal cavities.

The use of contrasodium allows for sharp visualization of uterine and tubal anatomy without the prolonged inflammation risk associated with oil-based contrast agents.

Physical Parameters in HSG

Optimizing HSG imaging requires appropriate adjustment of technical parameters, including:

a) **kVp and mAs**: X-ray energy must adequately penetrate the pelvic region, typically between 70 – 90 kVp.
b) **Exposure time**: Should be as brief as possible to minimize motion artifacts and reduce radiation dose.
c) **Collimation and grid use**: Helps limit the imaging field and enhance image quality.

Additionally, calculating dose-area product (DAP) and estimating mean ovarian dose are critical to ensuring patient safety, particularly because female reproductive organs are highly sensitive to ionizing radiation [12].

The Role of Medical Physics in Diagnostic Radiology

Medical physics plays a central role in:

a) Calibrating and performing quality control on fluoroscopic equipment.
b) Adjusting imaging parameters in line with the ALARA (As Low As Reasonably Achievable) principle.
c) Estimating and reporting patient radiation dose.
d) Evaluating image quality (contrast-to-noise ratio, signal-to-noise ratio).
e) Educating medical personnel on radiation protection and imaging safety protocols.

In the context of HSG, medical physicists are involved in equipment quality assurance, biological risk analysis, and the optimization of procedural protocols to ensure both diagnostic efficacy and patient safety.

USE OF CONTRASODIUM IN HYSTEROSALPINGOGRAPHY (HSG)

Principles of HSG Examination

Hysterosalpingography (HSG) is a diagnostic radiological procedure performed to assess the morphology of the uterine cavity and the patency of the fallopian tubes, especially in the evaluation of female infertility. The procedure involves injecting a contrast agent into the uterine cavity via a cervical cannula, followed by real-time X-ray fluoroscopic imaging. The contrast medium fills the uterus and, if the fallopian tubes are unobstructed, flows into the peritoneal cavity, which can then be visualized [12].

The HSG procedure involves two primary components: (1) a contrast medium—either water-or oil-based, and (2) an X-ray imaging system, typically in fluoroscopy mode. The contrast medium allows visualization of the tubal lumen and uterine cavity due to its high atomic number and density, which significantly absorb X-rays compared to surrounding tissues [13].

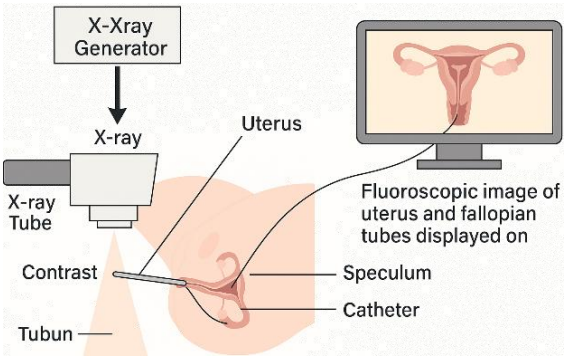

Figure 1. Principle of HSG examination.

Characteristics of Contrasodium

Contrasodium refers to iodinated, water-soluble contrast media such as Iopromide, Ioxaglate, or Iohexol. These agents are generally non-ionic and low-osmolar, designed

to minimize the risk of allergic reactions and intravasation. Key physical properties of contrasodium include:

a) **High atomic number (Z = 53 for iodine)** → enhances X-ray contrast.
b) **High optical density** → improves lumen delineation.
c) **Low osmolality** → reduces the risk of pain and tissue irritation [9].

Comparatively, oil-based contrast agents (e.g., Lipiodol) are more viscous and provide longer-lasting contrast but carry higher risks of embolism and adverse effects if intravasation occurs [3].

Key Characteristics of Contrasodium:

a) **Water-soluble**: Easily mixes with bodily fluids and is rapidly excreted.
b) **Radiopaque**: Contains iodine (Z = 53), which efficiently absorbs X-rays, providing clear contrast between the uterine/tubal lumen and surrounding tissues.
c) **High osmolality**: Enhances X-ray absorption but may also cause temporary discomfort or cramping shortly after injection [10].
d) **Low to moderate viscosity**: Facilitates easy injection and uniform distribution throughout the uterine cavity and fallopian tubes.

X-Ray Interactions with Contrast Media and Tissues

In medical physics, the absorption of X-rays by materials is governed by the photoelectric effect and Compton scattering. The photoelectric effect dominates at lower X-ray energies (< 50 keV) and increases exponentially with the atomic number (Z^3), while inversely related to X-ray energy (E^3) [3, 14].

Table 1. Comparison of physical properties of contrast media in HSG.

Parameter	Water-based contrasodium	Oil-based contrasodium
Type	Non-ionic, low-osmolar	Ionic, high-viscosity
Viscosity	Low	High
Duration of visualization	Short (≤ 5 minutes)	Long (up to 30 minutes)
Risk of allergic reaction	Low	Moderate
Risk of intravasation	Lower	Higher
Pregnancy effectiveness (OR)	1.0 [15]	1.51 [15]
Serious adverse effects	Very rare	Possible lipid embolism

Iodinated contrast media (high-Z) induce significantly more photoelectric interactions than soft tissues (low-Z), creating strong intensity differences on radiographic images. This explains the high efficacy of contrasodium in visualizing reproductive tract lumens during HSG.

A high atomic number (Z) enhances the photoelectric effect, resulting in brighter and clearer imaging. Therefore, contrasodium is highly effective in distinguishing the lumen from surrounding tissues during hysterosalpingography (HSG).

Table 2. X-ray interactions with tissues and contrast media.

Material	Effective atomic number (Z)	Dominant interaction (< 50 keV)	Radiographic appearance
Soft tissue (muscle, fat)	~ 7 – 8	Compton scattering	Low absorption
Bone	~ 13 – 14	Photoelectric & Compton	Moderate contrast
Contrasodium (iodine, Z = 53)	~53	Predominantly photoelectric	High absorption → bright white area

Advantages and Limitations of Contrasodium

Advantages:

a) High-contrast imaging under fluoroscopy.
b) Lower infection risk compared to oil-based contrast.
c) Rapid elimination from the body, making it suitable for hypersensitive patients

Limitations:

a) High osmolality may cause transient cramping or discomfort during injection.
b) Less effective than oil-based agents in improving pregnancy outcomes post-HSG [16–18].
c) Small risk of allergic reactions to iodine, particularly in hypersensitive individuals.

Medical Physics Considerations in Contrasodium Use

X-ray exposure in HSG is a particular concern due to the sensitivity of female reproductive organs to ionizing radiation. Therefore, the ALARA (As Low As Reasonably Achievable) principle must be applied. Technical parameters such as tube voltage (kV), tube current (mA), exposure time, source-to-image distance (SID), and fluoroscopy mode (continuous or pulsed) directly affect entrance surface dose (ESD) and effective dose [7].

Studies have shown that pulsed fluoroscopy and automated exposure control (AEC) can reduce radiation dose by 50% – 75% without compromising diagnostic quality [14]. Additional protection measures such as the use of lead aprons over the lower abdomen and ovarian shields are also recommended to minimize secondary exposure.

In clinical practice, the selection and use of contrasodium should consider:

a) Viscosity and osmolality appropriate for diagnostic needs and patient comfort.
b) Optimal X-ray energy (typically 70 – 90 kVp) to balance penetration and image contrast.
c) Dose monitoring to ensure safety, especially given the proximity to radiosensitive reproductive organs.

The role of the medical physicist is crucial in ensuring that HSG protocols meet established standards, both in terms of image quality and radiation protection for patients and healthcare personnel.

MEDICAL PHYSICS ASPECTS IN THE OPTIMIZATION OF HSG EXAMINATIONS

Optimization in hysterosalpingography (HSG) aims to achieve the highest possible diagnostic image quality while minimizing radiation exposure to the patient. Medical physics plays a central role in achieving this balance through the application of radiation physics principles, selection of optimal imaging parameters, and implementation of radiation protection protocols aligned with the ALARA (As Low As Reasonably Achievable) principle.

Selection of Imaging Parameters

Technical parameters significantly affect both image quality and patient dose. Medical physicists assist in determining the optimal combination of the following:

a) Tube voltage (kVp): Typically ranges between 70 – 90 kVp. Higher kVp enhances tissue penetration but may reduce image contrast. The choice should be tailored to the patient's body habitus and the contrast agent characteristics [3].
b) Tube current and exposure time (mAs): Should be adequate to ensure a sufficient signal-to-noise ratio (SNR) without unnecessarily increasing dose.
c) Beam collimation: Limiting the radiation field to the uterus and pelvic area reduces off-target exposure and improves local contrast [12].
d) Use of anti-scatter grids: These reduce scattered radiation but require adjustments in mAs due to partial absorption of primary photons.

Radiation Dose Measurement and Monitoring

An essential function of medical physics in HSG is quantifying patient dose, particularly given the sensitivity of the uterus and ovaries to ionizing radiation. Common parameters include:

a) Dose-Area Product (DAP): Expressed in $mGy \cdot cm^2$, representing total radiation dose multiplied by the irradiated area.
b) Entrance Surface Dose (ESD): The estimated dose to the skin surface at the X-ray entry point.
c) Ovarian Effective Dose (OED): Used to estimate risk to reproductive tissues and the probability of deterministic or stochastic effects.

Phantoms and dosimeters are utilized by medical physicists to verify actual dose levels and to develop protocols that maintain diagnostic quality while minimizing exposure.

Influence of Contrast Sodium's Physical Characteristics on Image Quality

Contrast agents enhance visualization of anatomical structures in X-ray-based procedures. The physical characteristics of contrast sodium (kontrasodium) directly influence image contrast, distribution, and patient comfort, and must be understood within the framework of medical physics.

a) **Iodine Content and High Atomic Number**

Contrast sodium contains iodine (Z = 53), a highly radiopaque element that enhances X-ray absorption via the photoelectric effect. This interaction is dominant in the 30 – 80 keV energy range used in diagnostic imaging. Higher iodine concentration (300 – 370 mg I/mL) increases:

- Linear attenuation coefficient, producing sharper contrast between the uterine/tubal lumen and surrounding tissues.
- Visualization of fine structures such as the fallopian tubes and uterine lumen [9].

However, increased iodine concentration must be balanced with patient comfort and radiation control.

b) **Osmolality**

Contrast sodium is hyperosmolar, meaning it has a higher osmolality than plasma. This affects:

- Patient comfort, as high osmolality may cause uterine cramping or pain.
- Contrast distribution, as high osmolality draws fluid from surrounding tissues, potentially impacting visibility.

While hyperosmolar agents like diatrizoate provide high image contrast, they can induce tubal spasms that hinder interpretation [10].

c) **Viscosity**

Viscosity influences injection speed and distribution:

- Moderate viscosity is preferred for controlled flow into the fallopian tubes.
- Low viscosity may result in rapid flow that impairs observation, whereas high viscosity complicates injection and increases discomfort.

Contrast sodium typically offers ideal viscosity for HSG compared to more viscous, oil-based agents.

d) **Surface Tension and Dispersion**

Surface tension characteristics affect the agent's ability to:

- Spread evenly across the endometrial cavity.
- Enter narrow fallopian tubes.

Uniform distribution supports better visualization of anomalies like polyps, septa, or tubal obstructions.

e) **Effect on Contrast-to-Noise Ratio (CNR)**

Contrast sodium improves CNR by:

- Enhancing intensity differences between contrast-filled structures and background tissues.
- Enhancing intensity differences between contrast-filled structures and background tissues.

However, uneven or overly rapid distribution may cause image artifacts.

Radiation Dose Optimization

Medical physicists play a critical role in ensuring that radiation doses during HSG remain within safe, diagnostically effective limits. Commonly used safety indicators include Entrance Surface Dose (ESD) and Effective Dose. A study in Nigeria reported ESD values between 15 – 34 mGy and effective doses from 1.2 – 2.5 mSv [7].

Key optimization strategies include:

- Use of pulsed fluoroscopy instead of continuous mode to reduce cumulative exposure time.
- Pemilihan tegangan tabung (kV) dan arus tabung (mA) yang sesuai, biasanya 70 – 90 kV dan < 200 mA.
- Use of additional filters and automatic exposure control (AEC) systems.
- Adjustment of source-to-image distance (SID) to minimize magnification and skin dose.

Such strategies help limit radiation to reproductive organs without compromising diagnostic accuracy [14].

Image Quality Evaluation

Medical physicists are responsible for assessing and maintaining image quality in HSG procedures. Key parameters include:

- Image contrast: Determined by the absorption difference between contrast sodium and soft tissue.
- Spatial resolution: The ability to distinguish fine anatomical details such as narrow fallopian tubes.
- Image noise: Influenced by the number of X-ray photons reaching the detector. Lower noise enhances diagnostic accuracy.

Physicists use phantom tests and image analysis to evaluate system consistency and dose density (DAP) as a surrogate for total exposure quality.

Contrast Sodium vs. Other Contrast Media

Contrast medium selection greatly influences image quality and biological risk. From a physics standpoint, water-soluble, low-osmolar contrast sodium offers several advantages:

- Reduced scatter due to uniform distribution and lower viscosity.
- High photoelectric interaction due to iodine content, enhancing X-ray absorption and visualization.
- Rapid clearance, reducing overall exposure time.

In contrast, oil-based agents like Lipiodol provide prolonged visualization but have higher viscosity and risks such as lipid embolism [3]. While both are radiographically effective, sodium-based agents are more manageable in terms of dose and distribution.

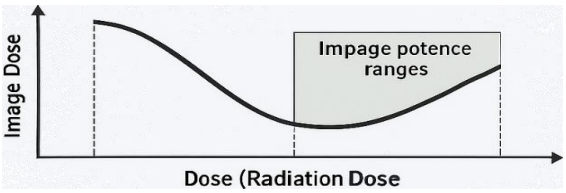

Figure 2. Dose vs image quality.

Table 3. Comparison of image quality between contrast sodium and oil-based media

Evaluation parameter	Contrast sodium (water-based)	Oil-based contrast
Radiographic Contrast	High	Very High
Image Sharpness (Resolution)	Good	Good
Visualization Duration	Short (~5 min)	Long (~30 min)
Distribution in Cavity	Even	Often localized
Image Artifacts	Minimal	Potential bubbles
Noise Risk	Low (fluoroscopy)	Low
Total Radiation Dose	Lower	Higher

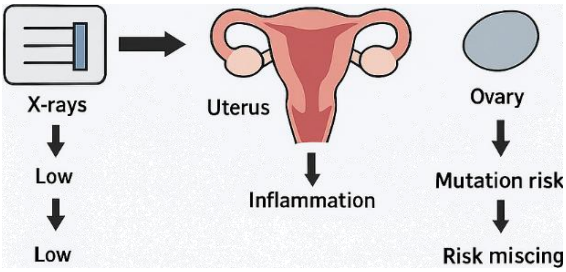

Figure 3. Radiation effects on female reproductive organs.

SAFETY AND SIDE EFFECTS OF CONTRASODIUM USAGE

Radiation protection for women of reproductive age is of critical importance. The principles of Justification and Optimization established by the International Commission on Radiological Protection (ICRP) are implemented in every imaging procedure.

Key measures include:

- Shielding, such as the use of lead aprons over the lower pelvis.
- Digital recording of exposure parameters for dose auditing purposes.
- Routine monitoring of the X-ray system by medical physicists, including detector calibration and QA/QC testing.

In cases where pregnancy is suspected, the medical physicist plays a vital role in estimating fetal dose and associated risks, and may recommend alternative protocols or delay the examination [15–17]. Potential risks and adverse effects include:

- Allergic reactions and hypersensitivity responses.
- Biological effects of radiation exposure on reproductive organs.
- Preventive actions and incident management.

LITERATURE REVIEW

Previous Studies on the Effectiveness of Contrasodium in HSG

Several studies support the effectiveness of water-based iodinated contrast media (contrasodium) in enhancing visualization of the female reproductive tract. Roest et al. (2020) reported that the use of contrasodium yielded adequate diagnostic outcomes in detecting fallopian tube occlusion, abnormal uterine structure, and intra-cavitary adhesions, with a sensitivity ranging from 81% – 90% [6]. Furthermore, contrasodium allows real-time morphological imaging of the uterus via fluoroscopy, enabling immediate interpretation by gynecologists.

Ahinko-Hakamaa et al. (2020) noted that water-based contrast is more easily absorbed by the body and rarely causes severe side effects such as embolism or intense pain [12]. Moreover, the duration of X-ray exposure tends to be shorter due to the rapid visualization of the contrast medium, making it suitable for low-radiation protocols.

Comparative Clinical Outcomes Using Different Contrast Media

Several studies have compared the clinical effectiveness of water-based (contrasodium) versus oil-based contrast agents. A meta-analysis by Tsui and Sofy (2023) revealed that oil-based contrast increased the likelihood of spontaneous pregnancy after HSG, with an odds ratio of 1.51 (95% CI: 1.23 – 1.86) [5]. However, this benefit was counterbalanced by a higher risk of intravasation and lipid embolism, particularly in patients with a history of pelvic surgery or endometriosis.

A randomized controlled trial by Dreyer et al. (2017) found that the pregnancy rate within six months post-HSG was higher in the oil-based group (39.7%) compared to the water-based group (29.1%), although the difference was not statistically significant after adjusting for age and BMI [18].

From a safety perspective, oil-based contrast agents have a higher intravasation rate (4.8% vs. 1.3%), as reported in a national survey in the Netherlands by Roest et al. (2020), although no fatal incidents were observed [6]. Therefore, the choice of contrast medium should consider the patient's risk factors, clinical indications, and institutional capabilities.

Table 4. Variation in radiation dose during HSG examinations.

Study	Country	Effective Dose (mSv)	Notes
[7]	Nigeria	1.2 – 2.5	High dose variation among hospitals
[8]	Sudan	1.6 – 4.3	ESD up to 35.7 mGy
[19]	Global	< 2 (recommended)	Emphasis on protecting women of reproductive age
[6]	Netherlands	1.9 (average)	National survey of 5,165 patients

Studies on Radiation Dose and Risk Management in Women of Reproductive Age

Several studies have evaluated the radiation dose received by patients during HSG procedures and how technical settings influence biological risk. Achuka et al. (2020) studied patients in Nigeria and found effective doses ranging from 1.2 to 2.5 mSv, whereas in Sudan, doses reached up to 4.3 mSv [7], indicating substantial inter-facility variability.

Kamburoğlu et al. (2019) concluded that pulsed fluoroscopy, optimization of kV/mAs, and the use of automatic exposure control (AEC) can reduce the dose by 40% – 70% without compromising image quality [14]. Medical physicists play a vital role in developing low-exposure protocols, implementing dose auditing systems, and ensuring the use of organ shielding for the uterus and ovaries.

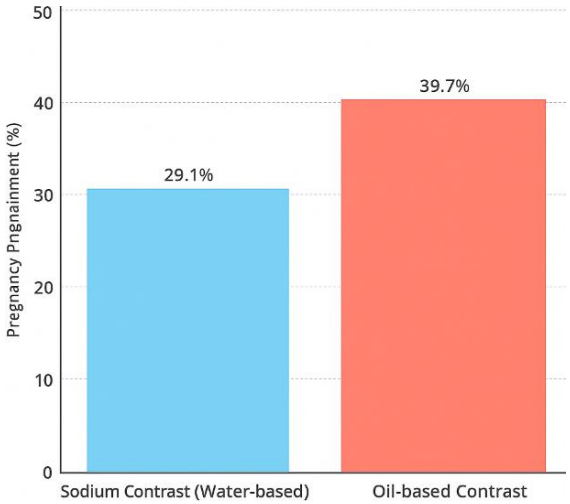

Figure 4. Pregnancy rate within six months following HSG [18].

The WHO (2016) also emphasized that X-ray exposure in women of reproductive age should be synchronized with the menstrual cycle and ideally avoided during the ovulatory and early luteal phases to minimize potential risks to the embryo in case of early conception [19].

DISCUSSION

Analysis of the Role of Medical Physics in the Diagnostic Effectiveness of HSG

The role of medical physics in Hysterosalpingography (HSG) examinations extends beyond merely setting technical parameters. It also encompasses aspects of safety, diagnostic effectiveness, and clinical efficiency. Previous studies [7] and [14] emphasized that interventions by medical physicists—such as adjusting tube voltage, exposure time, and selecting appropriate fluoroscopy modes—significantly contribute to reducing radiation exposure without compromising image quality.

This is particularly important since HSG is performed on women of reproductive age, who are especially sensitive to radiation, particularly in the ovaries and uterus. The optimization approach based on the ALARA (As Low As Reasonably Achievable) principle positions medical physics as a key discipline that bridges clinical needs with long-term patient safety.

Effectiveness of Sodium Contrast from Clinical and Medical Physics Perspectives

From a clinical perspective, sodium contrast offers excellent performance in visualizing the fallopian tubes and uterine cavity, with shorter imaging times and a better safety profile compared to oil-based contrast agents [4, 12]. For patients at risk of lipid embolism, sodium contrast is a rational choice due to its minimal intravasation and rapid elimination from the

body. From the viewpoint of medical physics, sodium contrast offers several advantages:

- Uniform distribution within the cavity → avoids image artifacts or noise.
- Sufficient X-ray absorption → generates high-contrast images.
- Shorter exposure duration → reduces total patient dose.

However, its limitation lies in its shorter retention time, requiring faster and more precise fluoroscopic techniques. This demands high technical skills from the operator and exposure optimization from the medical physicist's side.

Clinical Outcome Comparison Between Contrast Agents

Although oil-based contrast has been associated with higher post-HSG pregnancy rates [18–20], this benefit is accompanied by a higher risk of side effects such as intravasation and lipid embolism [6]. Therefore, careful patient selection is crucial. In settings with limited resources and vulnerable populations, such as in developing countries, sodium contrast becomes a safer and more technically manageable option.

Medical physicists can assist clinicians in selecting risk-based protocols, for example by using dose modeling software (such as DoseWatch or PCXMC) to estimate radiation exposure effects on patients' reproductive organs.

Challenges and Recommendations

Identified challenges in the implementation of medical physics in HSG include:

- Lack of training for radiologic technologists on low-dose protocols.
- Variations in equipment quality and calibration across facilities.
- Not all hospitals have actively involved medical physicists.

Recommendations include:

- Implementation of standard operating procedures (SOPs) based on medical physics in all HSG procedures.
- Routine dose audits with transparent reporting.
- Training fluoroscopy operators on exposure control and image interpretation

CONCLUSION

Based on the literature review and analysis of the role of medical physics in Hysterosalpingography (HSG), several conclusions can be drawn. First, sodium contrast (a water-based contrast medium) is considered a safe, effective, and efficient option for HSG procedures. As a non-ionic iodinated compound, it possesses favorable physical properties that enable optimal X-ray absorption without significantly increasing biological risks. Second, the role of medical physicists is crucial in optimizing HSG procedures. Their involvement spans from setting technical parameters and managing radiation dose to evaluating diagnostic image quality. The application of the ALARA (As Low As Reasonably Achievable) principle serves as a fundamental guideline in performing HSG, particularly for women of reproductive age. Third, while oil-based contrast agents have been associated with higher pregnancy rates following HSG, they also carry greater risks of adverse effects such as intravasation and lipid embolism. In contrast, sodium contrast offers a better balance between image quality and biological safety. Fourth, radiation doses in HSG procedures vary globally and are heavily influenced by equipment quality, operator competence, and the active presence of medical physicists at healthcare facilities. According to WHO recommendations, the effective dose should not exceed 2 mSv per procedure.

To improve the overall quality and safety of HSG examinations, several recommendations are proposed. First, all reproductive radiology centers should involve medical physicists actively in the planning, execution, and evaluation of HSG, particularly regarding low-dose protocols and image quality assessment. Second, ongoing training for radiographers and gynecologists is essential, especially in the

application of pulsed fluoroscopy, Automatic Exposure Control (AEC), and protective shielding for reproductive organs. Third, the selection of contrast media should be tailored to the patient's risk profile and specific clinical objectives (e.g., pure diagnostic versus fertility-enhancing procedures). Patients at risk of lipid embolism should avoid oil-based contrast agents. Finally, further local and national research is urgently needed to collect comprehensive HSG dose data in Indonesia. This is critical given the current lack of population-based data, which hinders the development of effective regulations and the establishment of national protocols.

REFERENCES

1. Practice Committee of the American Society for Reproductive Medicine. (2015). Diagnostic evaluation of the infertile female: a committee opinion. *Fertility and Sterility*, **103**(6), e44–e50.
2. Ludwin, A. & Ludwin, I. (2019). Diagnostic imaging techniques for assessment of tubal patency. *Ultrasound in Obstetrics & Gynecology*, **53**(5), 647–653.
3. Kasprzyk, L. & Kasprzyk, L. (2020). Physical parameters affecting the distribution of X-ray dose during hysterosalpingography.
4. Roest, I., Rosielle, K., van Welie, N., Dreyer, K., Bongers, M., Mijatovic, V., & Koks, C. (2021). Safety of oil-based contrast medium for hysterosalpingography: a systematic review. *Reproductive BioMedicine Online*, **42**(6), 1119–1129.
5. Tsui, S. & Sofy, A. A. (2023). A meta-analysis of fertility and adverse outcomes in oil-and water-based contrast for hysterosalpingography. *Turkish Journal of Obstetrics and Gynecology*, **20**(1), 64.
6. Roest, I., Van Welie, N., Mijatovic, V., Dreyer, K., Bongers, M., Koks, C., & Mol, B. W. (2020). Complications after hysterosalpingography with oil-or water-based contrast: results of a nationwide survey. *Human Reproduction Open*, **2020**(1), hoz045.
7. Achuka, J. A., Aweda, M. A., Usikalu, M. R., & Aborisade, C. A. (2020). Assessment of patient absorbed radiation dose during hysterosalpingography: A pilot study in Southwest Nigeria. *Journal of Biomedical Physics & Engineering*, **10**(2), 131.
8. Alzimami, K., Sulieman, A., Babikir, E., Alsafi, K., Alkhorayef, M., & Omer, H. (2015). Estimation of effective dose during hystrosalpingography procedures in certain hospitals in Sudan. *Applied Radiation and Isotopes*, **100**, 2–6.
9. Heuser, L. J. (2022). Safety and imaging characteristics of iodinated contrast agents in reproductive radiology: A comparative study. *Journal of Radiology in Reproductive Medicine*, **11**(2), 103–110.
10. Geenen, R. W., Van Der Molen, A. J., Dekkers, I. A., Bellin, M. F., Bertolotto, M., Correas, J. M., & Brismar, T. B. (2024). Contrast media for hysterosalpingography: systematic search and review providing new guidelines by the Contrast Media Safety Committee of the European Society of Urogenital Radiology. *European Radiology*, **34**(10), 6435–6443.
11. Pratama, H. Y., Zaldi, Z., Laszuarni, L., & Lubis, D. M. (2021). Perbandingan Sekresi Air Mata Sebelum dan Sesudah Penggunaan Gadget pada Mahasiswa Fakultas Kedokteran Universitas Muhammadiyah Sumatera Utara Angkatan 2015 Menggunakan Uji Schirmer 1. *Jurnal Pandu Husada*, **2**(1), 53–57.
12. Ahinko-Hakamaa, K. M., Tinkanen, H., & Paavonen, J. (2020). Hysterosalpingography in assessing female infertility: a review. *Acta Obstetricia et Gynecologica Scandinavica*, **99**(4), 479–486.
13. Mijatovic, V., Dreyer, K., Emanuel, M. H., & Hompes, P. G. A. (2019). Comparison of oil-based versus water-based contrast in hysterosalpingography: a randomized

clinical trial. *Fertility and Sterility*, **112**(6), 1231–1237.
14. Kamburoğlu, K. (2019). Effect of exposure parameters on diagnostic accuracy and radiation dose in fluoroscopy-guided imaging: a clinical review. *Radiation Protection Dosimetry*, **185**(3), 382–390.
15. Bushong, S. C. (2020). *Radiologic Science for Technologists*: Physics, Biology, and Protection (11th ed.). Elsevier.
16. Akbar, A. (2020). Gambaran faktor penyebab infertilitas pria di Indonesia: meta analisis. *Jurnal Pandu Husada*, **1**(2), 66–74.
17. Nasution, M. S. & Akbar, A. (2025). Resistance Training Has an Effect on Lowering Insulin Resistance Based on HOMA IR Examination in Poly Cystic Ovarian Syndrome (PCOS) Patients: Meta-Analysis. *Buletin Farmatera*, **10**(3), 190–197.
18. Dreyer, K., van Rijswijk, J., Mijatovic, V., et al. (2017). Oil-based or water-based contrast for hysterosalpingography in infertile women. *New England Journal of Medicine*, **376**(21), 2043–2052.
19. World Health Organization. (2016). *Radiation protection in medical applications*. WHO Press.
20. Lubis, H. M. L. (2017). High-Grade Endometrial Stromal Sarcoma. *Buletin Farmatera*, **2**(2), 67–75.

IPC

Indonesian Physics Communication

Department of Physics, Universitas Riau, Pekanbaru, Indonesia
p-ISSN 1412-2960 | e-ISSN 2579-521X

Vol. 22 | No. 2
July 2025

Web: https://kfi.ejournal.unri.ac.id
E-mail: kfi@ejournal.unri.ac.id

Preliminary study on the utilization of cabbage waste as a raw material for activated carbon in supercapacitor applications

Intan Syahputri, Awitdrus*
Department of Physics, Universitas Riau, Pekanbaru 28293, Indonesia

*Corresponding author: awitdrus@lecturer.unri.ac.id

ABSTRACT

This study aims to utilize cabbage waste as an active carbon material for supercapacitor electrodes through an environmentally friendly approach without chemical activation. The fabrication process includes pre-carbonization at 200°C for 1 hour, carbonization at 600°C, and physical activation at 850°C. The resulting carbon material exhibits a porous structure essential for ion storage, despite the absence of chemical activation. Electrochemical testing using the galvanostatic charge-discharge method with Na_2SO_4 electrolyte concentrations of 0.5 M, 1 M, and 1.5 M demonstrated a highest specific capacitance of 155.87 F/g at 1.5 M concentration. The increase in electrolyte concentration enhances ion mobility and charge storage capacity. This research indicates that cabbage waste can serve as an effective active carbon source for supercapacitors, with further performance improvements expected through chemical activation in future studies.

Keywords: Cabbage waste; carbon electrode; Na_2SO_4; specific capacitance; supercapacitor

Received 12-05-2025 | Revised 26-05-2025 | Accepted 03-06-2025 | Published 31-07-2025

INTRODUCTION

Electrical energy is a primary necessity used in various aspects of life. Electronic devices such as mobile phones and computers require a supply of electrical energy to function. The high mobility of users drives the need for portable devices that can be used in various locations. The use of these devices demands energy storage media that are efficient and affordable. An ideal energy storage device is one that can balance energy density and power density, as found in supercapacitors. Supercapacitors have several advantages, including fast recharge capability, high power density, large charge storage capacity, short charge and discharge times, and longer lifespan [1].

The electrode and electrolyte are two of the most important components in a supercapacitor system. Various materials can be used as the base for electrodes, including activated carbon, metal oxides, and conductive polymers. Among these, activated carbon stands out due to its abundant availability, low production cost, high electrical conductivity, large surface area, good chemical stability, and relatively simple synthesis process [2]. On the other hand, electrolytes serve as ion-conducting media between the positive and negative electrodes. During the charging and discharging processes, ions in the electrolyte migrate toward the electrodes, forming an electrical double layer or participating in redox reactions on the electrode surface, depending on the type of capacitance involved [3].

One of the commonly used aqueous electrolytes in supercapacitor research is sodium sulfate (Na_2SO_4). This electrolyte is non-corrosive, non-toxic, environmentally friendly, and safe for large-scale energy applications. These advantages make it an ideal choice for energy storage systems that require high stability and operational safety. Several studies have also shown that Na_2SO_4 provides good cycling stability with high capacitance retention after thousands of charge–discharge cycles [4].

The synthesis of activated carbon from sugar palm frond electrodes using 0.5 M KOH as an activator with Na_2SO_4 electrolyte produced a capacitance value of 79 F/g at 0.5 M

concentration, measured by the cyclic voltammetry (CV) method [5]. The synthesis of sodiated manganese oxide P2-$Na_{2/3}MnO_2$ using a hydrothermal method followed by annealing at 900 °C for 12 hours produced a high specific capacitance of 234 F/g, while the non-sodiated Mn_2O_3 annealed at 400 °C delivered only 115 F/g. Both materials were tested in a 1.0 M Na_2SO_4 aqueous electrolyte using a three-electrode system at a current density of 0.4 A/g [4]. This study reports the effect of electrolyte concentration on the electrochemical performance of a supercapacitor based on Reduced Graphite Oxide (RGO) using sodium sulfate (Na_2SO_4) electrolyte at various concentrations of 0.5 M, 1 M, 1.5 M, and 2 M. The supercapacitor achieved a maximum specific capacitance of 176 F/g in 1 M Na_2SO_4 solution, with an energy density of 47 Wh/kg and a power density of 700 W/kg [6].

Agricultural and vegetable waste are abundant sources of biomass that have not yet been optimally utilized. One commonly produced type of vegetable waste is cabbage waste (*Brassica oleracea*), particularly the outer leaves that are not used for consumption or market distribution. This waste is generally discarded or used as animal feed, despite its chemical composition being highly promising for development as a carbon precursor, especially for energy applications such as supercapacitor electrodes [7].

The outer cabbage leaves are known to contain lignocellulosic components consisting of cellulose, hemicellulose, and lignin. The cellulose content in dried cabbage leaves reaches approximately 63%, with hemicellulose and lignin at 15% and 14%, respectively. This composition indicates that cabbage waste has a stable carbon structure and is rich in functional groups that can be carbonized to produce activated carbon materials. Moreover, its abundant availability and low processing cost make cabbage waste an ideal candidate for environmentally friendly electrode materials [8]. The use of cabbage as a vegetable often generates waste that goes unutilized. This cabbage waste is commonly found in markets, where producers frequently discard the outer layers of the cabbage as they are considered unsuitable for consumption due to dirt and potential impact on the selling price [9].

In this study, cabbage waste was carbonized at 600 °C in a CO_2 atmosphere and physically activated at 850 °C using N_2 gas without chemical activation. Na_2SO_4 electrolyte concentrations of 0,5 M, 1 M, and 1,5 M were varied to evaluate electrode performance using CV and galvanostatic charge-discharge methods.

RESEARCH METHODOLOGY

Material Source

The raw material for carbon electrode fabrication, cabbage waste, was sourced from Pasar Selasa, Tampan District, Riau Province.

Activated Carbon Preparation

The preparation of activated carbon from cabbage waste involves three main steps: pre-carbonization, carbonization, and physical activation. In the pre-carbonization stage, 30 grams of cabbage waste are weighed and placed into a stainless steel tube, which is then heated in an oven at 200°C for 1 hour to make the sample brittle and easier to grind. Carbonization were begins at room temperature (30°C) until reaching 302°C, which is maintained for 1 hour. Subsequently, the sample is further heated inside a furnace up to 600°C in a nitrogen (N_2) atmosphere. Finally, in the physical activation stage, nitrogen gas is replaced with carbon dioxide (CO_2) at 600°C, and the temperature is increased to 850°C. This temperature is held for 2 hours and 30 minutes before being allowed to cool gradually to room temperature. The physical activation using CO_2 gas aims to enhance the surface area and remove tar deposits within the pores by creating new pores through reactions with activated carbon [10].

Supercapacitor Cell Fabrication

Several components are required to fabricate a supercapacitor cell, including current collectors, two carbon electrodes, electrolyte, and separator. Chicken egg membrane is used as the separator. To prevent cell leakage through holes, Teflon supports are made with diameters matching the electrodes. The Teflon ring is placed in the center of the support hole, and glue is applied on the back of the support body. Then, stainless steel shaped according to the electrode diameter is placed on top of the Teflon ring. After soaking the carbon electrodes in Na_2SO_4 solution for 48 hours, they are removed and placed on the stainless steel using a spatula or tweezers. The two support bodies are reinforced and clamped to ensure the electrodes and ions fully contact the surface of the stainless steel.

Characterization

Mass loss measurement is conducted to determine how much the material's mass decreases after thermal treatment. The dried cabbage waste is first weighed to obtain the initial mass (m_0), then heated through the pre-carbonization process at a specific temperature and duration. After the process is complete, the sample is cooled and weighed again to obtain the final mass (m_1). The percentage of mass loss is calculated by comparing the difference between the initial and final mass relative to the initial mass. The measurement is repeated three times to ensure data accuracy.

Density is a parameter that reflects the mass compactness of electrode material per unit volume (g/cm³). Too low a density can reduce volumetric capacity, while too high a density can hinder electrolyte ion diffusion into the material's pores. Therefore, an optimal density is crucial to balance specific capacitance and ion transfer efficiency [11]. Density (ρ) can be calculated using the formula [12]:

$$\rho = \frac{m}{v} \quad (1)$$

where, ρ represents density (g/cm³), m is the dry mass of the sample (g), and v is the volume of the material (cm³). Density is the mass per unit volume. To determine the density of the pressed pellets, the diameter and thickness are measured using a caliper, while the pellet mass is weighed using a digital scale. Density measurements are performed before and after pyrolysis. Densities before and after pyrolysis were compared to assess the effects of carbonization and activation on the carbon material's physical properties.

Electrachemical Measurement

Electrochemical characterization using the CV method is conducted with a Physics CV UR RadAs 2508 v.1.0 instrument. The CV method produces voltammogram curves and determines the specific capacitance of the supercapacitor made from active carbon electrodes derived from cabbage waste, using a chicken eggshell membrane as the separator. Specific capacitance is measured at potentials ranging from 0 to 1 V with scan rates of 1 mV/s, 2 mV/s, 5 mV/s, and 10 mV/s. The graphs and data are saved on a computer in JPG and Microsoft Excel formats. The CV test yields data on discharge and charge currents, which are processed using SigmaPlot software.

Galvanostatic Charge-Discharge (GCD) is a method used to determine the specific capacitance of the supercapacitor cell by measuring charge and discharge times [13]. GCD is performed by applying a constant positive and negative current to charge and discharge the material within a predetermined potential range. Specific capacitance is measured at potentials from 0 to 1 V with current densities of 1, 2, 5, and 10 A/g. The measurement results are processed using SigmaPlot to obtain data and curves showing the relationship between current and voltage. The specific capacitance can be calculated from the discharge time using the formula:

$$C_{sp} = \frac{2.I.\Delta t}{m.\Delta v} \quad (2)$$

RESULTS AND DISCUSSION

Physical Property Characterization

Pre-carbonization is the initial stage to transform organic material into carbon, causing the sample to change color to brown and become more brittle, thus facilitating the crushing process. This stage was carried out at a temperature of 200°C for 1 hour. The sample was weighed with an initial weight of 30 grams before the pre-carbonization process, then weighed again after the process was completed.

Table 1. Mass loss data.

M_1 (gr)	M_2 (gr)	Mass loss (gr)	Mass loss (%)
30	22.45	7.55	34
30	22.9	7.1	31
30	23.15	6.85	30
30	23.21	6.79	29
30	22.1	7.9	36
Average shrinkage			32

Table 1 shows the percentage of mass loss before and after the pre-carbonization process. After pre-carbonization, the remaining mass of cabbage waste was 113.81 grams from an initial mass of 150 grams, resulting in a mass loss percentage of 32%. This process caused the evaporation of water from the sample's compounds but did not affect lignin, cellulose, and hemicellulose at temperatures below 300°C. Under these conditions, the sample could be pressed into carbon pellets without the addition of a binder due to its self-binding properties. This characteristic is marked by the change in the sample's texture, becoming more brittle and easier to grind [14].

Density measurement was conducted to determine the change in material compactness before and after the pyrolysis process. Density was calculated based on the mass and volume of the material (g/cm³), and shrinkage was calculated to understand the extent of change caused by pyrolysis. For the KU sample (cabbage waste without activation), the density before pyrolysis was 1.010 g/cm³, and it decreased to 0.734 g/cm³ after pyrolysis.

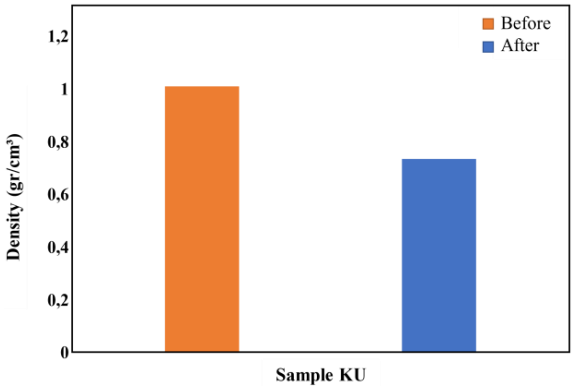

Figure 1. Density measurement results.

Based on Equation (1) and (2), a density reduction of 37.602% occurred, indicating thermal degradation of organic components such as hemicellulose, cellulose, and lignin present in the cabbage waste. During pyrolysis, volatile compounds evaporate, resulting in a porous carbon structure with lower density. This porous structure is advantageous for supercapacitor applications as it allows an increase in specific surface area and charge storage capacity. However, without an activation process (e.g., using KOH), pore development may remain limited, which could affect the overall electrochemical performance.

Electrochemical Characterization

The CV measurement results produced a slightly distorted rectangular-shaped curve, indicating that the supercapacitor exhibits typical Electric Double Layer Capacitance (EDLC) characteristics. A scan rate of 1 mV/s means the voltage is increased gradually by 1 mV every second until reaching the maximum voltage of 1000 mV. At this scan rate, there is a longer time available, allowing ions from the electrolyte solution to diffuse evenly and optimally fill the pores of the carbon electrode. Therefore, the 1 mV/s scan rate is often used to obtain more accurate specific capacitance measurements [15].

Figure 2 (a) shows the electrochemical characterization of cabbage-waste-based carbon electrodes using the cyclic voltammetry (CV) method over a voltage range of 0 – 1 V. The graph displays three curves with an elliptical

shape characteristic of Electric Double Layer Capacitor (EDLC) charge storage mechanisms, indicating that energy storage occurs capacitively without significant faradaic reaction contributions [16].

Figure 2 (b), (c), and (d) present the cyclic voltammetry (CV) curves of cabbage-waste-derived carbon electrodes recorded at scan rates of 1 mV/s, 2 mV/s, and 5 mV/s, respectively. KU-1.5 sample exhibits the largest CV curve area, which corresponds to the highest specific capacitance. This is attributed to the increased concentration of Na^+ and SO_4^{2-} ions in the 1.5 M electrolyte solution, which enhances the formation of the electrical double layer on the electrode surface. In other words, the higher the electrolyte concentration, the greater the charge density that can accumulate [17].

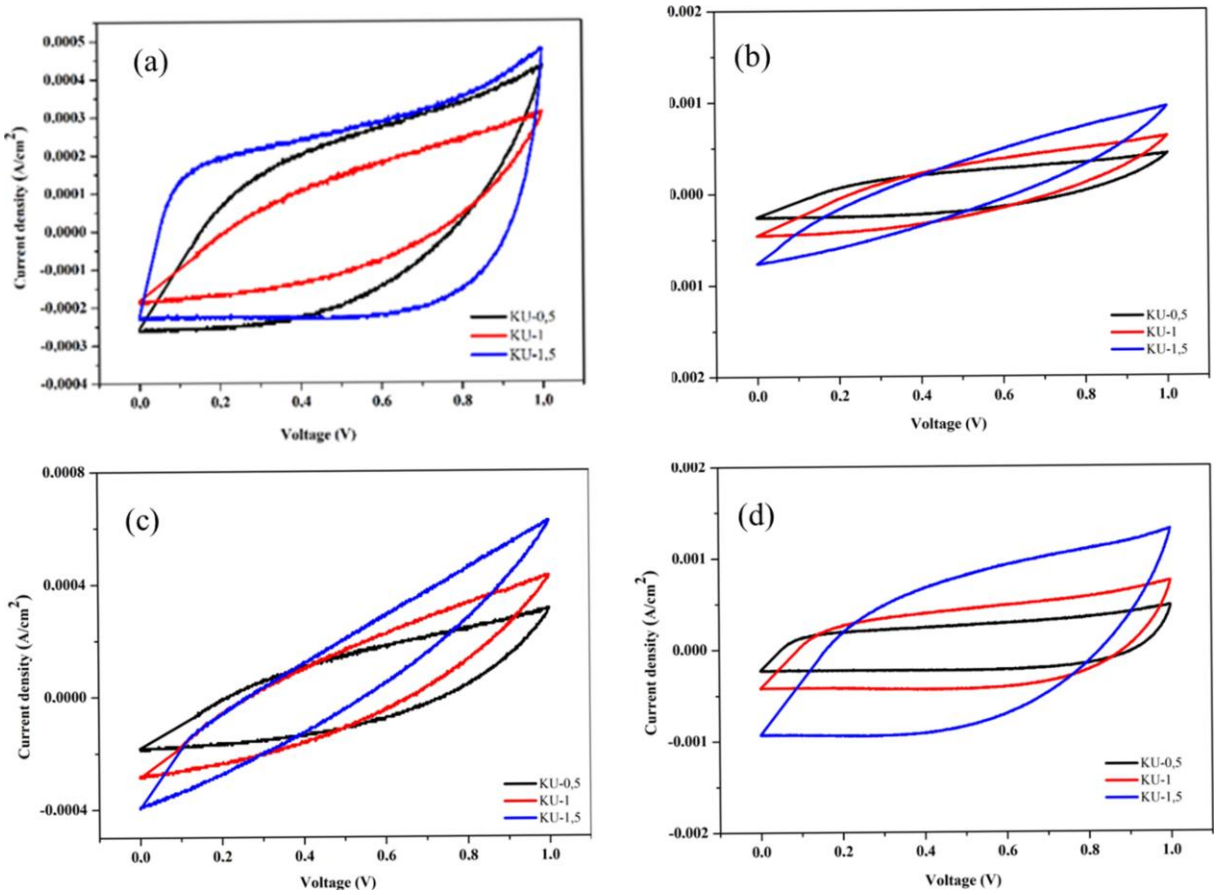

Figure 2. CV curves at different scan rates: (a) scan rate of 1 mV/s comparison and (b) KU-0.5, (c) KU-1, and (d) KU-1.5.

Nevertheless, at excessively high concentrations, diffusion resistance may occur due to increased electrolyte viscosity. However, in this graph, KU-1.5 still demonstrates the best performance, indicating that at this level, the viscosity has not significantly hindered ion diffusion.

Galvanostatic Charge-Discharge (GCD) is a technique used to evaluate the electrochemical kinetics and stability of materials during charge-discharge cycles. In this study, activated carbon electrodes derived from cabbage waste were tested using a constant current of 1 A, as shown in Figure 3. The results are presented in the form of triangular curves, which reflect the ion charging and discharging behavior on the electrode surface.

Figure 3 shows that all three electrode samples KU-0.5, KU-1, and KU-1.5 exhibit curves that are generally symmetrical between the charge and discharge processes. This indicates that the dominant energy storage mechanism is based on the Electric Double Layer Capacitor (EDLC), which stores charge

electrostatically without involving redox reactions [18].

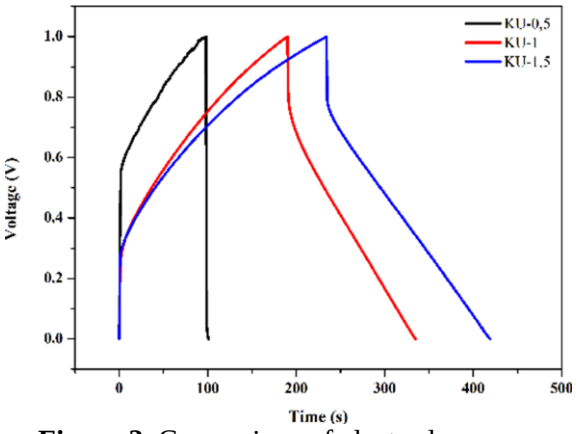

Figure 3. Comparison of electrode curves.

According to the graph, increasing the concentration of Na_2SO_4 electrolyte leads to a longer discharge time in the samples. This suggests that a higher ion concentration in the solution enhances the efficiency of ion transport toward the electrode surface and into the carbon pores, thereby increasing energy storage capacity. The specific capacitance (Cs) values calculated from the GCD curves show an increasing trend with higher electrolyte concentrations. For the KU-0.5 sample, the specific capacitance was 32.52 F/g, which is the lowest value obtained. This is attributed to the limited number of ions in the solution, resulting in suboptimal formation of the electrostatic charge layer. For KU-1, the specific capacitance increased significantly to 121.06 F/g, indicating that a 1 M Na_2SO_4 concentration provides a balance between solution viscosity and ion availability for interaction with the electrode surface [19].

Figure 4 shows The KU-1.5 sample demonstrated the best performance, with the highest specific capacitance value of 155.87 F/g. Its longer discharge time and the most symmetrical curve indicate that a 1.5 M concentration offers a sufficient number of ions for rapid diffusion into the electrode pore structure, without compromising system stability [20].

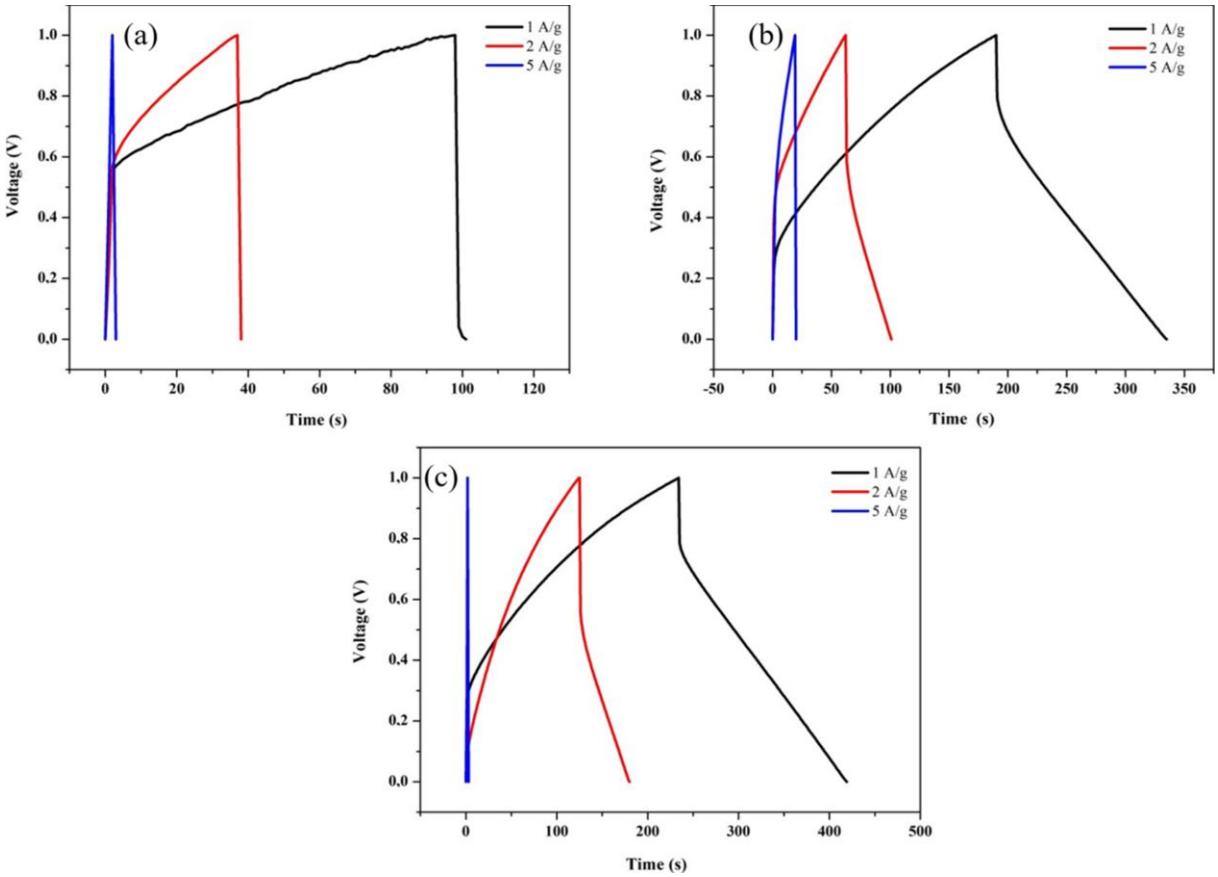

Figure 4. GCD curves at different scan rates (a) KU-0.5, (b) KU-1, and (c) KU-1.5.

Overall, it can be concluded that the electrochemical performance of cabbage-waste-derived carbon electrodes is highly influenced by the electrolyte concentration. Increasing the Na_2SO_4 concentration from 0.5 M to 1.5 M significantly improves the specific capacitance, demonstrating that a simple modification in electrolyte conditions can substantially enhance the energy storage capacity of biomass-based supercapacitors.

CONCLUSION

This study demonstrates that cabbage waste can be utilized as a source of activated carbon for supercapacitor electrodes through an environmentally friendly process without chemical activation. The electrode fabrication involved pre-carbonization at 200°C for 1 hour, main carbonization at 302°C, and physical activation at 850°C using a furnace. These steps successfully produced porous carbon material, as indicated by the reduction in mass and density due to the thermal degradation of organic components.

Electrochemical testing using the Galvanostatic Charge-Discharge (GCD) method with Na_2SO_4 electrolyte at concentrations of 0.5 M, 1 M, and 1.5 M showed an increase in specific capacitance with increasing electrolyte concentration. The highest capacitance value of 155.87 F/g was achieved at 1.5 M, indicating the crucial role of electrolyte concentration in enhancing ion transport and charge storage within the porous carbon structure.

Overall, cabbage waste has significant potential as a carbon precursor for supercapacitor applications, with optimal performance observed at 1.5 M Na_2SO_4 electrolyte concentration. However, to further enhance micropore formation, surface area, and electrode performance, chemical activation (e.g., KOH) is recommended for future studies.

REFERENCES

1. Dar, M. A., Majid, S. R., Satgunam, M., Siva, C., Ansari, S., Arularasan, P., & Ahamed, S. R. (2024). Advancements in Supercapacitor electrodes and perspectives for future energy storage technologies. *International Journal of Hydrogen Energy*, **70**, 10–28.
2. Ahmad, F., Shahzad, A., Danish, M., Fatima, M., Adnan, M., Atiq, S., Asim, M., Khan, M. A., Ain, Q. U., & Perveen, R. (2024). Recent developments in transition metal oxide-based electrode composites for supercapacitor applications. *Journal of Energy Storage*, **81**, 110430.
3. Shah, S. S., & Aziz, M. A. (2024). Properties of electrode materials and electrolytes in supercapacitor technology. *J. Chem. Environ*, **3**(1), 10–56946.
4. Nechikott, A. A. & Nayak, P. K. (2023). Electrochemical capacitance properties of pre-sodiated manganese oxide for aqueous Na-ion supercapacitors. *RSC Advances*, **13**(21), 14139–14149.
5. Suwandi, D. A., Taer, E., Farma, R., & Syahputra, R. F. (2021). Effect of aqueous electrolyte to the supercapacitor electrode performance made from sugar palm fronds waste. *Journal of Physics: Conference Series*, **1951**(1), 012009.
6. Krishnan, P. & Biju, V. (2022). Effect of electrolyte concentration on the electrochemical performance of RGO-Na2SO4 supercapacitor. *Materials Today: Proceedings*, **54**, 958–962.
7. Pandey, D., Kumar, K. S., & Thomas, J. (2024). Supercapacitor electrode energetics and mechanism of operation: Uncovering the voltage window. *Progress in Materials Science*, **141**, 101219.
8. Ansari, K. B., Mashkoor, R., Naim, M. A., Raheman, A. S., Ansari, M. Y., Khan, P., Hasib, R., & Shkir, M. (2025). A critical review on pure and hybrid electrode supercapacitors, economics of HESCs, and future perspectives. *Journal of Energy Storage*, **112**, 115564.
9. Xiong, W., Meng, J., Zhang, Y., Fan, G., Pan, C., Shen, C., & Long, Y. (2025). Effect of alternating current electric fields on the preservation of fresh-cut Chinese

cabbage and spinach. *Innovative Food Science & Emerging Technologies*, **102**.
10. Hegde, S. S. & Bhat, B. R. (2024). Biomass waste-derived porous graphitic carbon for high-performance supercapacitors. *Journal of Energy Storage*, **76**, 109818.
11. Phor, L., Kumar, A., & Chahal, S. (2024). Electrode materials for supercapacitors: A comprehensive review of advancements and performance. *Journal of Energy Storage*, **84**, 110698.
12. Zhang, Y., Li, X., Li, Z., & Yang, F. (2024). Evaluation of electrochemical performance of supercapacitors from equivalent circuits through cyclic voltammetry and galvanostatic charge/discharge. *Journal of Energy Storage*, **86**, 111122.
13. Mei, Y., Liu, S., Wu, L., Zhou, B., Wang, Z., Huang, Z. H., Zhu, Y., & Wang, M. X. (2024). Kelp derived hierarchically porous carbon aerogels with ultrahigh surface area for high-energy-density supercapacitor in aqueous electrolyte. *Journal of Energy Storage*, **77**, 109878.
14. Tian, Y., Wang, S., Liu, N., Xue, Q., Qi, X., Liu, H., Cabot, A., & Liao, L. (2025). Rapid Joule heating processing of nickel-based flexible supercapacitors. *Chemical Engineering Journal*, **507**, 160765.
15. Hardianto, Y. P., Shah, S. S., Shuaibu, A. D., Mohamed, M., Sarker, S., Alzahrani, A. S., & Aziz, M. A. (2025). Modeling supercapacitors with the simplified Randles circuit: Analyzing electrochemical behavior through cyclic voltammetry and Galvanostatic charge-discharge. *Electrochimica Acta*, **513**, 145552.
16. Hefnawy, A., El Nady, J., Hassan, A. M., Mahgoub, F. M., Ebrahim, S., Emanfaloty, R. A., & Elshaer, A. M. (2025). Machine learning model of polypyrrole based-supercapacitor electrode: Fabrication, characterization, and prediction. *Journal of Alloys and Compounds*, **1019**, 179240.
17. Mousavianfard, S. A., Molaei, A., Manouchehri, M., Foroozandeh, A., Shahmohammadi, A., & Dalvand, S. (2025). RETRACTED: Enhanced supercapacitor performance using [Caff-TEA]+[ZnBr3]− ionic liquid electrode in aqueous Na_2SO_4 electrolyte. *Journal of Energy Storage*, **109**, 115232.
18. Aziz, S. B., Hama, P. O., Aziz, D. M., Sadiq, N. M., Woo, H. J., Kadir, M. F., Abdulwahid, R. T., Al-Asbahi, B. A., Ahmed, A. A., & Hassan, J. (2025). EDLC supercapacitor with enhanced charge-discharge cycles designed from plasticized biopolymer blend electrolytes: Biomaterials will be the future of energy storage devices. *Journal of Energy Storage*, **114**, 115841.
19. Tarek, M., Yasmeen, F., & Basith, M. A. (2025). High-voltage symmetric supercapacitors developed by engineering DyFeO 3 electrodes and aqueous electrolytes. *Journal of Materials Chemistry A*, **13**(1), 499–516.
20. Rohith, R., Prasannakumar, A. T., Manju, V., Thomas, M., Mohan, R. R., & Varma, S. J. (2024). An insight into the electrochemical performance of nanostructured V2O5 in aqueous neutral electrolytes and fabrication of 2V, high energy density, symmetric supercapacitor. *Electrochimica Acta*, **503**, 144911.

IPC

Indonesian Physics Communication

Department of Physics, Universitas Riau, Pekanbaru, Indonesia
p-ISSN 1412-2960 | e-ISSN 2579-521X

Vol. 22 | No. 2
July 2025

Web: https://kfi.ejournal.unri.ac.id
E-mail: kfi@ejournal.unri.ac.id

Evaluation of noise values and homogenity of CT scan image results on head phantom after daily calibration

Evelin Trivena Samaliwu*, Gregoria Illya
Departement of Physics, Matana University, Tangerang 15810, Indonesia

*Corresponding author: evelin.samaliwu@student.matanauniversity.ac.id

ABSTRACT

Evaluation of CT scan image quality is a crucial aspect in ensuring accurate medical diagnosis. This research aims to evaluate noise values and image homogeneity of CT scans on a head phantom after daily calibration. Evaluation of these two parameters is critical because high noise can interfere with image contrast and lead to clinical misinterpretation, while low homogeneity may indicate artifacts or system inconsistencies that potentially reduce diagnostic reliability. Measurements were performed using Region of Interest (ROI) at five points (one in the center and four at the edges at 12, 3, 6, and 9 o'clock positions) across six image slices, for both head and body modes. The CT scan system used was Siemens SOMATOM go.Top, with primary scanning parameters for each mode: 120 kV voltage, 265 mA current (head) and 220 mA (body), as well as Hr40f and Br40f kernels. Research results show that the CT number homogeneity values in head mode ranged from -1.96 to 0.81 HU, and in body mode from -1.78 to 1.28 HU; all were within the tolerance limit of 0 ± 4 HU. Noise values for head mode ranged from 3.49 – 3.67 HU and body mode from 4.98 – 5.37 HU, also within standard tolerance limits. These findings indicate that the CT scan system functions properly and meets diagnostic imaging quality standards. Additionally, these results support the importance of implementing periodic quality control as part of improving radiological service quality and strengthening patient safety standards in medical facilities.

Keywords: CT scan; homogeneity; noise; quality control

Received 29-04-2025 | Revised 15-06-2025 | Accepted 08-07-2025 | Published 31-07-2025

INTRODUCTION

A CT scan (Computed Tomography Scan) is a diagnostic procedure that utilizes X-rays and computer technology to produce detailed images of internal organs, including the head, neck, chest, abdomen, and upper and lower limbs [1]. This technology is highly effective in assessing the condition of blood vessels, including those in the head, heart, and limbs. A CT scan can be used to evaluate the heart's blood vessels without the use of heart-lowering medications. Furthermore, this technique also helps assess blood flow (perfusion) in the brain. The information obtained through a CT scan is crucial for decision-making regarding stroke treatment, accelerating intervention, and reducing the risk of disability.

However, the image quality produced by a CT scan is significantly affected by two main factors: noise and CT value homogeneity. High noise can cause the loss of important image details and reduce tissue contrast, while low homogeneity can indicate an uneven signal distribution, either due to systemic interference, beam imbalance, or detector errors. The challenge is that noise and homogeneity measurements often exhibit variability between machines and over time, especially if consistent quality control (QC) is not performed. Furthermore, there is the potential for calibration errors or limited instrument accuracy, which can impact the reliability of imaging results.

Quality Assurance (QA) is a program designed to maintain optimal diagnostic image quality with minimal risk and discomfort to patients. CT scan QA is performed using a built-in phantom to ensure the system's stability and accuracy in producing high-quality diagnostic images, as well as verifying that the radiation dose remains within safe limits before

use on patients. This quality assurance has been explained in publications by the International Atomic Energy Agency (IAEA) and the International Society of Radiographers and Radiological Technologists (ISRRT), which emphasize the importance of regular evaluations to maintain image quality [2, 3]. This QA includes Quality Control (QC) conducted periodically, ranging from daily, weekly, monthly, and even annually, to ensure optimal system performance [4]. CT scan image quality can be assessed by the noise level and the homogeneity of CT values in the image by measuring the standard deviation in the Region of Interest (ROI) [5].

Noise is an important indicator for detecting system problems such as detector interference or poor calibration, which can degrade image quality. Noise describes the reduction in contrast resolution of a CT scan image and is calculated in the Region of Interest (ROI), where its value can be determined from the ROI standard deviation [6]. Homogeneity in a CT scan system ensures that CT values remain consistent throughout the resulting image area, which aims to improve imaging reliability in clinical analysis and diagnosis [7]. Homogeneity calculations are used to identify potential artifacts that can affect the quality of CT scan results. Homogeneity is calculated by determining the absolute value of the difference between the average CT value in the central ROI and the average CT value of the four ROIs at the periphery.

Several previous studies have highlighted the importance of daily calibration in reducing noise and improving CT value homogeneity in CT scan imaging. One study by Lestari and Heru (2022) evaluated the noise and uniformity values of CT scan images by comparing the results before and after daily calibration using a water phantom [6]. The results of this study showed a decrease in standard deviation (noise) of 0.01 HU in the head protocol and 0.81 HU in the abdomen protocol after calibration, as well as an increase in uniformity of 0.258 HU and 1.56 HU, respectively. This study demonstrates that daily calibration can have a positive impact on CT image quality.

However, the approach used in previous studies still has several limitations. For example, measurements were only performed on a single central ROI and did not systematically cover the entire peripheral ROI area. Furthermore, these studies did not detail the influence of specific CT machine technical parameters (such as reconstruction kernel and tube current), and did not include slice variation as an evaluative factor.

Insufficient QC can lead to decreased image quality. If the resulting image is difficult to diagnose due to noise or artifacts, a repeat scan may be necessary, which can result in the patient receiving an excessive radiation dose [8]. This study aims to fill this gap by conducting a comprehensive evaluation of noise and spatial homogeneity of CT values across six image slices, using five ROI measurement points (center and four o'clock directions at 12, 3, 6, and 9 o'clock) in both head and body modes. Furthermore, this study used the Siemens SOMATOM go.Top CT scanner system with detailed parameter specifications, which can provide a stronger context for daily QC practices in hospitals. With a more systematic and representative measurement design, this study provides an additional contribution to understanding the performance of CT scanner systems after daily calibration, which has not been thoroughly explored in previous studies.

RESEARCH METHOD

This research was conducted using an experimental approach, with the scanned object being a head phantom from a CT scanner system that had been calibrated according to manufacturer standards. This phantom was 20 cm in diameter and served as a simulation of human head tissue for image quality evaluation. Noise can be calculated using the following Equation (1) [9, 10]:

$$SD = \sqrt{\frac{\sum(x_i - \mu)^2}{n-1}} \quad (1)$$

SD = Standard deviation
x_i = Number of pixel values in ROI
μ = Average pixel value in ROI
n = Total number of pixels in ROI

SD is the standard deviation, where x_i is the number of pixel values or CT values in each ROI, is the average of all CT values in the ROI, and n is the total number of pixels in the ROI. Noise will be zero if all pixels have uniform values, while excessive variation in pixel values will cause an increase in noise [11]. Measurements were performed repeatedly to ensure consistency of results [12]. Scans were performed using head CT protocols (based on head characteristics) and abdominal CT protocols (based on body/abdomen characteristics). The scan parameters used are presented in Table 1 for head mode and Table 2 for body mode.

Table 1. Typical head mode [13].

Parameters	System A
Voltage	120 kV
Current	265 mA
Scan time	1 s
Rotation time	1 s
Shaped filter	Standard
Body region	Head
Kernel	Hr40f

Table 2. Typical body mode (babdomen) [13].

Parameters	System A
Voltage	120 kV
Current	220 mA
Scan time	0.5 s
Rotation time	0.5 s
Shaped filter	Standard
Body region	Body
Kernel	Br40f

Scanning is performed by first placing a 20 cm diameter phantom on the gantry. This process includes installing the phantom support on the examination table, placing the phantom on the support, and aligning the phantom's center with the vertical and horizontal laser indicators to ensure it is at the gantry's isocenter, as shown in Figure 1. The operator can then proceed by opening the "Settings" menu on the computer screen and selecting the "Daily QA" option. The next step is to click the "Go" button to start the system. After waiting for 19 seconds, the operator is prompted to press the "Press Start" button in the "Route Control" section to continue the QC process. The system will then process the data, and within approximately 10 minutes, the QC results will be automatically displayed on the screen [13].

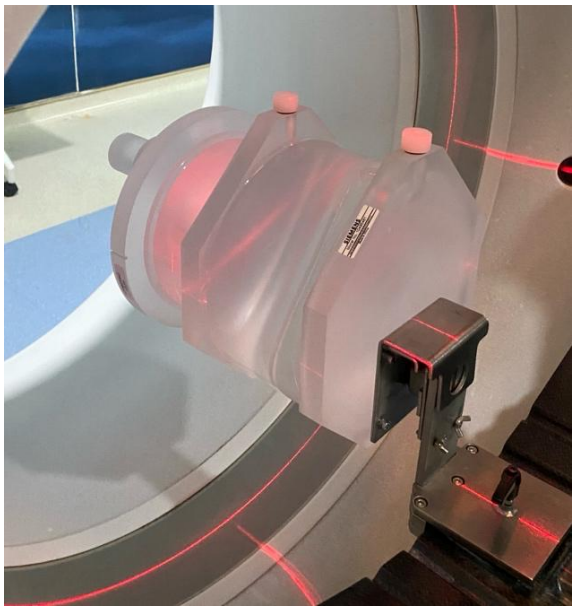

Figure 1. Phantom position at the gantry isocenter [14].

CT values are expressed in Hounsfield Units (HU), a standard feature on CT scanners. HU describes the degree of attenuation of X-rays after passing through an object, reflecting differences in density between organs [15]. HU measurements to assess noise and homogeneity are performed by defining a 10 mm measurement area called a Region of Interest (ROI). The ROI is placed in the center and at the 12, 3, 6, and 9 o'clock positions. ROI placement for both experimental protocols (Head and Abdomen) is performed in the same manner.

Figure 2 shows the determination and measurement of 10 mm ROIs at five points

(center, and at the 12, 3, 6, and 9 o'clock positions) to obtain homogeneity values.

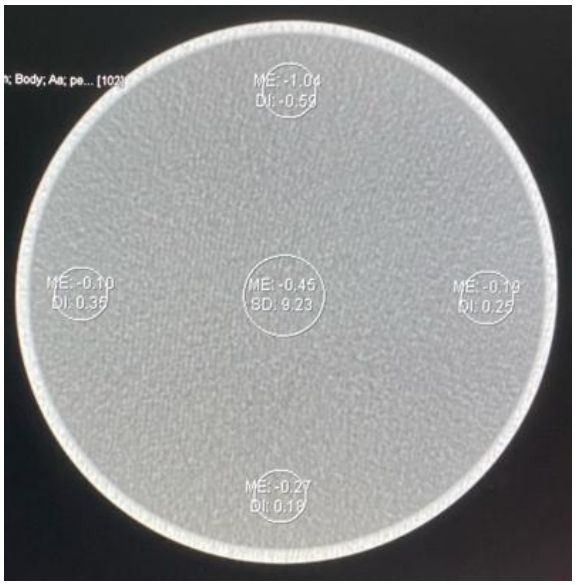

Figure 2. Determining and measuring ROI [14].

Measuring noise and homogeneity in CT scan images presents potential challenges that require attention, particularly those related to external factors such as variations in electrical voltage and room environmental conditions. Unstable electrical voltage can affect the energy output of the X-ray tube, thus impacting the quality of the resulting image. Furthermore, room temperature, humidity, and vibration can also affect instrument performance, including detector sensitivity. Improper phantom placement in the center of the gantry and inconsistencies in calibration procedures can also contribute to increased noise variation in the resulting image.

Ideally, CT values are similar throughout the scan area, and the difference between the central ROI and the peripheral ROI should not exceed 0 ± 4 HU (Hounsfield Units) [2, 13]. The smaller this difference, the better the level of homogeneity achieved. Meanwhile, the permissible limit for noise in CT systems is a standard deviation of 3.90 HU ± 15% for adult heads and 5.02 HU ± 15% for adult heads [13]. Quality control on CT scans is necessary periodically to produce accurate HU values [11].

RESULT AND DISCUSSION

Quality control, which includes evaluating the noise and homogeneity of CT scan images, was performed after daily calibration to identify any deviations that could degrade image quality. The following results were obtained.

Table 3. Head homogeneity results [14].

Slice	Center (HU)	O'clock direction (HU)			
		3	6	9	12
1	-1.96	0.69	0.81	0.71	0.46
2	-1.19	0.42	0.40	0.50	0.21
3	-1.44	0.59	0.32	0.56	0.31
4	-1.67	0.47	0.36	0.27	0.24
5	-1.33	0.36	0.48	0.47	0.33
6	-0.80	0.38	0.35	0.11	0.27

Table Figure 3 shows that the head mode homogeneity values range from -1.96 to 0.81 HU, with the lowest value in the first slice at the center of the ROI (-1.96 HU) and the highest value in the first slice at the 6 o'clock edge of the ROI (0.81 HU). All values obtained remain within the permissible tolerance limit of 0 ± 4 HU for the water phantom, according to applicable standards. This indicates that the measurement results still meet the specified criteria without any significant deviations.

Table 4. Body homogeneity results [14].

Slice	Center (HU)	O'clock direction (HU)			
		3	6	9	12
1	-1.78	1.04	1.16	0.96	0.59
2	-0.82	0.56	0.38	0.52	0.72
3	-1.40	0.78	0.86	1.28	1.04
4	-1.62	0.80	0.62	1.00	0.76
5	-1.16	0.95	0.91	0.83	0.80
6	-0.46	0.54	0.47	0.39	0.31

In Table 4 it can be seen that the homogeneity of the body mode ranges from -1.78 HU to 1 HU, with the lowest values in the first slice at the ROI center (-1.78 HU) and in the fourth slice at the 9 o'clock edge of the ROI (1 HU). All values obtained were within the permissible tolerance limits of 0 ± 4 HU for the water phantom, according to applicable standards. This homogeneity value indicates that the distribution of X-rays received by the

detector remains even, resulting in consistent and reliable image quality [16].

Table 5. Head noise results [14].

Slice	Results (HU)	Status
1	3.67	In tolerance
2	3.55	In tolerance
3	3.53	In tolerance
4	3.58	In tolerance
5	3.49	In tolerance
6	3.50	In tolerance

The results in Table 5 show that the image noise value in head mode is in the range of 3.49 to 3.67 HU. This value is still within the specified tolerance limit, which is 2.88 to 4.48 HU (3.90 HU ± 15%).

Table 6. Body mode noise results [14].

Slice	Results (HU)	Status
1	5.37	In tolerance
2	5.18	In tolerance
3	5.04	In tolerance
4	5.14	In tolerance
5	5.02	In tolerance
6	4.98	In tolerance

In Table 6, the image noise values range from 4.98 to 5.37 HU, as shown in Table 4.6. Overall, the results show that all measured values are within the specified tolerance range. The range is between 4.27 and 5.77 HU, which is within the specified tolerance range of 5.02 HU ± 15%.

These findings have important implications for clinical practice, as high noise levels or low homogeneity can cause image artifacts and loss of fine structural detail. This can increase the risk of misinterpretation by radiologists, especially in complex anatomical areas such as the brain or abdomen. Therefore, maintaining noise and homogeneity levels within acceptable limits is crucial for producing accurate images and supporting sound clinical decision-making. This also helps avoid the need for repeat scans, which can increase patient radiation exposure. This study suggests that CT image quality evaluation should not be limited to noise and homogeneity parameters, but should also include other aspects such as spatial resolution and low-contrast detection capability. Furthermore, the use of multiple phantom types and regular, long-term monitoring are recommended to improve the accuracy of quality control and the overall reliability of the CT system.

CONCLUSION

Daily quality control (QC) on CT scans was successfully implemented by evaluating two main parameters: CT value homogeneity and image noise using a 20 cm diameter water phantom. The CT value homogeneity test results for the head mode showed values ranging from -1.96 to 0.81 HU, while for the body mode, they ranged from -1.78 to 1.28 HU. Both modes were within the permissible tolerance limit of 0 ± 4 HU. Meanwhile, the image noise test results for the head mode showed values ranging from 3.49 to 3.67 HU, within the tolerance range of 2.88 to 3.90 HU, and for the body mode, they ranged from 4.98 to 5.37 HU, also within the tolerance range of 4,275.77 HU, as stipulated by Siemens Healthineers and the IAEA. This difference indicates that technical parameters, such as tube current and reconstruction kernel, affect the performance of the resulting images.

This finding underscores the importance of consistently implementing daily quality control (QC) as a preventative measure to maintain the quality of diagnostic imaging. Implementing noise and homogeneity evaluations as key indicators in daily QC can help radiologists detect potential system malfunctions early. This has a direct impact on reducing the risk of misdiagnosis and minimizing the need for repeat scans, thereby improving patient safety and the efficiency of CT scanner use in medical facilities. Overall, the QC results demonstrate that the CT scanner system performs optimally and meets applicable standards, making it suitable for diagnostic imaging services.

ACKNOWLEDGEMENTS

We would like to express our gratitude to all parties who have provided support and contributions to this research. Special appreciation goes to the Supervisor and all lecturers in the Physics Department at Matana University for their guidance and knowledge, as well as to the Hospital for providing the opportunity and facilities to conduct this research.

REFERENCES

1. Hamam, I. M. A., Utami, A. P., KM, S., Dewi, S. N., & Rad, S. T. (2021). *Teknik Pemeriksaan CT-Scan Kepala Studi Literatur Stroke Hemorrhagic*. Doctoral dissertation, Universitas 'Aisyiyah Yogyakarta.
2. IAEA. (2012). *Quality assurance programme for computed tomography: diagnostic and therapy applications*. International Atomic Energy Agency.
3. ISRRT. (2019). *Guidance Document on QA/QC inCT*. ISRRT.
4. Pertiwi, Y., Sella, V. M., & Iskandar, J. (2021). Analysis of Quality Control Computerized Tomography Scan (Ct Scan) Results in Indonesia Based on National and International Standards. *Al Insyirah International Scientific Conference on Health*, **2**, 108–116.
5. DeMaio, D. N. (2017). *Mosby's Exam Review for Computed Tomography-E-Book*. Elsevier Health Sciences.
6. Lestari, R. & Heru, N. (2022). Evaluasi Nilai Kebisingan dan Keseragaman Ctra CT Scan Sebelum dan Sesudah Kalibrasi Harian. *Jurnal Pengawasan Tenaga Nuklir*, **2**(1), 6–12.
7. Machmudah, N., Muttaqin, A., & Oktavia, A. (2025). Uji Kualitas Citra Pesawat CT-Scan Menggunakan Phantom ACR (American College of Radiology) di Instalasi Radiologi Rumah Sakit Universitas Andalas. *Jurnal Fisika Unand*, **14**(1), 45–51.
8. Almuslimiati, A., Milvita, D., & Prasetio, H. (2019). Analisis Nilai Noise dari Citra Pesawat CT-Scan pada Beberapa Rekonstruksi Kernel dengan Variasi Slice Thickness. *Jurnal Fisika Unand*, **8**(1), 57–63.
9. Kurniawan, A. N. K. N. & Soesanti, I. S. (2010). Evaluasi Nilai Noise Sebelum Dan Sesudah Kalibrasi Sebagai Salah Satu Wujud Kinerja Pesawat CT-Scan. *Forum Teknik*, **33**(3).
10. Lestari, A. A., Sutanto, H., & Arifin, Z. (2014). Analisis Noise Level Hasil Citra CT Scan Pada Tegangan Tabung 120 kV dan 135 kV Dengan Variasi Ketebalan Irisan (Slice Thickness). *Youngster Physics Journal*, **3**(3), 189–196.
11. Goldman, L. W. (2007). Principles of CT: radiation dose and image quality. *Journal of Nuclear Medicine Technology*, **35**(4), 213–225.
12. American College of Radiology (2017), *Computed Tomography: Quality Control Manual*. URL: https://www.acr.org.
13. Siemens Healthineers. (2017). *SOMATOM go.Top System Owner Manual*. Siemens Healthineers.
14. Samaliwu, E. T. (2025). Evaluasi Nilai Noise dan Homogeneity *Hasil Citra CT Scan pada Phantom Kepala setelah Kalibrasi Harian*. Program Studi Fisika Universitas Matana, Tangerang.
15. Zakirin, M., Diartama, A. A. A., Iffah, M., Mughnie, B., & Jeniyanthi, N. P. R. (2019). Uji Kesesuaian CT Number pada Pesawat CT Scan Multislice di Instalasi Radiologi RSUD Mangusada Badung. *IMEJING: Jurnal Radiografi Indonesia*, **3**(1).
16. Dewa, Y. R., Astina, K. Y., & Darmita, I. M. P. (2024). Pengujian Quality Control CT Number Air dan Evaluasi Artefak pada MSCT di Rumah Sakit Hewan Sunset Vet Kuta. *Kappa Journal*, **8**(3), 388–392.

IPC

Indonesian Physics Communication

Department of Physics, Universitas Riau, Pekanbaru, Indonesia
p-ISSN 1412-2960 | e-ISSN 2579-521X

Vol. 22 | No. 2
July 2025

Web: https://kfi.ejournal.unri.ac.id
E-mail: kfi@ejournal.unri.ac.id

A cosmological inflation model with inverse minimal and non-minimal coupling between scalar fields and curvature tensors

Getbogi Hikmawan[1,*], Freddy Permana Zen[1,2]

[1]Theoretical Physics Laboratory, Institut Teknologi Bandung, Bandung 40132, Indonesia
[2]Indonesia Center for Theoretical and Mathematical Physics, Institut Teknologi Bandung, Bandung 40132, Indonesia

*Corresponding author: getbogihikmawan@itb.ac.id

ABSTRACT

This work reviews the cosmological inflation model involving inverted minimal and non-minimal interactions between the scalar field ϕ and its derivatives with the space curvature tensor. The de Sitter exponential expansion and the decaying scalar field conditions are also reviewed to move the model towards the inflationary condition, where as a generator of inflation, the scalar field must decay at the end of time. The scalar and tensor perturbation equations, their respective spectral indices, and the tensor-to-scalar ratio have been calculated to study the nonlinearity of the reviewed model. It is shown that the spectral indices and tensor-to-scalar ratio of the model are in good agreement with the observational data.

Keywords: Cosmological perturbations; inflation; scalar field

Received 27-06-2025 | Revised 18-07-2025 | Accepted 21-07-2025 | Published 31-07-2025

INTRODUCTION

As a theory offering solutions to classical cosmological problems, inflation theory [1, 2] still leaves several issues related to its characteristics. Several studies involving measurements of the Cosmic Microwave Background (CMB), such as those conducted by COBE [3], the WMAP Collaboration [4], and the PLANCK Collaboration [5], provide support for an inflation theory in which the power spectrum of metric perturbations is comparable to CMB temperature fluctuations. The simplest inflation scenario is that a scalar field, called an inflaton, generates inflation when it is slow-rolled in an inflationary potential function $V(\phi)$. This scenario is called slow-roll inflation. However, the source of this inflation remains unknown.

Therefore, it is always possible to review cosmological inflation models involving scalar fields and their interactions with the curvature tensor. These range from modifications of the standard Theory of Relativity (TRU) to models with additional terms. One interesting model is the ADM formalism [6], which considers perturbation modes up to the second order via ADM variables. Furthermore, by selecting a gauge, the field perturbation can be substituted into a metric perturbation, so that the model can be analyzed solely as the evolution of the metric perturbation, and the results can then be compared with observational data.

Horndeski theory [7], one of several cosmological models involving scalar fields (often referred to as scalar-tensor theory), is the most feasible theory because its second-order field perturbation equations have solutions and do not contain the Ostrogradsky Ghost [8]. By choosing an arbitrary coefficient function, several well-known cosmological models such as minimal scalar field coupling [9], Brans-Dicke theory [10], Dilaton gravity [11], f(R) gravity [12], derivative coupling [13, 14], Gauss-Bonnet coupling [15, 16], and others can be derived. In this study, we explore the choice of coefficient functions in Horndeski theory to obtain a new inflationary model.

This paper is structured as follows: section 2 discusses the setup of the Horndeski Lagrangian model, incorporating the selected coefficient functions, and continues with an analysis of the non-perturbative background and its inflation solution. Section 3 calculates

the spectral indices for scalar and tensor perturbations, along with the tensor-to-scalar ratio. Section 4 (final) provides conclusions and a discussion for further research.

SETUP MODEL

Horndeski's Lagrangian theory has the following form:

$$L = \sum_{i=2}^{5} L_i \tag{1}$$

with,

$$L_1 = \mathrm{K}(\phi, X) \tag{2}$$

$$L_2 = -G_3(\phi, X)\Box\phi \tag{3}$$

$$L_4 = G_4(\phi, X)R - 2G_{4X}(\phi, X)(\Box\phi)^2 + 2G_{4X}(\phi, X)\left[\phi^{;\mu\nu}\phi_{;\mu\nu}\right] \tag{4}$$

$$L_5 = G_5(\phi, X)G_{\mu\nu}\phi^{;\mu\nu} + \frac{1}{3}G_{5X}(\phi, X)\left[(\Box\phi)^3 - 3(\Box\phi)\left(\phi_{;\mu\nu}\phi^{;\mu\nu}\right) + 2\left(\phi_{;\mu\nu}\phi^{;\mu\sigma}\phi^{;\nu}_{;\sigma}\right)\right] \tag{5}$$

In this Lagrangian, the coefficient function (K, G_3, G_4, G_5) is a function of the scalar field ϕ and $X \equiv -\phi_{;\mu}\phi^{;\mu}/2$, the kinetic energy of the scalar field. The indexes in the coefficient functions indicate partial derivatives, $G_{Ix} \equiv \partial G_i/\partial X$ and $G_{i\phi} \equiv \partial G_i/\partial\phi$, where $\Box \equiv \partial^\mu \partial_\mu = \partial^2/\partial t^2 - \nabla^2$ is the d'Alembert operator, R is the Ricci scalar, and $G_{\mu\nu}$ is the Einstein tensor.

In this study, the coefficient functions are considered as follows:

$$\begin{aligned} \mathrm{K} &= X \\ G_3 &= 0 \\ G_4 &= \frac{M_{pl}^2}{2} - \frac{1}{2}\zeta\phi^2 \\ G_5 &= \xi\phi \end{aligned} \tag{6}$$

where $M_{pl}^2 = 1/8\pi G \approx 1$. If we substitute the coefficient function (6) into the Lagrangian in Equation (2) to (5),

$$L = X + \left(\frac{1}{2} - \frac{1}{2}\zeta\phi^2\right)R + \xi\phi G_{\mu\nu}\phi^{;\mu\nu} \tag{7}$$

The Lagrangian above provides a cosmological model with minimal and non-minimal coupling between the curvature tensor and the scalar field and its derivatives, where ζ and ξ are the coupling constants for the scalar field and its derivatives, respectively.

The space-time metric of the universe with cosmological perturbations can be written in the form,

$$ds^2 = -dt^2 + h_{ij}dx^i dx^j \tag{8}$$

Considering the Maldacena gauge to improve the time and spatial reparameterization [19],

$$h_{ij} = a(t)^2 e^{2\Theta}\left(\delta_{ij} + \gamma_{ij} + \frac{1}{2}\gamma_{il}\gamma_{lj}\right) \tag{9}$$

where, a(t) is the scale factor, Θ is the scalar perturbation, and γ is the tensor perturbation. The tensor perturbation is traceless ($\gamma_{ii} = 0$) and divergence-free ($\partial_i\gamma_{ij} = 0$), and is defined only up to the second order, since higher-order terms do not contribute to the action function. If we consider the decomposition theorem [18] for cosmological perturbations, each perturbation mode evolves separately, so each perturbation mode can be analyzed independently of each other.

The tensor perturbation γ_{ij} can be expressed in terms of two polarization modes,

$$\gamma_{ij} = h_+\widehat{\gamma_{ij}}^{+} + h_\times\widehat{\gamma_{ij}}^{\times} \tag{10}$$

Considered in the Fourier space, $\widehat{\gamma_{ij}}^{+}$ and $\widehat{\gamma_{ij}}^{\times}$ satisfy the normalization conditions $\widehat{\gamma_{ij}}(\boldsymbol{k})\widehat{\gamma_{ij}}(-\boldsymbol{k})^* = 2$ and $\widehat{\gamma_{ij}}^{+}(\boldsymbol{k})\widehat{\gamma_{ij}}^{+}(-\boldsymbol{k})^* = 0$ [20].

Scalar Perturbation

The dynamic equation for each pertubation mode is obtained from the second order Lagrangian equation,

$$\mathcal{L}_2^{(s)} = a^3 Q_s \left[\dot{\Theta}^2 - \frac{c_s^2}{a^2}(\partial\Theta)^2\right] \quad (11)$$

$$Q_s \equiv \frac{2L_S(9\mathcal{W}^2 + 8L_S w)}{\mathcal{W}^2} \quad (12)$$

$$c_s^2 \equiv \frac{2}{Q_s}\left(\dot{\mathcal{M}} + H\mathcal{M} - \mathcal{E}\right) \quad (13)$$

with,

$$L_S = \frac{1}{2}\left(1 - \zeta\phi^2 - \xi\frac{\dot{\phi}^2}{2}\right) \quad (14)$$

$$\mathcal{W} = 2\left[H - \zeta\left(H\phi^2 + \phi\dot{\phi}\right) - \frac{3\xi H\dot{\phi}^2}{2}\right] \quad (15)$$

$$\begin{aligned} w = 3\big[&-9H^2 + 9\zeta\left(H^2\phi^2 + 2H\phi\dot{\phi}\right) \\ &+27\xi H^2\dot{\phi}^2\big] \end{aligned} \quad (16)$$

$$\mathcal{M} = \frac{4\zeta^2\phi^4 + 4\zeta\xi\phi^2\dot{\phi}^2 + \xi^2\dot{\phi}^4 + 16L_S - 4}{8\left[H\left(2L_S - \xi\dot{\phi}^2\right) - \xi\phi\dot{\phi}\right]} \quad (17)$$

$$\mathcal{E} = \frac{1}{2}\left[1 - \zeta\phi^2 + \frac{\xi\dot{\phi}^2}{2}\right] \quad (18)$$

In Fourier space, the equation of motion for a scalar perturbation (Θ) can be written in the form,

$$\ddot{\Theta} + \left(3H + \frac{\dot{Q}_s}{Q_s}\right)\dot{\Theta} + c_s^2\frac{k^2}{a^2}\Theta = 0 \quad (19)$$

To obtain the solution to equation (19), we consider the Bunch-Davies vacuum function,

$$\Theta(\tau,k) = \frac{iHe^{ic_s k\tau}}{2(2c_s k)^{3/2}\sqrt{Q_s}}(1 + ic_s k\tau) \quad (20)$$

On the superhorizon scale, $c_s k \ll aH$, the power spectrum is defined at $\tau \approx 0$ by,

$$\begin{aligned} \langle\Theta(0,\boldsymbol{k_1})\Theta(0,\boldsymbol{k_2})\rangle = &\frac{2\pi^2}{k_1^3}P_\Theta(k_1)(2\pi)^3 \\ &\delta^{(3)}(\boldsymbol{k_1} + \boldsymbol{k_2}) \end{aligned} \quad (21)$$

So if we consider the solution of Equation (20),

$$\Theta(0,k) = \frac{iH}{2(c_s k)^{3/2}\sqrt{Q_s}} \quad (22)$$

the power spectrum can be obtained,

$$P_\Theta = \frac{H^2}{8\pi^2 c_s^3 Q_s} \quad (23)$$

Furthermore, to characterize the fluctuations in the scalar perturbation power spectrum, the spectral index n_s is defined,

$$\begin{aligned} n_s - 1 \equiv &\frac{d\ln P_\Theta}{d\ln k}\Big|_{c_s k = aH} \\ &= 2\frac{\dot{H}}{H} - \frac{\dot{Q}_s}{HQ_s} - 3\frac{\dot{c}_s}{Hc_s} \end{aligned} \quad (24)$$

Since the perturbation evolves towards a constant on this scale, we will review the estimate of $c_s k = aH$ to evaluate the spectral index at inflation. The PLANCK collaboration data suggest that the scalar spectral index is limited to $n_s = 0.9665 \pm 0.0038$ at the 68% confidence level [5].

Tensor Perturbation

For tensor perturbation, the second-order Lagrangian equation has the form,

$$\mathcal{L}_2^{(t)} = \frac{a^3}{4}Q_t\left[\dot{\gamma}_{ij}^2 - \frac{c_t^2}{a^2}\left(\partial_k\gamma_{ij}\right)^2\right] \quad (25)$$

$$Q_t = \frac{1}{2}\left(1 - \zeta\phi^2 - \xi\frac{\dot{\phi}^2}{2}\right) \quad (26)$$

$$c_t^2 = \frac{1 - \zeta\phi^2 + \xi\frac{\dot{\phi}^2}{2}}{1 - \zeta\phi^2 - \xi\frac{\dot{\phi}^2}{2}} \quad (27)$$

Analogous to scalar perturbations, each polarization in the tensor perturbation $h_\lambda(\lambda = +,\times)$ satisfies the equation of motion,

$$\ddot{h_\lambda} + \left(3H + \frac{\dot{Q}_t}{Q_t}\right)\dot{h_\lambda} + c_t^2\frac{k^2}{a^2}h_\lambda = 0 \quad (28)$$

Therefore, the solution for each polarization,

$$h_\lambda(\tau,k) = \frac{iHe^{-ic_tk\tau}}{2(2c_tk)^{\frac{3}{2}}\sqrt{Q_t}}(1+ic_tk\tau) \quad (29)$$

so that the power spectrum for the tensor perturbation can be obtained,

$$P_h = \frac{H^2}{2\pi^2 Q_t c_t^3} \quad (30)$$

The factor of two arises because there are two polarizations of the tensor perturbation. The spectral index on $c_tk = aH$ is defined,

$$n_t \equiv \frac{d\ln P_\Theta}{d\ln k}|_{c_tk=aH} = 2\frac{\dot{H}}{H} - \frac{\dot{Q}_t}{HQ_t} - 3\frac{\dot{c}_t}{Hc_t} \quad (31)$$

Tensor-to-Scalar Ratio

The tensor-to-scalar ratio can be approximated via,

$$r \equiv \frac{P_h}{P_\Theta} = 4\frac{Q_s c_s^3}{Q_t c_t^3} \quad (32)$$

The PLANCK collaboration gave a value of $r < 0.10$ at the 95% confidence level.

COSMOLOGICAL PERTURBATION ANALYSIS

This study examines the de Sitter expansion, which causes the Hubble parameter to be constant,

$$a(t) \sim \exp(H_0t) \rightarrow H(t) = \frac{\dot{a}}{a} = H_0 \quad (33)$$

The situation when the scalar field decays at large t is examined:

$$\phi \sim \exp(\phi_0 t) \quad (34)$$

$$\dot{\phi} \sim \phi_0\exp(\phi_0 t) \quad (35)$$

$$\ddot{\phi} \sim \phi_0^2\exp(\phi_0 t) \quad (36)$$

where, ϕ_0 must be negative to ensure scalar field decay. In this study, we will consider the special case where the minimal and non-minimal couplings are inversely related,

$$\zeta = \frac{1}{\xi} \quad (37)$$

After substituting the above conditions into the spectral index equation, we will plot the graphs for various values of ϕ_0. Furthermore, since it has been shown that inflation occurs when the universe undergoes exponential expansion beyond 60 e-folds [18], we consider $H_0 = 60$ and, based on background calculations [21], we consider the values $\zeta = 10^{-2}$, 10^{-3}, 10^{-4}, and 10^{-5}.

Scalar Perturbation

The spectral index of the scalar perturbation for the case plotted as a contour map as a function of time can be seen in Figure 1. As explained in the previous section, ϕ_0 must be negative and $H_0 > 60$ to ensure that the scalar field decays and inflation occurs. As seen in Figure 1, changes in the zeta value cause the curve to shift slightly toward higher times, indicating that the dynamics begin at different times. However, for each ζ, there is a value of ϕ_0 that can produce spectral index values close to scale invariance ($n_s \cong 1$), with slight differences.

Tensor Perturbation

Similar to the scalar perturbation, the spectral index of the scalar perturbation for the case plotted as a contour map as a function of time can be seen in Figure 2. As seen in Figure 2, changes in the zeta value do not significantly affect the spectral index values. However, for each ζ, there is a value of ϕ_0 that can provide spectral index values close to scale invariance ($n_t \cong 0$), with slight differences.

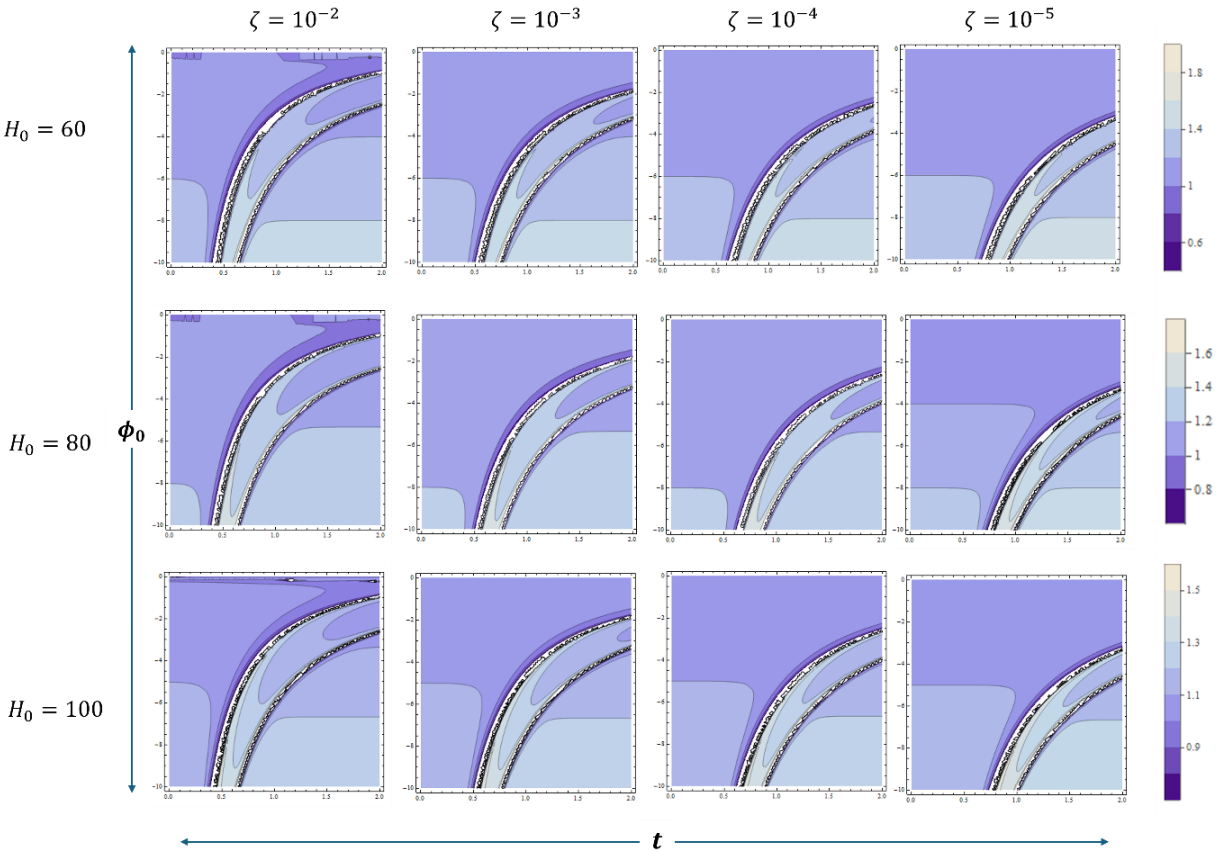

Figure 1. Contour plot of the scalar perturbation spectral index as a function of time and ϕ_0 for the cases H_0 = 60, 80 and 100 as well as $\zeta = 10^{-2}$, 10^{-3}, 10^{-4} and 10^{-5}.

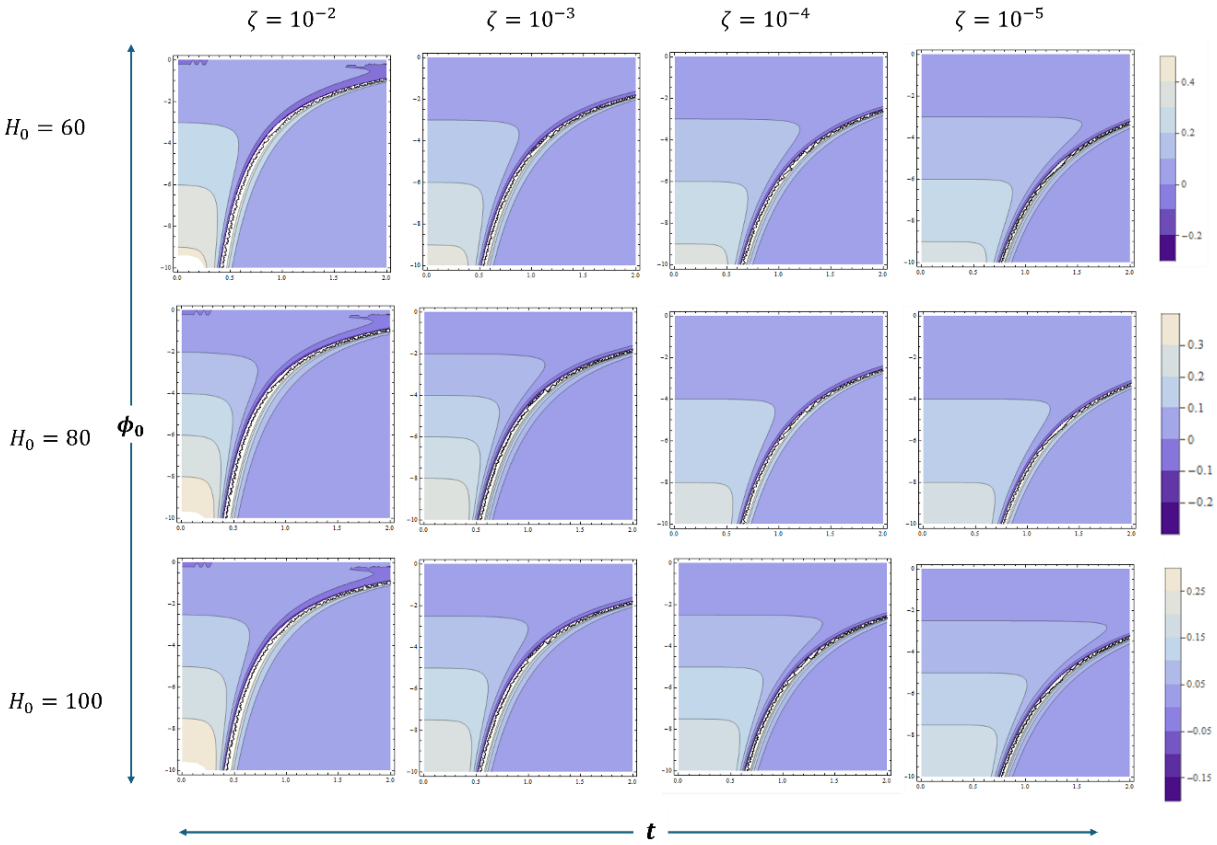

Figure 2. Contour plots of the spectral index perturbation tensor as a function of time and ϕ_0 for the cases H_0 = 60, 80 and 100 as well as $\zeta = 10^{-2}$, 10^{-3}, 10^{-4} and 10^{-5}.

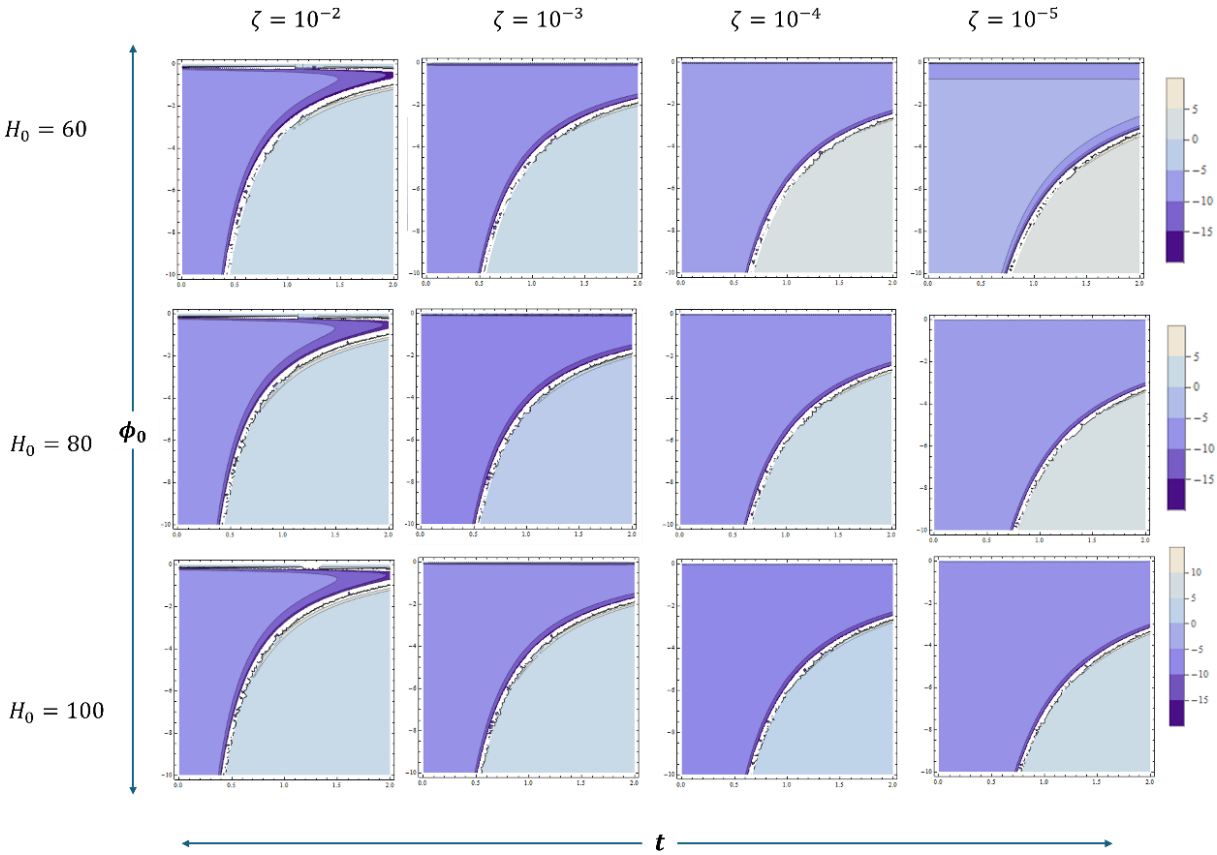

Figure 3. Contour plots of the tensor-to-scalar ratio as a function of time and ϕ_0 for the cases H_0 = 60, 80 and 100 as well as $\zeta = 10^{-2}$, 10^{-3}, 10^{-4} and 10^{-5}.

Tensor-to-Scalar Ratio

A plot of the tensor-to-scalar ratio as a function of time can be seen in Figure 3. The different ζ values exhibit similar behavior as for scalar and tensor perturbations. However, they still align with the observed data, with r < 0.10.

CONCLUSION

This study examines Horndeski's theory to construct a new cosmological inflationary model by selecting coefficient functions in the Horndeski Lagrangian that are free from the Ostrogradsky ghost. It also examines the Hubble parameter, which remains constant during inflation, and the scalar field decays as the inflationary period ends. Furthermore, the inverse relationship between the couplings, ζ=1/ξ, is examined. By examining these approximations, spectral indices for scalar and tensor perturbations, as well as their tensor-to-scalar ratios, are derived and mapped for several values of the Hubble parameter (H_0) and the power of the scalar field (ϕ_0). As can be seen in Figures 1 and 2, the spectral indices are close to scale invariant and match the observational data. The same is true for the tensor-to-scalar ratio.

In this study, the system is "forced" to undergo inflation, considering the constant value of the Hubble parameter due to the complexity and nonlinear nature of the model under consideration. In future work, a more comprehensive analysis can be reviewed because it has the potential to provide good insights into cosmological inflation.

ACKNOWLEDGEMENTS

GH and FZ would like to thank the PPMI KK ITB 2025 Program for financial support during the conduct of this research.

REFERENCES

1. Guth, A. H. (1981). Inflationary universe: A possible solution to the horizon and flatness problems. *Physical Review D*, **23**(2), 347.
2. Starobinsky, A. A. (1980). A new type of isotropic cosmological models without singularity. *Physics Letters B*, **91**(1), 99–102.
3. Smoot, G. F., Bennett, C. L., Kogut, A., Wright, E. L., Aymon, J., Boggess, N. W., Cheng, E. S., De Amici, G., Gulkis, S., Hauser, M. G., Hinshaw, G., Jackson, P. D., Janssen, M., Kaita, E., Kelsall, T., Keegstra, P., Lineweaver, C., Loewenstein, K., Lubin, P., Mather, J., Meyer, S. S., Moseley, S. H., Murdock, T., Rokke, L., Silverberg, R. F., Tenorio, L., Weiss, R., & Wilkinson, D. T. (1992). Structure in the COBE differential microwave radiometer first-year maps. *Astrophysical Journal*, **396**(1), L1–L5.
4. Hinshaw, G., Larson, D., Komatsu, E., Spergel, D. N., Bennett, C., Dunkley, J., Nolta, M. R., Halpern, M., Hill, R. S., Odegard, N., Page, L., Smith, K. M., Weiland, J. L., Gold, B., Jarosik, N., Kogut, A., Limon, M., Meyer, S. S., Tucker, G. S., Wollack, E., & Wright, E. L. (2013). Nine-year Wilkinson Microwave Anisotropy Probe (WMAP) observations: cosmological parameter results. *The Astrophysical Journal Supplement Series*, **208**(2), 19.
5. Akrami, Y., Arroja, F., Ashdown, M., Aumont, J., Baccigalupi, C., Ballardini, M., Banday, A. J., Barreiro, R. B., Bartolo, N., Basak, S., Benabed, K., & Savelainen, M. (2020). Planck 2018 results-X. Constraints on inflation. *Astronomy & Astrophysics*, **641**, A10.
6. Gleyzes, J., Langlois, D., Piazza, F., & Vernizzi, F. (2013). Essential building blocks of dark energy. *Journal of Cosmology and Astroparticle Physics*, **2013**(08), 025.
7. Horndeski, G. W. (1974). Second-order scalar-tensor field equations in a four-dimensional space. *International Journal of Theoretical Physics*, **10**(6), 363–384.
8. Ostrogradsky, M. (1850). Memoires sur les equations differentielles, relatives au probleme des isoperimetres. *Mem. Acad. St. Petersbourg* **6**(4), 385–517.
9. Armendariz-Picon, C., Damour, T., & Mukhanov, V. (1999). k-Inflation. *Physics Letters B*, **458**(2-3), 209–218.
10. Brans, C. & Dicke, R. H. (1961). Mach's Principle and a Relativistic Theory of Gravitation. *Physical Review*, **124**, 124.
11. Gasperini, M. & Veneziano, G. (2003). The pre-big bang scenario in string cosmology. *Physics Reports*, **373**(1-2), 1–212.
12. Sotiriou, T. P. & Faraoni, V. (2010). f (R) theories of gravity. *Reviews of Modern Physics*, **82**(1), 451–497.
13. Amendola, L. (1993). Cosmology with nonminimal derivative couplings. *Physics Letters B*, **301**(2-3), 175–182.
14. Suroso, A. & Zen, F. P. (2013). Cosmological model with nonminimal derivative coupling of scalar fields in five dimensions. *General Relativity and Gravitation*, **45**(4), 799–809.
15. Kanti, P., Gannouji, R., & Dadhich, N. (2015). Gauss-bonnet inflation. *Physical Review D*, **92**(4), 041302.
16. Hikmawan, G., Soda, J., Suroso, A., & Zen, F. P. (2016). Comment on "Gauss-Bonnet inflation". *Physical Review D*, **93**(6), 068301.
17. Arnowitt, R., Deser, S., & Misner, C. W. (1960). Canonical variables for general relativity. *Physical Review*, **117**(6), 1595.
18. Dodelson, S. (2003). *Modern Cosmology*. Oxford: Elsevier, 147.
19. Maldacena, J. (2003). Non-Gaussian features of primordial fluctuations in single field inflationary models. *Journal of High Energy Physics*, **2003**(05), 013.
20. Tsujikawa, S. (2015). The effective field theory of inflation/dark energy and the

Horndeski theory. *Lect. Notes Phys.*, **892**, 97–136.
21. Hikmawan, G., Suroso, A., & Zen, F. P. (2019). Cosmological inflation with minimal and non-minimal coupling of scalar field from Horndeski theory. *Journal of Physics: Conference Series*, **1204**(1), 012007.

IPC

Indonesian Physics Communication

Department of Physics, Universitas Riau, Pekanbaru, Indonesia
p-ISSN 1412-2960 | e-ISSN 2579-521X

Vol. 22 | No. 2
July 2025

Web: https://kfi.ejournal.unri.ac.id
E-mail: kfi@ejournal.unri.ac.id

Preparation of activated carbon electrodes from orange peel biomass with various separator materials for supercapacitor applications

Rahmatan Lil Alamin, Awitdrus*
Department of Physics, Universitas Riau, Pekanbaru 28293, Indonesia

*Corresponding author: awitdrus@lecturer.unri.ac.id

ABSTRACT

Activated carbon electrodes from orange peel biomass materials for supercapacitor applications with variety of type separator have been prepared. Activated carbon was prepared by pyrolysis process at 800° under N2 gas envinroment. Electrochemical characterization was tested on avariety of separators, i.e, JR-800-W (using Whatman paper number 40), JR-800-E (using eggshell membrane, and JR-800-O (using orange fruit membrane). The results of chemical measurement for the cyclic voltammetry method on the three samples are capacitance values of 191.82 F/g on JR-800-W, 115.08 F/g on JR-800-E, and 94.17 F/g on JR-800-O. The capacitance value in the galvanostatic charge-discharge method are 174.24 F/g with IR drop of 0.067 for sample JR-800-W, 133.22 F/g with IR drop of 0.14 for sample JR-800-E, and 116.8 F/g with IR drop of 0.36 for sample JR-800-O. Whatman paper separators produce good electrochemical properties, indicating the use of separators can affect the performance of activated carbon electrodes for supercapacitor applications.

Keywords: Activated carbon electrode; orange peel; separator; supercapacitor

Received 28-05-2025 | Revised 12-06-2025 | Accepted 19-06-2025 | Published 31-07-2025

INTRODUCTION

According to the International Energy Agency (IEA), worldwide electrical energy consumption has increased significantly in the past five years. Global electrical energy consumption reached 22,000 TWh in 2019, and will increase to 28,000 TWh in 2023. They predict that the world's Electricity consumption will grow 3.4% through 2026. Almost all electrical energy comes from fossil fuels [1].

The topic of energy storage technology is increasingly becoming a concern discussed by various groups. Energy storage media such as batteries and capacitors are considered effective as low-voltage storage solutions. However, batteries and capacitors are not yet the best solution for maximum energy storage. The power density is not too high and the charging time is relatively long which is a shortcoming of the battery, so it is necessary to innovate to create other alternative energy storage in large quantities and can be used for a long time. Supercapacitors offer significant advantages and have been widely applied in modern society, especially in managing renewable energy sources. One of the promising applications is wearable devices, electric vehicles, and stationary energy storage systems. Supercapacitors are becoming significant energy conversion devices due to their extremely fast charge/discharge rate, environmentally friendly, durable, independent of time and weather conditions, and high specific power exceeding batteries [2]. One aspect that affects the effectiveness of supercapacitors is the use of electrode materials. Carbon is one type of material used for making electrodes because of its high specific surface area. Various types of carbon are used in making electrodes, one of which is activated carbon. Activated carbon also known as activated charcoal is a type of graphite that is rough and not perfectly structured. Activated carbon is characterized by a wide spectrum of pores of various sizes [3].

Conventional separator materials used in supercapacitors such as rubber, plastic films, aquagels, resorcinol formaldehyde polymers,

and polyolefins have been employed primarily to prevent electronic conduction between the electrodes. However, these materials often suffer from long-term issues such as drying, structural collapse, or low ionic conductivity. Therefore, there remains a critical need for separator materials that are highly porous to facilitate efficient ionic transport while simultaneously acting as effective electronic insulators between opposing electrodes The type of separator material that is widely used at present is the nafiion membrane which, although efficient for the role of supercapacitor separator, is very expensive and has limited availability [4].

Orange peel waste is one of the most common wastes found in the environment. Mueller (2017) [5] reported that in 2014 citrus production worldwide reached 68 million tons, most of which was used for the juice industry which produced 3.8 million tons of orange peel waste per year. Sweet orange peel contains 6%-19.801% lignin, 46-69% cellulose, and 6% hemicellulose [6]. Sweet orange peel has abundant cellulose compared to rice merang 33%-43% [7], pine seeds 44% [8], coconut fiber 43,44% [9] which indicates an abundant carbon source so that it has the potential to be used in making activated carbon if given the right treatment.

The main objective of this work was to analyze the effect of different type of separator materials on the performance of supercapacitor activated carbon electrodes using Whatman paper, eggshell membrane, and orange fruit membrane.

MATERIALS AND METHOD

Activated Carbon Preparation

Orange peel waste was obtained and collected from Pekanbaru City, Riau province. The processing of orange peel waste includes drying under sunlight and using an electric oven at 110℃ for 2 hours, pre-carbonization at 200℃ for 2 hours. Sample was activated using ZnCl2 0.5 M. The pyrolysis process was carried out under N_2 gas pressure at temperatures of 800℃.

Preparation of Separator

The separator materials selected were Whatman paper grade 40, eggshell membrane, and orange fruit membrane. The three separator materials were soaked using sulfuric acid (H_2SO_4) with a concentration of 1 M. Samples are coded JR-800-W for whatman paper separator, code JR-800-E for eggshell membrane separator, and code JR-800-O for orange fruit membrane separator.

Physical - Electrochemical Characterization

Physical characterization was performed by measuring electrode density by measuring mass and volume, while electrochemical performance was evaluated using cyclic voltammetry (CV) at scan rates of 1, 2, 5 mV/s. Galvanostatic charge-discharge (GCD) to determine specific capacitance at a current density of 1 2, 5 A/g with a maximum potential of 1 V, and internal resistance.

RESULTS AND DISCUSSION

Physical Property Analysis

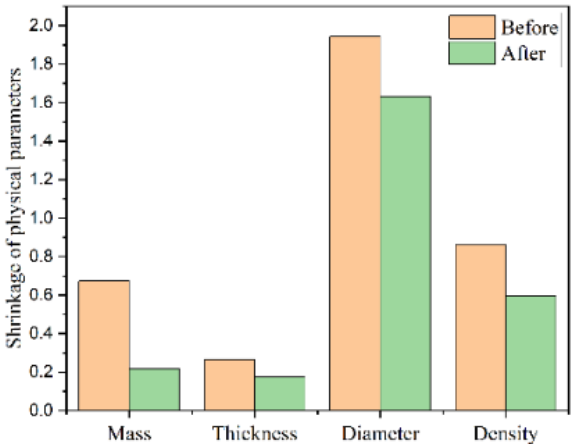

Figure 1. Electrode density before and after pirolysis process.

Figure 1 shows the electrode density before and after the pyrolysis process. The average density is calculated using the Equation (1):

$$p = \frac{m}{v} \quad (1)$$

where, m is the average mass, and v is the average volume of the electrode. The resulting decrease in electrode density is 0.268388 g/cm^2 with a percentage of 31.125%, causing more volatile compounds to be lost, thus reducing the density of the sample. The decrease in density causes the carbon pore walls to collapse, resulting in high porosity. Pyrolysis process depends on temperature, pressure, and the composition contained in the biomass to produce an increase in the number of pores contained. Composition occurs at different temperature levels. Cellulose, hemicellulose compounds are decomposed at 200℃ – 350℃ which evaporates volatile compounds,and lignin can be decomposed at temperatures above 500℃ which produces products such as tar and activated charcoal [10].

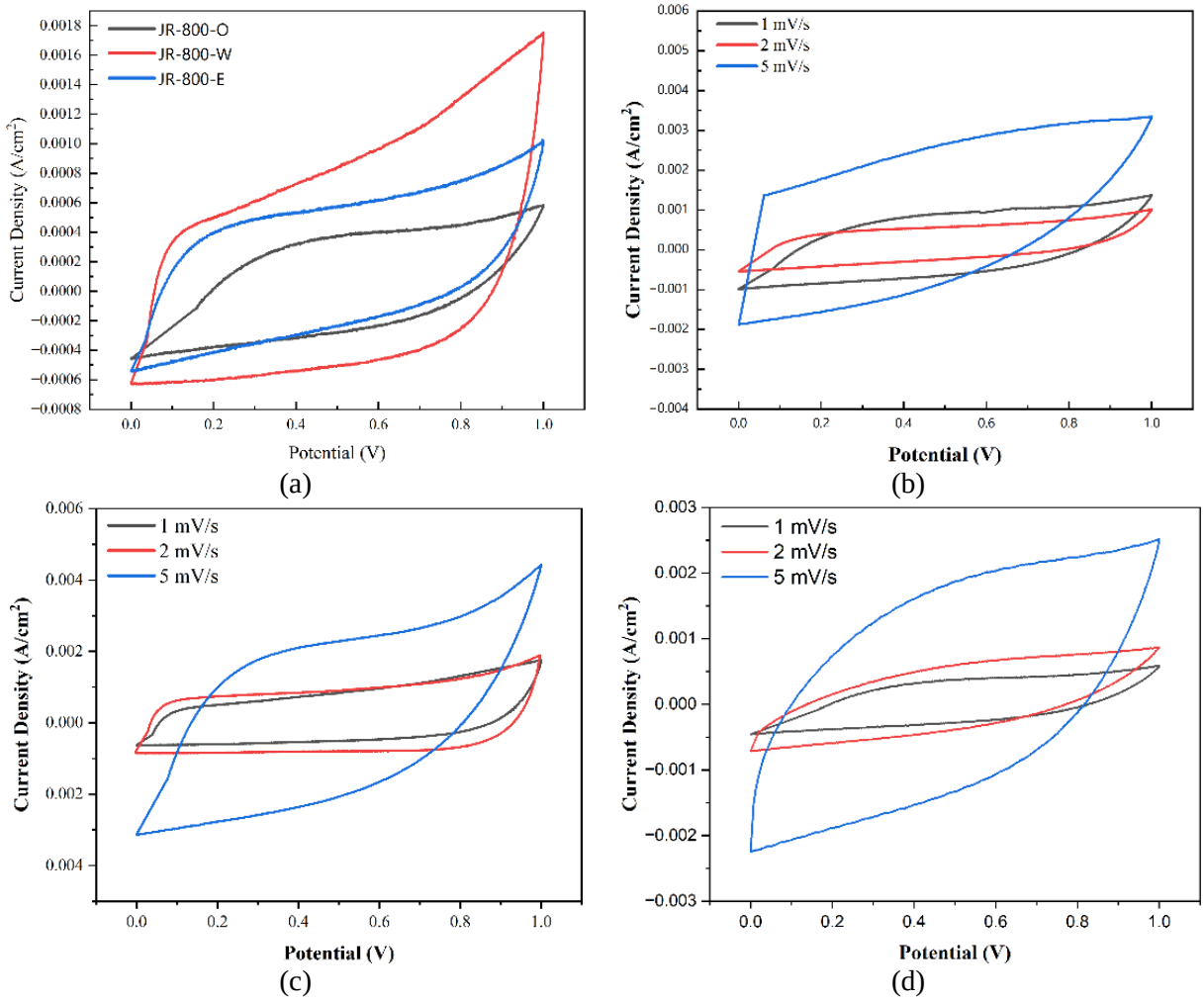

Figure 2. CV curve of (a), various separator, (b), JR-800-O (c), JR-800-W (d), JR-800-E at various scan rate.

Electrochemical Properties

CV (Cyclic Voltammetry) measurement results from orange peel carbon electrodes on variations of JR-800-O, JR-800-W, and JR-800-E separator materials. The specific capacitance results of the three variations are highest in JR-800-W at 191.82 F/g, followed by JR-800-E at 115.08 F/g, and JR-800-O at 94.17 F/g. This is reinforced by Figure 2 (a) which shows that the JR-800-W curve area is larger, indicating that more ions participate in the formation of the electric double layer [11]. Whatman paper separators have a uniform microporous

structure and excellent electrolyte absorption, which allows ions in the electrolyte to diffuse quickly and efficiently towards the electrode surface. This structure supports optimal formation of an electrical double layer, resulting in high capacitance [6]. The eggshell membrane is composed of interwoven fibrous protein layers (primarily collagen and keratin), which exhibit limited ionic conductivity and uneven surface morphology. These factors hinder full electrolyte infiltration and create tortuous ion pathways, thereby reducing effective ion transport and charge storage capability. Nevertheless, its partial permeability allows better performance than dense plant-based membranes, supporting its viability as a low-cost bioseparator [4]. The inferior performance of this separator is attributed to its dense and heterogeneous structure, characterized by compact cellulose-lignin cell wall layers with low porosity and poor electrolyte affinity. These features impede electrolyte absorption and slow down ion migration, which not only limits the active surface area for electric double layer formation but also introduces significant internal resistance. Moreover, the non-uniform swelling behavior upon contact with electrolyte contributes to mechanical instability and inconsistent ionic pathways across the electrode–separator interface [6]. The JR-800-W remains the best performer showing good electrochemical, stability and performance at various scan rates [12].

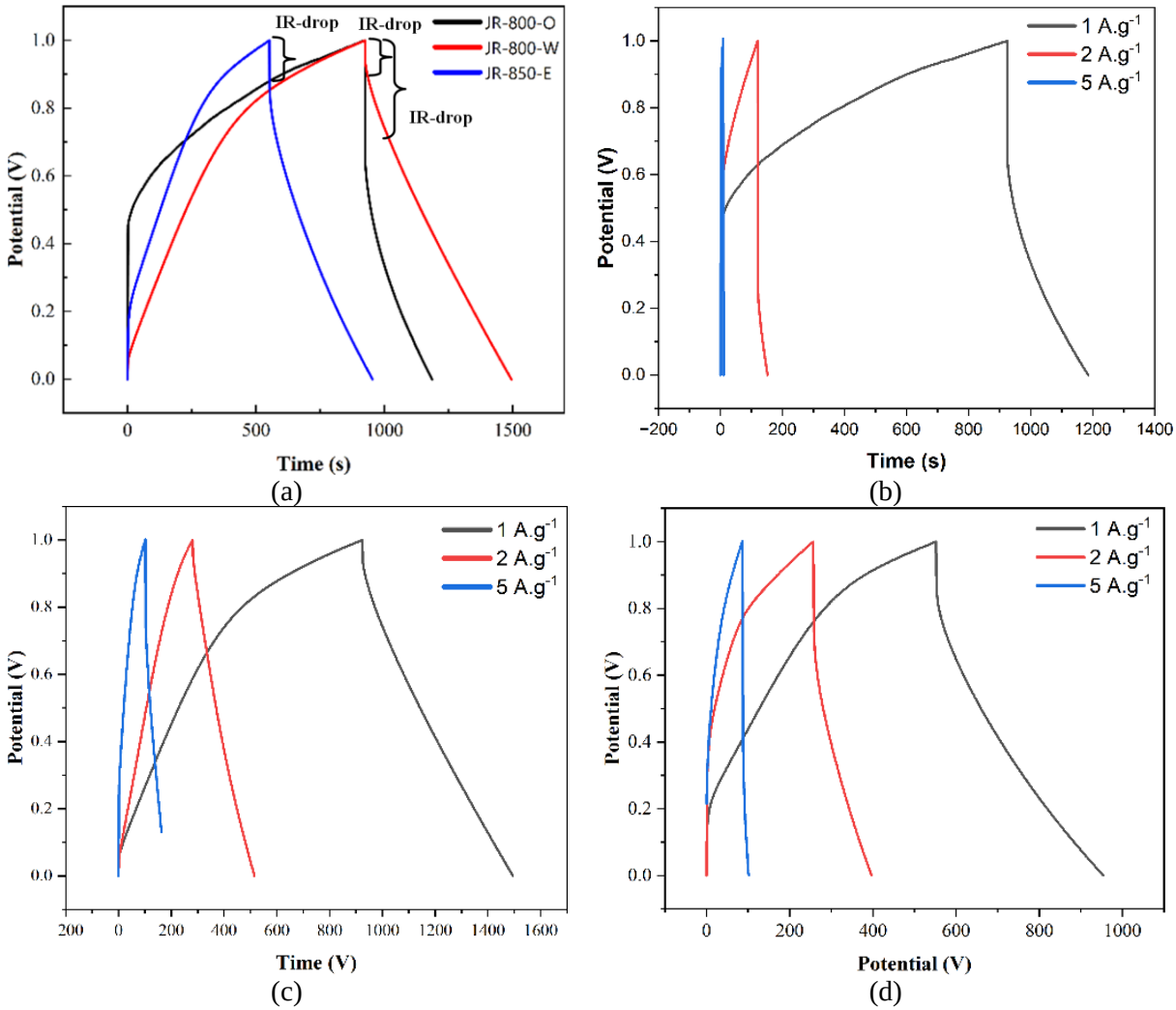

Figure 3. GCD curve of (a), various separator, (b), JR-800-O (c), JR-800-W (d), JR-800-E at various current densities.

The GCD curve Figure 3 (a) shows a symmetrical triangular shape indicating high reversibility of the carbon electrode as an EDLC. As a result, JR-800-W again showed the highest value. IR drop is seen to be the smallest in JR-800-W at 0.067 Ω with a specific capacitance value of 174.24 F/g followed by JR-800-E at 0.14 Ω with a specific capacitance value of 133.22 F/g, and JR-800-O at 0.36 Ω with a specific capacitance value of 116.8 F/g, indicating lower internal resistance in JR-800-W and better energy efficiency. The low IR drop in the Whatman separator is due to the uniform microstructure, making the diffusion of electrolyte ions easier and more efficient. Eggshell membranes have an inhomogeneous structure due to the uneven structure of the collagen layer inhibiting ion diffusion between surfaces resulting in higher internal resistance than whatman separators. Low porosity is possessed by the orange membrane separator, resulting in the highest internal resistance. This is in line with previous findings. Figure 3 (b), (c), (d) shows that an increase in current density leads to a decrease in specific capacitance values for all samples. This is because at high current densities, electrolyte ions have less time to diffuse into the electrode pores [13], however, JR-800-W retains relatively high values, supporting previous findings.

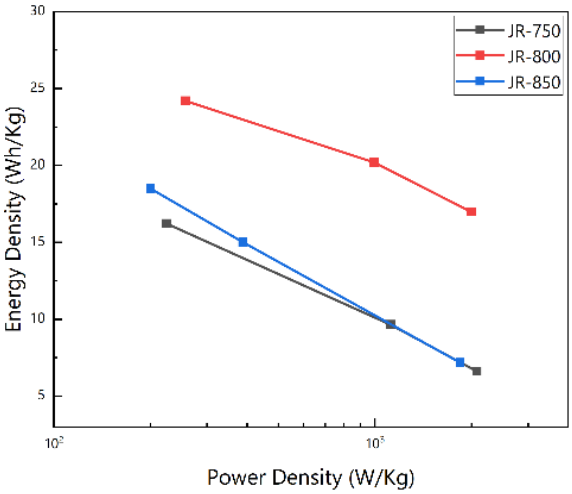

Figure 4. Ragone plot.

Figure 4 show the Ragone plot of three separator variations. This reflect the optimal ion accessibility and minimal internal resistance offered by the uniform microstructure and excellent wettability of the Whatman paper separator variations. This reflect the optimal ion This finding aligns with previous reports that emphasize the role of high-porosity, thin separators in improving ion transport kinetics and minimizing IR drop, thus enhancing both energy and power output simultaneously [11, 4].

In contrast, the JR-800-E and JR-800-O samples exhibited a significant trade-off between energy and power densities. The eggshell membrane (JR-800-E), while biologically derived and cost-effective, exhibited a moderately lower E_{sp} and P_{sp}. This reduction is attributed to the membrane's irregular fibrous morphology and semi-permeable protein layers that introduce tortuosity in ion pathways and increase ionic resistance [4]. Similarly, the JR-800-O separator produced the lowest performance, with an estimated likely due to its dense cellulose-lignin structure, poor electrolyte uptake, and limited ionic mobility.

CONCLUSION

This study demonstrated that the type of separator material significantly influences the electrochemical performance of activated carbon electrodes derived from orange peel biomass for supercapacitor applications. Among the three separators tested Whatman filter paper no. 40 (JR-800-W), eggshell membrane (JR-800-E), and orange fruit membrane (JR-800-O) the JR-800-W sample consistently exhibited the highest specific capacitance in both CV (191.82 F/g) and GCD (174.24 F/g) analyses. This superior performance is attributed to the uniform microporous structure and excellent electrolyte absorption of Whatman paper, which promotes faster ion diffusion and more efficient electric double-layer formation. The eggshell membrane separator (JR-800-E) showed moderate performance, with sufficient ionic mobility but slightly higher internal resistance.

Meanwhile, the orange fruit membrane (JR-800-O) demonstrated the lowest performance due to its dense, non-uniform structure and limited electrolyte uptake, resulting in reduced ion transport and higher IR drop. These findings affirm that choosing a separator with high porosity, good wettability, and mechanical stability is critical to optimizing the energy storage efficiency and cycling stability of supercapacitor devices.

REFERENCES

1. IEA. (2024). Electricity Market Report. *Electricity Market Report*.
2. Zhang, J., Song, S., Xue, J., Li, P., Gao, Z., Li, Y., Zhang, Z., Feng, H., & Luo, H. (2018). Nitrogen-rich Porous carbon derived from biomass as high performance electrode materials for supercapacitors. *International Journal of Electrochemical Science*, **13**(6), 5204–5218.
3. Ganjoo, R., Sharma, S., Kumar, A., & Daouda, M. M. (2023). *Activated carbon: Fundamentals, classification, and properties*. Rotal Sociesty of Chemistry.
4. Yu, H., Tang, Q., Wu, J., Lin, Y., Fan, L., Huang, M., Lin, J., Li, Y., & Yu, F. (2012). Using eggshell membrane as a separator in supercapacitor. *Journal of Power Sources*, **206**, 463–468.
5. Mueller, N. (2017) *How sustainable homes around the world area paving the way to the future*. Garden Collage Magazine.
6. Ayala, J. R., Montero, G., Coronado, M. A., García, C., Curiel-Alvarez, M. A., León, J. A., Sagaste, C. A., & Montes, D. G. (2021). Characterization of orange peel waste and valorization to obtain reducing sugars. *Molecules*, **26**(5), 1348.
7. Murtini, E. S. (2021). The effect of carbonized rice straw levels on the dawet gel properties. *Advances in Food Science, Sustainable Agriculture and Agroindustrial Engineering (AFSSAAE)*, **4**(1), 1–7.
8. Diandari, A. F. & Dewi, L. M. (2020). Anatomical characterization of wood decay patterns in Hevea brasiliensis and Pinus merkusii caused by white-rot fungi: Polyporus arcularius and Pycnoporus sanguineus. *IOP Conference Series: Earth and Environmental Science*, **528**(1), 012048.
9. Simanjuntak, M. T. & Awitdrus, A. (2022). Fabrikasi elektroda karbon dari sabut kelapa muda dengan aktivasi fisika sebagai aplikasi superkapasitor. *Indonesian Physics Communication*, **19**(2), 65–68.
10. Igliński, B., Kujawski, W., & Kiełkowska, U. (2023). Pyrolysis of waste biomass: technical and process achievements, and future development-a review. *Energies*, **16**.
11. Li, J., Jia, H., Ma, S., Xie, L., Wei, X. X., Dai, L., Wang, H., Su, F., & Chen, C. M. (2022). Separator design for high-performance supercapacitors: requirements, challenges, strategies, and prospects. *ACS Energy Letters*, **8**(1), 56.
12. Houdhury, N. A. (2020). Development of cellulose-based green separator membranes for energy storage devices: A review. *Sustainable Energy Technologies and Assessments*, **37**, 100590.
13. Yunita, A., Farma, R., Awitdrus, A., & Apriyani, I. (2023). The effect of various electrolyte solutions on the electrochemical properties of the carbon electrodes of supercapacitor cells based on biomass waste. *Materials Today: Proceedings*, **87**.

IPC

Indonesian Physics Communication

Department of Physics, Universitas Riau, Pekanbaru, Indonesia
p-ISSN 1412-2960 | e-ISSN 2579-521X

Vol. 22 | No. 2
July 2025

Web: https://kfi.ejournal.unri.ac.id
E-mail: kfi@ejournal.unri.ac.id

Preliminary study on the potential use of *Averrhoa bilimbi L.* as a supercapacitor electrode material

Lailatul Rahmi, Awitdrus*
Department of Physics, Universitas Riau, Pekanbaru 28293, Indonesia

*Corresponding author: awitdrus@lecturer.unri.ac.id

ABSTRACT

The global energy crisis and environmental damage caused by the use of fossil fuels have driven the development of environmentally friendly energy storage technologies, one of which is the supercapacitor. This study aims to explore the potential of *Averrhoa bilimbi L.* (belimbing wuluh) as a source of activated carbon for supercapacitor applications. Activated carbon from belimbing wuluh pulp was synthesized through a carbonization process at 800°C. Morphological characterization using SEM showed a porous surface that had not yet developed optimally, while EDX analysis identified carbon, oxygen, and magnesium as the dominant elements. Electrochemical characterization was carried out using CV and GCD methods with variations in H_2SO_4 electrolyte concentration (1, 2, and 3 M). The electrode tested with 1 M showed the best performance, with a specific capacitance of 45.98 F/g (CV) and 96.81 F/g (GCD). These results indicate that belimbing wuluh has potential as a sustainable natural material for the development of environmentally friendly supercapacitors.

Keywords: Belimbing wuluh; non-activated carbon; supercapacitor; sulfuric acid

Received 12-05-2025 | Revised 26-05-2025 | Accepted 03-06-2025 | Published 31-07-2025

INTRODUCTION

The global energy crisis and environmental degradation caused by the use of fossil fuels have become critical issues driving the development of more environmentally friendly energy storage technologies, such as supercapacitors [1]. In addition, the growth of the world population, which has reached 8 billion people, further exacerbates energy problems, as each individual consumes energy every second in various forms [2]. Supercapacitors typically store energy through physical charge separation, unlike batteries that rely on chemical reactions for energy storage. The working principle of supercapacitors depends on the electric charge carried by ions [3]. The main components of a supercapacitor include the electrolyte, current collector, electrode, and separator material [4].

The performance of supercapacitors heavily depends on the unique characteristics of the electrode materials used. Therefore, it is essential to investigate electrode materials in order to maximize the potential of supercapacitors [5]. Various types of biomass have been extensively studied for supercapacitor development. A wide range of natural resources including agricultural waste such as rice husks [6] and wheat straw [7], plant parts such as cinnamon sticks [8] and bamboo [9], as well as fruits like Japanese citron [10] and orange peels [11] have been explored. In addition, unique materials such as strobili fibers [12] and stone pine [13] have also been tested for their potential [14].

Belimbing wuluh is tropical plant is widely available and is not a seasonal crop [15]. The fruit is oval-shaped, measuring approximately 4 – 6 cm in length, with a glossy skin that ranges in color from green to yellow. Annual fruit production can reach up to 1,500 fruits per plant. The productivity or yield characteristics can be observed from the number of fruits produced per plant [16]. Belimbing wuluh contains various chemical components, including phenols, flavonoids, pectin, saponins, tannins, glycosides, and is also rich in minerals [17].

This research is a preliminary study aimed at exploring the utilization of carbon derived from belimbing wuluh. without chemical activation as an electrode material for supercapacitors. The carbon was obtained through a Carbonization process under a nitrogen (N_2) atmosphere and subsequently used as the active material for the electrode. Sulfuric acid (H_2SO_4) solution was employed as the electrolyte, with varying concentrations of 1M, 2M, and 3M, to investigate the effect of electrolyte concentration on the specific capacitance of the resulting supercapacitor.

RESEARCH METHODS

Materials

This study used belimbing wuluh collected from the Universitas Riau area. Starch flour was used to adhere the sample to the electrode plate, and H_2SO_4 (sulfuric acid) solutions with concentrations of 1, 2, and 3 M were used as the electrolytes.

Method

The belimbing wuluh biomass was washed, pressed, and then sun-dried for 2 – 3 days until a constant mass was achieved. Once dried, the biomass underwent a pre-carbonization process at 200°C for 30 minutes, followed by grinding and blending to obtain a fine carbon powder. The powder was then sieved using a 53-micrometer mesh with the aid of a brush to achieve a uniform particle size. Next, the sample was subjected to stepwise heating in a furnace: from room temperature to 400°C at a rate of 5°C/min over 1 hour and 14 minutes, held for 1 hour; then increased to 600°C over 40 minutes, held for another hour; and finally raised to 800°C over 40 minutes and maintained for 2 hours. This entire process was carried out in a closed system under a nitrogen (N_2) atmosphere. After pyrolysis, the carbon was cooled to room temperature and neutralized by rinsing with distilled water for 3 – 4 days until a neutral pH (~7) was achieved. The sample was then dried in an oven at 110°C for 24 hours. For electrode fabrication, 0.1 grams of carbon powder was mixed with a starch solution (2 grams of starch flour in 20 mL of distilled water), which was heated and stirred. The resulting carbon paste was applied onto a stainless steel current collector. Whatman paper was used as a separator to assemble the supercapacitor cell. The steps involved in preparing the sample into a supercapacitor electrode are illustrated in Figure 1 below.

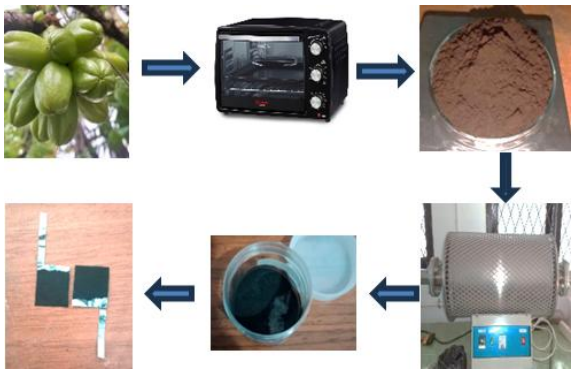

Figure 1. Sample fabrication process.

Characterization

Physical characterization using scanning electron microscopy (SEM) produces microscopic images of the carbon electrode. These images allow for the observation of pore shapes and sizes on both the surface and internal structure of the electrode. SEM data provides crucial information about the morphological characteristics of the electrode material derived from bilimbi fruit. Meanwhile, energy dispersive X-ray (EDX) analysis offers detailed information about the elemental composition of the activated carbon electrode produced from bilimbi fruit. This data can be further used to analyze the material's intrinsic properties.

Electrochimical Study

Electrochemical characterization was conducted using cyclic voltammetry (CV). From the CV tests, charging and discharging current data were obtained, which were then

used to calculate the specific capacitance value using Equation (1) as shown below [18]:

$$C_{sp} = \frac{(I_c - I_d)}{s\ x\ m} \quad (1)$$

Characterization using galvanostatic charge-discharge (GCD) was performed to further evaluate the electrochemical performance of the electrode. The data obtained from the GCD test were subsequently used to calculate the specific capacitance value using Equation (2) as follows [19]:

$$C_{sp} = \frac{2\,I.\Delta t}{m.\Delta V} \quad (2)$$

RESULTS AND DISCUSSION

Surface Morphology Analysis

Scanning Electron Microscopy (SEM) characterization was carried out to observe the surface morphology and pore size distribution of the bilimbi-derived carbon electrode. Figure 2 presents the SEM image of the carbon electrode at 1000x magnification. The SEM micrograph reveals that the carbon material possesses an irregular, stacked particle structure, forming a dense and interconnected surface. This type of morphology may contribute to good mechanical strength and structural stability, which are beneficial for maintaining the integrity of the electrode during supercapacitor operation.

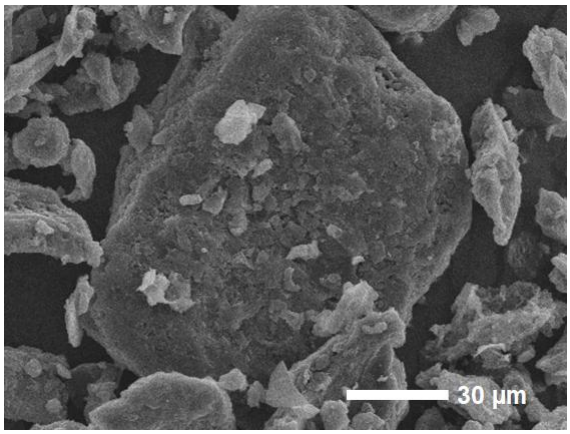

Figure 2. SEM characterization results.

The relatively smooth surface and minimal pore presence indicate that the carbonization process produced a compact material. However, the limited number of open pores may reduce the available active surface area for electrolyte ion interaction. This can affect electrochemical performance, particularly in terms of specific capacitance and charge transfer efficiency [20]. In other words, although the resulting structure is stable and well-integrated, further development of porosity is still necessary to optimize the energy storage characteristics of this material.

Elemental Composition Analysis

Based on the results of Energy Dispersive X-ray (EDX) analysis, the carbon material was found to be predominantly composed of carbon, with an atomic percentage of 92.66%. This high carbon content indicates that the carbonization process successfully produced a carbon-rich structure, which is essential for supercapacitor electrode materials. In addition to carbon, oxygen was also detected at 7.14%, likely originating from residual oxygen-containing functional groups such as hydroxyl, carbonyl, or carboxyl on the material's surface. These groups play a crucial role in enhancing hydrophilicity and interactions with electrolyte ions, thereby supporting electrochemical performance [21]. Furthermore, a small amount of magnesium (0.20% atomic) was identified, which may be attributed to residual inorganic compounds from the synthesis process or the original raw material. The presence of these elements provides a comprehensive understanding of the material's chemical composition and its potential contribution to electrode performance.

Electrochemical Characterization

The CV test results in the form of curves can be seen in Figure 3. The shape of the curve, which approaches a rectangular profile, indicates that the charge storage mechanism in this carbon material occurs via electric double

layer capacitance (EDLC), characterized by a stable and reversible electrochemical response. The specific capacitance values of each sample were determined based on the cathodic (Ic) and anodic (Id) current data obtained at a scan rate of 5 mV/s.

The Ic value represents the maximum current during the reduction process (charge storage), while the Id value corresponds to the maximum current during the oxidation process (charge release). These two current values are used to calculate the area under the CV curve, which is then converted into the specific capacitance value [22].

The calculation results show that the electrolyte with a concentration of 1M yields the highest specific capacitance of 45.98 F/g, followed by 2M at 41.10 F/g, and the lowest at 3M with 20.75 F/g at a scan rate 5 mV/s. This trend indicates that increasing the electrolyte concentration does not necessarily enhance the material's performance. At higher concentrations such as 3 M, the solution's viscosity increases, which hinders ion diffusion into the electrode pores [23]. Therefore, it can be concluded that the optimal electrolyte concentration of bilimbi fruit-based aqueous solution in this system is 1M, as it provides the most efficient charge transfer and the highest specific capacitance, in accordance with the observations from the previous CV curve analysis.

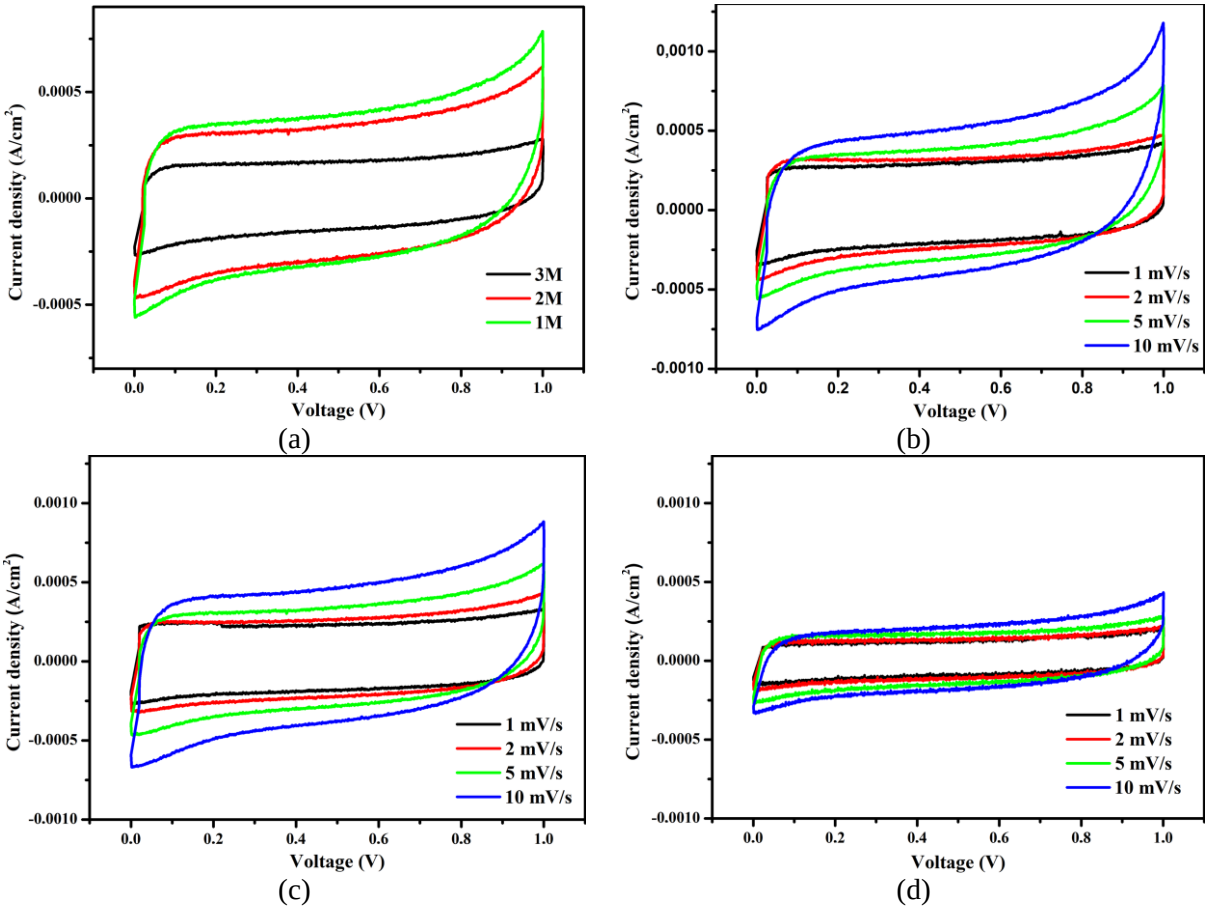

Figure 3. CV curves at different concentrations: (a) scan rate 5 mV/s for comparison (b) 1 M, (c) 2 M, (d) 3 M.

Figure 4 shows the GCD curves of the sample-based electrolyte concentrations, illustrating how the performance of the electrodes varies with different electrolyte strengths. The curves exhibit a nearly triangular shape, indicating good capacitive behavior, and show that the charge–discharge process occurs in a highly reversible manner. This triangular shape reflects the ideal behavior of an electric double-layer capacitor, confirming that the

electrodes can store and release charge effectively without significant resistance or polarization. The data also suggest that the electrode structure is stable and efficient in different electrolyte environments.

Based on the GCD curve shown in Figure 4, it can be observed that the discharge time increases as the electrolyte concentration decreases. This indicates that the specific capacitance increases with decreasing electrolyte concentration, with values of 30.33 F/g for 3M, 38.48 F/g for 2M, and 56.61 F/g for 1M, respectively. The GCD curve demonstrates that the discharge profile for the 1M electrolytes exhibits the longest discharge time, indicating a higher charge storage capability compared to higher concentrations. This phenomenon may be attributed to reduced viscosity and enhanced ion diffusion at lower concentrations, allowing for more efficient charge transfer during the discharge process.

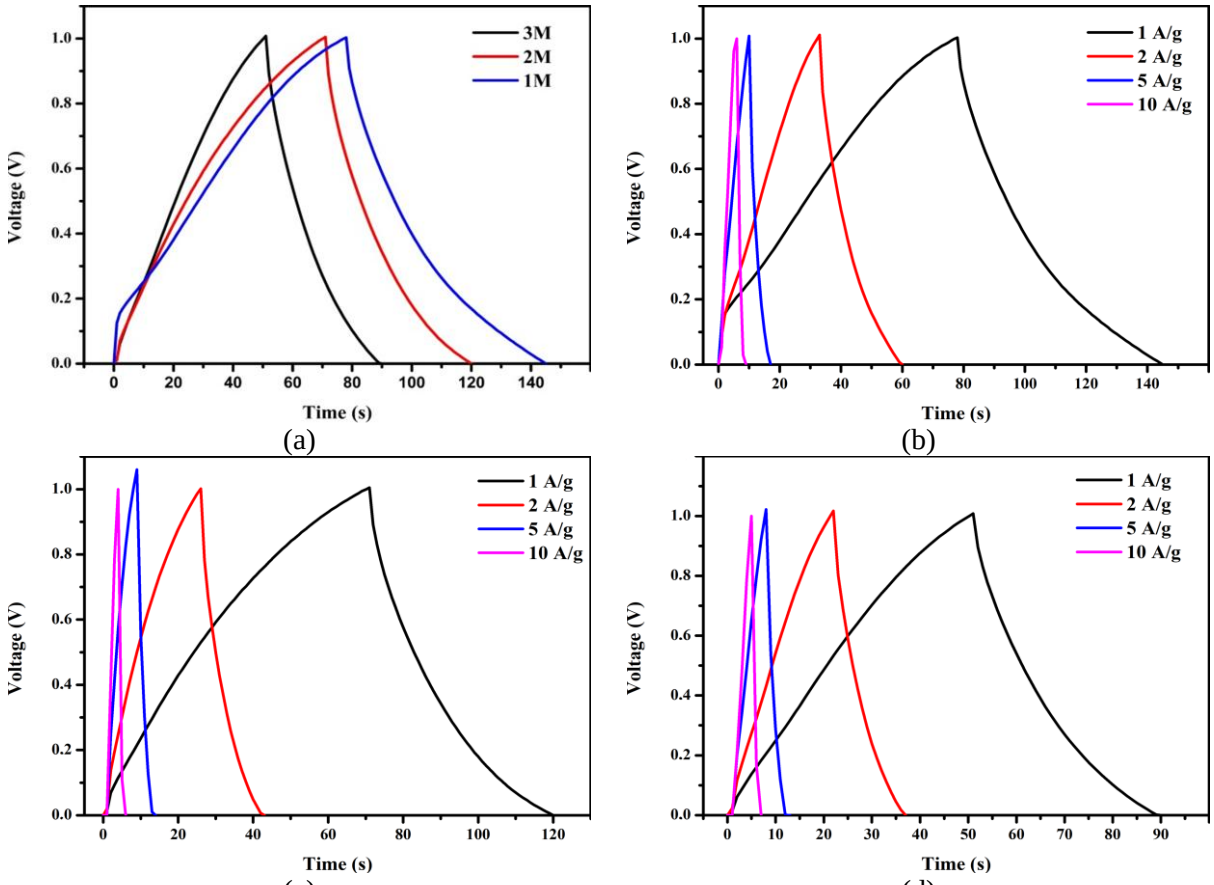

Figure 4. GCD curves at different concentrations: (a) rapat arus 1 A/g for comparison, (b) 1 M, (c) 2 M, (d) 3 M.

The specific capacitance obtained from the GCD method is generally lower compared to the values calculated using CV. This discrepancy is attributed to differences in testing duration, where CV typically involves a longer scan time, allowing the system greater opportunity to absorb and store charge moreeffectively. Consequently, although CV tends to yield higher capacitance values, the capacitance derived from GCD more accurately represents the actual performance of the electrode under constant current operational conditions [24].

CONCLUSION

This study demonstrated that the type of separator material significantly influences the electrochemical performance of activated carbon electrodes derived from orange peel

biomass for supercapacitor applications. Among the three separators tested Whatman filter paper no. 40 (JR-800-W), eggshell membrane (JR-800-E), and orange fruit membrane (JR-800-O) the JR-800-W sample consistently exhibited the highest specific capacitance in both CV (191.82 F/g) and GCD (174.24 F/g) analyses. This superior performance is attributed to the uniform microporous structure and excellent electrolyte absorption of Whatman paper, which promotes faster ion diffusion and more efficient electric double-layer formation. The eggshell membrane separator (JR-800-E) showed moderate performance, with sufficient ionic mobility but slightly higher internal resistance. Meanwhile, the orange fruit membrane (JR-800-O) demonstrated the lowest performance due to its dense, non-uniform structure and limited electrolyte uptake, resulting in reduced ion transport and higher IR drop. These findings affirm that choosing a separator with high porosity, good wettability, and mechanical stability is critical to optimizing the energy storage efficiency and cycling stability of supercapacitor devices.

REFERENCES

1. Zhang, Q., & Wei, K. (2024). A comparative study of fractional-order models for supercapacitors in electric vehicles. *International Journal of Electrochemical Science*, **19**(1), 100441.
2. Phor, L., Kumar, A., & Chahal, S. (2024). Electrode materials for supercapacitors: A comprehensive review of advancements and performance. *Journal of Energy Storage*, **84**, 110698.
3. Wang, Q., Ma, Y., Liang, X., Zhang, D., & Miao, M. (2019). Flexible supercapacitors based on carbon nanotube-MnO_2 nanocomposite film electrode. *Chemical Engineering Journal*, **371**, 145–153.
4. Zhang, J., Gu, M., & Chen, X. (2023). Supercapacitors for renewable energy applications: A review. *Micro and Nano Engineering*, **21**, 100229.
5. Vazhayil, A., Thomas, J., Thomas, T., Hasan, I., & Thomas, N. (2024). Mn-substituted $NiCo_2O_4$/rGO composite electrode for supercapacitors and their electrochemical performance boost by redox additive in alkaline electrolyte. *Journal of Energy Storage*, **84**, 110789.
6. Arkhipova, E. A., Novotortsev, R. Y., Ivanov, A. S., Maslakov, K. I., & Savilov, S. V. (2022). Rice husk-derived activated carbon electrode in redox-active electrolyte–new approach for enhancing supercapacitor performance. *Journal of Energy Storage*, **55**, 105699.
7. Gou, G., Huang, F., Jiang, M., Li, J., & Zhou, Z. (2020). Hierarchical porous carbon electrode materials for supercapacitor developed from wheat straw cellulosic foam. *Renewable Energy*, **149**, 208–216.
8. Abdelrahim, A. M., Abd El-Moghny, M. G., El-Sekhel, O. H., Salama, O. A., El-Shakre, M. E., & El-Deab, M. S. (2023). Wrapping massive MnO2 around in-situ defective carbon felt with strong interaction for superb supercapacitive performance. *Colloids and Surfaces A: Physicochemical and Engineering Aspects*, **677**, 132441.
9. Nguyen, T. B., Yoon, B., Nguyen, T. D., Oh, E., Ma, Y., Wang, M., & Suhr, J. (2023). A facile salt-templating synthesis route of bamboo-derived hierarchical porous carbon for supercapacitor applications. *Carbon*, **206**, 383–391.
10. Trinh, K. T. & Tsubota, T. (2023). Supercapacitors composed of Japanese cedar bark-based activated carbons with various activators. *Materials Chemistry and Physics*, **307**, 128148.
11. Salama, R. S., Gouda, M. S., Aboud, M. F. A., Alshorifi, F. T., El-Hallag, A. A., &

Badawi, A. K. (2024). Synthesis and characterization of magnesium ferrite-activated carbon composites derived from orange peels for enhanced supercapacitor performance. *Scientific Reports*, **14**(1), 8223.

12. Taer, E., Taslim, R., Mustika, W. S., & Fadli, E. (2021). Surface modification: unique ellipsoidal/strobili-fiber structure of porous carbon monolith for electrode supercapacitor. *Nanoscience and Technology: An International Journal*, **12**(4).
13. Nordenström, A., Boulanger, N., Iakunkov, A., Li, G., Mysyk, R., Bracciale, G., Bondavalli, P., & Talyzin, A. V. (2022). High-surface-area activated carbon from pine cones for semi-industrial spray deposition of supercapacitor electrodes. *Nanoscale Advances*, **4**(21), 4689–4700.
14. Damayanti, F., Astuti, I. P., Zulkarnaen, R. N., & Sunarti, S. (2020). Nutritional contents and the utilization of Indonesian native starfruits: Averrhoa dolicocarpa and A. leucopetala. *Biodiversitas Journal of Biological Diversity*, **21**(4).
15. Anjarsari, S., Rahman, D. Y., & Sulistyowati, R. (2024). Pembuatan Bio-Baterai Berbahan Dasar Sari Belimbing Wuluh dan NaCl sebagai Sumber Ion serta Onggok Singkong sebagai Matriks. *Jurnal Penelitian Fisika dan Terapannya (JUPITER)*, **6**(1), 1–10.
16. Insan, R. R., Faridah, A., Yulastri, A., & Holinesti, R. (2019). Using belimbing wuluh (averhoa blimbi l.) as a functional food processing product. *Jurnal Pendidikan Tata Boga Dan Teknologi*, **1**(1), 47–55.
17. Sharma, S. & Chand, P. (2024). Enhanced electrochemical performance of fabricated asymmetric supercapacitor in redox additive electrolyte. *Ceramics International*, **50**(3), 5775–5786.
18. Bandara, T. M. W. J., Alahakoon, A. M. B. S., Mellander, B. E., & Albinsson, I. (2024). Activated carbon synthesized from Jack wood biochar for high performing biomass derived composite double layer supercapacitors. *Carbon Trends*, **15**, 100359.
19. Diantoro, M., Aturroifah, N. I. M., Luthfiyah, I., Utomo, J., Hamidah, I., Yuliarto, B., Rusydi, A., Maensiri, S., & Meevasana, W. (2025). 3D-porous activated carbon morphological modification of Manihot esculenta tuber and Bambusa blumeana stem for high-power density supercapacitor: Biomass waste to sustainable energy. *Carbon Resources Conversion*, 100313.
20. Lesbayev, B., Auyelkhankyzy, M., Ustayeva, G., Yeleuov, M., Rakhymzhan, N., Maltay, A., & Maral, Y. (2023). Recent advances: Biomass-derived porous carbon materials. *South African Journal of Chemical Engineering*, **43**(1), 327–336.
21. Qin, Q., Wang, J., Tang, Z., Jiang, Y., & Wang, L. (2024). Mesoporous activated carbon for supercapacitors derived from coconut fiber by combining H3PO4-assisted hydrothermal pretreatment with KOH activation. *Industrial Crops and Products*, **208**, 117878.
22. Agrawal, A., Gaur, A., & Kumar, A. (2023). Fabrication of Phyllanthus emblica leaves derived high-performance activated carbon-based symmetric supercapacitor with excellent cyclic stability. *Journal of Energy Storage*, **66**, 107395.
23. Kremer, L. S., Danner, T., Hein, S., Hoffmann, A., Prifling, B., Schmidt, V., Latz, A., & Wohlfahrt-Mehrens, M. (2020). Influence of the electrolyte salt concentration on the rate capability of ultra-thick NCM 622 electrodes. *Batteries & Supercaps*, **3**(11), 1172–1182.

24. Beyers, I., Bensmann, A., & Hanke-Rauschenbach, R. (2023). Ragone plots revisited: A review of methodology and application across energy storage technologies. *Journal of Energy Storage*, **73**, 109097.

IPC

Indonesian Physics Communication

Department of Physics, Universitas Riau, Pekanbaru, Indonesia
p-ISSN 1412-2960 | e-ISSN 2579-521X

Vol. 22 | No. 2
July 2025

Web: https://kfi.ejournal.unri.ac.id
E-mail: kfi@ejournal.unri.ac.id

Comparison of electrochemical performance of supercapacitor electrodes based on electrolyte solution variation

Rosianna Purba, Awitdrus*
Department of Physics, Universitas Riau, Pekanbaru 28293, Indonesia

*Corresponding author: awitdrus@lecturer.unri.ac.id

ABSTRACT

The increasing global energy demand has accelerated the progress of renewable energy technologies and the creation of effective energy storage solutions such as supercapacitors. In this study, biomass obtained from the peel of the matoa fruit (*Pometia pinnata*) was employed as a raw material to produce activated carbon for supercapacitor electrodes. The preparation process consisted of an initial carbonization step, followed by chemical activation using a 0.7 M potassium hydroxide (KOH) solution, and then additional carbonization and physical activation stages. The synthesized material was characterized through density measurements and electrochemical testing, including cyclic voltammetry (CV) and galvanostatic charge-discharge (GCD) methods, conducted with KOH electrolytes at concentrations of 2, 4, and 6 M. Results demonstrated that combining chemical activation with pyrolysis yielded better outcomes than physical activation alone, as shown by a decrease in activated carbon density, indicating enhanced porosity and surface area. CV analysis revealed that increasing the KOH electrolyte concentration improved the supercapacitor's performance, reflected in higher specific capacitance during charge-discharge cycles. Moreover, GCD experiments showed that electrodes treated with 6 M KOH electrolyte achieved the greatest specific capacitance, energy density, and power density, recorded at 170.52 F/g, 23.68 Wh/kg, and 580.00 W/kg, respectively. These findings highlight that activated carbon derived from matoa fruit peel is a highly promising material for supercapacitor electrodes, combining excellent electrochemical characteristics, efficiency, and stable cycling behavior.

Keywords: Activated carbon; electrolyte; matoa fruit peel; supercapacitor

Received 14-05-2025 | Revised 28-05-2025 | Accepted 04-06-2025 | Published 31-07-2025

INTRODUCTION

Global energy consumption is rapidly rising, primarily due to population expansion and fast-paced economic growth. Nevertheless, the heavy reliance on fossil fuels contributes to numerous environmental issues, including climate change, air quality deterioration, and the exhaustion of natural resources [1]. The extensive use of fossil fuels today has detrimental effects on the environment, particularly contributing to global warming and climate change. As a result, there is a rising demand for clean, renewable energy sources. These sustainable energy options are seen as the best alternatives to replace fossil fuels in the future.

Significant progress has been made in creating affordable renewable energy solutions, such as wind energy, solar energy, and biomass [2]. Shifting from conventional fossil fuels to renewable energy represents a crucial move toward achieving sustainable development. This shift depends largely on effective energy conversion and storage, with energy storage systems playing a vital role in facilitating the transition [3].

A major obstacle in harnessing renewable energy is its intermittent availability, which leads to fluctuations in power supply. This makes energy storage solutions like batteries and supercapacitors essential. Supercapacitors, in particular, offer advantages such as long-term energy retention and higher storage capacity [4].

Supercapacitors are storage devices developed from conventional capacitors. Supercapacitors have higher power density and better cycle endurance, making them highly effective in energy storage systems that are able

to respond to rapid power changes. There are two types of supercapacitors: electrochemical double layer capacitors (EDLC) that rely on adsorptive storage and pseudo-capacitors that use the Faradaic mechanism [5].

Biomass as an abundant renewable energy source on earth has an important role in supporting sustainability. Biomass is not only utilized for generating energy but also acts as the primary raw material for producing activated carbon. Research on carbonization techniques to convert waste into porous carbon is growing, especially because of its potential in various industrial applications [6].

KOH is a basic electrolyte because the energy density of supercapacitors using KOH is usually the same as the electrically conductive energy density [7]. The selection of electrolytes using appropriate ion size is essential to achieve optimal supercapacitor performance, Taer et al., (2020) emphasizes the significance of electrolyte ion size within the electrode.

Biomass carbon is one of the materials often used for activated carbon. Several previous studies have developed methods of making activated carbon for electrodes such as rice husk [9], bagasse [10], banana stem fiber [11] and matoa fruit peel [12]. This research uses biomass from matoa fruit peels using variations of KOH electrolyte solutions of 2 M, 4 M and 6 M using 0.7 M KOH activating agent as a supercapacitor electrode.

RESEARCH METHODS

Materials

This study used matoa (Pometia pinatta) fruit peel biomass material obtained from Tualang Village in Riau. Before the process of making supercapacitor electrodes, matoa fruit peels were dried and pre-carbonized. Carbon was activated using 0.7 M KOH activating agent. Electrochemical characterization with Cyclic Voltammetry and Galvanostatic Charge Discharge methods.

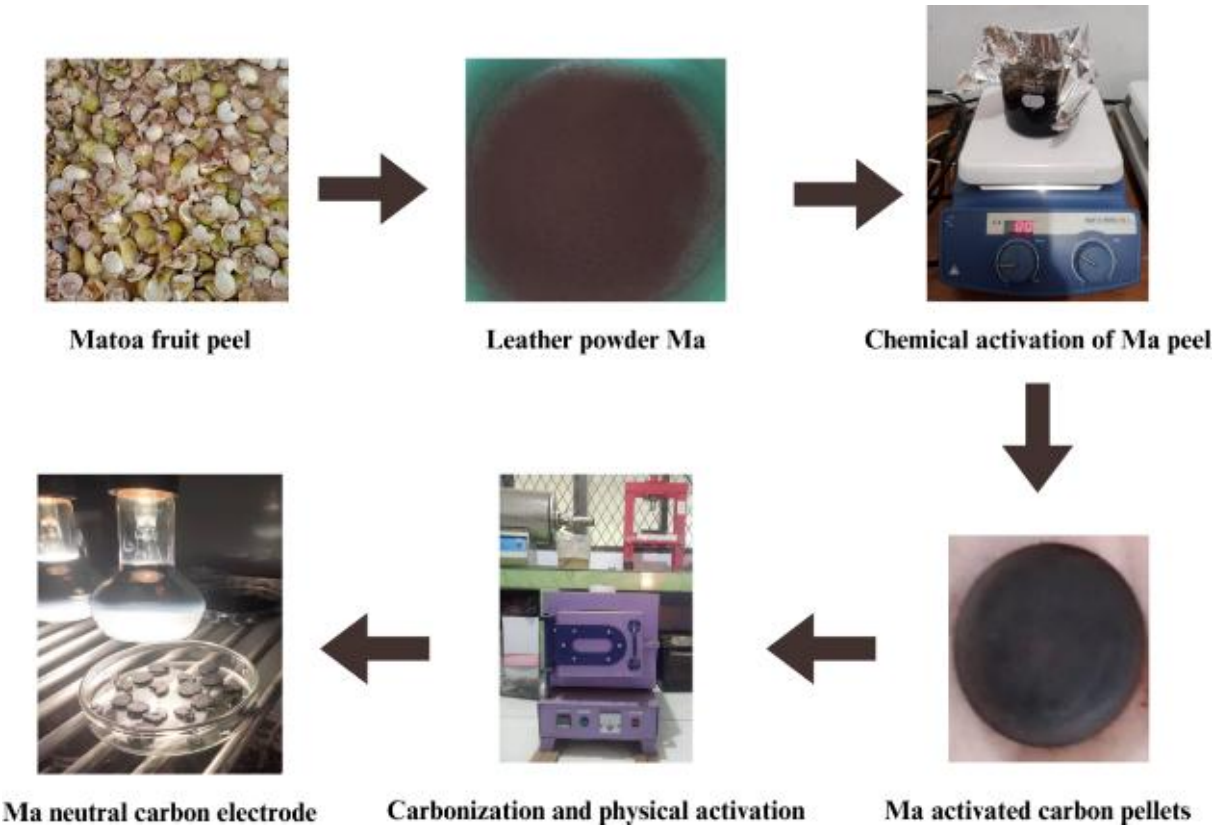

Figure 1. Manufacturing process of Ma electrode.

Sample Preparation of Matoa Fruit Peel Biomass Activated Carbon

This preparation begins using collecting matoa fruit peels and then cut into small pieces up to 3 – 4 cm in size and dried under the sun for 4 – 5 days. A total of 30 grams of biomass was pre-carbonized in an oven at 200°C for 2 hours. The resulting carbon was crushed and sieved using a 53 μm sieve to obtain a fine powder.

Chemical activation was carried out by mixing 20 grams of carbon powder into a 0.7 M KOH solution (100 ml of distilled water), stirred at 80°C and a rotation rate of 350 rpm for 15 minutes until homogeneous. Next, 20 grams of carbon powder was mixed using the KOH solution and stirred again under the same conditions for 2 hours. The mixture was kept at room temperature for 2 days, then dried in an oven at 110°C for 3 days.

The activated carbon produced was sieved again and formed into coin-shaped pellets measuring 8 mm in diameter and 2 mm in thickness by applying a pressure of 8 tons. Subsequent carbonization was performed in a furnace where the temperature was gradually increased from 30°C to 302°C at a rate of 1°C per minute and maintained for one hour, followed by a slow ramp-up to 600°C at 3°C per minute under a nitrogen atmosphere. Physical activation was continued by changing the N_2 gas to CO_2 and raising the temperature to 850°C (10°C/min), maintained for 2 hours and 30 minutes.

After controlled cooling using N2 to room temperature, the activated carbon was neutralized using distilled water to a pH close to 7 and dried again. The activated carbon was polished, washed and immersed in electrolyte before electrochemical testing.

Density is a quantity that shows the mass per unit volume of a material. In activated carbon material, density measurement is very important to determine the level of mass change and porosity in the material. Density is usually expressed in grams per cubic centimeter (gr/cm^3). The density of each object is different depending on the mass and volume of the object [13]. Density can be calculated using:

$$p = \frac{m}{v} \tag{1}$$

$$v = \pi r^2 t \tag{2}$$

Electrode material research, measurement of electrochemical properties can be done using methods such as Cyclic Voltammetry (CV), and Galvanostatic Charge-Discharge (GCD). These methods provide data such as: specific capacitance, current density, cycle stability and electron transfer kinetics. CV electrochemical testing aims to calculate the capacitance of supercapacitor cells [14].

Galvanostatic Charge-Discharge (GCD) testing is employed to evaluate the capacitive behavior, identify possible reversible faradaic processes, and determine key performance metrics of electrochemical capacitors, including capacitance, energy storage capacity, and power output [15]. This method is utilized to determine the electrochemically active surface area, double-layer capacitance, and hydrogen crossover current by employing a galvanostatic power source to acquire the necessary voltage readings [16]. The following formulas are applied to calculate the specific capacitance, energy density, and power density of supercapacitor electrodes during galvanostatic charge-discharge (GCD) experiments [17]:

$$C_{sp} = \frac{2\,I.\Delta t}{m.\Delta V} \tag{3}$$

$$E_{sp} = \frac{C_{sp}\,\Delta V^2}{2} \times \frac{1000}{3600} \tag{4}$$

$$P_{sp} = 3600\,\frac{E_{sp}}{\Delta t} \tag{5}$$

In this formula, I represents the current in amperes (A), t denotes the time in seconds (s), V stands for the voltage in volts (V), and m indicates the mass of the electrode in grams (g).

RESULTS AND DISCUSSION

Density Measurement

The low density of activated carbon generally indicates a porous structure, resulting from the chemical activation and pyrolysis process that opens and enlarges the pores, thus lowering the density. Measuring the density of activated carbon is crucial because it has a direct impact on the material's surface area and its ability to adsorb substances [18]. Figure 2 presents the changes in carbon's physical attributes such as mass, thickness, diameter, and density comparing values recorded prior to and following the pyrolysis treatment. Among these, thickness experiences the greatest shrinkage, followed by diameter, while changes in mass and density are comparatively minor. Post pyrolysis, the shrinkage of all parameters decreases, suggesting that the activated carbon's structure has become more stable and the mass to volume ratio remains consistent.

The almost stable density indicates the activated carbon produced has a porous and stable structure. The reduction in mass, diameter, thickness, volume, and density of the pellets following carbonization is due to the material breaking down during this process. During carbonization, elements such as oxygen, hydrogen, non-carbon components, as well as impurities are released from the material, leaving a carbon skeleton using a specific structure and the formation of pores in the carbon [19].

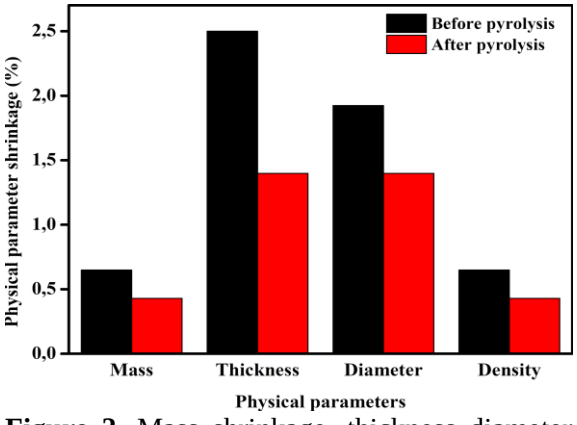

Figure 2. Mass shrinkage, thickness diameter and electrode density Ma.

Measurement of Electrochemical Properties

Electrochemical property measurement is an analytical process used to determine the characteristics of a material or system based on its response to electrical stimuli in an electrolyte environment. The primary goal of evaluating electrochemical characteristics is to assess the suitability of a material for use as an electrode in supercapacitor devices. The results of these measurements are very important to determine the performance, efficiency and lifetime of materials in electrochemical devices [20].

Cyclic Voltammetry (CV) is a widely utilized electrochemical method for analyzing the properties of electrode materials. This technique involves applying a linearly varying potential over time in repetitive cycles, while simultaneously recording the resulting current.

Figure 3 is the results of Cyclic Voltammetry (CV) measurements of matoa fruit peel biomass samples that have been activated using 0.7 M KOH, then tested in KOH electrolyte using variations in concentrations of 2 M, 4 M and 6 M. The voltage (V) is shown on the x-axis, while the current density (A/cm²) is displayed on the y-axis. Each curve shows that the higher the scan rate, the larger the area under the curve which signifies an increase in charge storage capacitance. At elevated scan rates (10 mV/s), the curve's shape starts to deviate from the perfect rectangular form, suggesting the presence of internal resistance and restricted ion movement within the electrode.

Visually, the CV curve for 4 M KOH has the highest peak current density, followed by 2 M KOH and 6 M KOH. This indicates that at a concentration of 4 M KOH, the speed of charge transfer at the electrode surface increases, as demonstrated by the elevated current produced. The figure indicates that a high electrolyte concentration increases the amount of K+ and OH- ions available in the solution. Cyclic Voltammetry (CV) is a widely utilized electrochemical method for analyzing the properties of electrode materials. This

technique involves applying a linearly varying potential over time in repetitive cycles, while simultaneously recording the resulting current. However, when viewed from the shape of the curve, all samples display a curve shape that tends to be symmetrical and resembles a rectangle, indicating good capacitive characteristics and high reversibility of the KOH electrode material.

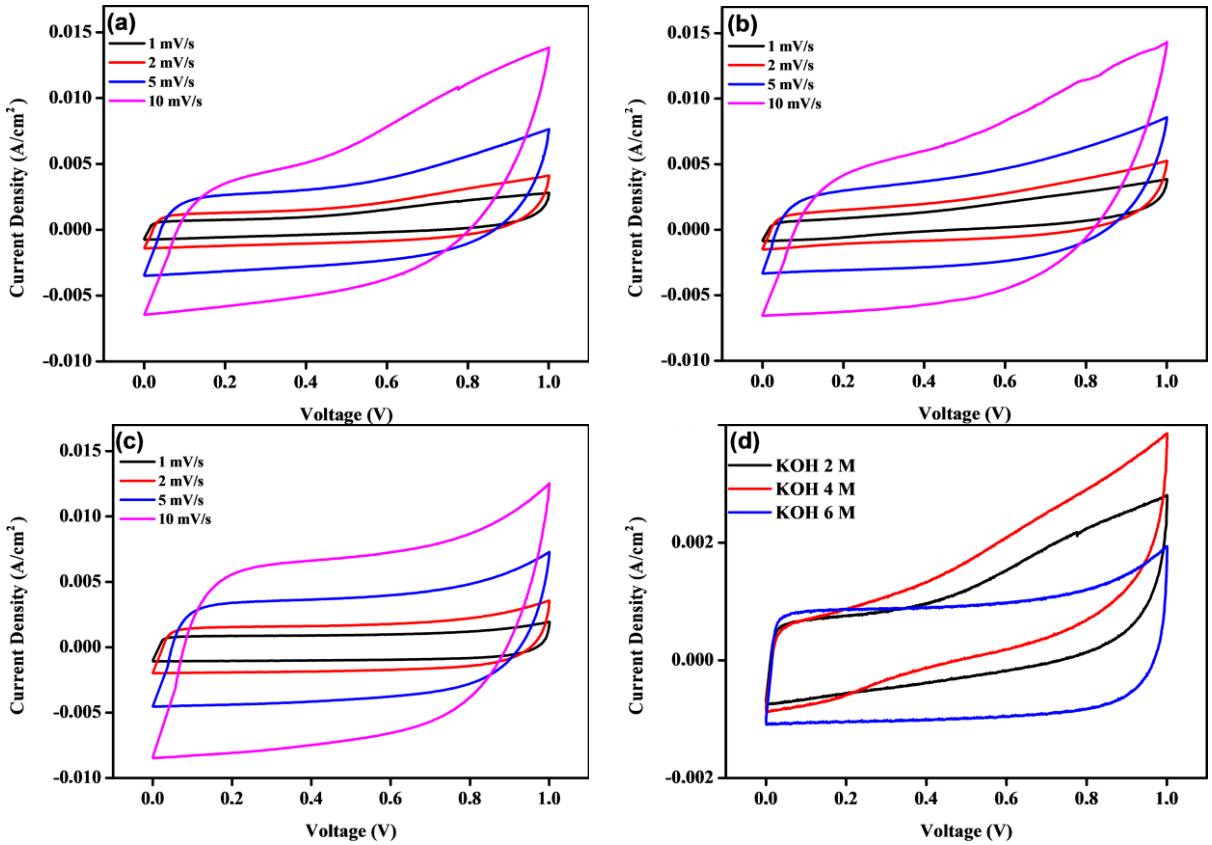

Figure 3. CV measurements of (a) 2 M KOH electrolyte, (b) 4 M KOH electrolyte, (c) 6 M KOH electrolyte, (d) comparison of (a), (b), (c) at a scan rate of 1 mV/s.

The electrode's specific capacitance in a 6 M KOH electrolyte generally exhibits a tendency to higher due to the lower current density value in CV generally associated using better charge transfer efficiency and less parasitic reaction. In addition, the symmetrical and stable curve shape at 6 M KOH indicates that the electrode is able to work optimally under high concentration electrolyte conditions, making it suitable for supercapacitor applications that require stability and high efficiency.

Galvanostatic Charge Discharge (GCD) is a technique in electrochemical testing where a steady current is used to both charge and discharge an electrode designed for energy storage. A constant current GCD process is applied so that the change in voltage versus electrode. A constant current GCD process is applied so that the change in voltage versus time during charging and discharging can be observed. These GCD curves provide important information about the specific capacitance, energy storage efficiency, internal resistance and cycle stability of the electrode material [21].

Figure 4 shows the Galvanostatic Charge Discharge (GCD) curve of the matoa fruit peel biomass-based electrode activated using 0.7 M KOH using three variations of KOH electrolyte concentration (2 M, 4 M, 6 M). This GCD curve illustrates the relationship between voltage (V) and time (s) during the charging and discharging process at constant current. Visually, the GCD curve for 6 M KOH shows the longest charge discharge time compared to

2 M KOH and 4 M KOH. This indicates that the electrode using 6 M KOH electrolyte is able to store and release charge in a longer time which is an indication of higher energy storage capacity. The shape of the curve which tends to be symmetrical and linear also indicates good capacitive characteristics and reversible charge discharge process.

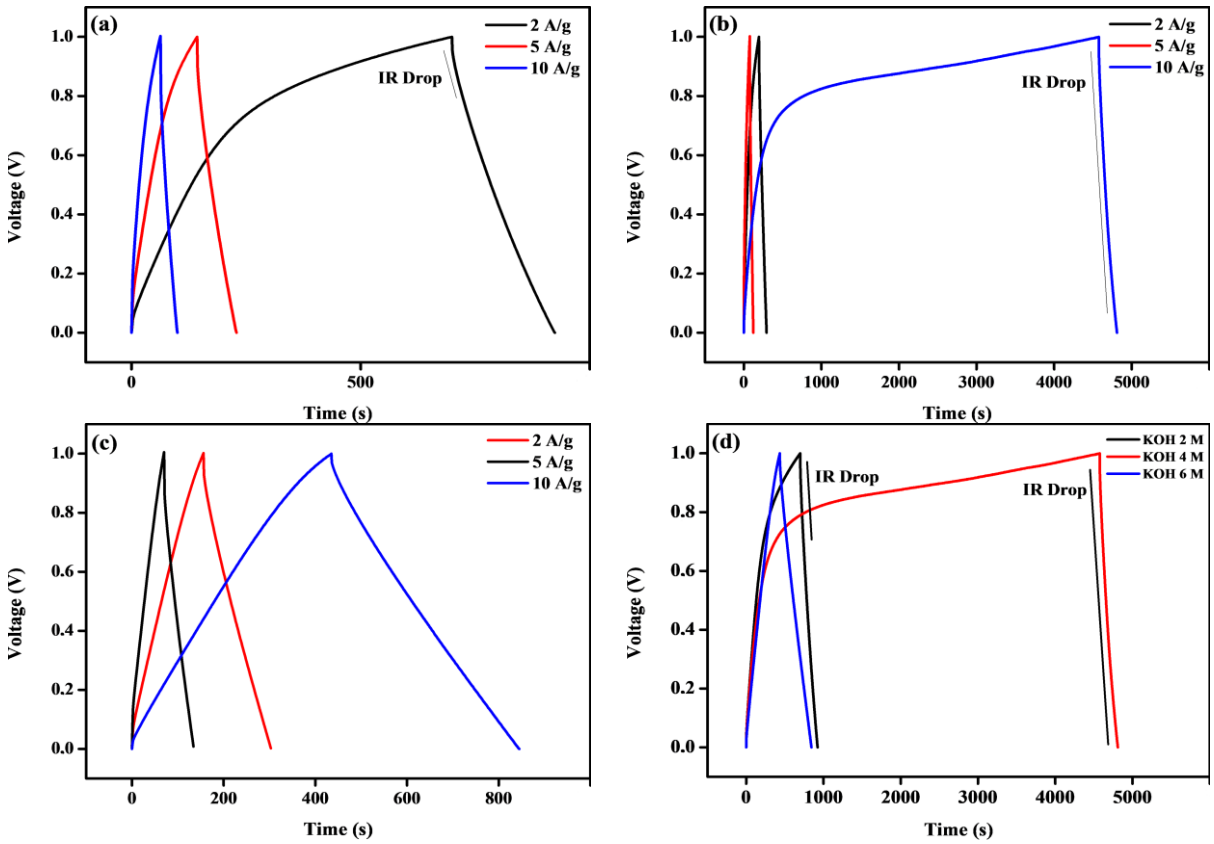

Figure 4. GCD measurements of (a) 2 M KOH electrolyte, (b) 4 M KOH electrolyte, (c) 6 M KOH electrolyte, (d) comparison of (a), (b), (c) at a scan rate of 2 A/g.

Table 1. GCD measurement results data.

Sample code	C_{sp} (F/g)	P_{sp} (W/kg)	E_{sp} (Wh/kg)
KOH 2 M	95.51	561.87	22.53
KOH 4 M	99.15	511.11	13.77
KOH 6 M	170.52	580.00	23.68

Data Table 1 is the GCD data of specific capacitance (Csp), specific power (Psp) and specific energy (Esp) measurements for each electrolyte variation. The data indicate that the electrode utilizing a 6 M KOH electrolyte exhibits the greatest specific capacitance (Csp) at 170.52 F/g, along with the highest specific energy (Esp) of 23.68 Wh/kg. Additionally, the specific power (Psp) reaches its peak value of 580 W/kg with the 6 M KOH electrolyte.

The high specific capacitance value at 6 M KOH indicates that the electrode is able to store more charge per unit mass which is also reflected in the longer discharge time on the GCD curve. This indicates that at higher KOH concentrations the number of ions available to interact using the electrode surface increases so that the charge storage process takes place more efficiently. Moreover, the material generates higher specific energy, demonstrating its efficient capability to store and discharge energy. In contrast, at 2 M and 4 M KOH although the final voltage achieved is almost the same the discharge time is shorter and the capacitance value and specific energy are lower. This can be caused by the limited number of ions available at lower electrolyte concentrations so that the charge storage process is not as efficient as at 6 M KOH. Figure 4 (d) comparison of the three electrolyte concentrations at a current density of 2 A/g

clarifies the advantages of 6 M KOH, where the longest discharge time indicates low internal resistance and high ion transfer efficiency. The combination of KOH-activated porous activated carbon and high concentration KOH electrolyte provides the best supercapacitor performance, especially in terms of specific capacitance and cycle efficiency [22].

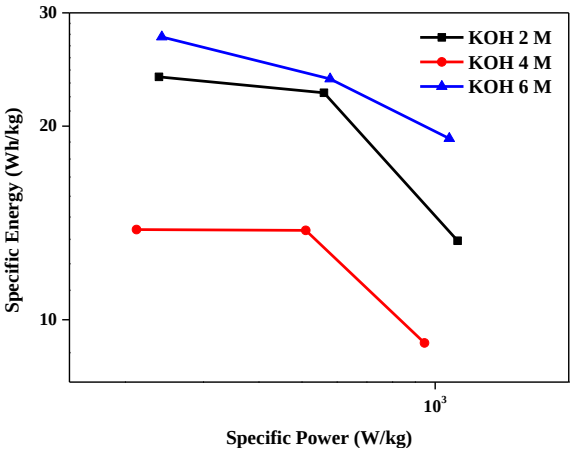

Figure 5. Plot Ragone.

Ragone plots illustrate the balance between specific energy and specific power in energy storage systems like supercapacitors. Typically, as specific power—which reflects the ability to deliver energy quickly—increases, the specific energy tends to decline [23]. Comparing the performance of the three electrolyte variations, the 6 M KOH sample shows efficient performance in storing and releasing energy at both low and high rates. This occurs because of the efficient interaction between ions and the electrode surface, allowing for greater charge storage and release during the charging and discharging cycles. The decrease in specific energy at high power is a common phenomenon in supercapacitors because at high currents the discharge time is shorter so that the total energy released is smaller. Overall, KOH 6 M is the most recommended electrolyte for the application of 0.7 M KOH-activated matoa fruit quit biomass-based supercapacitors because it is able to keep the specific energy high even at high specific power. The 6 M KOH electrolyte also showed good performance to improve the supercapacitor efficiency for both long-term energy applications and instant power needs.

CONCLUSION

This study demonstrated that the type of separator material significantly influences the electrochemical performance of activated carbon electrodes derived from orange peel biomass for supercapacitor applications. Among the three separators tested Whatman filter paper no. 40 (JR-800-W), eggshell membrane (JR-800-E), and orange fruit membrane (JR-800-O) the JR-800-W sample consistently exhibited the highest specific capacitance in both CV (191.82 F/g) and GCD (174.24 F/g) analyses. This superior performance is attributed to the uniform microporous structure and excellent electrolyte absorption of Whatman paper, which promotes faster ion diffusion and more efficient electric double-layer formation. The eggshell membrane separator (JR-800-E) showed moderate performance, with sufficient ionic mobility but slightly higher internal resistance. Meanwhile, the orange fruit membrane (JR-800-O) demonstrated the lowest performance due to its dense, non-uniform structure and limited electrolyte uptake, resulting in reduced ion transport and higher IR drop. These findings affirm that choosing a separator with high porosity, good wettability, and mechanical stability is critical to optimizing the energy storage efficiency and cycling stability of supercapacitor devices.

REFERENCES

1. Maradin, D. (2021). Advantages and disadvantages of renewable energy sources utilization. *International Journal of Energy Economics and Policy*, **11**(3), 176–183.
2. Bhattarai, H. (2022). Renewable energy and energy storage systems. *Energy Conversion: Methods, Technology and Future Directions*, 269–289.
3. Li, C., Feng, Y., & Niu, W. (2022). Optimization of microwave-assisted

hydrothermal carbonization and potassium bicarbonate. *Journal of Energy Storage*.
4. Rahman, M. M., Oni, A. O., & Kumar, A. (2020). Assessment of energy storage technologies: A review. *Energy Conversion and Management*, **223**.
5. Deshpande, A., Rawat, S., & Hotha, S. (2023). Converting renewable saccharides to heteroatom doped porous carbons as supercapacitor electrodes. *Carbon*, **214**.
6. Gür, E., Semerci, T. G., & Semerci, F. (2022). Sugar beet pulp derived oxygen-rich porous carbons for supercapacitor applications. *Journal of Energy Storage*.
7. Asti, R. D. & Putra, A. (2024). *Pengaruh Jenis Larutan Elektrolit Terhadap Sifat Elektrokimia Superkapasitor*. Program Studi Kimia, Universitas Negeri Padang, **8**.
8. Taer, E., Putri, A., & Yusra, D. A. (2021). The effect of potassium iodide (KI) addition to aqueous-based electrolyte. *Materials Today: Proceedings*, **44**.
9. Chen, Z., Wang, X., & Wang, Z. (2020). Rice husk-based hierarchical porous carbon for high performance supercapacitors. *Carbon*, **161**.
10. Zou, X., Dong, C., & Yang, H. (2023). Engineering of N, P co-doped hierarchical porous carbon from sugarcane bagasse. *Colloids and Surfaces A*, **672**, 131715.
11. Priya, D. S., Kennedy, L. J., & Anand, G. T. (2023). Effective conversion of waste banana bract into porous carbon electrod. *Results in Surfaces and Interfaces*, **10**.
12. Taer, E. & Taslim, R. (2021). Matoa Fruit peel-based Activated Carbon and its Application as an Electrode. *Journal of Physics: Conference Series*, **2049**(1).
13. Zhang, X., Han, R., & Liu, B. (2023). Porous and graphitic structure optimization of biomass-based carbon materials from 0D to 3D for supercapacitors: A review. *Chemical Engineering Journal*, **460**.
14. Hartati, S. D., Taer, E., & Taslim, R. (2016). Pengaruh variasi suhu aktivasi fisika terhadap sifat fisis dan elektrokimia elektroda karbon superkapasitor dari limbah kulit pisang. *Spektra*, **1**(2), 165.
15. Licht, F., Davis, M. A., & Andreas, H. A. (2020). Charge redistribution and electrode history impact galvanostatic charging/discharging and associated figures of merit. *Journal of Power Sources*.
16. Hu, Z., Xu, L., & Jiang, H. (2018). Comprehensive analysis of galvanostatic charge method for fuel cell degradation diagnosis. *Applied Energy*, **212**, 1321.
17. Wang, M. X., He, D., & Yang, H. (2023). Green fabrication of hierarchically porous carbon microtubes from biomass waste via self-activation for high-energy-density supercapacitor. *Journal of Power Sources*.
18. Mardiah, M. A., Awitdrus, R. F., & Taer, E. (2021). Characterization of physical properties for activated carbon from garlic skin.acitors. *J. Aceh Phys. Soc.*, **10**(4), 102.
19. Desmagrini, D., Awitdrus, A., & Farma, R. (2021). Synthesis of activated carbon electrodes from date seeds with a variety of separators for supercapacitor cell. *Journal of Aceh Physics Society*, **10**(3).
20. Taer, E., Zulkifli, Z., Sugianto, S., Syech, R., & Taslim, R. (2015). Analisa Siklis Voltametri Superkapasitor Menggunakan Elektroda Karbon Aktif Dari Kayu Karet. *Prosiding Seminar Nasional Fisika*, **4**.
21. Apriwandi, A., Taer, E., & Farma, R. (2021). Analysis of Cyclic Voltammetry dan Galvanostatic Charge Discharge Electrode Supercapacitor. *Journal of Aceh Physics Society*, **10**(4), 94–101.
22. Brousse, T., Bélanger, D., & Sugimoto, W. (2017). Materials for electrochemical capacitors. *Springer Handbook of Electrochemical Energy*, 495–561.
23. Huda, A. N., Lestari, I., & Hidayat, S. (2022). Pemanfaatan Karbon Aktif dari Sekam Padi Sebagai Elektroda Superkapasitor. *Jurnal Ilmu dan Inovasi Fisika*, **6**(2), 102–113.

IPC

Indonesian Physics Communication

Department of Physics, Universitas Riau, Pekanbaru, Indonesia
p-ISSN 1412-2960 | e-ISSN 2579-521X

Vol. 22 | No. 2
July 2025

Web: https://kfi.ejournal.unri.ac.id
E-mail: kfi@ejournal.unri.ac.id

The effect of copper doping on the structural properties and composition of iron oxide nanoparticles of Ulakan Pariaman Beach sand prepared by the ball milling method

Diny Fandriani, Erwin*
Department of Physics, Universitas Riau, Pekanbaru 28293, Indonesia

*Corresponding author: erwin.amiruddin@lecturer.unri.ac.id

ABSTRACT

This study explores the utilization of beach sand from Ulakan Pariaman as a source of iron oxide-based magnetic material through processes of separation, refinement, and copper (Cu) doping. The samples were processed using an iron sand separator (ISS) to separate iron oxide from other oxides, followed by treatment with a neodymium iron boron (NdFeB) magnet and ball milling technique with variations in milling time and ball size Cu doping was applied to compositions of $(Fe_2O_3)_{100-x}Cu_x$ where x = 0; 5; 10; 15; and 20 wt.%, to investigate changes in structural and magnetic properties. XRD characterization revealed the dominance of the spinel phase of magnetite (Fe_3O_4) and a partial transformation to maghemite (γ-Fe_2O_3) indicated by changes in peak width and intensity. XRF analysis confirmed a decrease in Fe content and an increase in Cu concentration, suggesting ionic substitution within the crystal lattice. Magnetic susceptibility with higher increasing Cu content, demonstrating a positive effect of doping on the material's magnetic response.

Keywords: Ball milling; copper dopping; iron oxide nanoparticles; magnetic susceptibility; natural sand

Received 22-05-2025 | Revised 06-06-2025 | Accepted 13-06-2025 | Published 31-07-2025

INTRODUCTION

Indonesia is a country rich in natural resources, including iron oxide minerals, which are found abundantly along the coast. Iron sand is a source of iron oxide minerals that holds significant potential in various technological applications, such as the steel industry, magnetic materials, and functional nanomaterials [1]. One area with iron sand resources is Ulakan Beach, Pariaman, West Sumatra, which has not been optimally utilized in the development of advanced nanotechnology-based materials.

Nanotechnology utilizes atoms and molecules on a much smaller scale, around 100 nanometers. One example of a highly developed nanomaterial is Fe_3O_4 nanoparticles. Iron sand has potential as a source of nanoparticles because it contains magnetic minerals such as magnetite (Fe_3O_4), hematite (α-Fe_2O_3), and maghemite (γ-Fe_2O_3). To create Fe_3O_4 nanoparticles with a homogeneous and fine grain size, several synthetic methods are used, such as coprecipitation, sol-gel, solid-state, hydrothermal, molten salts, and others [2-4]. However, to improve the performance of this material, modification is required through doping techniques with other elements, such as copper (Cu) to optimize its structural and magnetic properties.

Transition metal element doping has been widely used to improve the magnetic and electrical properties of iron oxide-based materials. Copper (Cu) is a dopant that can affect the structural and magnetic properties of iron oxide by replacing some of the Fe3+ ions in the crystal lattice, thus causing changes in the lattice parameters and crystal structure of the material [5]. According to research conducted by Chaudari (2024) [6], Cu doping in Fe_2O_3 can cause a phase change from hematite (α- Fe_2O_3) to maghemite (γ-Fe_2O_3) with a cubic crystal structure that has better ferromagnetic

properties than hematite. This phenomenon occurs due to the difference in ionic radii between Cu^{2+} (0.73 Å) and Fe^{3+} (0.64 Å), which causes lattice distortion and a decrease in crystal size [7].

In this study, copper (Cu) doping was carried out on iron oxide nanoparticles originating from Ulakan Pariaman beach sand to understand how the crystal structure and magnetic properties change.

RESEARCH METHODS

This study used natural sand from Ulakan Beach in Pariaman, West Sumatra Province. Sampling was conducted at five different locations: A, B, C, D, and E. The sampling method used a grid model at each predetermined location, with a sampling area of 1 meter × 1 meter. The distance between sampling points was set at 200 cm, and four samples were taken at each location, each weighing 1 kg, resulting in a total sample collection of 20 kg from the five locations. The natural sand samples were dried under sunlight to remove water content, facilitating the separation of magnetic and non-magnetic particles. After the samples dried, they were separated using an iron sand separator (ISS). This process separates the magnetic and non-magnetic particles. Before the samples were processed on the ISS, they were weighed to determine their mass.

The working principle is that the dried sample is slowly inserted into a vibrator that flows to a conveyor which is then carried by a belt to an electromagnetic wheel which is where the magnetic and non-magnetic particles are separated. Then the concentrate container is filled with samples containing magnetic particles while samples that do not contain magnetic particles will enter the sand container. Samples that have gone through the separation of magnetic and non-magnetic particles are the products of the ISS crushed using a BM tool for 3 hours using 18 iron balls with a diameter of 1.5 cm. This BM process aims to produce a smoother product. Samples that have gone through this process are then separated using Neodymium Iron Boron (NdFeb) magnets. This process is called the first stage of BM (Product BM1). Next, repeat the steps that have been done for the BM1 product, but with an extended time of 15 hours and using the same number and diameter of balls. Then, perform the third step, repeating steps 1 and 2 using 50 0.5 cm diameter iron balls and 18 1.5 cm diameter balls for 102 hours. Thus, the total time spent during the ball milling process is 120 hours, resulting in a very fine concentrate.

The results of this 120-hour ball milling process are separated into five parts: BM3A, BM3B, BM3C, BM3D, and BM3E. Each BM3A, BM3B, BM3C, BM3D, and BM3E product is doped with copper at varying weight percentages (%wt). BM3A was not doped 0%wt, BM3B was doped at 5%wt (0.95 grams of sample and 0.05 grams of copper), BM3C was doped at 10%wt (0.9 grams of sample and 0.1 grams of copper), BM3D was doped at 15%wt (0.85 grams of sample and 0.15 grams of copper), and BM3E was doped at 20%wt (0.8 grams of sample and 0.2 grams of copper). Furthermore, the BM3B, BM3C, BM3D, and BM3E products were Ball Milled for 20 hours, resulting in nanoparticles called BM4A, BM4B, BM4C, BM4D, and BM4E. The BM4 product was divided into three parts: BM4A with a weight percentage of 0 wt%, BM4B with a weight percentage of 5 wt%, and BM4C with a weight percentage of 10 wt%. Each product was then placed in a glass bottle for testing using a Vibrating Sample Magnetometer (VSM) and a Scanning Electron Microscope (SEM).

The coreless magnetic induction measurement used a Pasco PS-2162 probe sensor and a solenoid with 2,500 turns, measuring 3 cm in diameter and 10 cm in length. The Pasco PS-2162 probe sensor was connected to a laptop with Data Studio software installed. The coreless solenoid B0 magnetic induction measurement was performed by setting a fixed distance of 1 mm from the sensor. The Pasco PS-2162 probe was energized without inserting a sample into the

solenoid, with currents of 0.1 A, 0.2 A, 0.4 A, 0.6 A, and 0.8 Amperes. The magnetic susceptibility value is calculated by dividing the total magnetic induction (B_T) by the magnetic induction of the solenoid without a core (B_0), then dividing by the magnetic induction of the solenoid without a core (B_0).

Next, the crystallinity properties were analyzed using the X-Ray Diffraction (XRD) method on several samples, including BM4 products such as BM4A (0 wt% Cu), BM4B (5 wt% Cu), and BM4C (10 wt% Cu). Composition testing using X-Ray Fluorescence (XRF) on Ulakan natural sand and ball milled products was conducted using several BM4 product samples, namely BM4A (0 wt% Cu) and BM4B (5 wt% Cu).

RESULTS AND DISCUSSION

Solenoid Magnetic Induction Measurement

The solenoid magnetic induction was measured using a Pasco PS-2162 Probe magnetic sensor connected to a laptop with a cylindrical solenoid measuring 10 cm long (L), 3 cm in diameter (D), and 2,500 turns (N). The solenoid core measured was Ulakan Pariaman beach sand, which had been ball milled for 120 hours. The BM4 product, doped with copper (Cu), was used. The magnetic induction measurement data for the coreless solenoid (B0) with a fixed spacing of 1 mm as a function of current is shown in Figure 1.

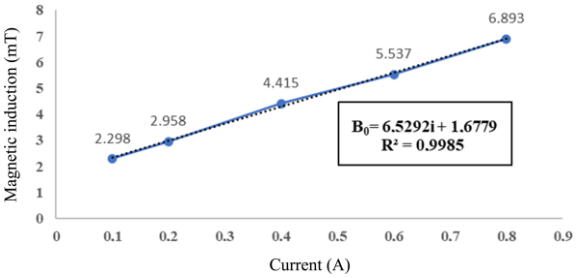

Figure 1. Graph of the coreless magnetic induction as a function of current with a fixed spacing of 1 mm.

Figure 1 shows that the magnetic induction in the solenoid increases linearly with increasing current. Based on the measurement results, the magnetic induction value at a current of 0.1 A was 2.298 mT, increasing to 6.893 mT when the current reached 0.8 A. This relationship can be represented by the linear regression equation $B_0 = 6.5292i + 1.6779$ with $R^2 = 0.9985$. When I = 0 mA, B_0 will be 1.6779 mT, indicating a very strong relationship between current and magnetic induction and following a linear pattern with a high degree of accuracy.

This is consistent with the basic concept of the magnetic field in a solenoid: magnetic induction is proportional to the flowing electric current. This increase in magnetic induction occurs because the greater the current passing through the solenoid coil, the stronger the magnetic field generated within it. This increase is consistent with the theory of magnetic induction in solenoids: if the current is increased, the magnetic induction value in each sample will increase linearly. This phenomenon has been extensively studied in modern electromagnetism studies, where various magnetic field-based applications, such as magnetic sensors and data storage devices, rely heavily on the linear relationship between magnetic induction and electric current [5].

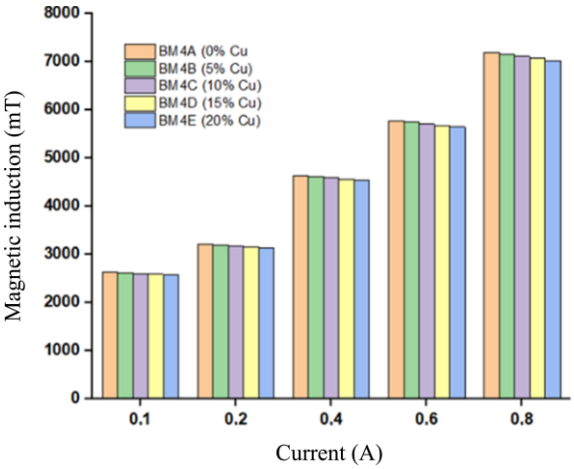

Figure 2. Magnetic induction of a solenoid with varying current and copper (Cu) doping.

Figure 2 shows the results of magnetic induction measurements of a solenoid with varying current. The magnetic induction value increases with increasing applied electric

current. It can be observed that at a current of 0.1 A, the magnetic induction value ranges from 2.583 mT to 2.633 mT, while at a current of 0.8 A, the magnetic induction value increases to approximately 7.032 mT to 7.196 mT. This increase is consistent with the magnetic field theory in solenoids, which states that the generated magnetic field is directly proportional to the applied electric current.

The effect of copper (Cu) doping on magnetic induction of the undoped Cu sample (BM4A) has the highest magnetic induction value compared to samples doped with Cu at various concentrations. In BM4A (0% Cu) with a current of 0.8 A, the magnetic induction reached 7.196 mT, while in BM4E (20% Cu), the value decreased to 7.032 mT. This decrease indicates that the addition of Cu to the Fe_2O_3 material reduces its magnetic properties. This is due to the diamagnetic nature of Cu^{2+}, which disrupts the spin interactions between the Fe^{2+} and Fe^{3+} ions in Fe_2O_3, thereby reducing the total magnetization. On an atomic scale, Cu^{2+} ions replace Fe ions in the Fe_2O_3 crystal lattice, disrupting the electron spin interactions that contribute to the material's magnetic properties.

Magnetic Susceptibility

Figure 3 show data and a graph of magnetic susceptibility values for Cu-doped copper with a current of 0.8 A, varied using Cu at different concentrations (wt.%): 0 wt.%; 5 wt.%; 10 wt.%; 15 wt.%; and 20 wt.% were ball milled for 20 hours. The magnetic susceptibility values of each sample were 4395.76×10^{-5}; 3760.08×10^{-5}; 3211.29×10^{-5}; 2617.33×10^{-5}; and 2018.87×10^{-5}. The susceptibility value for Cu doping results decreased with increasing concentration. This decrease is due to the basic nature of Cu which is a diamagnetic material. Diamagnetism in Cu arises because all of its electron orbitals are fully filled, so it does not have an intrinsic magnetic moment. When diamagnetic Cu^{2+} ions replace some of the paramagnetic Fe^{3+} ions in the Fe_2O_3 lattice, the contribution to the total magnetic moment decreases. Furthermore, the presence of Cu^{2+} ions also disrupts the spin regularity in the lattice, which further weakens the magnetic interactions between Fe^{3+} ions. Therefore, the higher the Cu doping concentration added, the lower the magnetic susceptibility value.

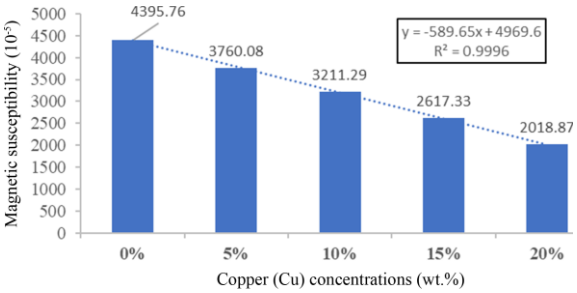

Figure 3. Graph of magnetic susceptibility values for Cu-doped copper (Cu) with a current of 800 mA.

X-Ray Diffraction (XRD) Results

Figure 4 shows the X-ray diffraction results of a BM4A sample (0 wt.% Cu), which exhibits a diffraction pattern typical of the magnetite phase (Fe_3O_4) with a cubic spinel structure. The main diffraction peaks appear at 2θ angles of approximately 28.12°, 30.12°, 33.2°, 35.36°, 43.43°, 53.19°, 56.51°, and 62.34°, which correspond to the crystal planes (012), (220), (104), (311), (400), (422), (511), and (440).

The highest peak is at an angle of 35.36° with a Miller index of (311), which is a significant peak of the main phase formed, the magnetite Fe3O4 phase. Based on calculations using the Scherrer equation, the average crystallite size for the BM4A sample is 28.93 nm with a smaller FWHM value than the other samples, namely 0.3071°. This indicates that BM4A still has high crystallinity with minimal disruption in its crystal lattice structure.

Figure 5 shows the X-ray diffraction pattern after doping with 5 wt.% Cu. There is a change in the intensity of the diffraction peaks. The main diffraction peaks appear at 2θ angles of approximately 29.82°, 35.38°, 43.58°, 53.56°, 56.68°, and 62.49°, which correspond to the (220), (311), (400), (422), (511), and (440) crystal planes, which are typical of the spinel magnetite (Fe_3O_4) structure. Several major peaks, such as (220), (311), (400), and (511),

exhibit a slight shift toward larger angles and a decrease in intensity, indicating lattice distortion due to partial substitution of Fe^{2+} ions by Cu^{2+} ions.

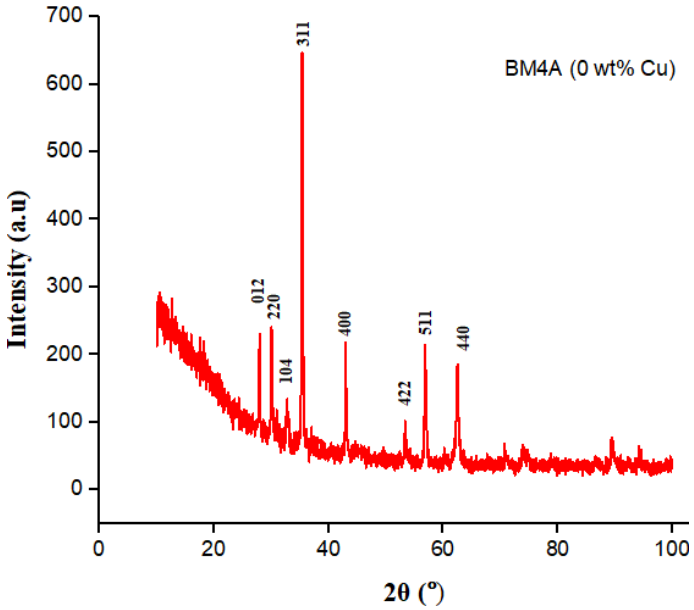

Figure 4. X-ray diffraction pattern of a BM4A sample doped with 0 wt.% Cu.

Cu doping of 5 wt.% causes an increase in the Full Width at Half Maximum (FWHM) value to 0.3365°, which contributes to a decrease in the crystallite size to 24.81 nm. This indicates that Cu doping disrupts the crystal regularity (decreased crystallinity) and amplifies the lattice distortion effect. The primary phase remains the spinel magnetite (Fe_3O_4) structure, rather than hematite (α-Fe_2O_3), as supported by the position and pattern of the diffraction peaks. This is consistent with research conducted by Kołodziej (2023) [8], which states that doping transition metal ions into iron oxide can cause changes in lattice parameters, a decrease in crystallite size, and a decrease in crystallinity due to ion size mismatch.

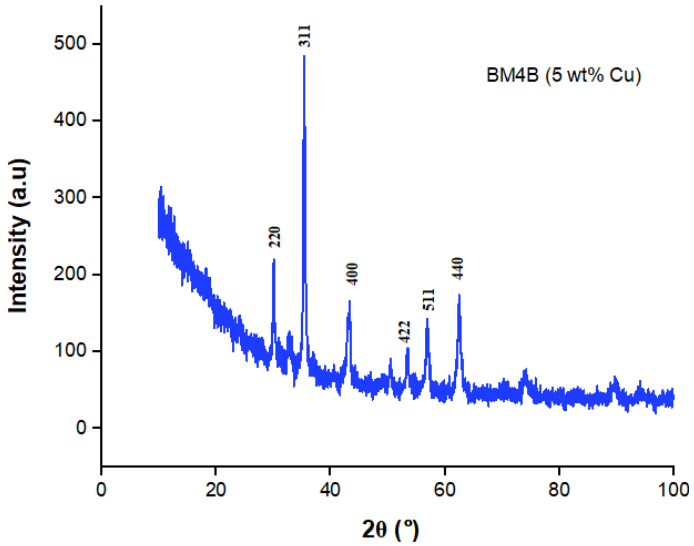

Figure 5. X-ray diffraction pattern of a BM4B sample doped with 5 wt.% Cu.

Figure 6 shows the X-ray diffraction pattern of a BM4C sample (10 wt.% Cu). The main diffraction peaks appear at 2θ angles around 30.18°, 35.42°, 43.03°, 50.78°, 53.64°, 57.25°,

and 62.74°, which correspond to the (220), (311), (400), (422), (024), (511), and (440) crystal planes, respectively, which are the reference for the $CuFe_2O_4$ spinel phase. Additionally, there are additional minor peaks around 28.10° and 32.91°, which likely indicate the emergence of minor phases such as CuO or other mixed oxides due to increased Cu doping.

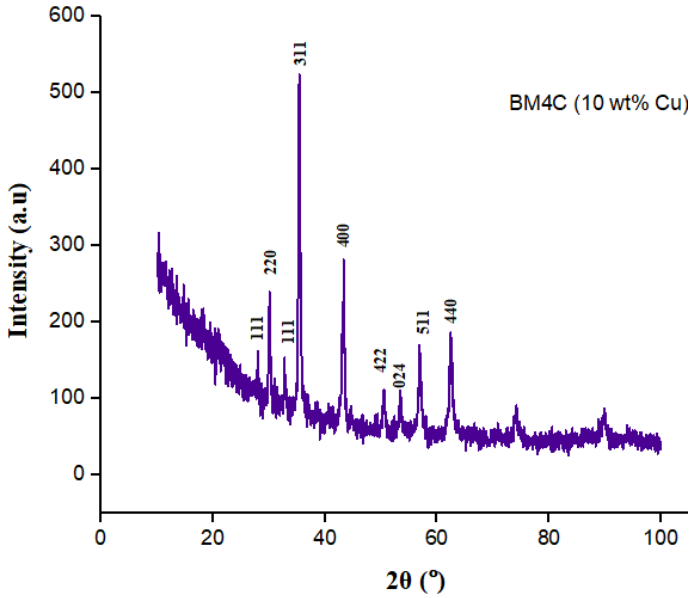

Figure 6. X-ray diffraction pattern of a BM4C sample doped with 10 wt.% Cu.

The main peaks, such as (311) and (400), shift further toward larger 2θ angles, indicating lattice distortion due to increased substitution of Cu^{2+} ions into Fe^{2+} ion positions in the spinel structure. The crystallite size of the BM4C sample decreased to 23.93 nm with a larger FWHM (0.3490°) than the BM4A and BM4B samples. The increased FWHM indicates greater imperfections in the crystal structure. The decreased crystallite size indicates decreased crystallinity due to doping. The main phase in the BM4C sample is dominated by the spinel structure (Fe_3O_4 and/or $CuFe_2O_4$).

However, the increased peak width and decreased intensity of the main peak may indicate a possible partial transformation of the structure to maghemite (γ-Fe_2O_3), which has a cubic spinel structure with high lattice defects and a diffraction pattern very similar to magnetite.

Table 1. Strongest diffraction peaks (strongest lines) for each sample.

Cu doping (wt.%)	hkl	Angle 2θ (°)	FWHM (°)	Crystalline size (nm)
0 (BM4A)	(311)	35.36	0.3071	28.93
5 (BM4B)	(311)	35.38	0.3365	24.81
10 (BM4C)	(311)	35.42	0.3490	23.93

Table 1 shows that increasing the Cu concentration increases the FWHM (Full Width at Half Maximum). The higher the FWHM, the smaller the crystallite size, and vice versa. Samples BM4A, BM4B, and BM4C have average crystallite sizes of 28.93 nm, 26.44 nm, and 25.51 nm, respectively. The smaller atomic size of Cu compared to Fe results in a decrease in crystallite size and an increase in the diffraction angle at 2θ, approximately 35°.

X-Ray Fluorescence (XRF) Results

According to Figure 7, the data obtained show that magnetic elements include Al (Aluminum), Ti (Titanium), Mn (Manganese), Fe (Iron), and Ni (Nickel). Meanwhile, non-

magnetic elements include Si (Silicon), P (Phosphorus), Ca (Calcium), S (Sulfur), Ag (Silver), and Cu (Copper). Before Cu doping, the Fe content in the sample was 74.88%. However, after doping with 5 wt.% Cu, the Fe content decreased to 69.41%, indicating that some Fe ions had been replaced by Cu in the crystal structure. Conversely, the Cu concentration increased drastically from 0.017% to 13.161%, indicating the success of the Cu doping process in the material.

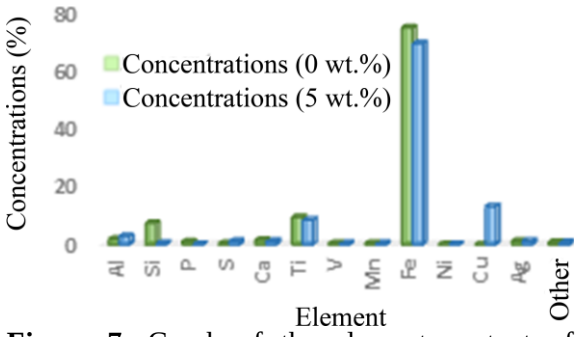

Figure 7. Graph of the element content of Ulakan Pariaman beach sand after 120 hours of multi-step ball milling and 20 hours of ball milling with copper (Cu) doping.

In addition to Fe and Cu, several other elements also experienced changes in concentration after the ball milling and doping processes. The Si content decreased drastically from 7.357% to 0.43%, indicating that most of the silicate compounds were eliminated during the milling process. Other elements, such as Al and Ni, experienced small increases, while elements such as Ti, Mn, and V experienced slight decreases. These changes can occur due to mechanochemical effects during the milling process, which cause redistribution of elements within the material and changes in its microstructure. These changes in elemental composition are also influenced by the duration of the ball milling process, which affects particle size and element distribution within the material.

CONCLUSION

The susceptibility value for Cu doping results increases with increasing concentration. The XRD characterization results show that the beach sand particles processed using ball milling have a magnetite phase (Fe_3O_4) with a cubic spinel structure, and the BM4C sample remains dominated by the spinel structure (Fe_3O_4 and/or $CuFe_2O_4$). However, the increase in peak width and decrease in the intensity of the main peak may indicate the possibility of partial transformation of the structure into maghemite (γ-Fe_2O_3), which has a cubic spinel structure with high lattice defects and a diffraction pattern very similar to magnetite. The addition of Cu doping causes a decrease in crystallite size with sizes for BM4A, BM4B and BM4C samples of 28.93 nm, 24.81 nm and 23.93 nm, respectively. The results of X-Ray Fluorescence (XRF) identification indicate that the beach sand processed using ball milling contains various elements, both magnetic and non-magnetic. Elements included in the magnetic group include Al, Ti, Mn, Fe, and Cu, while non-magnetic elements include Si, P, Ca, Ag, and other elements.

REFERENCES

1. Budiman, A. (2014). Pemetaan Persentase Kandungan Dan Nilai Suseptibilitas Mineral Magnetik Pasir Besi Pantai Sunur Kabupaten Padang Pariaman Sumatera Barat. *Jurnal Fisika Unand*, **3**(4), 242–248.
2. Oktaviani, E., Nasri, M. Z., & Deswardani, F. (2020). Sintesis dan karakterisasi nanopartikel Fe_3O_4 (Magnetite) dari pasir besi sungai Batanghari Jambi yang dienkapsulasi dengan polyethylene glycol (Peg-4000). *Jurnal Pendidikan Fisika Tadulako Online*, **8**(3), 97–103.
3. Erwin, E. & Putra, S. U. (2018). Sifat Magnetik Dan Ukuran Partikel Magnetik Serta Komposisi Material Pasir Besi Pantai Kata Pariaman Sumatera Barat Di Sintesa Dengan Iron Sand Separator Dan Ball Milling. *Journal Online of Physics*, **3**(2), 11–14.
4. Amiruddin, E., Awaluddin, A., Sihombing, M., Royka, A., & Syahrul, T. (2020).

Morphology and structural properties of undoped and cobalt doped magnetic iron oxide particles for improving the environmental quality. *International Journal of Engineering and Advanced Technology (IJEAT)*, **9**(6), 2249–8958.

5. Lassoued, A., Lassoued, M. S., Dkhil, B., Gadri, A., & Ammar, S. (2017). Structural, optical and morphological characterization of Cu-doped α-Fe2O3 nanoparticles synthesized through co-precipitation technique. *Journal of Molecular Structure*, **1148**, 276–281.
6. Chaudhari, D. S., Upadhyay, R. P., Shinde, G. Y., Gawande, M. B., Filip, J., Varma, R. S., & Zbořil, R. (2024). A review on sustainable iron oxide nanoparticles: syntheses and applications in organic catalysis and environmental remediation. *Green Chemistry*, **26**(13), 7579–7655.
7. Griffiths, D. J. (2023). *Introduction to electrodynamics*. Cambridge University.
8. Kołodziej, T., Piętosa, J., Puźniak, R., Wiśniewski, A., Król, G., Kąkol, Z., Biało, I., Tarnawski, Z., Ślęzak, M., Podgórska, K., Niewolski, J., Gala, M. A., Kozłowski, A., Honig, J. M., & Tabiś, W. (2023). Impact of hydrostatic pressure, nonstoichiometry, and doping on trimeron lattice excitations in magnetite during axis switching. *Physical Review B*, **108**(24), 245148.

IPC

Indonesian Physics Communication

Department of Physics, Universitas Riau, Pekanbaru, Indonesia
p-ISSN 1412-2960 | e-ISSN 2579-521X

Vol. 22 | No. 2
July 2025

Web: https://kfi.ejournal.unri.ac.id
E-mail: kfi@ejournal.unri.ac.id

Relation of reflectance intensity and chemical contents of oil palm fresh fruit bunches using multispectral imaging

Nisa Arpyanti, Minarni Shiddiq*, Rahmondia Nanda Setiadi, Fisal Rabin, Ihsan Okta Harmailil, Vicky Vernando Dasta
Department of Physics, Universitas Riau, Pekanbaru 28293, Indonesia

*Corresponding author: minarni.shiddiq@lecturer.unri.ac.id

ABSTRACT

Multispectral imaging has been widely used for the classification of fruits and vegetables. This technique offers both spectral and spatial resolution, enabling the evaluation of fruit quality based on its chemical properties. This study aims to analyze the relationship between reflectance intensity obtained from multispectral imaging and the chemical composition of oil palm fresh fruit bunches (FFBs), specifically oil content and free fatty acid (FFA) levels, measured using the Soxhlet extraction method. The multispectral imaging system consists of a monochrome camera and an LED light source with eight wavelengths ranging from 680 nm to 900 nm. FFB images were processed using Python scripts to extract reflectance intensity. The Python scripts were also used to analyze the correlation between reflectance intensity and both oil content and FFA levels. A total of 15 unripe and 15 ripe FFB samples were used. Correlation analysis was focused on the 780 nm wavelength due to its high reflectance intensity. The results showed that the correlation coefficient between reflectance intensity and oil content was r = -0.39 for unripe fruits and r = 0.29 for ripe fruits, while the combined data yielded a strong correlation of r = 0.92. For FFA, the correlation was r = -0.41 for unripe fruits, r = -0.34 for ripe fruits, and r = 0.72 for the combined dataset. These findings demonstrate that multispectral imaging is a promising non-destructive method for classifying the ripeness of oil palm FFBs based on oil content and FFA levels.

Keywords: Free fatty acid; multispectral imaging; oil content; oil palm fresh fruit bunch; ripeness

Received 26-05-2025 | Revised 10-06-2025 | Accepted 17-06-2025 | Published 31-07-2025

INTRODUCTION

Multispectral imaging is one of the imaging techniques widely used in the agricultural sector to evaluate fruits and vegetables. This method combines spectroscopy with traditional imaging techniques, resulting in images that possess both spectral and spatial resolution. Multispectral imaging enables the evaluation of internal characteristics of fruits across a broad range of wavelengths, including ultraviolet (UV), visible, and infrared regions. In contrast, traditional imaging is limited to a narrower spectral range, typically confined to the three visible bands: Red, Green, and Blue (RGB). The application of multispectral imaging in agriculture is extensive and includes various uses for crops, fruits, and vegetables. These applications include monitoring seed health and quality [1], detecting citrus greening disease [2], monitoring olive tree growth [3], and evaluating the ripeness of oil palm fresh fruit bunches (FFB) [4].

The prediction of chemical composition using multispectral and hyperspectral imaging has been widely applied as a non-destructive method in the agricultural sector. This approach relies on spectral information generated from the interaction between light and the sample across various wavelengths, enabling the identification and quantification of specific chemical compounds such as moisture, sugar, oil, and free fatty acids without damaging the sample. This method, commonly referred to as chemometrics, serves as an alternative to conventional techniques such as Soxhlet extraction, which are time-consuming and require skilled personnel. Several applications of multispectral and hyperspectral imaging for chemical content prediction include the

estimation of moisture, dry matter, and firmness in date cultivars [5], as well as oil content prediction in maize seeds [6].

Currently, LED (light-emitting diode)-based multispectral imaging systems are widely used due to their cost-effectiveness compared to systems utilizing filter wheels. The primary components of this system include an LED light source and a monochrome camera equipped with a lens. The LED light source consists of an array of LEDs with different wavelengths, which can be activated sequentially. This LED array replaces halogen lamps, whose light is typically filtered using color filters mounted on a filter wheel. The LEDs used in this configuration generally have narrow bandwidths but offer fast response times and allow rapid switching between wavelengths via current control. However, the spectral resolution tends to be lower due to the limited availability of LEDs at certain required wavelengths [7]. One of the advantages of using a monochrome camera is its broader sensitivity range, extending from ultraviolet (UV) to infrared (IR) regions [8].

Image processing is a critical step in multispectral imaging for evaluating fruits and vegetables. Reflectance intensity is the key parameter extracted from multispectral images. The image processing workflow begins with image calibration to correct for uneven lighting and sensor response. Calibration is performed by subtracting the object image with the white reference and black reference images. Following calibration, image segmentation is conducted to isolate the primary object from the background. After segmentation, the reflectance intensity at each wavelength is determined [9]. This reflectance intensity value represents the proportion of light reflected from the surface of the object at a specific wavelength, which can then be correlated with chemical parameters such as oil content, moisture, or free fatty acid levels.

Crude Palm Oil (CPO) is one of Indonesia's largest export commodities. The quality of CPO is significantly influenced by various factors, one of which is the quality of Fresh Fruit Bunches (FFB). A key determinant of FFB quality is the ripeness level, which is closely related to its oil content and free fatty acid (FFA) levels. The sorting and grading process of FFB in palm oil mills (POMs) is essential to ensure high-quality raw materials. However, this process is still predominantly carried out manually. Manual sorting is based on external attributes of the fruit, such as the number of loose fruits (brondolan) and changes in fruit color. This manual approach has several drawbacks, including subjectivity and operator fatigue during prolonged working periods [10]. Grading involves determining FFB quality based on internal characteristics such as oil and moisture content. This process requires skilled personnel, expensive equipment, and a significant amount of time [11]. Currently, non-destructive methods based on imaging and machine learning are being developed to enable faster and real-time sorting and grading of FFB [12].

This study aims to analyze the relationship between reflectance intensity and the chemical composition of Fresh Fruit Bunches (FFB), specifically oil content and free fatty acid (FFA) levels. The correlation between these variables is represented by the correlation coefficient. Reflectance intensity is derived from images obtained using an LED-based multispectral imaging system. Oil content and FFA levels are measured using the Soxhlet extraction method. The imaging system employs a monochrome camera and an array of LEDs with eight different wavelengths ranging from 680 to 900 nm. Python programming is utilized for image acquisition, processing, and the analysis of the correlation between reflectance intensity and chemical composition.

RESEARCH METHODS

This study utilizes an LED-based multispectral imaging system to investigate the relationship between the reflectance intensity of oil palm Fresh Fruit Bunches (FFB) and their chemical composition at two ripeness levels: unripe and ripe. The research consists of three

main stages: image acquisition, multispectral image processing, and the measurement of oil content and free fatty acid (FFA) levels. Each of these stages is interconnected and is illustrated in the flowchart presented in Figure 1.

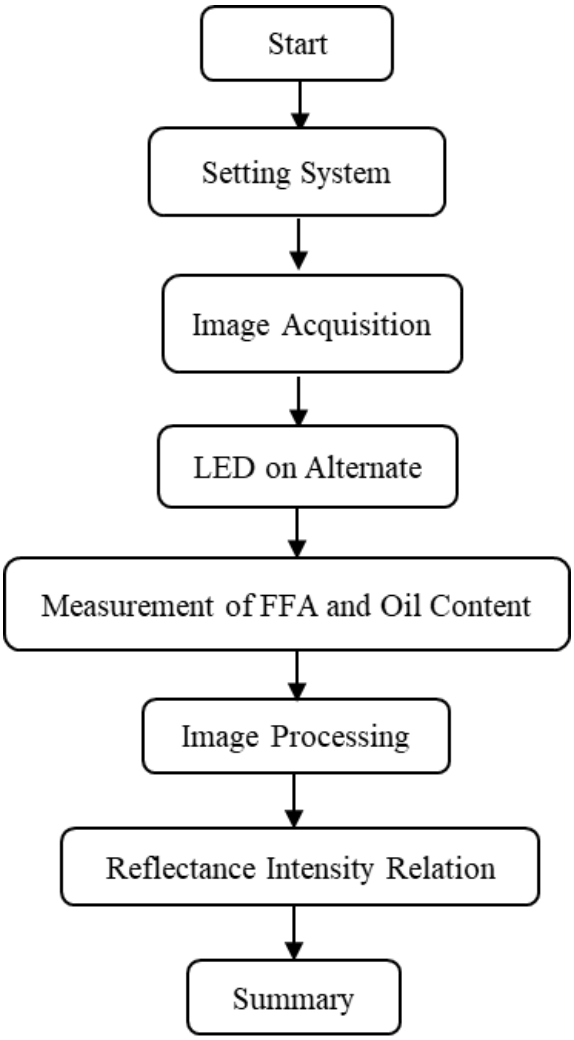

Figure 1. Research flowchart.

Image Acquisition

Figure 2 illustrates the schematic of the LED-based multispectral imaging system, which consists of a donut-shaped LED ring array with a monochrome camera positioned at the center. The LED array comprises eight different wavelengths: 680 nm, 700 nm, 750 nm, 780 nm, 800 nm, 850 nm, 880 nm, and 900 nm [13]. This LED unit replaces the conventional white light source combined with color filters, as the LEDs can be turned on and off individually using a current supply that enables rapid switching. In this study, each LED of a specific wavelength is activated sequentially, and the camera captures an image for each illumination. As a result, for every FFB sample, eight images are obtained, each corresponding to a different wavelength.

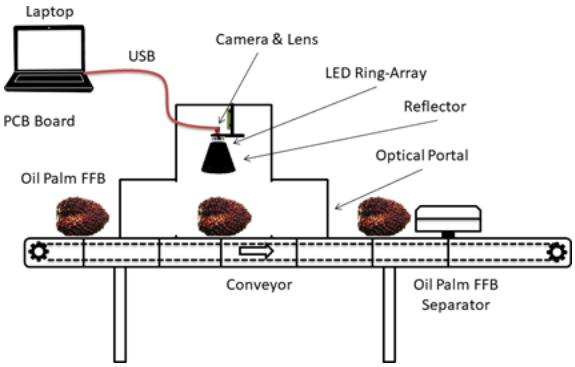

Figure 2. Multispectral imaging system.

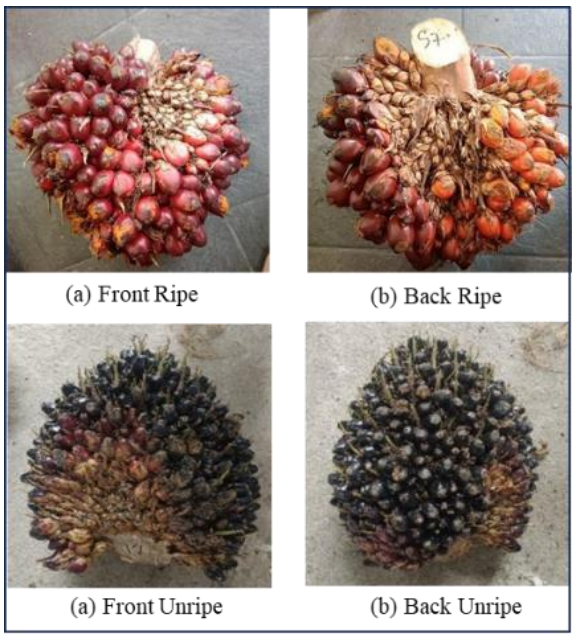

Figure 3. Oil palm fresh fruit bunches.

Figure 3 shows the FFB samples used in this study. The samples are categorized into two classes: unripe and ripe. Unripe FFB are characterized by the absence of loose fruits (brondolan) and have a dark purple to black coloration. In contrast, ripe FFB exhibit some degree of fruit detachment, with the bunch appearing reddish-yellow to orange in color. A total of 30 FFB samples were used in the study, consisting of 15 unripe and 15 ripe bunches.

Image Processing

The image processing system is divided into two components: hardware and software. The hardware consists of a laptop and USB cables that connect the camera and LED array to the laptop, allowing both to be directly controlled via an application on the computer. The laptop serves to provide commands to the camera and LEDs during the image acquisition process. On the other hand, the software component utilizes a Python-based program to process the image data captured by the camera. Image acquisition was carried out on 30 samples of oil palm Fresh Fruit Bunches (FFB), with two images taken from the front and back sides of each FFB, resulting in a total of 16 images per sample.

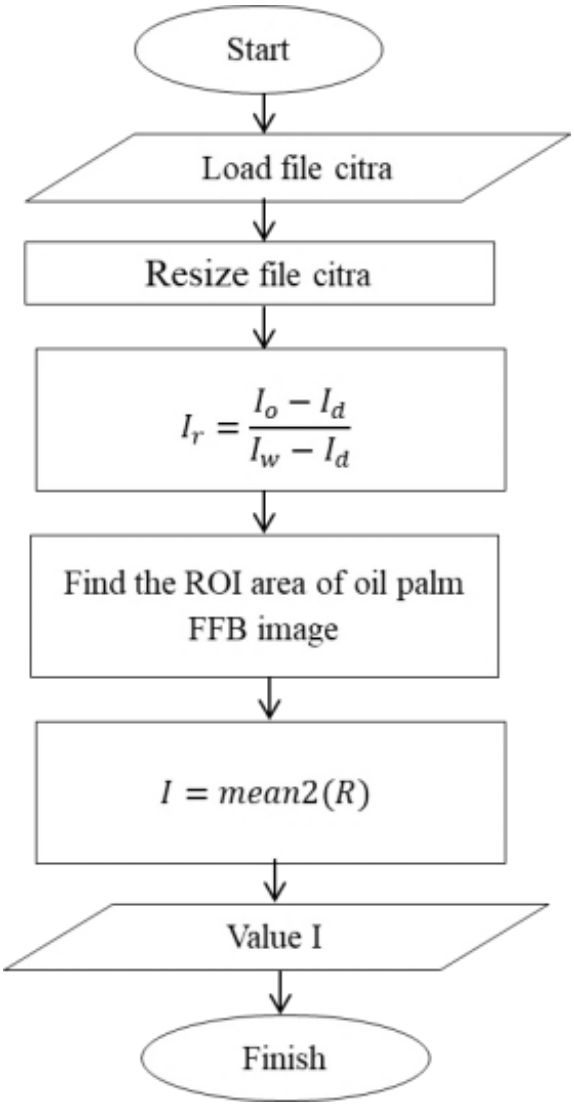

Figure 4. Oil palm fresh fruit bunches.

Multispectral image processing was performed using Python scripts following the data acquisition stage. Three types of images were processed: the sample image, the white reference, and the black reference. The white reference was used as a standard for maximum reflectance intensity, while the black reference served to eliminate the effect of dark current from the detector. These three images were then corrected and converted into an intensity matrix, which was ready for further analysis. Figure 4 was used to determine the average reflectance intensity (Ir), which was utilized in this study [14].

Chemical Content Measurement

Oil content and free fatty acid (FFA) measurements were carried out using a destructive method based on Soxhlet extraction. Since oil and FFA levels are highly sensitive to time, the measurements were performed immediately after image acquisition to maintain accuracy. The oil content measurement process began with collecting fruitlets from various parts of the Fresh Fruit Bunch (FFB), which were then peeled, ground, dried in an oven, and extracted using n-hexane solvent. The extract was then processed through Soxhlet extraction, followed by distillation, and finally weighed to obtain the oil mass. Meanwhile, FFA measurement was performed by extracting palm fiber using neutral alcohol, adding phenolphthalein indicator, and titrating the solution with a sodium hydroxide (NaOH) solution. All procedures were conducted immediately after sampling to ensure accurate and representative results for determining the ripeness level of the FFB [14].

RESULTS AND DISCUSSION

Reflectance Intensities

Multispectral image analysis was conducted on 30 Fresh Fruit Bunches (FFB) with two ripeness levels. The multispectral imaging system captured images using a monochrome

camera and an LED light source. The recorded images were then processed by applying white and black reference corrections [14]. Unripe fruits exhibit a dark purplish skin color, whereas ripe fruits display a reddish-orange hue. Figure 5 shows the average reflectance intensity of 15 unripe FFBs (blue) and 15 ripe FFBs (red) across each wavelength.

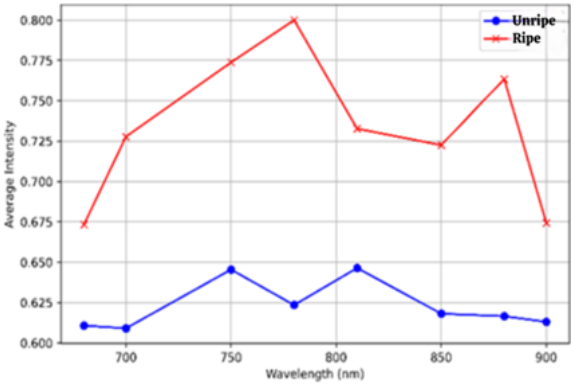

Figure 5. Average reflectance intensity at each LED wavelength for the two ripeness levels.

Figure 5 illustrates the average reflectance intensity at each LED wavelength used. Each data point represents the mean intensity derived from images of 15 FFB samples for each wavelength. Based on Figure 5, the reflectance intensity for the unripe category tends to increase at wavelengths of 750 nm and 810 nm. In contrast, the ripe category shows an increase at 750 nm, 780 nm, and 880 nm. However, both categories exhibit a decrease in reflectance intensity at wavelengths of 680 nm and 700 nm, indicating that the images at these wavelengths appear fainter compared to the others.

The interaction of infrared light with the chemical content of oil palm Fresh Fruit Bunches (FFB) influences the reflectance curve observed in Figure 5. Generally, as the fruit ripens, the red coloration produced by carotenoid compounds in oil palm increases. This indicates that the surface of ripe fruit reflects more light than that of unripe fruit. The wavelength range of 700 – 900 nm lies within the infrared spectrum, where electromagnetic waves interact at the molecular level, particularly with compounds such as anthocyanins. The anthocyanin content in ripe oil palm fruit is typically higher than in unripe fruit [15]. In the wavelength range of 680–750 nm, the reflectance intensity for both ripe and unripe samples remains relatively low. This phenomenon is likely due to the high absorption of light by chlorophyll pigments or other surface pigments found on oil palm fruit, especially in unripe samples [16].

Correlation Between Reflectance Intensity and Oil Content in Oil Palm Fruit

Based on the three graphs presented in Figure 6, the relationship between reflectance intensity and oil content is analyzed for two ripeness levels unripe and ripe as well as for the combined dataset. Figure 6 (a), which displays data exclusively for unripe fruit, reveals a negative correlation between reflectance and oil content, with a correlation coefficient of r = -0.39. This suggests that, in unripe oil palm fruit, an increase in oil content corresponds to a decrease in reflectance intensity. The internal structure of unripe fruit typically exhibits higher moisture content and denser tissue, which leads to greater absorption and multiple scattering of incident light. These optical properties result in a lower proportion of light being reflected back to the sensor [16]. From an optical standpoint, wet and complex biological tissues tend to absorb more light and produce diffuse scattering, thereby reducing coherence and directionality of reflected light [17].

Figure 6 (b) illustrates the relationship observed in ripe fruit, showing a positive correlation with a coefficient of r = 0.29. This suggests that as oil content increases, reflectance intensity also tends to increase, although the relationship is not statistically significant. The weakness of this correlation may be attributed to surface variability in ripe fruits and the non-uniform internal distribution of oil [18]. Reflectance in ripe fruit is strongly influenced by the complex interaction between light scattering and the spatial distribution of chemical compounds (such as oil and pigments), which may not follow a linear pattern.

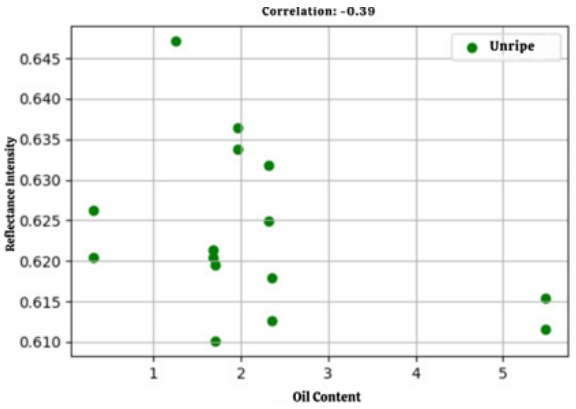

(a)

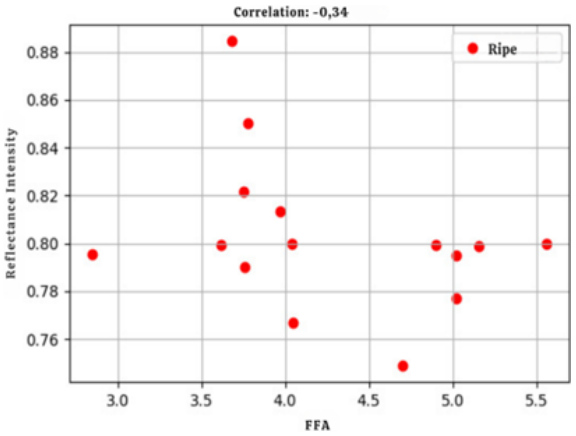

(b)

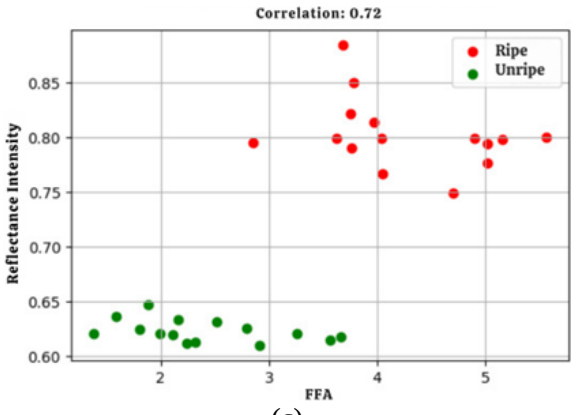

(c)

Figure 6. Correlation between relative reflectance intensity at 780 nm and oil content in oil palm fresh fruit bunch.

Figure 6 (c) presents the correlation between reflectance intensity and oil content based on the combined dataset of both unripe and ripe fruits. The result reveals a very strong positive correlation with a coefficient of r = 0.92, indicating that reflectance increases consistently with rising oil content. This phenomenon can be explained from a photonic perspective: ripe fruits with higher oil content and lower moisture levels compared to unripe ones tend to exhibit a higher internal refractive index and more organized light scattering behavior [19]. These optical characteristics lead to greater reflectance, suggesting that the accumulation of lipophilic compounds such as oil within the fruit tissue enhances reflectance at specific wavelengths.

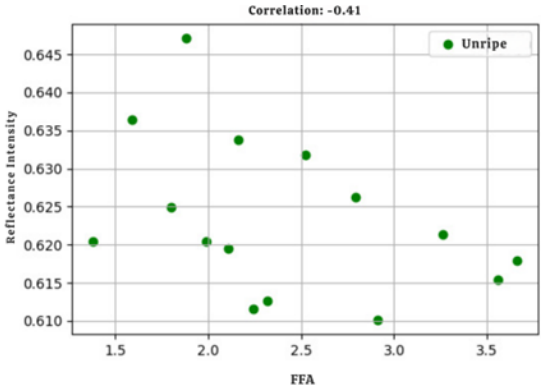

(a)

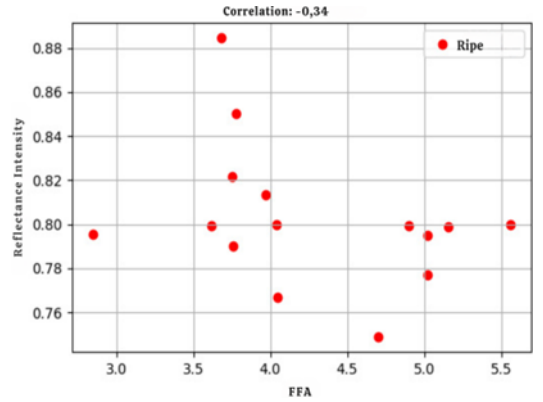

(b)

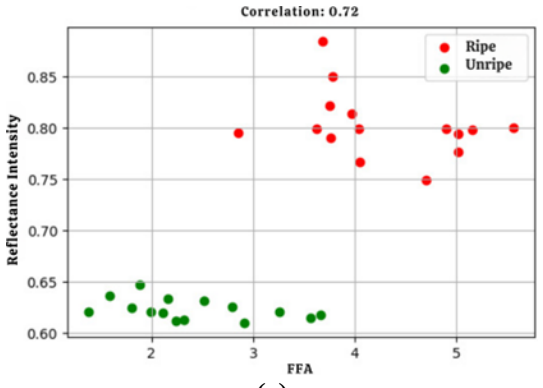

(c)

Figure 7. Correlation between relative reflectance intensity at 780 nm and free fatty acid (FFA) content.

Figure 7 represents the correlation between reflectance intensity and free fatty acid (FFA) content in oil palm fruit at different ripeness levels: unripe, ripe, and the combined dataset. Reflectance intensity refers to the fraction of light energy that is reflected back after electromagnetic waves—typically in the visible or near-infrared spectrum—interact with the surface of biological materials, in this case, the surface of oil palm fruit. Reflectance is strongly influenced by the optical properties of the fruit tissue, including the refractive index, absorption coefficient, cellular structure, and internal chemical composition.

In Figure 7 (a), which presents the data for unripe fruit, a negative correlation of r = –0.41 is observed between reflectance intensity and free fatty acid (FFA) content. This indicates that as FFA levels increase, reflectance values tend to decrease. This decline is likely due to the high moisture content and dense cellular structure of unripe fruit, which result in increased absorption coefficients and internal light scattering. The presence of hydrophilic compounds and tissue density may lead to a reduction in spectral reflectance [16].

Figure 7 (b) illustrates the relationship for ripe fruit, showing a weaker negative correlation of r = –0.34 between reflectance and FFA content. Although both unripe and ripe fruits exhibit a decrease in reflectance with rising FFA levels, the optical interaction in ripe fruit is more complex. This is due to tissue softening and elevated levels of oil and phenolic compounds, which affect light interaction within the biological matrix [19]. Phenolic compounds and lipid degradation may alter spectral absorption properties by modifying the refractive index and influencing light absorption behavior in plant tissue.

Figure 7 (c) displays the combined data from both unripe and ripe fruit, where the correlation between reflectance intensity and FFA content becomes strongly positive, with a correlation coefficient of r = 0.72. This inversion suggests a significant optical contrast between the two ripeness levels. Ripe fruits tend to have higher FFA levels and simultaneously exhibit greater reflectance, likely due to increased lipid content and reduced moisture levels, which lead to lower absorption and higher light reflectivity. In tropical fruits, high oil content can produce enhanced reflectance spectra as a result of reduced absorption in the near-infrared region.

CONCLUSION

Multispectral imaging proved effective as a non-destructive method for evaluating oil palm fresh fruit bunches (FFBs). Reflectance intensity, especially at 780 nm, showed strong correlations with oil content (r = 0.92) and free fatty acids (r = 0.72) when both ripeness levels were combined. These results highlight the potential of multispectral imaging for rapid and objective grading of FFBs in palm oil mills.

ACKNOWLEDGEMENTS

The authors would like to acknowledge DRTPM, Universitas Riau Institute of Research and Community Service (LPPM) and PTPN V Indonesia for supporting this study. This study was funded by DRTPM under Research Grant with contract number of 157/E5/PG.02.00.PL/2023.

REFERENCES

1. ElMasry, G., Mandour, N., Al-Rejaie, S., Belin, E., & Rousseau, D. (2019). Recent applications of multispectral imaging in seed phenotyping and quality monitoring—An overview. *Sensors*, **19**(5).
2. Chang, A., Yeom, J., Jung, J., & Landivar, J. (2020). Comparison of canopy shape and vegetation indices of citrus trees derived from UAV multispectral images for characterization of citrus greening disease. *Remote Sensing*, **12**(24), 4122.
3. Jurado, J. M., Ortega, L., Cubillas, J. J., & Feito, F. R. (2020). Multispectral mapping on 3D models and multi-temporal monitoring for individual characterization of olive trees. *Remote Sensing*, **12**(7).

4. Shiddiq, M., Herman, H., Arief, D. S., Fitra, E., Husein, I. R., & Ningsih, S. A. (2022). Wavelength selection of multispectral imaging for oil palm fresh fruit ripeness classification. *Appl. Opt.*, **61**.
5. Ibrahim, A., Alghannam, A., Eissa, A., Firtha, F., Kaszab, T., Kovacs, Z., & Helyes, L. (2021). Preliminary study for inspecting moisture content, dry matter content, and firmness parameters of two date cultivars using an NIR hyperspectral imaging system. *Frontiers in Bioengineering and Biotechnology*, **9**.
6. Zhang, L., Wang, Y., Wei, Y., & An, D. (2022). Near-infrared hyperspectral imaging technology combined with deep convolutional generative adversarial network to predict oil content of single maize kernel. *Food Chemistry*, **370**.
7. Monsalve, M. A. T., Osorio, G., Montes, N. L., Lopez, S., Cubero, S., & Blasco, J. (2020). Characterization of a multispectral imaging system based on narrow bandwidth power LEDs. *IEEE Trans. Instrum. Meas.*, **70**, 1–11.
8. Crowther, J. (2022). Monochrome camera conversion: Effect on sensitivity for multispectral imaging (Ultraviolet, Visible, and Infrared). *Journal of Imaging*, **8**(3), 54.
9. Jia, B., Wang, W., Ni, X., Lawrence, K. C., Zhuang, H., Yoon, S. C., & Gao, Z. (2020). Essential processing methods of hyperspectral images of agricultural and food products. *Chemometrics and Intelligent Laboratory Systems*, **198**.
10. Lai, J. W., Ramli, H. R., Ismail, L. I., & Wan Hasan, W. Z. (2023). Oil palm fresh fruit bunch ripeness detection methods: A systematic review. *Agriculture*, **13**(1), 156.
11. Tantanawat, T., Srimongkol, S., Yuttawiriya, R., Haewchin, A., Sangkapes, T., & Hattha, E. (2020). Development of a method for measuring oil content in oil palm mesocarp using a single-outlet piston press: a feasibility study. *Journal of Food Measurement and Characterization*, **14**(1).
12. Mansour, M. Y. M. A., Dambul, K. D., & Choo, K. Y. (2022). Object detection algorithms for ripeness classification of oil palm fresh fruit bunch. *International Journal of Technology*, **13**(6), 1326–1335.
13. Rabin, M. F., Shiddiq, M., Setiadi, R. N., Harmailil, I. O., Ramdani, R., & Permana, D. (2024). Classification of maturity levels of oil palm fresh fruit bunches using LED-based multispectral imaging methods and principal component analysis. *Indonesian Physics Communication*, **21**(1), 91–98.
14. Husein, I. R., Ningsih, S. A., & Alfahrezi, G. (2023). Oil Content and Free Fatty Acid Prediction of Oil Palm Fresh Fruit Bunches Using Multispectral Imaging and Partial Least Square Algorithm. Proceedings of the 4th International Seminar on Science and Technology (ISST 2022), **7**, 143.
15. Sinambela, R., Mandang, T., Subrata, I., & Hermawan, W. (2020). A ripeness study of oil palm fresh fruit at the bunch different positions. *Jurnal Keteknikan Pertanian*, **8**.
16. Ningsih, S. A., Shiddiq, M., Arief, D. S., & Husein, I. R. (2020). Pengunaan pencitraan multispektral pada panjang gelombang 520 nm dan 800 nm untuk mengevaluasi tingkat kematangan TBS kelapa sawit. *Komunikasi Fisika Indonesia*, **17**(3), 144.
17. Setiawan, A. W., Mengko, R., Putri, A. P. H., Danudirdjo, D., & Ananda, A. R. (2019). Classification of palm oil fresh fruit bunch using multiband optical sensors. *International Journal of Electrical and Computer Engineering*, **9**(4), 2386.
18. Azmi, M. H. I. M., Hashim, F. H., Huddin, A. B., & Sajab, M. S. (2022). Correlation study between the organic compounds and ripening stages of oil palm fruitlets based on the Raman spectra. *Sensors*, **22**(18).
19. Ali, M. M., Hashim, N., & Hamid, A. S. A. (2020). Combination of laser-light backscattering imaging and computer vision for rapid determination of oil palm fresh fruit bunches maturity. *Computers and Electronics in Agriculture*, **169**.

IPC

Indonesian Physics Communication

Department of Physics, Universitas Riau, Pekanbaru, Indonesia
p-ISSN 1412-2960 | e-ISSN 2579-521X

Vol. 22 | No. 2
July 2025

Web: https://kfi.ejournal.unri.ac.id
E-mail: kfi@ejournal.unri.ac.id

Bioelectricity and biomagnetism as keys to realization of neurotechnology

Erwin, Erman Taer, Afrinal Afrinal*
Department of Physics, Universitas Riau, Pekanbaru 28293, Indonesia

*Corresponding author: afrinal6742@grad.unri.ac.id

ABSTRACT

The importance of bioelectricity and biomagnetism in neurotechnology has been outlined in this study. There are three main processes in neurotechnology, namely: signal delivery, data storage and data processing. These neurotechnological processes require three essential things, namely measurements, tools and materials. This scientific study describes the form of signal delivery in neurotechnology, the form of data storage and the form of data processing. The measurement methods that can be applied have also been described along with the tools and materials. Bioelectricity plays a very important role in building neurotechnology. Meanwhile, biomagnetism is an important aspect that cannot be separated from the phenomenon of bioelectricity which also supports systems in neurotechnology. The phenomena of bioelectricity and biomagnetism in neurotechnology are described in this study along with measurement devices and materials. Measuring devices and materials must be modified as conditions permit in their working conditions. It has also been studied that natural neurotechnological data storage in living creatures is through muscle memory, signal delivery occurs in the form of bioelectricity and data processing is a combination of data delivery and storage. This study also examines the future prospects of neurotechnology along with its moral aspects.

Keywords: Bioelectricity; biomagnetism; muscle memory; neurotechnology

Received 19-05-2025 | Revised 03-06-2025 | Accepted 10-06-2025 | Published 31-07-2025

INTRODUCTION

Neurotechnology is a research area that is currently and actively being developed. This is considering the possible benefits that can be exploited from this research field; starting from the fields of medicine, health, defense and security, agriculture, communications and information, to the development of science and technology. In the medical field, brain and nervous disease and disorders can be reduced by the use of this technology; This also includes the treatment of Parkinson's disease, epilepsy, depression, obsessive compulsive disorder (OCD), acute headaches, chronic pain, high blood pressure, diabetes, rheumatoid arthritis and chronic colitis [1]. It is impossible to analyze all the potential benefits of this technology in detail, but it is worth noting that neurotechnology provides opportunities for the treatment of previously incurable diseases with new and better methods, and also increases human capacity; and through integration with artificial intelligence (AI), machines will be able to combine large amounts of information and make decisions very quickly and can improve the quality of resulting decisions [2].

The first documented event of bioelectricity was recorded in an Ancient Egyptian hieroglyph around 4000 BC which tells about the electrical properties of the scabbard fish; to Ragnar Granit who was a pioneer of bioelectromagnetism who received the Nobel Prize in 1967 [3]. Luigi Galvani in 1794 (De Viribus Electricitatis in Motu Musculari) demonstrated electrical phenomenon in animals by conducting electrical experiments on dead frog legs and finding the frog's legs twitching; bioelectricity research continues to be developed by scientists including Emil du Bois-Reymund [4], EJ Lund [5], HS Burr [6] to Lionel Jaffe and Richard Nuccittelli [7-9]. Luigi Galvani (1791) was the first physicist to observe electrical signals in animal tissue; Hodgkin and Huxley (1952) succeeded in measuring the membrane potential of squid

axons; Neher and Sakmann laid the foundation for the study of ion channels in cell membranes [10]. Bioelectricity has experienced a very long and continuous period of development until now. Its application in the health and medical fields continues to be explored for use for the benefit of society.

The early period of biomagnetism began with the work of Baule and McFee (1963) in measuring magnetic fields in the human heart; then continued with the use of SQUID (Superconducting Quantum Interference Device) by Ed Edelsall, David Cohen and Jim Zimmerman [11]. SQUID is an ideal way of biological research, for example investigating neural activity in the brain [12]. Biomagnetism is an interdisciplinary research field that aims to understand the modulation, image, repair of human organs with internal and external magnetic fields; in the past few decades, biomagnetism has grown rapidly and its applications have expanded from the diagnosis of neural or heart disease to efforts to understand the basic mechanisms of the human brain and heart [13]. This scientific discipline provides prospects for researchers to profile and investigate the working properties of the human brain and nervous system with the aim of developing neuroscientific understanding. Very complex investigations are involved in this line of research. Detailed understanding and adequate measurement are absolute conditions necessary to ground neuroscience in neurotechnological applications.

The two foundations of Indonesia's development progress are schools and hospitals [14]. These two foundations can be considered as the basis for the progress of a nation in general. School can be interpreted as the development of science and technology. Hospitals can be interpreted as efforts to improve the quality of public health. These two basics of progress have one main goal, namely realizing social welfare. Neurotechnology is one aspect that can be empowered to make this happen.

The rate of environmental degradation is increasing across the globe; Environmental change occurs at a faster pace than previously thought [15]. This bad condition will be followed by a series of other unexpected problems. Scarcity of natural resources and socio-economic problems are real consequences that can occur if the situation gets worse. The population growth rate shows significant figures from year to year [16]. After a period of rapid population growth, demographers predict that world population will peak by the end of the century [17]. An increase in number of people means an increase in the need for food, water, housing, energy, health services, transportation and many others; also, all consumption contributes to ecological destruction, increased conflict, and carries a greater risk of being impacted by wide-scale disasters such as pandemics [18]. If this condition is not immediately addressed, the situation the world will get worse and reach a condition where the damage cannot be minimized or even repaired.

An estimated 16% of the world's population experiences significant disability; people with disabilities are at risk of depression, asthma, stroke, obesity or poor oral health ; people with disabilities experience many injustices in the health sector [19]. Various methods have been used to overcome this problem, but often the improvements have not been significantly positive. More effective alternatives are needed to overcome this unpredictable and very undesirable problem.

An important point that must be stated is the enriching capabilities of neurotechnology that can transform the contents of the mind into material form which then provides the ability to cross the divide between “things that are possible and things that are actually” [20]. This implies the infinity of neurotechnological possibilities because human thought is limitless. With this infinite potential, it becomes energy to not only create new innovations in society, but also provide new discoveries that are very useful for life. So that the realization of the two basic principles of Indonesia's progress, overcoming environmental damage,

anticipating population problems and solutions to human disability problems, is not impossible.

This study aims to provide ideas, motivation and directions for efforts towards neurotechnology applications. The realization and rationalization of the objectives of this study lie in the process of measuring and analyzing two main aspects, namely bioelectricity and biomagnetism.

RESEARCH METHODS

The following research uses analysis and literature review methods, both digital, manual and audio-visual; and supported by Wolfram Mathematica® 9 software on the Microsoft Windows® platform (64-bit).

The postulation of a neuroscientific memory function formula was carried out by reviewing several available literature and data and referring to the general characteristics of human memory.

Simple analogies such as computer systems, games of throwing and catching a ball and reflex movements are also used to provide visualization of neurotechnological processes.

The measurement devices, tools and materials used in neurotechnology studies are described with reference to the latest research results.

RESULTS AND DISCUSSION

Key Processes of Neurotechnology

Digital computers built from mechanical elements or electrical binary elements (for example, switches) not only perform computational functions, but also provide a prototype or model for the study of neural transmission and neural switching [21]. By using a computer mechanism as a prototype, it can be seen that there are three main processes involved, three main processes which are also the main processes in neurotechnology, namely: signal delivery, data storage and data processing. If we refer back to the computer mechanism model, when the computer is turned on and word processing software is run, a user can type "A" on the keyboard and almost immediately the monitor displays "A". The stroke or signal "valued" with the letter A is sent from the keyboard into the computer's "brain" system. Then the computer's "brain" system will process ("think") the data, and transmit its decision to the monitor with display "A". Next, the data containing the letter "A" will be stored in the computer's memory system, the user can give a save command input signal to the computer using the keyboard and mouse and the computer's brain will decide to save the data in its memory so that the data can be remembered (opened) again later.

When two people play catch and throw a ball or someone accidentally steps on a thumbtack in the street, all of this involves three main neurotechnological processes [22]. In the game of throwing and catching the ball, when the ball is headed towards player 1, his eyes will receive a signal of the ball's arrival, this signal is transmitted by the eye's nervous system to the brain, then the brain will process (think about) this data or signal, the decision signal will be sent to the entire movement system player 1 (hands, feet, body position, back muscle position, etc.) to catch the ball that is heading towards him. When someone accidentally steps on a thumbtack on the road, a signal of injury to the foot will be sent to the reflex system to immediately lift the foot, and also sent to the brain; the brain then gives the command to the mouth to shout “Ouch!” and eyes to see objects that signal injury to the foot. These two models are highly simplified cases of very complex real events, but provide sufficient visualization of the three main neurotechnological processes.

The processes responsible for transmitting signals are action potentials, synaptic transmission and neurotransmitters [23]. Action potentials are sometimes also called spikes, nerve impulses or discharges.

Data storage occurs in a mechanism called muscle memory. Muscle memory is a form of procedural memory that involves the consolidation (use of several) specific motor

tasks into memory through repetition, which has also been used as a synonym for the term motor learning [24, 25]. When you hear the term muscle memory, the image that comes to mind is the condition of muscles that are able to remember certain movements, such as dribbling the ball in soccer or playing the song Happy Birthday on the piano [26]. Neuroscientifically, the entire process of storing data (or storing memories) in humans and vertebrates occurs through the muscle memory process.

In general, the storage memory of a data storage device, such as a flash disk, is directly proportional and is a linear function of the memory/storage capability of the material [27-29]. Brain storage memory for each individual depends on each individual's memory abilities [30]. Exceptional memory depends on genetics, brain development and experience [31, 32]. The recall curve throughout life varies in the form of a normal curve/normal curve deformed over time [33, 34]. Normal and pathological aging affects neural data at different levels and profoundly affects the mind and brain [35]. Episodic memory and working memory decline with age [36]. The frequency of repetition (attempts to repeat) is very important in reproducing a content (memory) [37]. The exponential learning (remembering effort) equation indicates a slowly decreasing increase, is one of the equations that describes the learning (or remembering) process [38]. The learning curve shows that the performance percentage is a deformed exponential function of the amount of effort exerted in the learning process [39]. A family of curves can be expressed in terms of differential equations [40]. Meanwhile, differential equations can be solved using the variable separation method [41].

The function of neuroscientific memory can be postulated [42] as follows:

$$\mathrm{M}_e(\beta, W, t) = \mu(\beta).m(W).T(t) \quad (1)$$

$$\mathrm{A}\,\beta\,\mu'(\beta) + \mu(\beta) = 0 \quad (2)$$

$$B\,m'(W) + m(W) = 0 \quad (3)$$

$$T''(t) + C.(t - D)\,T'(t) + E.T(t) = 0 \quad (4)$$

M*e*(*β*, *W*, *t*) is a function of neuroscientific memory. M*e* ≥ 0,M*e* ∈ R. *β* s the ability to remember of the subject/object/material. W represents all effort, energy and ways to "learn" or store data. *t* is time. *β*, *W*, *t* ≥ 0; *β*, W, *t* ∈ R. And also *μ*, *m*, *T* ≥0; *μ*, *m*, *T* ∈ R. A, B, C, D and E are corresponding constants. The accent marks in Equations (2) to (4) indicate the first and second derivatives of the function, respectively.

Data storage in neuroscience is very different from computer systems. In computer systems, data is stored on the hard disk in the form of magnetic domains, whereas in neuroscience or neurotechnology, data is stored through a process called muscle memory. In the brain, when forming memories, neurons make new proteins and expand the network of neurons and synapses that make neurotransmitters work efficiently; and there is no single location where all memories are stored, different parts of the brain store different memories, when a memory is recalled this part of the memory works together with other parts to produce a consolidated memory [43]. The network of connections (like cables) in the brain is always changing, when new memories are formed, the number of synapses increases thereby increasing the number of connections in the brain [44].

The computer system "thinks" (processes data) with a central processing unit (CPU) which contains a microprocessor. Humans think (process data) with their brains, which are composed of neurons. This data processing occurs when there is activity of neurons in the brain which is indicated by phenomenon of fire up/light up/ignition in parts of the brain [45]. Data processing in neuroscience and neurotechnology is not as simple as that in computer systems. Neuroscience cannot answer questions such as contemplation, affection, innovation, desires, morality, preferences and so on, all of which are examples of states when

the brain processes data. In other words, neuroscience is unable to explain why neurons activate in the way they do when the subject experiences these things; and what causes the human brain to be capable of contemplation, compassion, innovation, desire, morality, preferences and so on? This question cannot be answered by science but can be answered by philosophy; After all, science begins with philosophy, so the use of philosophy in analyzing this problem is a justifiable and valid scientific process.

Humans can live because they are given a spirit or life by God [46]. God gave reason to man, it is reason that is his guardian and that controls him [47, 48]. Humans are moved by a force called will [49]. So that what causes man to reflect, innovate and do contemplation on himself is his spirit (life), will and reason. This is also one of the proofs of God's existence.

To analyze and study the main processes in neurotechnology three very important things are needed, namely: measurements, equipment or instruments, and materials/objects/subjects of measurement. Measurements, equipment /instruments, and materials/objects/subjects must be properly modified and conditioned according to the working conditions.

The application of a technology can be realized if each element that makes up the technology has been measured sufficiently and the performance of the technology has also been measured sufficiently. The same applies to neurotechnology.

Bioelectricity for Neurotechnology

One of the main processes of neurotechnology is signal transmission. Neurons communicate with each other through electrochemical processes [44]. As a result, bioelectricity has become an integral part of neurotechnology.

In electricity there are quantities such as electric current, electric potential, energy, resistance, inductance and capacitance [50]. The semiconductivity character of a material must also be a concern, because integrated circuits can be made into electronic neuron models [3]. The electronic quantities of action potentials, synaptic transmission and neurotransmitters must also be measured. Neurons and neurotransmitters must be characterized. Characterization methods that can be used include: optical microscope, Ultraviolet-Visible (UV-Vis), Fourier-Transform Infrared Spectroscopy (FTIR), Photoluminescence (PL), Wavelength-dispersive X-ray Spectroscopy (WDXS), Dynamic Light Scattering (DLS).), Dielectric Thermal Analysis (DETA) [51], Electrochemical Impedance Spectroscopy (EIS) [52], and analytical chemistry [53].

Organic material as measurement material can be giant squid nerves [54]. Animals such as cockroaches and frogs can also be used as measurement material [55]. Places that can be sources of measurement material: slaughterhouses, fish markets and places selling fishermen's catches, people's markets, agricultural land, houses, livestock and others. For squid nerve material, the voltage clamp method can be used [56]. For noninvasive measurements , human subjects can be used using a bioelectrical signal recording device (electromyography) with modeling represented in the Hodgkin-Huxley equation, which is an approximation of electrical activity in neurons [57]. To extract the electrical dimensions of the specimen quantitatively, glass microelectrode techniques (invasive), the vibrating voltage probe (noninvasive), the vibrating ion-selective microelectrode (noninvasive), and studies using fluorescence (somewhat invasive) are used. Electroencephalogram (EEG) is a testing technique that measures electrical activity in the brain, this equipment can be used to study the brain electrically [58].

Biomagnetism for Neurotechnology

One of Maxwell's equations [59] is stated as:

$$\nabla \times \mathbf{B} = \mu_0 \boldsymbol{J} + \mu_0 \epsilon_0 \frac{\partial \boldsymbol{E}}{\partial t} \quad (5)$$

Descriptively, this equation states that changes or spatial variations in a magnetic field will produce a current density along with an electric field that changes from time to time. This principle can be used as a method for imaging brain biomagnetism (brain imaging). Hippocampal theta oscillations are one important aspect of brain imaging that utilizes biomagnetism. Hippocampal theta oscillations are a key brain signal that indicates various aspects of cognition and behavior including memory and spatial navigation [60]. Despite this, human hippocampal recordings still show divergent theta correlations to memory formation [61].

There are several brain imaging techniques including Computed Axial Tomography (CAT), Magnetic Resonance Imaging (MRI), Positron Emission Tomography (PET), Single-photon Emission Computed Tomography (SPECT), Cranial Ultrasound, Functional Magnetic Resonance Imaging (fMRI), Diffuse Optical Imaging (DOI), Event-related Optical Signal (EROS), Magnetoencephalography (MEG), Functional Ultrasound Imaging (fUS) and Quantum optically-pumped magnetometer [62]. One popular technique is MEG which utilizes a detector called SQUID (Superconducting Quantum Interference Device) [63].

If the bioelectricity and biomagnetism of the brain have been quantized, mapped and measured well and sufficiently; then the road to neurotechnology applications will be wide open.

Neurotechnology Prospects

Using two basic references to Indonesia's progress, the direction of development and prospects for neurotechnology are divided into two main paths, namely the science and technology path and the path to improving the quality of public health.

On the path of science and technology, neurotechnology can present the prospect of a Brain-Computer Interface (BCI) that enables Radical Closure, the "creation" of objects through thought, Id-Machines (a technology that gives substantial reality to humans' deepest hopes and fantasies), and communication technology between mind [20]. Radical Closure means disconnected from the environment, but open to diagrams, or to other realities, or to nothingness [64].

Neurotechnology uses the knowledge and tools of mathematics, physics, chemistry, biology and engineering to help reduce the burden of brain-related diseases [65]. Neuroscientists apply a wide range of scientific disciplines including anatomy, biochemistry, computer science, pharmacology, physiology, psychology and zoology [66]. However, neurotechnology will require other scientific disciplines in its development, such as philosophy, law, related social sciences, materials science, and brain surgery.

On the pathway to improving the quality of public health, neurotechnology can be used as a means of examination (e.g. neuroimaging and thermography) and also intervention (e.g. transcranial stimulation, implants, brain-machine interfacing); and its use to gain knowledge about the function of the human nervous system, especially to understand the processes involved in health and disease [67]. Neurotechnology includes a variety of devices, algorithms and methodologies that can monitor or modulate neural activity, including nerve stimulators, brain implants and bioprostheses ; This technological capability provides a capable device for carrying out targeted therapies for sufferers of neurological disorders [68].

Ian Burkhart has been a test subject for a BCI designed to control simulated muscles; a device was inserted into his brain through a surgical procedure, resulting in Ian being able to move his fingers just by thinking about it [69]. Neurotechnology has been proven to have enormous potential to improve the lives and well-being of people affected by paralysis, neurological disorders, mental illness and depression [70]. In recent years, developments in neurotechnology have opened up new opportunities for people with disabilities, promising to improve quality of life and promote inclusivity [71]. The prospect of

neurotechnology in improving the quality of public health is very real.

Neurotechnological Morality

Neuroethics is a study of the implications of neuroscience on human self-understanding, ethics and policy [72]. In addition, neuroethics is also an interdisciplinary field that focuses on ethical issues caused by increasing understanding of the brain and the ability to monitor and influence it [73]. There are two big categories regarding neuroethics issues, namely something that comes from what can be done and something that comes from what is known [74, 75]. Something that comes from what can be done is all the efforts, techniques, methods and experiments that can be done; such as neuroimaging, psychopharmacology, brain implants, brain-machine interfaces and others. Meanwhile, something that comes from what is known includes behavior, personality, consciousness and a state of spiritual transcendance. Neuroethics then becomes the basis for dealing with the moral principles of neurotechnology.

Learning from the broad spectrum of problems that have emerged after the presence of smartphone technology, neurotechnology morality will be categorized into Artificial Intelligence (AI) morality, individual morality of technology users, social morality of technology users and a combination of the three. The moral field is the field of human life seen from the aspect of goodness as a human being, while the actual moral attitude is called morality [76]. AI morality, the individual morality of technology users and the social morality of technology users must be adjusted to the norms that apply in that society. There are five norms that apply in Indonesian society, namely religious norms, legal norms, customary norms, moral norms and civility norms. Neurotechnological morality must be able to include these five norms.

CONCLUSION

There are three main processes of neurotechnology, the three are signal delivery, data storage and data processing. Contemplation is one example of data processing that neuroscience cannot explain. It has been shown that philosophy is also involved in the analysis of Neuroscience and neurotechnology. Neurotechnological applications can be realized when the bioelectricity and biomagnetism of the brain have been properly quantized, mapped and measured. Neurotechnology has enormous prospects for Indonesia's progress. Neurotechnological morality must include the five norms that apply in Indonesian society.

REFERENCES

1. Stieglitz, T. (2021). Why Neurotechnologies? About the Purposes, Opportunities and Limitations of Neurotechnologies in Clinical Applications. *Neuroethics*, **14**(1), 5–16.
2. Beck, S. (2021). *Diffusion on Both Ends: Legal Protection and Criminalisation in Neurotechnological Uncertainty*. In Clinical Neurotechnology meets Artificial Intelligence: Philosophical, Ethical, Legal and Social Implications, 127–139, Cham: Springer International Publishing.
3. Malmivuo, J. & Plonsey, R. (1995). *Bioelectromagnetism: Principles and Applications of Bioelectric and Biomagnetic Fields*. New York: Oxford University Press.
4. Finkelstein, G. (2013). *Emil du Bois-Reymond: Neuroscience, Self, and Society in Nineteenth-Century Germany*. Boston: MIT Press.

5. Lund, E. J. (1947). *Bioelectric Fiends and Growth*. LWW, **64**(3), 253, Austin: University of Texas Press.
6. Burr, H. S. & Northrop, F. S. C. (1935). The Electro-Dynamic Theory of Life. *The Quarterly Review of Biology*, **10**(3), 322–333.
7. Frayer, J. (2023). *The History of Using Bioelectricity in Medicine*. URL Access: https://www.rst sanexas.com/blog/the-history-of-using-bioe lectricity-in-medicine/
8. Jaffe, L. F. & Nuccitelli, R. (1974). An Ultrasensitive Vibrating Probe for Measuring Steady Extracellular Currents. *The Journal of Cell Biology*, **63**(2), 614–628.
9. Nuccitelli, R. (1995). Endogenous Electric Fields Measured in Developing Embryos. *Advances in Chemistry*, **250**. 109–124.
10. Park, S. H., Kim, E. H., Chang, H. J., Yoon, S. Z., Yoon, J. W., Cho, S. J., & Ryu, Y. H. (2013). History of Bioelectrical Study and the Electrophysiology of the Primo Vascular System. *Evidence-Based Complementary and Alternative Medicine*, **2013**(1), 486823.
11. Cohen, D. (2004). Boston and the History of Biomagnetism. *Neurology and Clinical Neurophysiology*, **114**, 1–4.
12. Sternickel, K. & Braginski, A. I. (2006). Biomagnetism Using SQUIDs: Status and Perspectives. *Superconductor Science and Technology*, **19**(3), S160.
13. Im, C. H., Jun, S. C., & Sekihara, K. (2017). Recent Advances in Biomagnetism and its Applications. *Biomedical Engineering Letters*, **7**(3), 183–184.
14. Hatta, M. (1953). *Bung Hatta's Speech: 2 Basics of Indonesia's Progress (1953)*. URL Access: https://www.youtube.com/watch?v=Oi_mj 2z5S24
15. The United Nations (UN). (2016). *Rate of Environmental Damage Increasing Across Planet but Still Time to Reverse Worst Impacts*. URL Access: https://www.un.org/sustainable development/blog/2016/05/rate-of-environ mental-damage-increasing-across -planet-but-still-time-to-reverse-worst-impacts/
16. Worldometer. (2023). *2023 World Population*. URL Access: https://www.worldometers.info/world-population/#:~:text=Population%20in%20the%20world%20is,it%20was%20at%20around%202%25.
17. Ritchie, H., Rodés-Guirao, L., Mathieu, E., Gerber, M., Ortiz-Ospina, E., Hasell, J., & Roser, M. (2023). *Population Growth*. URL Access: https://ourworldindata.org/population-growth
18. Bish, J. J. (2020). *Overpopulation: Cause and Effect*. URL Access: https://www.populationmedia.org/ the-latest/overpopulation-cause-and-effect
19. World Health Organization (WHO). (2023). *Disability*. URL Access: https://www.who.int/news-room/ fact-sheets/detail/disability-and-health
20. Haworth, M. (2018). *Neurotechnology and the End of Finitude*. Minneapolis: University of Minnesota Press.
21. Casey, E.J. (1962). *Biophysics Concepts and Mechanisms*. New York: Reinhold Publishing Corporation.

22. Science ABC. (2022). *What Are Neurons and How Do They Work?*. URL Access: https://www.youtube. com/watch?v=HUuUUJktL6E
23. Bear, M. F., Connors, B. W. , & Paradiso, M.A. (2016). *Neuroscience Exploring the Brain*. Philadelphia: Wolters Kluwer.
24. Krakauer, J. W. & Shadmehr, R. (2006). Consolidation of motor memory. *Trends in Neurosciences*, **29**(1), 58–64.
25. Ehret, J. (2019). *Using Neuroscience to Train Smarter, Not Harder*. URL Access: https://www.swimm ingworldmagazine.com/news/using-neuroscience-to-train-smarter-notharder/#google _ vignette
26. McManus, M.R. (2023). *What You Should Know About Muscle Memory to Help You Stay Fit*. URL Access: https://edition.cnn.com/2023/06/21/health/ muscle-memory-explainer-wellness/index. html
27. Kingston Technology Corporation. (2023). *Storage Chart*. URL Access: https://www.kingston.com/ en/memory-cards/storage-chart
28. Enfain. (2023). *Flash Drive Capacity Chart*. URL Access: https://enfain.com/faq/flash-drives-capacity -chart/
29. Toshiba Corporation. (2016). *Flash Memory*. URL Access: https://www.mouser.com/datasheet/2/1034 /catalog_en_20160331_ALQ00211-313225 5.pdf
30. Carnegie, D. (1947). *Little Known Facts About Well Known People*. Kingswood Surrey: The World's Work (1913) LTD.
31. Gordon, B. (2013). *Does Photographic Memory Exist?*. URL Access: https://www.scientificamerican. com/ article/i-developed-what-appears-to-be-a-ph/
32. Calinger, R. S. (2016). *Leonhard Euler: Mathematical Genius in the Enlightenment*. New Jersey: Princeton University Press.
33. Conway, M. A. & Haque, S. (1999). Overshadowing the Reminiscence Bump: Memories of a Struggle for Independence. *Journal of Adult Development*, **6**(1), 35–44.
34. Jansari, A. & Parkin, A. J. (1996). Things that Go Bump in Your Life: Explaining the Reminiscence Bump in Autobiographical Memory. *Psychology and Aging*, **11**(1), 85.
35. Ballesteros, S., Nilsson, L. G., & Lemaire, P. (2009). Ageing, Cognition, and Neuroscience: An Introduction. *European Journal of Cognitive Psychology*, **21**(2-3), 161–175.
36. Nyberg, L., Lövdén, M., Riklund, K., Lindenberger, U., & Bäckman, L. (2012). Memory Aging and Brain Maintenance. *Trends in Cognitive Sciences*, **16**(5), 292–305.
37. Ebbinghaus, H. (2013). [Image] Memory: A Contribution to Experimental Psychology. *Annals of Neurosciences*, **20**(4), 155.
38. Leibowitz, N., Baum, B., Enden, G., & Karniel, A. (2010). The Exponential Learning Equation as a Function of Successful Trials Results in Sigmoid Performance. *Journal of Mathematical Psychology*, **54**(3), 338–340.

39. Syndeon Soft. (2023). *The Learning Curve*. URL Access: http://www.flashcardlearner.com/articles/the-learning-curve/
40. Spiegel, M. R. (1971). *Schaum's Outline of Advanced Mathematics for Engineers and Scientists*. New York: The McGraw-Hill Companies, Inc.
41. Boas, M. L. (2006). *Mathematical Methods in the Physical Sciences Third Edition*. Massa-chusetts: John Wiley & Sons, Inc.
42. Weisstein, E. W. (2002). *The CRC Concise Encyclopedia of Mathematics*. Florida: CRC Press Company.
43. The World of Science. (2021). *How Are Memories Created & Stored? Brain Anatomy*. URL Access: https://www.youtube.com/watch?v=UTO6O0DNkgw
44. ScienceABC II. (2023). *How Does The Brain Store and Retrieve Memories?*. URL Access: https://www.youtube.com/watch?v=B3HWrmwY4zY
45. Be Smart. (2021). *How Your Brain Makes Its Own Electricity*. URL Access: https://www.youtube.com/watch?v=UZthGjcuTDs
46. Hamka. (1990). *Tafsir Al-Azhar Volume 7*. Singapore: National Library Pte Ltd.
47. Hamka. (2020). *Philosophy of Life*. Jakarta: Republika Publishers.
48. Lennox, J. (2023). *Oxford Mathematician Destroys Atheism (15 Minute Brilliancy!)*. URL Access: https://www.youtube.com/watch?v=VrIvwPConv0
49. Schopenhauer, A. (1909). *The World As Will And Idea*. London: Kegan Paul, Trench, Trübner & Co.
50. Nahvi, M. & Edminister, J. (2004). *Schaum's Outlines Teori dan Soal-soal Rangkaian Listrik Edisi Keempat*. Jakarta: Penerbit Erlangga.
51. Wikipedia. (2023). *Characterization (Materials Science)*. URL Access: https://en.wikipedia.org/wiki/Characterization_(materials_science)
52. Wikipedia. (2023). *Dielectric Spectroscopy*. URL Access: https://en.wikipedia.org/wiki/Dielectric_spectroscopy
53. Wikipedia. (2023). *Analytical Chemistry*. URL Access: https://en.wikipedia.org/wiki/Analytical_chemistry
54. The Physiological Society. (2015). *The squid and its giant nerve fibre Part 1*. URL Access: https://www.youtube.com/watch?v=I6jxrxcLxiI
55. Gage, G. & Marzullo, T. (2022). *How Your Brain Works: Neuroscience Experiments for Every-One*. Massachusetts: The MIT Press.
56. Sinauer Associates, Inc. (2018). *The Voltage Clamp Method*. URL Access: https://www.youtube.com/ watch?v=3F-Uw1RZqAQ
57. Purdue University. (2016). *Introduction to Bioelectricity | PurdueX on edX | Course About Video*. URL Access: https://www.youtube.com/watch?v=gH819ka2EmU
58. Mayo Foundation for Medical Education and Research (MFMER). (2023). *EEG*

(electro-encephalogram). URL Access: https://www.mayoclinic. Org

59. Griffiths, D. J. (2013). *Introduction to Electrodynamics*. Illinois: Pearson Education, Inc.
60. Zhang, H. & Jacobs, J. (2015). Traveling Theta Waves in the Human Hippocampus. *Journal of Neuroscience*, **35**(36), 12477–12487.
61. Rudoler, J. H., Herweg, N. A., & Kahana, M. J. (2023). Hippocampal Theta and Episodic Memory. *Journal of Neuroscience*, **43**(4), 613–620.
62. Wikipedia. (2023). *Neuroimaging*. URL Access: https://en.wikipedia.org/wiki/Neuroimaging
63. Alt Shift X. (2015). M*agnetoencephalography: Measuring Brain Activity with Magnetism*. URL Access: https://www.youtube.com/watch?v=BLfwZ1NPNKY
64. Toufic, J. (2019). *Radical Closure*. Singapore: National Gallery Singapore.
65. Imperial College London. (2023). *Neurotechnology*. URL Access: https://www.imperial.ac.uk/study/courses/postgraduate-taught/neurotechnology/
66. University of Otago. (2023). *Study Neuroscience at Otago*. URL Access: https://www.otago.ac.nz/courses/subjects/neur
67. White, S. W., Richey, J. A., Gracanin, D., Bell, M. A., LaConte, S., Coffman, M., Trubanova, A., & Kim, I. (2015). The Promise of Neurotechnology in Clinical Translational Science. *Clinical Psychological Science*, **3**(5), 797–815.
68. News Medical. (2022). *Neurotechnology Shows Potential for Future Medical Interventions in Humans*. URL Access: https://www.news-medical.net/news/20221109/Neurotechnology-shows-potential-for-future-medical-interventions-in-humans.aspx
69. UNESCO. (2023). *From Paralysis to Possi-bilities: Journey with Neurotechnology*. URL Access: https://www.unesco.org/en/articles/paralysis-possibilities-journey-neurotechnology
70. UNESCO. (2023). *Ethics of Neurotechnology*. URL Access: https://www.unesco.org/en/ethics-neurotech#:~:text=Neurotechnology%20is%20a%20%20fast%2Dexpanding,technologies%20that%20interact%20with%20it
71. International Disability Alliance (IDA). (2023). *Neurotechnology and the Rights of Persons with Disabilities*. URL Access: https://www.ohchr.org/sites/default/files/documents/hrbodies/hrcouncil/advisorycommittee/neurotechnology/03-ngos/ac-submission-cso-international-disability-alliance.docx
72. International Neuroethics Society (INS). (2023). *Basics of Neuroethics*. URL Access: https://www.neuroethicssociety.org/what-is-neuroethics
73. Stanford Encyclopedia of Philosophy (SEP). (2021). *Neuroethics*. URL Access: https://plato.stanford.edu/entries/neuroethics/
74. Wikipedia. (2023). *Neuroethics*. URL Access: https://en.wikipedia.org/wiki/Neuroethics

75. Wikipedia. (2023). *Developmental Bioelectricity*. URL Access: https://en.wikipedia.org/wiki /Developmental_bioelectricity#cite_note-51
76. Magnis-Suseno, F. (1987). *Etika Dasar, Masalah-masalah Pokok Filsafat Moral*. Yogyakarta: Penerbit Kanisius.

IPC

Indonesian Physics Communication

Department of Physics, Universitas Riau, Pekanbaru, Indonesia
p-ISSN 1412-2960 | e-ISSN 2579-521X

Vol. 22 | No. 2
July 2025

Web: https://kfi.ejournal.unri.ac.id
E-mail: kfi@ejournal.unri.ac.id

Synthesis and characterization of optical properties of barium titanate ($BaTiO_3$) with the addition of moringa, banana, matoa, and ketapang leaves extracts

Rahmi Dewi, Apriwandi, Yanuar Hamzah, Eza Tirta Sari*, Kheny Kernila Butarbutar, Nadja Melika Putri, Nazhiwa Nathania, Surya Ardika Aritonang, Titin Hartini, Fitri Hayati, Maharani Nur Maslyah, Seli Novalin Sawitri, Siti Komariah, Septia Nursyahara, Nasywa Nuraini, Rihla Datul Aisy, Putri Safira, Rusmanianty, Dinda Pratiwi, Adela, Veny Sriulina Pasaribu, Vina Naomi Azhara, Ayang Febrita

Department of Physics, Universitas Riau, Pekanbaru 28293, Indonesia

*Corresponding author: eza.tirta0199@student.unri.ac.id

ABSTRACT

Environmentally friendly synthesis of barium titanate ($BaTiO_3$) nanoparticles was conducted using natural leaf extracts of *Moringa oleifera*, *Musa spp.*, *Pometia pinnata*, and *Terminalia catappa* as green dopants via the sol-gel method. This study aims to evaluate the influence of different leaf extracts on the optical properties of $BaTiO_3$ characterized by UV-Vis spectroscopy. Each sample exhibited distinct absorption spectra, reflecting variations in phytochemical composition among the extracts. The results showed that *Terminalia catappa* and *Pometia pinnata* extracts produced the highest band gap values, 3.36 eV and 3.35 eV respectively, indicating optical activity in the ultraviolet region. *Musa spp.* extract resulted in a band gap of 2.81 eV, while *Moringa oleifera* extract yielded the lowest value of 2.59 eV. These differences suggest that the type of plant extract significantly affects the optical characteristics of the synthesized $BaTiO_3$. This research highlights the potential use of local biomass in the development of functional $BaTiO_3$-based materials through green synthesis approaches.

Keywords: Band gap; $BaTiO_3$; green synthesis; leaf extract; UV-Vis spectroscopy

Received 18-06-2025 | Revised 02-07-2025 | Accepted 10-07-2025 | Published 31-07-2025

INTRODUCTION

In the modern era, the development of science and technology relies heavily on human ability to engineer materials on a smaller scale, especially at the nanometer level (1 – 100 nm). Within this size range, all properties (chemical, physical, and biological) change fundamentally in both individual atoms/molecules and their masses. New applications of nanoparticles and nanomaterials are growing rapidly in various fields due to their completely new or improved properties based on their size, distribution and morphology. This phenomenon is caused by high surface effects and quantum effects, which result in drastic changes in the conductivity, reactivity, stability and optical properties of the material [1].

One of the inorganic nanoparticles that is widely researched is barium titanate ($BaTiO_3$). Barium titanate ($BaTiO_3$) is an inorganic ceramic material based on a perovskite structure (ABO_3) which has ferroelectric properties at room temperature. This distinctive structure allows the titanium (Ti^{4+}) ion to shift slightly from its symmetrical position in the crystal lattice, generating a spontaneous dipole moment that can be manipulated by an external electric field. In addition, this material also shows good thermal and optical stability, and has a high dielectric constant that can be adapted to the synthesis method and processing conditions [2]. However, conventional $BaTiO_3$ synthesis processes often involve hazardous chemicals and extreme conditions that are not environmentally friendly.

As a solution to this challenge, a green synthesis approach has been developed which utilizes plant extracts as reducing and stabilizing agents in the formation of

nanoparticles. This method is considered more economical, safe and environmentally friendly. Leaf extracts contain phytochemical compounds such as flavonoids, polyphenols, tannins and alkaloids which are able to reduce metal ions to nanoforms and at the same time prevent particle agglomeration [3, 4].

In the context of Indonesia which is rich in biodiversity, the use of local plants for nanoparticle synthesis has great potential. Several plants such as Moringa oleifera leaves, banana leaves (*Musa spp.*), matoa leaves (*Pometia pinnata*) and ketapang leaves (*Terminalia catappa*) are known to contain various bioactive compounds. Differences in the composition of these compounds are expected to influence the size, shape and optical properties of the resulting nanoparticles.

To determine the optical characteristics of the synthesized nanoparticles, the UV-Vis (Ultraviolet-Visible Spectroscopy) characterization technique was used. This technique is able to identify typical absorption peaks of nanoparticles, and is used to calculate band gap energy which is closely related to particle size and electronic structure [5].

This research aims to analyze the UV-Vis spectrum characteristics of $BaTiO_3$ nanoparticles synthesized using extracts of Moringa leaves, banana leaves, matoa leaves and Ketapang leaves. By comparing the optical characterization results of each extract, it is hoped that the influence of the phytochemical composition on the performance and quality of $BaTiO_3$ nanoparticles produced in a green way can be determined.

LITERATURE REVIEW

Barium titanate ($BaTiO_3$) is a lead-free ferroelectric material with a perovskite crystal structure. This material exhibits spontaneous polarization properties that can be reversed by an external electric field, making it ideal for use in various electronic applications [6]. As the Curie temperature approaches, the structure of $BaTiO_3$ undergoes a phase transition from cubic to tetragonal, which significantly affects its dielectric and ferroelectric response [7]. The properties of $BaTiO_3$ are strongly influenced by the morphology and particle size, which can be controlled through synthetic methods such as the sol-gel process, resulting in a very homogeneous material at the nanoscale [8]. Doping with La^{3+} has been shown to lower the transition temperature, reduce the crystallite size, and increase the ferroelectric relaxant properties which are relevant to the development of $BaTiO_3$-based materials [9]. In addition, $BaTiO_3$ thin films synthesized on flexible substrates show excellent ferroelectric stability, making them ideal for further characterization through UV-Vis spectroscopy, which can detect optical interactions and electronic structure modifications [10].

The sol-gel method is a wet chemical synthesis technique that allows precise control over the composition and structure of materials at the nanometer scale. This makes it ideal for producing materials such as BaTiO3 with small crystallite sizes and high homogeneity [11]. This process involves the hydrolysis and condensation of metal precursors to form a gel, which is then dried and calcined. In the synthesis of $BaTiO_3$, it has been shown that rapid heating can increase the dielectric constant and reduce surface roughness [12]. Furthermore, the incorporation of complexing agents and natural porogens, such as tannins, facilitates the development of ideal pore structures for applications in optics, sensors, and biomedicine [13, 14].

UV-Vis spectrophotometry is an optical characterization method used to analyze the interaction of light with materials, especially to detect changes in electronic energy due to chemical bonds or particle aggregation [15]. This technique uses a wavelength of 300 – 800 nm to monitor electronic transitions, making it suitable for observing changes in the optical structure of ferroelectric materials $BaTiO_3$ [16].

RESEARCH METHODS

This research begins with the preparation of the tools and materials used. The glass bottle to

be used is washed first then sonicated for 5 minutes using Aquades and 5 minutes using alcohol at a temperature of 40°C. Then dried in the oven at 150°C for 30 minutes to remove any impurities that are still attached.

Next, all the chemicals to make the BT (barium titanate) solution are weighed accurately using a digital scale with an accuracy of up to three digits after the decimal point. With a composition of 1.234 grams of Ba powder, 3 drops of Acetyl Aceton as the solvent, stirred for 2 hours and 2 grams of Ti powder with 5 ml of Ethanol + 5 ml of alcohol as the solvent and stirred for 25 hours. Leave the solution for at least one night at a temperature of 4°C to form a gel or clear solution which will be used for the next process.

Next, leaf extract was made as a natural doping agent. In this study, 4 leaf extracts were used, namely moringa leaves (*Moringa oleifera*), banana leaves (*Musa spp.*), matoa leaves (*Pometia pinnata*) and ketapang leaves (*Terminalia catappa*). Old leaves are washed clean, then dried in the oven at 150°C for 30 minutes. The dried leaves are ground using a blender until they become powder. A total of 5 grams of leaf powder was then dissolved in 100 mL of distilled water and heated at 80°C for approximately 10 minutes while stirring, until the solution was brownish in color. The extract is then filtered and stored in the refrigerator to maintain its stability.

For the doping process, the previously prepared leaf extracts were added to the solution and stirred again for 3 hours using a magnetic stirrer until mixed homogeneously. The final solution was stored in a tightly closed glass bottle and ready for the UV-VIS characterization process.

RESULTS AND DISCUSSION

Synthesis Results of $BaTiO_3$ with Moringa Leaves (*Moringa oleifera*)

UV-Vis absorbance spectrum of barium titanate using a UV-Vis Spectrometer at a resolution of 1 nm with a wavelength range of 300-800 nanometers. Figure 1 shows the UV-Vis absorption of $BaTiO_3$ synthesis with Moringa leaf extract.

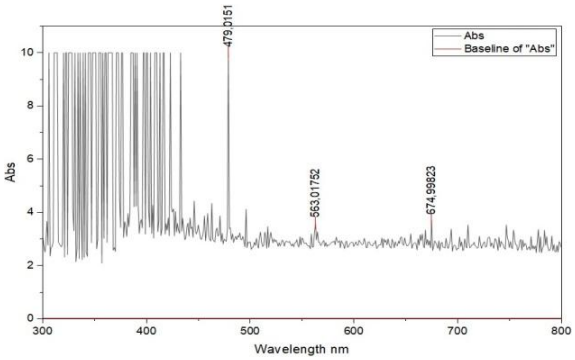

Figure 1. UV-Vis absorbance spectrum of the $BaTiO_3$ compound synthesized using moringa leaf extract.

UV-Vis analysis of the spectrum shown shows a number of important peaks at a number of wavelengths, namely at 479.02 nm, 563.02 nm, and 674.99 nm. The first peak at 479.02 nm shows a high level of absorbance, possibly related to the electronic transition of the molecule in the UV-Vis range, indicating that the target compound interacts with light at that wavelength. The second peak detected at 563.02 nm showed a decrease in absorbance compared to the previous peak, but remained significant enough to indicate the presence of other components in the sample, which could be indicated as dyes or compounds with absorbance in the green color range. The last peak at 674.99 nm shows a lower absorbance level, which is usually associated with the red color group.

Synthesis Results of $BaTiO_3$ with Banana Leaves (*Musa spp.*)

The absorbance spectrum in Figure 2 shows the optical characteristics of the Barium Titanate compound synthesized using the sol-gel method based on banana leaf extract. The highest absorbance peak was detected at a wavelength of around 441 nm with an absorbance intensity of more than 10 a.u., which indicates an electronic transition from

the valence band to the conduction band, typical for semiconductor materials. This peak indicates that the barium titanate compound formed has a fairly good crystalline structure and is able to absorb light energy in the UV-Vis spectrum range.

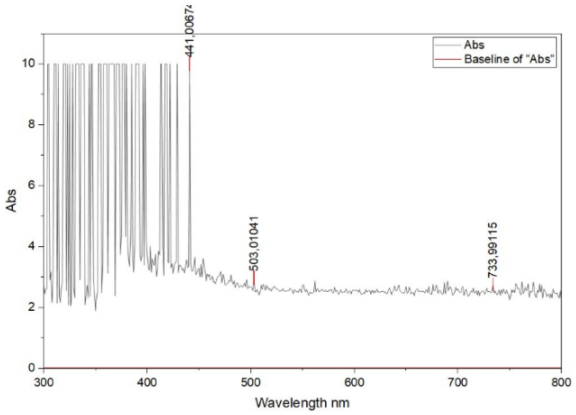

Figure 2. UV-Vis absorbance spectrum of the $BaTiO_3$ compound synthesized using banana leaf extract.

In addition, the spectrum shows a gradual decrease in absorbance after 500 nm, with slight signal interference in the 300 – 450 nm range, possibly caused by the presence of residual organic compounds from banana leaf extract that have not been completely decomposed. The presence of a small absorption at around 733 nm indicates the possible existence of oxygen defects or electron-hole recombination on the material surface.

Synthesis Results of $BaTiO_3$ with Matoa Leaves (*Pometia pinnata*)

Seen in Figure 3, the sample graph shows the results of UV-Vis spectroscopic characterization of the results of the synthesis of BaTiO3 with matoa leaf extract in the wavelength range of 300 – 800 nm. The absorbance curve (Abs) describes the intensity of light absorption by the sample at each wavelength tested.

It can be seen that there is a very significant absorption peak at a wavelength of around 370 nm, with a very high absorbance value, close to 10. This peak is likely the main absorption band of the sample, and can be used to calculate the bandgap energy if necessary.

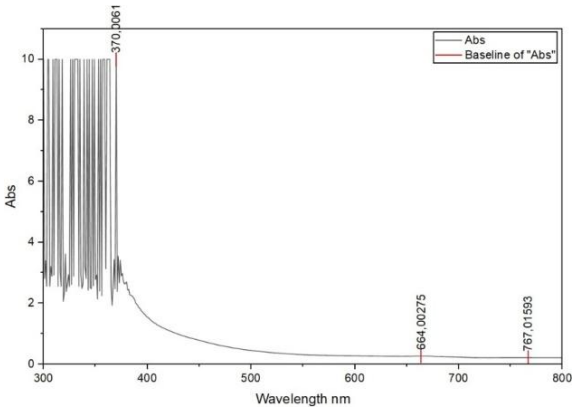

Figure 3. UV-Vis absorbance spectrum of the $BaTiO_3$ compound synthesized using matoa leaf extract.

Apart from that, two other small peaks were also detected at wavelengths of 664 nm and 767 nm, with relatively low absorbance values. These peaks may be related to minor electronic transitions, excitation defects, or the presence of trace compounds or contaminants. The region between 400 – 800 nm shows a sharp decrease in absorbance, indicating that the sample has high transparency in the visible region. This could indicate that the sample has potential applications as an optoelectronic material, such as in solar cells or optical sensors.

Synthesis Results of BaTiO3 with Ketapang Leaves (*Terminalia catappa*)

The UV-Vis absorbance spectrum of the solution resulting from the synthesis of barium titanate using ketapang (Terminalia catappa) leaf extract is shown in Figure 4. Measurements were carried out in the wavelength range 300 – 800 nm using a resolution of 1 nm.

The graphic results show three main absorption peaks at wavelengths of 368.997 nm, 375.007 nm, and 407.981 nm with very high absorbance values of more than 10 absorbance units (a.u). This shows that the synthesized material has a strong ability to absorb light in the ultraviolet region, which indicates a transition of electrons from the

valence band to the conduction band, as generally occurs in semiconductor materials.

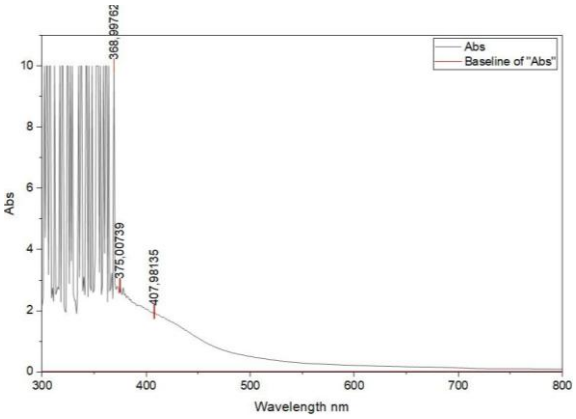

Figure 4. UV-Vis absorbance spectrum of the $BaTiO_3$ compound synthesized using ketapang leaf extract.

Table 1. Band gap energy of the $BaTiO_3$ compound synthesized using green leaf extract.

Sample type	E_{gap} (eV)
$BaTiO_3$ + moringa leaf extract	2.59
$BaTiO_3$ + banana leaf extract	2.81
$BaTiO_3$ + matoa leaf extract	3.35
$BaTiO_3$ + ketapang leaf extract	3.36

After passing a wavelength of 407 nm, the absorbance curve shows a consistent decrease and tends to stabilize towards a wavelength of 800 nm. This decrease in absorbance indicates that the material has a limited optical response outside the UV region. This graph shows that barium titanate synthesized using ketapang leaf extract successfully forms an optically active structure in the UV region.

From the results of the UV-Vis Spectrophotometer Characterization of $BaTiO_3$ with green leaf extract which has been explained, the band gap energy results can be shown in Table 1. Ketapang and matoa leaf extracts produce the largest band gap (± 3.35 – 3.36 eV), indicating optical activity in the UV region making them suitable for applications such as UV sensors or photocatalysts. Banana leaves produce a medium band gap (± 2.81 eV), absorbing light in the violet to blue region. Meanwhile, Moringa leaves have the smallest band gap (± 2.59 eV), allowing wide absorption of visible light and potentially being used in solar cells or photodetectors.

CONCLUSION

This research succeeded in synthesizing and characterizing barium titanate ($BaTiO_3$) material using the sol-gel method with the addition of moringa leaf extract, banana leaves, matoa leaves and ketapang leaves as natural doping agents. The main aim is to observe the influence of the phytochemicals of each extract on the optical properties of the resulting material. The UV-Vis characterization results show that each extract produces different light absorption spectra and band gap values. Ketapang and matoa leaf extracts produced the highest band gaps of around 3.36 eV and 3.35 eV, indicating optical activity in the UV region and potential application in UV sensors or photocatalysts. Banana leaves have a moderate band gap (2.81 eV), while moringa leaves show the lowest band gap (2.59 eV), allowing light absorption in the visible region, making them potential candidates for solar cell or photodetector applications. Thus, the use of leaf extract as a green agent in the synthesis of $BaTiO_3$ is proven not only to be environmentally friendly but also to significantly influence the optical characteristics of the material.

REFERENCES

1. Ahmed, S., Ahmad, M., Swami, B. L., & Ikram, S. (2016). A review on plants extract mediated synthesis of silver nanoparticles for antimicrobial applications: A green expertise. *Journal of Advanced Research*, **7**(1), 17–28.
2. Wodecka-Duś, B., Dziwoki, T., Wójcik, A., Dziubek, K., Adamus-Włodarczyk, A., Jaskólski, D., & Lenartowicz-Klik, M. (2020). *Mechanochemical Synthesis of $BaTiO_3$ Powders and Evaluation of Their Acrylic Dispersions*. **13**(15), 3275.
3. Singh, J., Dutta, T., Kim, K.-H., Rawat, M., Samddar, P., & Kumar, P. (2018).

'Green' synthesis of metals and their oxide nanoparticles: Applications for environmental remediation. *Journal of Nanobiotechnology*, **16**(84).
4. Sharma, V. K., Yngard, R. A., & Lin, Y. (2009). Silver nanoparticles: Green synthesis and their antimicrobial activities. *Advances in Colloid and Interface Science*, **145**(1–2), 83–96.
5. Manoj, D., & Santhosh, P. (2021). UV–Vis spectroscopic analysis of synthesized ZnO nanoparticles using banana peel extract. *Materials Todasy: Proceedings*, **43**, 2647–2651.
6. Azuma, H., Ogawa, T., Ogata, S., Kobayashi, R., Uranagase, M., Tsuzuki, T., & Wendler, F. (2025). Unique temperature-dependence of polarization switching paths in ferroelectric $BaTiO_3$: A molecular dynamics simulation study. *Acta Materialia*, **296**, 121216.
7. Carroll, E. L., Killeen, J. H., Feteira, A., Dean, J. S., & Sinclair, D. C. (2025). Influence of electrode contact arrangements on polarisation-electric field measurements of ferroelectric ceramics: A case study of $BaTiO_3$. *Journal of Materiomics*, **11**, 100939.
8. Ouyang, J., Xue, Y., Yuan, M., Song, C., Wang, K., Zhao, Y., Cheng, H., Zhu, H., & Liu, C. (2025). Resolving nanograin morphology and sub-grain nanodomains via scanning probe acoustic microscopy in high energy density $BaTiO_3$ ferroelectric films. *Journal of Materiomics*, **11**, 100893.
9. Moutaouaffiq, A., Belhajji, M., Didi Seddik, A., Tahiri, A., Ali, E., Hajji, L., Rjeb, A., Paramasivam, P., Ghoneim, S. S. M., & Abou Sharaf, A. B. (2025). Lanthanum-doped $BaTiO_3$ ceramics: Structural, dielectric, and ferroelectric properties. *Results in Engineering*, **25**, 104466.
10. Liu, X., Wei, C., Sun, T., Zhang, F., Li, H., Liu, L., Peng, Y., Li, H., & Hong, M. (2025). A $BaTiO_3$-based flexible ferroelectric capacitor for non-volatile memories. *Journal of Materiomics*, **11**, 100870.
11. Paalo, M., Yegit, S. S., Moumaneix, L., Kallio, T., & Janes, A. (2025). Synthesis of zirconium carbide via sol-gel method as a precursor for micro- and mesoporous carbide-derived carbon materials. *Carbon Trends*, **19**, 100494.
12. Liu, Y., Li, S., Gallucci, F., & Rebrov, E. V. (2024). Sol-gel synthesis of tetragonal $BaTiO_3$ thin films under fast heating. *Applied Surface Science*, **661**, 160086.
13. Arzani, F. A., Pechina, B., & dos Santos, J. H. Z. (2025). Tannin as a porogenic agent in the synthesis of silica by an acid-catalyzed sol-gel process. *Results in Surfaces and Interfaces*, **20**, 100561.
14. Lincuna, J. R. S., Ueda, K., & Narushima, T. (2025). Citric acid-assisted sol–gel synthesis of highly reactive borate-based bioactive glass powders. *Journal of Non-Crystalline Solids*, **666**, 123637.
15. Guo, Y., Han, Z., Zhang, J., Lu, Y., Li, C., & Liu, G. (2024). Development of a high-speed and ultrasensitive UV/Vis-CM for detecting total triterpenes in traditional Chinese medicine and its application. *Heliyon*, **10**, 32239.
16. Berasarte, I., Bordagaray, A., Garcia-Arrona, R., Ostra, M., & Vidal, M. (2025). Silver nanoparticles for the colorimetric determination of electrolytes by UV–vis spectrophotometry and digital image analysis. *Sensing and Bio-Sensing Research*, **49**, 100831.

IPC

Indonesian Physics Communication

Department of Physics, Universitas Riau, Pekanbaru, Indonesia
p-ISSN 1412-2960 | e-ISSN 2579-521X

Vol. 22 | No. 2
July 2025

Web: https://kfi.ejournal.unri.ac.id
E-mail: kfi@ejournal.unri.ac.id

Reflectivity of Bragg grating fiber on human respiration using InGaAs photodiode converter system

Dian Putri Oktavia[1], Saktioto[1,*], Dwi Hanto[2], Syamsudhuha[3], Rina Amelia[4], Tengku Emrinaldi[1]

[1]Department of Physics, Universitas Riau, Pekanbaru 28293, Indonesia
[2]Research Center for Photonics, KST BJ HABIBIE, South Tangerang 15314, Indonesia
[3]Department of Mathematics, Universitas Riau, Pekanbaru 28293, Indonesia
[4]Department of Community Medicine, Universitas Sumatera Utara, Medan 20155, Indonesia

*Corresponding author: saktioto@lecturer.unri.ac.id

ABSTRACT

Respiration is a vital process characterized by exchanging oxygen and carbon dioxide. Indicators such as respiratory rate are essential for detecting pathological conditions, such as pneumonia and heart failure. This research aims to develop a respiratory sensor system based on fiber Bragg grating (FBG) as an innovative alternative in high electromagnetic field environments. The system utilizes FBG optical fibers to detect strain changes due to respiratory activity, providing a sensitive, safe, and highly electromagnetic environment-compatible solution. The study used FBG with variations in reflectivity of 30%, 50%, 70%, and 90%. FBGs are installed inside oxygen masks at five different points to monitor wavelength changes during respiratory activity. The measurement method involves an optical system with an interrogator and an electrical method using an InGaAs photodiode converter to convert an optical signal into an electrical signal visualized in LabVIEW. Respondents were tested in three activities: stillness, walking, and running. Variations in sensor reflectivity and position in masks were evaluated to determine sensitivity to respiratory changes. The data is collected as a graph of wavelength against time. The result showed that the change in the wavelength of the FBG correlated with the intensity of respiratory activity. The reflectivity of 90% results in the highest sensitivity, allowing for more accurate detection of strain changes. The position of the sensor at the center point of the mask demonstrates the most linear results, indicating optimal sensitivity. Physical activity, such as running, produces the greatest strain on the optical fiber. This study proves the potential of FBG as a precision medical sensor for respiratory monitoring applications.

Keywords: Fiber Bragg grating; InGaAs; optical fiber; reflectivity; uniform

Received 28-04-2025 | Revised 12-05-2025 | Accepted 15-05-2025 | Published 31-07-2025

INTRODUCTION

Breathing is the exchange of oxygen and carbon dioxide between the body's cells and the environment [1]. Measuring respiratory rate is an important indicator of the body's systems because it is highly sensitive to pathological changes in humans, such as pneumonia, heart disease, and clinical deterioration [2]. Therefore, appropriate technological solutions for measuring respiratory rate have important implications for healthcare, the workplace, and sports.

Several studies have been conducted on measuring respiratory rate using optical sensors using FBGs. The FBG is placed on the chest surface, utilizing the FBG's sensing properties. When humans breathe, movement occurs on the chest surface, and the FBG measures the resulting strain changes [3]. The FBG, as a respiratory sensor, is placed under the nose using a V-shaped rubber band and a sensor holder attached to the nose. The FBG is connected to a Micron Optics data acquisition device to monitor airflow in and out of the nose. Respiratory patterns can be viewed on the device as a strain-versus-time curve [4].

Another study conducted by Liang et al., 2006, utilized the FBG's temperature parameter to measure respiratory rate [5]. The FBG was placed on the nose with the aid of an oxygen mask and connected to a laser source and then a

detector to read the output signal on an oscilloscope. The results of this study indicate that respiratory flow rate can be estimated from the sensor's response in the form of a voltage-time graph. Previous FBG research has used only one optical method and has minimal variation in the activity and placement of the FBG among respondents.

This study developed a respiratory rate sensor system using an FBG with a wavelength of 1550 nm and varying reflectivity (30%, 50%, 70%, and 90%). The optical signal from the FBG was converted into an electrical signal using an Indium Gallium Arsenide (InGaAs) photodiode, which has high sensitivity and fast response in the 1100 – 1700 nm range [6]. Data from the sensor was analyzed using LabVIEW software, and respiratory patterns were observed through changes in the FBG's wavelength.

LITERATURE REVIEW

Respiratory System

The human respiratory system consists of the airways and lungs, which are responsible for gas exchange. Respiratory monitoring is important in the diagnosis and treatment of respiratory diseases, as well as for monitoring patient condition during physical rehabilitation. One way to monitor respiration is by using sensors that can detect changes in pressure or wavelength associated with body movement due to breathing [7].

FBG-based sensor systems have been widely used for these applications due to their ability to detect strain in optical fibers caused by body movement. When a person breathes, chest and abdominal movements can change the wavelengths reflected by the FBG, which can be measured to obtain information about breathing patterns [8].

Fiber Bragg Grating (FBG) Technology

Fiber Bragg Grating (FBG) is an optical sensor technology that works by altering the wavelength of light reflected by an optical fiber when changes occur in the fiber, such as strain or temperature. FBGs offer advantages in accuracy and resistance to electromagnetic interference that often plagues traditional sensor technologies [9].

FBGs are used in a variety of applications, including temperature, pressure, and strain sensors. In respiratory applications, FBGs can be used to detect small movements generated by changes in air volume during breathing. This technology has proven particularly useful in medical applications and mechanical measurements [8].

Indium Gallium Arsenide (InGaAs) Photodiodes

InGaAs photodiodes are semiconductor devices sensitive to infrared wavelengths and are used in applications requiring light detection in this wavelength range. These photodiodes perform better in FBG-based sensor systems due to their superior ability to detect weak signals originating from the optical wavelengths used [10].

InGaAs photodiodes are used in various optical communications and remote sensing applications due to their ability to detect wavelengths longer than visible light.

RESEARCH METHODS

This study used an experimental method by testing an FBG-based sensor system mounted on an oxygen mask to detect wavelength changes during breathing activity. The system consists of an FBG optical fiber attached to an oxygen mask worn by the test subjects. The testing process recorded wavelength changes that occurred while the subjects were stationary, walking, and running.

The research design involved several steps, starting with a light source (TLS), followed by an OSA (Optical Light Sensor) to observe the FBG reflectivity spectrum, and then installing the FBG sensor on the mask (as shown in Figure 1). This data was then analyzed, as

shown in Figure 1, to capture data during breathing activity. The resulting data were then analyzed in the form of a wavelength versus time plot displayed in LABView. The obtained data were analyzed to evaluate the sensor system's sensitivity to human respiration. (See Figure 2 for the research design)

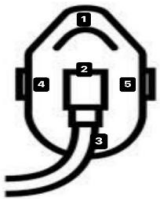

Figure 1. Illustration of the FBG position on the mask.

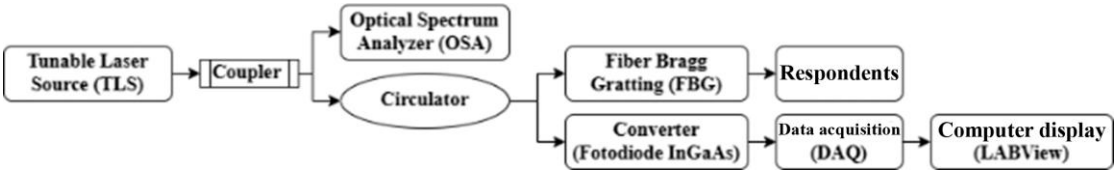

Figure 2. Research design.

RESULTS AND DISCUSSION

Test Results

Test results showed that the FBG sensor with 90% reflectivity produced a higher reflection intensity, as seen in the reflectivity spectrum, indicating that the sensor system was more sensitive to wavelength changes. The placement of the FBG on the mask also affected the linearity of wavelength changes across each respondent's activity. Running resulted in the largest wavelength changes, followed by walking and standing still.

Discussion

The discussion of the test results showed that the FBG sensor with an InGaAs photodiode performed well in detecting wavelength changes during human breathing. The influence of reflectivity on the sensitivity of the sensor system also showed significant results, with higher reflectivity improving the system's detection capability. Figure 3 shows the wavelength changes at each reflectivity level, with reflectivity levels of 30%, 50%, 70%, and 90% symbolized by A, B, C, and D, respectively.

The wavelength changes based on the FBG placement point show that position 2, in the center of the mask, shows a linear trend as the respondent's activity increases. The figure shows testing conducted at 50% reflectivity.

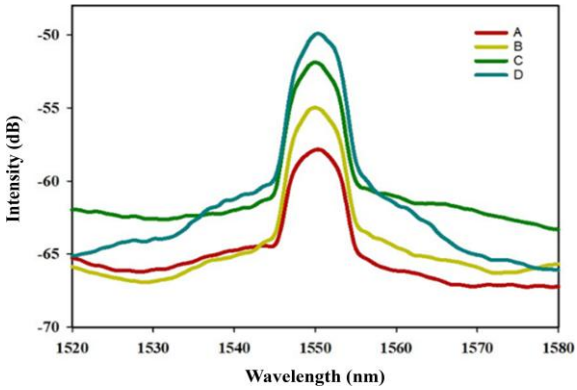

Figure 3. FBG reflectivity spectrum.

The FBG strain value is determined using the following equation:

$$\varepsilon = \frac{\Delta\lambda_B \; activity}{1550 \; nm \; (1 - 0.22)} \quad (1)$$

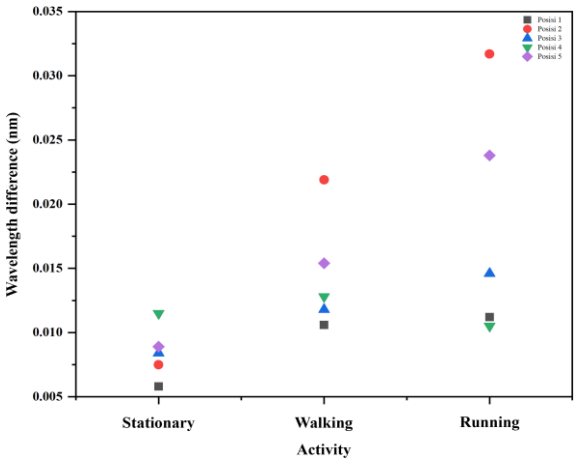

Figure 4. Difference in wavelength changes based on activity.

The respondent's activity influences the wavelength changes in the FBG. The strain

values for each measured activity indicate that running has the greatest FBG strain value (see Figure 4). The strain values and graph based on activity are shown in Table 1 and Figure 5.

Table 1. FBG strain values based on respondent activity.

FBG	Strain value (10^{-5})		
	Stationary	Walking	Running
A	1.16	1.28	1.91
B	0.62	1.81	2.62
C	0.70	1.34	2.10
D	1.01	0.97	1.43

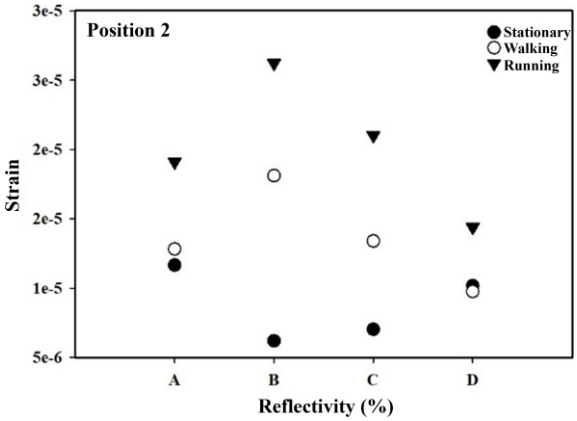

Figure 5. FBG strain between activities.

Increased activity causes an increase in lung pressure and volume, which directly affects the changes in wavelength detected by the FBG sensor.

CONCLUSION

This research has successfully developed an FBG-based sensor system with an InGaAs photodiode that can detect wavelength changes during human breathing. This system has great potential for medical applications, particularly for respiratory monitoring in patients with respiratory disorders.

REFERENCES

1. Ganong, W. F. (1991). Respiratory adjustment in health & disease. *Review of Medical Physiology*, **37**, 632–647.
2. Cretikos, M. A., Bellomo, R., Hillman, K., Chen, J., Finfer, S., & Flabouris, A. (2008). Respiratory rate: the neglected vital sign. *Medical Journal of Australia*, **188**(11), 657–659.
3. Tavares, C., Leitão, C., Lo Presti, D., Domingues, M. F., Alberto, N., Silva, H., & Antunes, P. (2022). Respiratory and heart rate monitoring using an FBG 3D-printed wearable system. *Biomedical Optics Express*, **13**(4), 2299–2311.
4. Pant, S., Umesh, S., & Asokan, S. (2018). Fiber Bragg grating respiratory measurement device. *2018 IEEE MeMeA*, 1–5.
5. Liang, Y., Mazzolini, A. P., & Stoddart, P. R. (2006). Fibre Bragg grating sensor for respiratory monitoring. *ACOFT/AOS 2006*, 75–77.
6. Rajamani, V., & Chakrabarti, P. (1999). Noise performance of an InP/InGaAs superlattice Avalanche Photodiode. *Optical And Quantum electronics*, **31**(1), 69–76.
7. Saktioto, S., Bintang, S. H. M., Emrinaldi, T., Zamri, Z., Samudra, M. R., & Soerbakti, Y. (2025). Existence of Fiber Bragg Grating Sensors Based on Power Input and Transmission Distance. *Journal of the Physical Society of Indonesia*, **1**(1), 45–50.
8. Kaniewski, J., Muszalski, J., & Piotrowski, J. (2004). Recent advances in InGaAs detector technology. *Physica Status Solidi (A)*, **201**(10), 2281–2287.
9. Personick, S. D. (2013). *Fiber optics: technology and applications*. Springer Science & Business Media.
10. Saktioto, S., Syafri, A. A., Mulhida, M., Widiyatmoko, B., Hanto, D., Soerbakti, Y., Fardinata, R., Okfalisa, O., Irawan, D., & Amelia, R. (2025). Wearable FBG strain flexibility in supplemental oxygen-assisted respiratory examination. *Journal of Applied Science and Engineering*, **28**(11), 2139–2147.